TUM School of Computation, Information and Technology
Technische Universität München

Whole Brain Vasculature Analysis Using Advanced Learning Models

Johannes Christian Paetzold

Vollständiger Abdruck der von der TUM School of Computation, Information and Technology der Technischen Universität München zur Erlangung des akademischen Grades eines

Doktors der Naturwissenschaften (Dr. rer. nat.)

genehmigten Dissertation.

Vorsitzender:
Prof. Dr. Stephan Günnemann

Prüfende der Dissertation:
1. Prof. Dr. Bjoern H. Menze
2. apl. Prof. Dr. Jan St. Kirschke

Die Dissertation wurde am 24.5.2022 bei der Technischen Universität München eingereicht und durch die TUM School of Computation, Information and Technology am 8.12.2022 angenommen.

Abstract

The brain's vascular network supplies oxygen to the brain's 86 billion neurons. Therefore, the microvasculature is firmly linked to the neural organization. As a result, both neurons and brain vessels build a complementary, ultra-complex network. Simultaneously, studying these networks is vital to understand human intelligence and brain functionality. The sheer complexity of the vascular network challenges conventional image processing methods beyond their limit, motivating the need for a dedicated set of machine learning concepts to extract a comprehensive hierarchical understanding of the vasculature. In response to this challenge, this thesis reports my work on the application and development of advanced machine learning models to understand brain vessel networks. Intriguingly, the neurons and their functional organization inspired the artificial intelligence methods, which we use to study their own organization, making the brain and its neurons and vessels a unique research domain. At the core of my work are three studies that contribute to the fields of machine learning and vascular biology. 1) In the first study, we show the first deep-learning-based segmentation of the entire brain vasculature down to the capillary level, enabling a compact representation, analysis, and new quantifications of vascular anatomy and collateralization. 2) Given the unsolved challenges in vessel and curvilinear structure segmentation, we formulate a novel, topology-preserving loss function with theoretical proofs up to homotopy equivalence, named *clDice*. Our experiments show that *clDice* improves the network structure of the segmentations and outperforms previous approaches in segmentation accuracy. 3) Converting the whole-brain vasculature segmentations to a graph representation, we attain an orders of magnitude more compact, expressive representation of the vasculature. On this graph, we benchmark a diverse set of graph convolutional networks on the biologically relevant tasks of vessel prediction (link prediction) and vessel classification (node classification), paving the way towards concerted advancement of graph learning research and neuroscience. Additionally, the appendix includes an additional publication on the concept of transfer learning for tubular structure segmentation beyond vessels and microscopic data. In summary, this thesis' works contribute theory and experimentation to enhance the segmentation of tubular and curvilinear structures such as brain vessels and pave a path towards expanding graph learning research on spatial biological graphs.

Zusammenfassung

Neue Bildgebungsverfahren in Medizin und Biologie ermöglichen eine Bildgebung gesamter Organe und Organismen auf Zellebene. Methoden, wie zum Beispiel das “Tissue Clearing” in Kombination mit Fluoreszenzmikroskopie, erlauben es ganze, intakte Organe in Mikrometerauflösung darzustellen. Die Analyse solcher Datensätze erfordert die Entwicklung neuer komplexer Ansätze. Im Zuge der “Deep-Learning Revolution” für Bilddaten der letzten Dekade haben sich auch für medizinische Datensätze auf maschinellem Lernen basierende Methoden als aktuelles Mittel der Wahl positioniert. Dieses Promotionsprojekt hat die Zielsetzung spezielle “Learning-basierte” Ansätze für die Analyse der gesamten Blutgefäße des Hirns zu erforschen. Die Bildgebung der gesamten Blutgefäße eines (murinen) Hirns ermöglicht eine ganzheitliche Betrachtung der Einflüsse von neurodegenerativen Erkrankungen auf alle noch so kleine Kapillaren im Hirn. Das mikrovaskuläre System des Hirns ist aus wissenschaftlicher Sicht besonders interessant, da jedes einzelne Neuron von einer Kapillare mit Sauerstoff und Nährstoffen versorgt wird. Die Kombination von neuen bildgebenden Verfahren und der in dieser Arbeit entwickelten Methoden des maschinellen Lernens ermöglichen eine neue Dimension der rapiden, quantitativen Analyse aller Blutgefäße des Hirns. Bei dieser Arbeit handelt es sich um eine publikationsbasierte Dissertation, dementsprechend gestalten die drei Veröffentlichungen, die ein Peer-Review-Verfahren durchlaufen haben, den Kern der Arbeit. 1) Im ersten Beitrag wird eine “Deep-Learning-basierte” Methode, die die erste komplette Blutgefäßsegmentierung des Mäusehirns erreicht entwickelt. 2) Basierend auf diesen Erfahrungen, entwickeln wir im *clDice*-Beitrag die theoretischen Konzepte zur Segmentierung von Blutgefäßstrukturen mithilfe von digitaler Topologie weiter. 3) In einer weiteren Konferenzpublikation interpretieren wir die Blutgefäße des Hirns als einen Graphen und wenden Konzepte des maschinellen Lernens auf Graphen an um fehlende Blutgefäßverbindungen anhand der Graphstruktur zu identifizieren.

Acknowledgements

Since I read the first Feynman book sometime in my Master's, I occasionally asked myself, “What would Richard do?” My answer to that question was often be curious, passionate about life, and most importantly, be with the people around you. Fortunately, I had such an incredible group of colleagues, advisors, mentors, friends, and family around me. I deeply appreciate all your support. First and foremost, Bjoern, I could not have asked for a better environment to pursue my Ph.D. You gave me absolute freedom to work on projects I was passionate about and let me carry out my own research, but you always, unconditionally, had my back when it mattered. You provided infinite ideas, put me in touch with the right people to address any scientific questions, and provided feedback and motivation when needed. Thank you for being my supervisor. With the same intensity, I want to express my gratitude to Suprosanna and Ivan; this endeavor would have been an entirely different journey without you. In many regards, I see these last years as our collective achievement. We supported each other on so many fronts, we wrote rebuttals to reviewers and the Ausländerbehörde we traveled all over the globe, and most importantly, became the closest friends. We achieved what we set out to do, we published in the journals and conferences we wanted to publish in, we enjoyed Munich, and we researched the fields we were passionate about. Thank you for being in this together. △

Next, I want to acknowledge my colleagues in the IBBM, ITERM, and AimLab. Richard Feynman also said that you should surround yourself with five kinds of people: *the inspired, the passionate, the motivated, the grateful, and the open-minded.* I was so lucky to work with you, a brilliant group with such a balanced and diverse set of skills that are beyond Feynman's advice. A special thanks to Mihail, who was my biological counterpart with excellent computational know-how and relentless effort and kindness in so many projects. To Oliver, from whom I learned so much about organization, effectiveness, and focus. To Giles Tetteh, who helped me with many engineering problems; Anjany, my #1 colleague for beers and chats; and Fercho, the #1 for dancing. To Bran, we worked on and shared the first MICCAI paper: ”DiamondGAN.” To Chinmay, the GCN whisperer, and Florian, who so often provided a new angle to discussions. Another special mention belongs to Schorschi; just when I was looking for additional inspiration and collaborations, I found it with your arrival in Translatum and to Daniel and Martin, with whom I am looking forward to working in London. Furthermore, I would like to mention the influential scientific collaborators, foremost Ali, who was like a second supervisor to me and inspired me with his visions. Your ITERM institute's work on acquiring whole-brain vascular images through high-resolution fluorescence light-sheet microscopy (LSM) imaging only enabled the work in this thesis. Along with Ali, the ITERM AI Team with Izabela, Rami, Mayar, Louis, and Moritz. Jan and Bene from the Neuroradiology at TUM, you were always a pleasure to work with and explained many things about the clinical routine to me. Ulrich Bauer for his patience and talent in finding the right language to illustrate topological concepts and contributing my favorite piece of text in all of our papers: "In particular, since homology in degree 1 is the Abelianization of the fundamental group, these two groups are isomorphic." I want to thank Stephan Günnemann for heading the Thesis committee and helping me to get a foot into graph learning; and to all the other co-authors and research collaborations. Another significant recognition belongs to my brilliant Master's and Bachelor's students, starting with my first ever student Stefan, Nils, Alex, as well as Paul, and Julian, who are now pursuing their own doctoral studies, and Leon, a true out-of-the-box thinker. Thank you for your invaluable contributions to our joint research. To all my friends and teammates in volleyball and football, thank you for taking my mind off work, your patience when paper deadlines were close, and for all the good times in Munich, Biederstein, and around the globe. Marta, thank you for the years leading up to and in this thesis.

Finally, and most importantly, to my family - my parents, Christian and Berta, who encouraged my ambition, dealt with my character and unconditional support, my brother Uli for instilling my passion for science and his advice, my sister Eva for her genuine love, Jenny, my sunshine, you brighten up every day of my life, and the entire family: Matthias, Lena, Elia, Luca, Hannah and Mara and all the future additions and generations - this is your work, too.

Contents

List of Figures

List of Tables

Publication List

The following three publications constitute the core of my *cumulative doctoral thesis*. A * indicates shared first authorship.

[1] J. C. **Paetzold**, J. McGinnis, S. Shit, I. Ezhov, P. Büschl, C. Prabhakar, A. Sekuboyina, M. Todorov, G. Kaissis, A. Ertürk, et al. "Whole Brain Vessel Graphs: A Dataset and Benchmark for Graph Learning and Neuroscience." In: *Thirty-fifth Conference on Neural Information Processing Systems Datasets and Benchmarks Track (Round 2)*. 2021.

[2] S. Shit*, J. C. **Paetzold***, A. Sekuboyina, I. Ezhov, A. Unger, A. Zhylka, J. P. Pluim, U. Bauer, and B. H. Menze. "clDice-a Novel Topology-Preserving Loss Function for Tubular Structure Segmentation." In: *Proceedings of the IEEE/CVF Conference on Computer Vision and Pattern Recognition*. 2021, pp. 16560–16569.

[3] M. I. Todorov*, J. C. **Paetzold***, O. Schoppe, G. Tetteh, S. Shit, V. Efremov, K. Todorov-Völgyi, M. Düring, M. Dichgans, M. Piraud, et al. "Machine learning analysis of whole mouse brain vasculature." In: *Nature Methods* 17.4 (2020), pp. 442–449.

The following publication is printed in the appendix; it is related to the content of this thesis but not part of the cumulative thesis.

[1] J. C. **Paetzold***, O. Schoppe*, M. Todorov, A. Ertürk, and B. H. Menze. "Transfer learning from synthetic data reduces need for labels to segment brain vasculature and neural pathways in 3d." In: *International Conference on Medical Imaging with Deep Learning–Extended Abstract Track*. 2019.

The following additional 18 publications were further written *during the time of my doctoral thesis.* A * indicates shared first authorship.

2022

[1] I. Horvath, J. C. **Paetzold**, O. Schoppe, R. Al-Maskari, I. Ezhov, S. Shit, H. Li, A. Ertuerk, and B. Menze. "METGAN: Generative Tumour Inpainting and Modality Synthesis in Light Sheet Microscopy." In: *Proceedings of the IEEE/CVF Winter Conference on Applications of Computer Vision*. 2022, pp. 227–237.

2021

[1] S. Shit, D. Das, I. Ezhov, J. C. **Paetzold**, A. F. Sanches, N. Thuerey, and B. H. Menze. "Velocity-To-Pressure (V2P)-Net: Inferring Relative Pressures from Time-Varying 3D Fluid Flow Velocities." In: *International Conference on Information Processing in Medical Imaging*. Springer. 2021, pp. 545–558.

[2] K. Payette, P. de Dumast, H. Kebiri, I. Ezhov, J. C. **Paetzold**, S. Shit, A. Iqbal, R. Khan, R. Kottke, P. Grehten, et al. "An automatic multi-tissue human fetal brain segmentation benchmark using the Fetal Tissue Annotation Dataset." In: *Scientific Data* 8.1 (2021), pp. 1–14.

[3] T. S. Jones, J. E. Franklin, J. Chen, F. Dietrich, K. D. Hajny, J. C. **Paetzold**, A. Wenzel, C. Gately, E. Gottlieb, H. Parker, et al. "Assessing urban methane emissions using column-observing portable Fourier transform infrared (FTIR) spectrometers and a novel Bayesian inversion framework." In: *Atmospheric Chemistry and Physics* 21.17 (2021), pp. 13131–13147.

[4] A. Sekuboyina, M. E. Husseini, A. Bayat, M. Löffler, H. Liebl, H. Li, G. Tetteh, J. Kukačka, C. Payer, D. Štern, et al. "VerSe: A Vertebrae labelling and segmentation benchmark for multi-detector CT images." In: *Medical image analysis* 73 (2021), p. 102166.

[5] A. Dima, J. C. **Paetzold**, F. Jungmann, T. Lemke, P. Raffler, G. Kaissis, D. Rueckert, and R. Braren. "Segmentation of Peripancreatic Arteries in Multispectral Computed Tomography Imaging." In: *International Workshop on Machine Learning in Medical Imaging*. Springer. 2021, pp. 596–605.

[6] F. Kofler, I. Ezhov, F. Isensee, F. Balsiger, C. Berger, M. Koerner, J. C. **Paetzold**, H. Li, S. Shit, R. McKinley, et al. "Are we using appropriate segmentation metrics? Identifying correlates of human expert perception for CNN training beyond rolling the DICE coefficient." In: *arXiv preprint arXiv:2103.06205* (2021).

[7] S. Shit, I. Ezhov, J. C. **Paetzold**, and B. Menze. "A nu-Net: Automatic Detection and Segmentation of Aneurysm." In: *International workshop on Cerebral Aneurysm Detection*. Springer. 2020, pp. 51–57.

[8] S. Shit, I. Ezhov, L. Mächler, J. Lipkova, J. C. **Paetzold**, F. Kofler, M. Piraud, B. H. Menze, et al. "Semi-Implicit Neural Solver for Time-dependent Partial Differential Equations." In: *arXiv preprint arXiv:2109.01467* (2021).

[9] I. Ezhov, T. Mot, S. Shit, J. Lipkova, J. C. **Paetzold**, F. Kofler, C. Pellegrini, M. Kollovieh, F. Navarro, H. Li, et al. "Geometry-aware neural solver for fast Bayesian calibration of brain tumor models." In: *IEEE Transactions on Medical Imaging* (2021).

2020

[1] S. Gerl*, J. C. **Paetzold***, H. He, I. Ezhov, S. Shit, F. Kofler, A. Bayat, G. Tetteh, V. Ntziachristos, and B. Menze. "A distance-based loss for smooth and continuous skin layer segmentation in optoacoustic images." In: *International Conference on Medical Image Computing and Computer-Assisted Intervention*. Springer. 2020, pp. 309–319.

[2] S. Zhao, M. I. Todorov, R. Cai, A.-M. Rami, H. Steinke, E. Kemter, H. Mai, Z. Rong, M. Warmer, K. Stanic, O. Schoppe, J. C. **Paetzold**, et al. "Cellular and molecular probing of intact human organs." In: *Cell* 180.4 (2020), pp. 796–812.

[3] A. B. Qasim, I. Ezhov, S. Shit, O. Schoppe, J. C. **Paetzold**, A. Sekuboyina, F. Kofler, J. Lipkova, H. Li, and B. Menze. "Red-GAN: Attacking class imbalance via conditioned generation. Yet another medical imaging perspective." In: *Medical Imaging with Deep Learning*. PMLR. 2020, pp. 655–668.

[4] A. Bayat, A. Sekuboyina, J. C. **Paetzold**, C. Payer, D. Stern, M. Urschler, J. S. Kirschke, and B. H. Menze. "Inferring the 3D standing spine posture from 2D radiographs." In: *International Conference on Medical Image Computing and Computer-Assisted Intervention*. Springer. 2020, pp. 775–784.

[5] A. Shekhar, J. Chen, J. C. **Paetzold**, F. Dietrich, X. Zhao, S. Bhattacharjee, V. Ruisinger, and S. C. Wofsy. "Anthropogenic CO2 emissions assessment of Nile Delta using XCO2 and SIF data from OCO-2 satellite." In: *Environmental Research Letters* 15.9 (2020).

2019

[1] J. C. **Paetzold***, O. Schoppe*, M. Todorov, A. Ertürk, and B. H. Menze. "Transfer learning from synthetic data reduces need for labels to segment brain vasculature and neural pathways in 3d." In: *International Conference on Medical Imaging with Deep Learning–Extended Abstract Track*. 2019.

[2] H. Li*, J. C. **Paetzold***, A. Sekuboyina, F. Kofler, J. Zhang, J. S. Kirschke, B. Wiestler, and B. Menze. "DiamondGAN: unified multi-modal generative adversarial networks for MRI sequences synthesis." In: *International Conference on Medical Image Computing and Computer-Assisted Intervention*. Springer. 2019, pp. 795–803.

[3] F. Navarro, S. Shit, I. Ezhov, J. C. **Paetzold**, A. Gafita, J. C. Peeken, S. E. Combs, and B. H. Menze. "Shape-aware complementary-task learning for multi-organ segmentation." In: *International Workshop on Machine Learning in Medical Imaging*. Springer. 2019, pp. 620–627.

Introduction

In 2012, AlexNet was the first convolutional neural network (CNN) to win the ImageNet competition, beating the runner up by 10.8 points in top-5 accuracy [1], [2]. This hallmark achievement marked the dawn of the widespread adaption of CNNs for image analysis. This revolution has been consistent across a vast set of application domains, with natural image analysis often paving the path for medical imaging and experimental biological imaging. Applications include fluorescence microscopy, video analysis, magnetic resonance imaging, and even optoacoustic imaging. At the same time, novel and improved imaging technologies substantially advanced individual images' resolution and information content. For example, clinical magnetic resonance imaging (MRI) devices can reach an in-plane resolution of sub-one-millimeter [3]. Moreover, in biological research, advanced microscopy techniques enable the imaging of whole rodents or human organs at a cellular resolution [4]. For example, the imaging of blood vessels in murine brains [5] and the human kidney [6] or cancer metastases in the whole mouse body [7] is possible.

Brain Vessels and Three Domains of Representation

In light of both scientific progress in machine learning and biological imaging, this thesis reports my research efforts on developing advanced machine learning concepts and theory for the analysis of the brain's vasculature. The brain's vasculature is integral to sustaining the 86 billion neurons of the cerebral biological neuronal network [8], which essentially defines human intelligence [9]. Both the billions of neurons and the brain vessels form an ultra-large, spatial, hierarchical, and structured network that is longer than 600 kilometers [10], see Chapter 4. In order to understand a network of this magnitude, we introduce three representation domains of the brain vasculature, see Figure 1.1. First, the *image representation*, where the invention of tissue clearing and light-sheet microscopy provided scientists with the method to image the whole brain vasculature at a micrometer resolution [5], [11]–[13]. While such images allow a visual interpretation of the smallest capillaries at a whole-brain scale, a rapid analysis and quantification of these terabyte images are impossible without

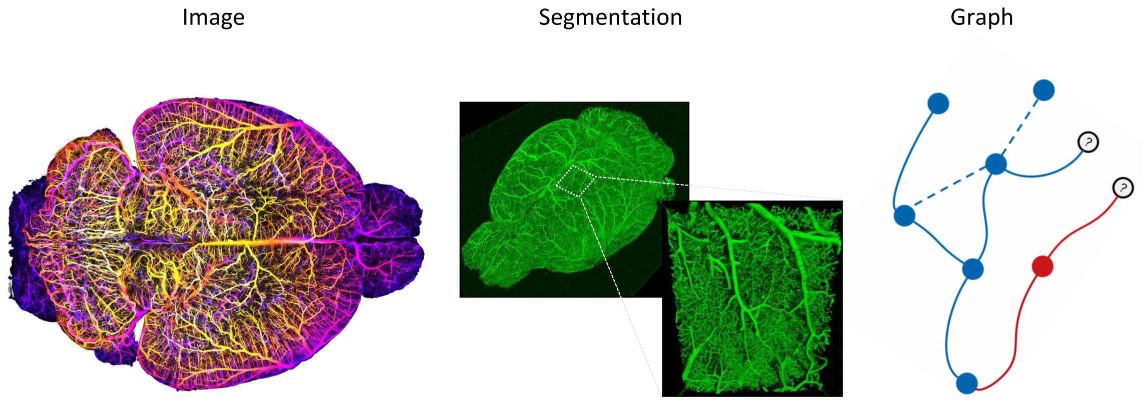

Figure 1.1: The three key domains of vessel representation as discussed in this thesis. A high-resolution image (left) is the base for applying a neural network for segmentation (centre). Based on this pixelwise segmentation an even more compact graph representation (right) can be extracted, enabling machine learning on graphs.

the use of massive computational resources. This motivates the need for a binary representation, a so-called segmentation of the brain vasculature. This *segmentation* is a representation that is multiple orders of magnitude more compact while still existing in the pixel domain. Subsequently, a segmentation can be transformed to a *graph representation* to generate an even more abstract and compact representation of the vascular connectome. Such a whole-brain vascular graph with millions of nodes and edges constructs a hierarchical description of the anatomy. It can facilitate research and understanding of a vast set of vascular pathologies. Moreover, graphs allow the use of an entirely new set of machine learning algorithms on graphs which can efficiently exploit the structural and functional priors that are present in such spatial and physical 3D vessel networks [14]–[16].

Contributions

The overarching objective of this thesis is to formulate novel machine learning concepts to enhance the understanding of the ultra-large cerebrovascular network. The core of this cumulative thesis constitute three peer-reviewed papers, which can be grouped into three conceptual blocks.

1. Segmenting the entire murine brain vasculature. This is described in Chapter 5: *Machine Learning Analysis of Whole Mouse Brain Vasculature, Nature Methods, Volume 17, April 2020.*

2. Advancing CNN based segmentation theory for blood vessels and curvilinear structures in Chapter 6: *clDice - a Novel Topology-Preserving Loss Function for Tubular Structure Segmentation, CVPR, June 2021*

3. Formalizing the brain vasculature as a homogeneous graph and benchmarking of graph learning methods to understand its structure Chapter 7: *Whole Brain Vessel Graphs: A Dataset and Benchmark for Graph Learning and Neuroscience (VesselGraph), NeurIPS, December 2021.*

In order to understand the structural organization of the brain vasculature, the first goal of this thesis was to develop a whole-brain vessel segmentation. When considering the state-of-the-art literature, we identified several deficiencies which translated to scientific problem statements for the given whole-brain vessel images. Supervised learning methods rely on expert-annotated image label pairs, which are expensive to acquire. To circumvent this issue, we develop a transfer learning approach using synthetic vessel data; see additional publication in Chapter A. Moreover, we find that purely pixel-based metrics and loss functions are not optimal for the segmentation of curvilinear and tubular structures such as vessels because their most important property is the connectedness of the vessels and not the pixel precision of their diameter, see Figure 2.2. This observation led to the development of *clDice*, see Chapter 6, where concepts of computational topology are used to develop a topology preserving loss function with theoretical guarantees to improve the connectedness in segmentations of vessels but also other network-like curvilinear structures such as roads or cell boundaries.

While such a segmentation is substantially more compact than actual images, it is difficult to interpret and quantify when millions of vessels are present. This motivates the development of an efficient way to represent vessels as a graph, which represents an efficient data structure for sparse encodings where bifurcation points represent nodes and connecting vessels are edges, see Figure 3.1. The third paper *VesselGraph*, tackles this idea and achieves a multiple orders of magnitude more compact representation of the brain vasculature, which preserves the important information such as the radius and encodes them as features. The extraction of such a vascular graph is an active research direction that we address using the *Voreen* software. This graph representation significantly speeds up quantification and analysis. Furthermore, this graph representation opens an avenue towards a whole new set of machine learning algorithms on graphs. For example, link prediction to predict missing vessel segments in the brain structures.

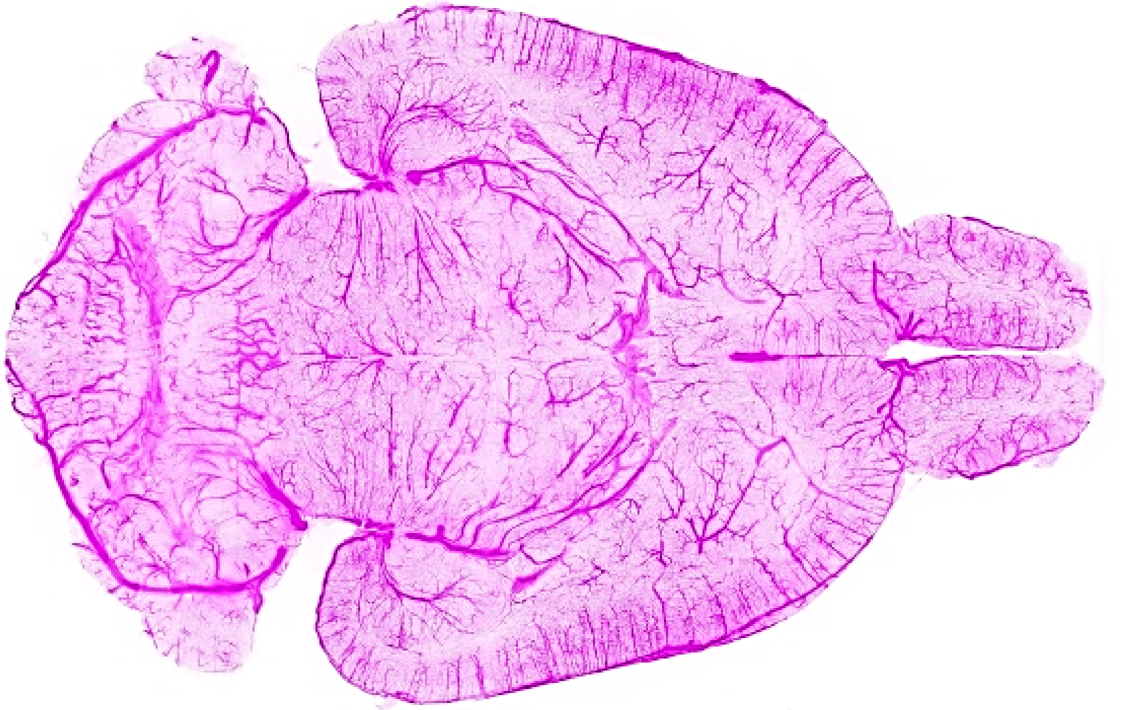

Figure 1.2: Whole-brain fluorescence microscopic vessel image using the approach introduced in Todorov & Paetzold et al. [11]; image published as such in Shit & Paetzold et al. [17].

Organization

Chronologically before the introduction, this publication-based dissertation text starts with an abstract in the English and German languages. Second, I recognize and appreciate my collaborators and family in the personal acknowledgment. Next, I provide a comprehensive list of all the publications written during my time as a doctoral student. In this chapter, the introduction describes the major contributions and places them in the broad scientific context. After the introduction, three background chapters follow, laying the groundwork and defining important terminology and concepts for my research articles. They are in successive order and link the three vascular representation domains described in Figure 1.1. First, in Chapter 2 the basis of *Deep Learning for Computer Vision* is discussed. Second, key concepts for *Machine*

Learning on Graphs are introduced in Chapter 3. To conclude the general chapters, the *Brain Vasculature* is anatomically described and visualized in Chapter 4. This background chapter describes highly prevalent brain vessel pathologies and introduces the most important imaging techniques. Next, the three original publications are presented in separate Chapters 5, 6, and 7. After the original publications, Chapter 8 describes current limitations, proposes future work, and discusses the contributions in light of the existing literature. Finally, the Appendices contain the bibliography, the additional publication A, and supplementary material of the original publications.

Deep Learning for Image Analysis

2.1 History of Convolutional Neural Networks for Segmentation

Shortly after AlexNet's win in the ImageNet competition [1], deep CNNs also became state of the art for pixel classification (or segmentation) in medical imaging [18]. Successively, fully convolutional neural networks (FCN) were introduced, which implemented multiple successive layers, where pooling operations are replaced by upsampling [19]. FCNs inspired the U-Net, which combines up and downsampling with skip connections [20]. To this date, the U-Net and its extensions to 3D [21], [22] are the most frequently used types of neural networks used in medical image segmentation. Inspired by these fundamental papers, many research groups, as well as the industry, employ the concepts of deep CNNs to large 3D images. In this context, CNNs are almost universally used across different foreground shapes and objects. To illustrate the vast applications in medical imaging, Figure 2.1 depicts the successful application of *nnU-net* to various medical image segmentation challenges [23].

2.2 Neural Networks

Inspired by the function of the brain, computational neural networks are compositions of computational units, the so-called neurons. In general, neural networks are organized in layers. If a neural network consists of many successive layers, it is called a deep neural network. Such deep neural networks often consist of an input layer that processes the original data, hidden layers, and an output layer that provides the predictions. Individual neurons $f(x)$ in a neural network can be generalized in the following manner:

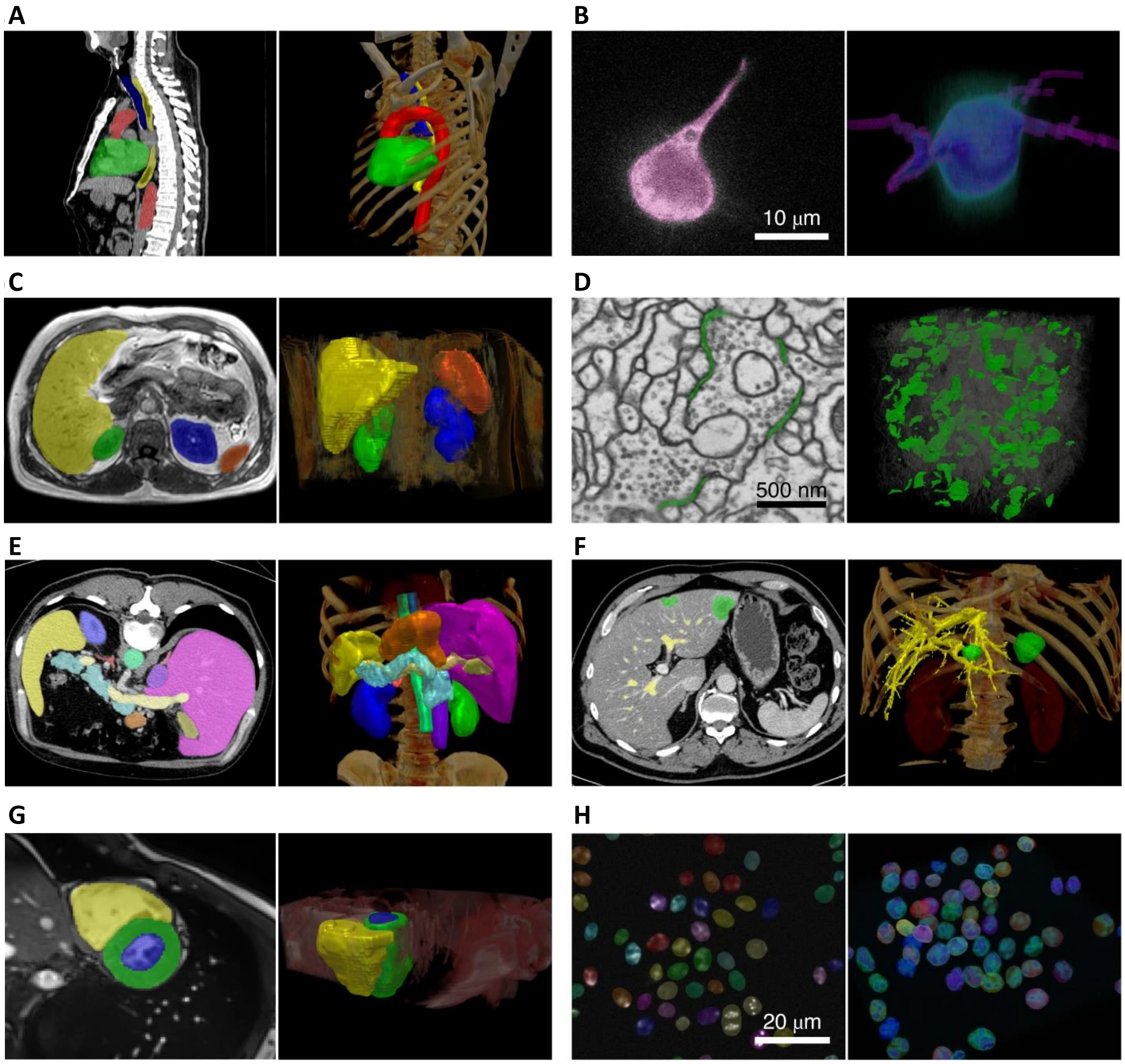

Figure 2.1: Successful applications of CNN based segmentation to a wide variety of medical and biological research datasets. A) Heart, aorta, esophagus, and trachea in a CT image, B) lung cancer cells in a microscopic image, C) liver, both kidneys and spleen in a CT image, D) synaptic clefts in electron microscopy, E) various abdominal organs in CT, F) liver tumors and hepatic vessels, G) ventricles and ventricular cavities in MR images and H) instances of cell nuclei. Images licensed for use in this thesis from *nn-Unet* [23], see Appendix E. The examples are depicted in 2D with the segmentation projected onto the raw 2D image data (left) and in 3D using volume rendering (right).

$$f(x) = \phi(\mathbf{w}^{\mathbf{T}}\mathbf{x} + \beta), \tag{2.1}$$

where $\mathbf{w} = (w_1, w_2, ..., w_n)$ represents the weight vector, $\mathbf{x}$ represents the input vector and β represents a bias term. The neuron is activated using an activation function $\phi(\cdot)$.

Activation Functions

Generally, an activation function modifies the input vector of a neuron before it is passed to a subsequent layer. This concept of activation functions is crucial to modeling ultra-complex non-linear relationships (or functions) in a neural network. A vast set of activation functions have been used in machine learning research. Typical properties are that activation functions need to be fully continuously differentiable, fix the input data to a fixed range, and are non-linear. Frequently used activation functions are formalized below, where $\mathbf{x}$ is the input.

$$\text{Sigmoid:} \qquad \phi(x) = \frac{1}{1 + e^{-x}}. \tag{2.2}$$

The *sigmoid* function is frequently used because it exhibits a smooth gradient, is efficient for classifiers, is evidently non-linear and suppresses the output to the range $[0, 1]$.

$$\text{ReLU:} \qquad \phi(x) = \left\{ \begin{matrix} x & x > 0 \\ 0 & x <= 0 \end{matrix} \right\}. \tag{2.3}$$

The rectified linear unit (ReLU) is one of the most frequently used activation functions because it is computationally less expensive then *sigmoid* and *tanh*. Moreover, its variant, the so-called *LeakyReLU* is frequently used, which leaves a constant and small gradient α instead of 0.

$$\text{LeakyReLU:} \qquad \phi(x) = \left\{ \begin{matrix} x & x > 0 \\ \alpha x & x <= 0 \end{matrix} \right\}. \tag{2.4}$$

The *Tanh* function squeezes the range to $[-1, 1]$ making the output centered around zero. Further, it has been shown that *Tanh* can exhibit steeper gradients than *sigmoid* [24].

$$\text{Tanh:} \qquad \phi(x) = \frac{e^x - e^{-x}}{e^x + e^{-x}}. \tag{2.5}$$

Evidently, a set of random weights in a neural network will not produce a sensible prediction. Therefore, neural networks have to be trained. In a supervised setting, as discussed in this thesis, a set of data-label pairs, the so-called training set, is used for training. Here, the training data is input into the network, which produces a prediction. This prediction is compared to the label using an objective function, also known as the loss function or cost function, see Section 2.4. A vital property of the loss function is that it has to be differentiable because the gradient of the loss function determines the update of the weights in the neural network.

Backpropagation

While training a neural network, the objective is to iteratively update the network weights in order to minimize the prediction error. This iterative update of all network weights is achieved using the concept of backpropagation [25]. In order to determine the direction of weight adjustment, the gradient of the error (L) of the cost function is calculated with respect to all weights $\mathbf{w} = (w_1, w_2, \ldots, w_n)$ as follows:

$$\nabla_{\mathbf{w}}(L) = \left(\frac{\partial(L)}{\partial w_1}, \frac{\partial(L)}{\partial w_2} \cdots \frac{\partial(L)}{\partial w_n} \right). \tag{2.6}$$

Now, as the number of weights and their gradient is known, the weights can be iteratively updated following the layer hierarchy of the neural network:

$$\Delta \mathbf{w} = -\gamma \nabla_{\mathbf{w}}(L), \tag{2.7}$$

where γ, the so-called learning rate controls the update step size in each training iteration. To find the minimum global error, modern deep learning uses the concept of gradient descent, for which a vast set of variants and optimizations, for example, stochastic gradient descent and batch gradient descent, exist [26].

2.3 Convolutional Neural Networks

Convolutional neural networks were designed to address the specific challenges and properties of images [1] and have proven to be highly efficient for most image analysis tasks such as classification [27] and segmentation [18]. The key concept for CNNs are convolutional layers where a neuron only receives an input from a subset of spatially adjacent neurons from the preceding layer, which are processed via a convolutional kernel. This concept enables to significantly reduce the number of parameters compared to fully connected layers [28]. Powerful CNN architectures such as ResNets [29] or U-Nets [20], [21] often combine convolutional layers with pooling and add up- and downsampling layers as well as fully connected layers to their architecture.

At this point in time, specialized solutions for specific segmentation problems often differ in regards to specialized pre- and post-processing pipelines, network depth and in the number of input and output channels. Another important concept is the use of tailored objective functions, which optimize the segmentation of a specific foreground object or object size. In the following section, the most frequently used loss functions and the *clDice* loss function, which is highly relevant for blood vessel segmentation, are introduced and formalized.

2.4 Loss Functions for Segmentation

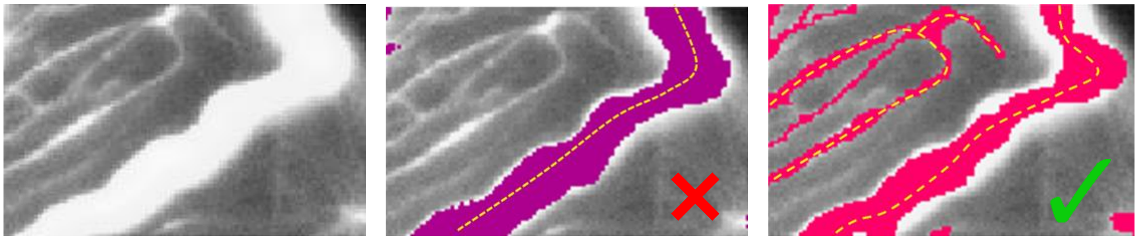

Figure 2.2: Two candidate segmentations in purple and red for the image slice on the left. Both segmentations reach similar dice scores compared to the ground truth, showcasing the need for dedicated loss functions. Figure published as such in Shit & Paetzold et al. [17].

Segmentation of medical images is most often optimized towards the objective of optimal pixel overlap between a segmentation and a ground truth label. This objective is relevant for structures of interest such as brain and liver tumors [30], [31] whole organs [32], [33], vertebrae [34], among others. For such application cases, the Dice loss function [21] and the cross entropy loss function are most frequently used.

Categorical cross entropy (CE) for N number of classes is defined as:

$$CE = -\sum_{l=1}^{N} y_l \log(p_l), \tag{2.8}$$

where y is the indicator (binary) if the class label l represents the correct classification for the observation and p is the predicted probability that our observation belongs to class l. To use CE as a loss function, we need to extend the formalization to the number of training samples M:

$$L_{CE} = -\frac{1}{M}\sum_{i=1}^{M}\sum_{l=1}^{N} y_l \log(p_l). \tag{2.9}$$

For binary segmentation problems the loss simplifies to the following, which is known as binary cross entropy loss (BCE):

$$L_{BCE} = -\frac{1}{M}\sum_{i=1}^{M} -(y\log(p) + (1-y)\log(1-p)). \tag{2.10}$$

The Dice loss tackles one of the problems in the cross entropy loss functions, which is a bias towards the dominating class. In medical image segmentation this dominant class is often the background. For pixelwise segmentation, the Dice loss is defined as follows:

$$L_{Dice} = 1 - \frac{2\sum_{i=1}^{N} p_i l_i + \epsilon}{\sum_{i=1}^{N} p_i^2 + \sum_{i=1}^{N} l_i^2 + \epsilon}, \tag{2.11}$$

where p_i is the predicted probability of pixel i, and l_i is the class label of pixel i for N number of pixels, with the *smoothing* term ϵ to avoid division by zero. Moreover, a weighted sum, mean or the total sum of BCE loss and Dice loss is frequently used for binary segmentation tasks [35].

For curvilinear structures such as streets in satellite images [36], blood vessels in medical images [37], or cell boundaries in microscopic images [38] the most critical characteristic of a good segmentation is the stringent connectedness of the components and not the absolute pixelwise accuracy of the segmentation, see Figure 2.2. To achieve this, topology-enforcing and topology-preserving loss functions were introduced for 2D curvilinear [39]–[41], and 3D tubular shapes [17]. One example, the *clDice* loss function, which is part of my thesis, is introduced and formalized in Chapter 6.

Machine Learning on Graphs

Machine learning on graphs, which is often referred to using its umbrella term: geometric deep learning [16], is a highly relevant task with almost omnipresent applications in data analysis, for example, shopping recommendations, content recommendations in social networks, drug design, route predictions for car navigation or biological network analysis [14]. Because of their universality a large number of research efforts are directed towards machine learning on graphs [42] such as graph convolutional networks (GCN) [43], generative modeling on graphs [44] and adversarial attacks on graph neural networks [45]. A fundamental prerequisite is the efficient encoding of relational data in a graph representation. Fortunately, most datasets can be effortlessly modeled in a graph of instances (nodes) and connections (edges). Modeling datasets as graphs is particularly advantageous if the relations between instances are sparse [14]. As such, graph representations are well-suited to model vascular connections in an abstract and efficient manner, see Figure 3.1.

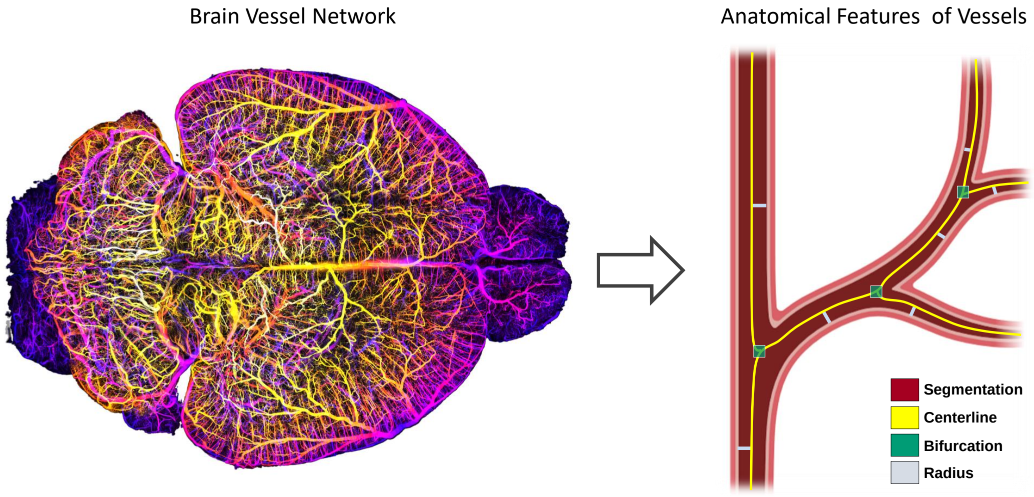

Figure 3.1: A whole-brain vessel image and a single vessel depiction, where the anatomical and morphological features and terminology are depicted [11].

3.1 Formalization of Graphs

A graph $\mathcal{G}$ can be formalized as $\mathcal{G} = (\mathcal{V}, \mathcal{E})$, where $\mathcal{V} = \{v_1, v_2, ...v_n\}$ is its set of vertices (or nodes) and $\mathcal{E} = \{e_{i,j}\}$ is its set of links (or edges) [46]. Naturally, we interpret a node as a bifurcation point and an edge as a connecting vessel, see Figure 3.1. The definition of an edge is a connection between two nodes (u, v), where both nodes are $u \in \mathcal{V}$ and $v \in \mathcal{V}$. If an edge does not have a directional property it is considered an *undirected edge* which can be formalized as:

$$(u, v) \in \mathcal{E} \leftrightarrow (v, u) \in \mathcal{E}. \tag{3.1}$$

An adjacency matrix $\mathcal{A}$ can be used to describe a full unweighted graph. Often, the nodes in $\mathcal{A}$ are organized in ascending order for both its rows and columns [47]. Using the adjacency matrix notation, the existence of an edge between node v and node u is described by:

$$\mathcal{A}[u, v] = \begin{cases} w & \text{if } (v, u) \in \mathcal{E} \\ 0 & \text{otherwise} \end{cases} \tag{3.2}$$

Where w indicates the weight of an edge, which reduces to $w = 1$ when no edge weights are used. This implies that $\mathcal{A}$ of an undirected graph is fully symmetric:

$$\mathcal{A}[v, u] = \mathcal{A}[u, v]. \tag{3.3}$$

Throughout this work our (vascular) graphs are interpreted as undirected graphs.

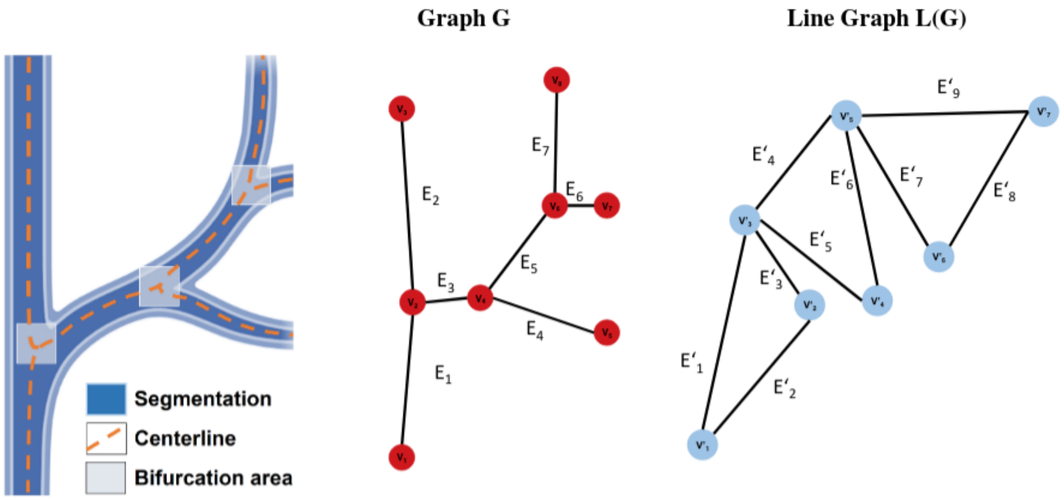

Figure 3.2: Depiction of an exemplary vessel tree with the spatial vessel Graph $\mathcal{G}(\mathcal{V}, \mathcal{E})$ with nodes $(\mathcal{V})$ and edges $(\mathcal{E})$. The bifurcation points in the vessel tree become the nodes $(\mathcal{V})$ and their connecting vessels are the edges $(\mathcal{E})$. Additionally, a line graph $L(\mathcal{G})$ of the spatial vessel graph $\mathcal{G}$; where each node (bifurcation point) becomes an edge; two nodes of $L(\mathcal{G})$ are adjacent if and only if their edges are incident in $\mathcal{G}$. This figure was first published in Paetzold et al. [15].

Line Graph Representation A line graph $L(\mathcal{G})$ is a different graph based on an undirected graph $\mathcal{G}$ which describes the adjacencies between the edges $\mathcal{E}$ of $\mathcal{G}$ [48]. An illustration of a base graph and line graph for vessels is depicted in Figure 3.2. We formally define a line graph as:

$$L(\mathcal{G}) := (\mathcal{V}', \mathcal{E}'), \tag{3.4}$$

where the edges of the base graph $\mathcal{G}$ become nodes:

$$\mathcal{V}' = \mathcal{E}, \tag{3.5}$$

and a new edge $\mathcal{E}'$ between the new nodes is created if and only if their edges are incident in $\mathcal{E}$.

$$\mathcal{E}' = \{\{e_{ij}, e_{ik}\} \text{ if } \exists\, (e_{ij}, e_{ik}) \in \mathcal{E}\}. \tag{3.6}$$

3.2 Fundamental Graph Learning Tasks

Four main problem statements for machine learning on graphs currently exist. Namely, link prediction, node property prediction or node classification, edge property prediction or edge classification, and graph level property prediction, also known as graph classification.

Link Prediction Link prediction in a graph $\mathcal{G}$ can be defined in the form of a classifier $\mathcal{F}_{link}$. Where the classifier $\mathcal{F}_{link}$ aims to predict a link $\mathcal{E}_p$ between two nodes (u, v). The existence of that link is indicated by 1:

$$\mathcal{F}_{link} : \mathcal{E}p \rightarrow \{0, 1\}. \tag{3.7}$$

Graph Level Classification The second task graph property prediction, also known as graph level classification aims at training a classifier $\mathcal{F}_{graph}$ which is able to predict a specific property $\mathcal{Y}$ out of a set of known class-labels $\mathcal{M}_Y$ for the entire graph $\mathcal{G}$.

$$\mathcal{F}_{graph} : \mathcal{G} \rightarrow \mathcal{Y} \in \mathcal{M}_Y. \tag{3.8}$$

Edge Classification Edge classification as a task can also be formalized as a classifier $\mathcal{F}_{edge}$. $\mathcal{F}_{edge}$ has the the goal of providing a prediction which class label $\mathcal{Y}$ out of a set of known edge-classes $\mathcal{C}_Y$ should be assigned to an edge $\mathcal{E}$:

$$\mathcal{F}_{edge} : \mathcal{V} \rightarrow \mathcal{Y} \in \mathcal{C}_Y. \tag{3.9}$$

Node Classification Node classification with classifier $\mathcal{F}_{node}$ aims to provide a prediction which class label $\mathcal{Y}$ out of a set of known node-classes $\mathcal{N}_Y$ should be assigned to a node $\mathcal{V}$:

$$\mathcal{F}_{node} : \mathcal{V} \rightarrow \mathcal{Y} \in \mathcal{N}_Y. \tag{3.10}$$

3.3 Graph Neural Networks

Considering the success of neural networks in machine learning tasks across many other data domains such as images (see Section 2.1) and text, the use of neural networks is natural. A key concept was the invention of Graph Convolutional Networks (GCNs) [43], which enabled the use of convolutional operators directly on the graphs. Another key concept was the development of the so-called message passing scheme [49], which allows the aggregation of the information of neighboring nodes and the successive application of convolutional layers. Recently, *attention* concepts have established themselves as the de-facto gold standard neural networks for some sequence-data tasks [50]; using similar concepts, Graph Attention Networks (GATs) add self-attention layers to the GNN [51], and achieve state-of-the-art results on a variety of graph benchmarks. Extending this concept, gated attention networks introduced the multi-head-attention concept to graph learning [52]. For more details on current GNNs and their successful application, please refer to the paper *Whole Brain Vessel Graphs: A Dataset and Benchmark for Graph Learning and Neuroscience (VesselGraph)*, chapter 7 in this thesis.

3.4 How Machine Learning can be Applied to Vessel Graphs

In Section 3.2 four fundamental graph machine learning task categories: link prediction, graph level classification, node classification and edge classification were introduced and formalized. All of these problem statements have a direct application to vessel graphs:

1. Link prediction can be interpreted as missing vessel prediction (to improve the structure) or as anatomical fidelity prediction.
2. Graph level property prediction can be used as a pathology prediction on the whole vascular network.
3. Edge property prediction can be used as a means for vessel classification, e.g., vessel size classification or functional classification.
4. Node property prediction can be used to either classify the bifurcation points or for vessel classification when the graph is transferred to a line graph representation.

The Brain Vasculature

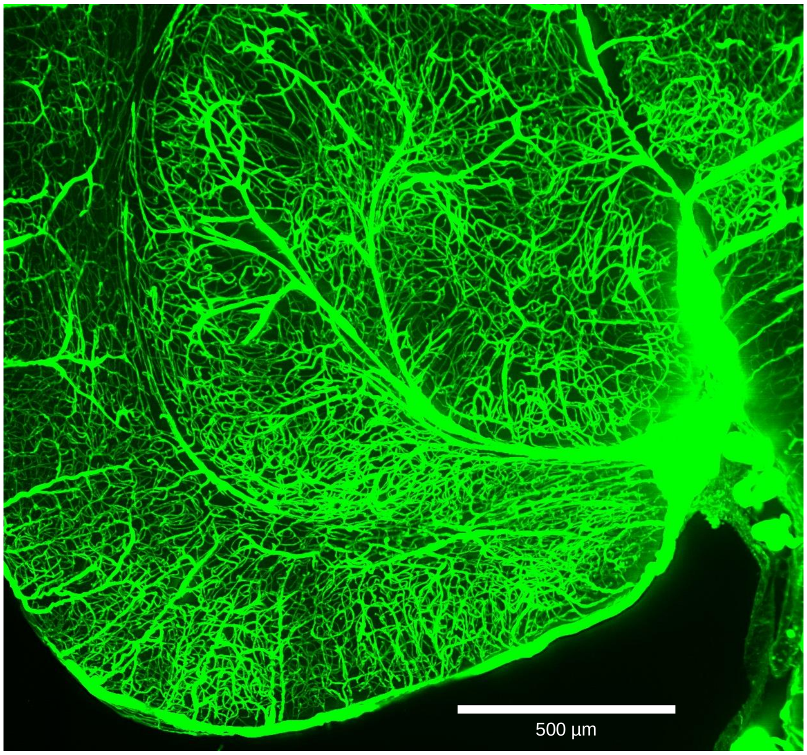

Figure 4.1: Section of a whole-brain fluorescence microscopic vessel image using the approach introduced in Todorov & Paetzold et al. [11]; hierarchical organization of large and successively smaller vessels is visible continuously down to the smallest capillary level.

The mammalian brain's cerebrovascular system reliably supplies the neurons and other brain tissue with oxygen, immune cells, and nutrients. Further, it is also responsible for the sensitive heat regulation of the brain. To maintain its functionality, the brain requires a sensitive balance of all these constituents, the so-called homeostasis.

To achieve this goal, the brains vasculature forms an ultra-complex, sensitive, and closed flow network. For example, in a murine brain, the number of vessels and branching points alone is in the order of multiple millions [5], [11], [12], [53]. In Table 4.1 a comprehensive list of the currently available whole mouse brain vessel datasets is provided. The table provides basic statistics on nodes and edges, which can be interpreted as bifurcation points and vessels, extracted by a unified graph extraction scheme based on the *Voreen* engine [15], [54]. Ji et al. provide more comparisons using reported statistics from the original papers [13].

Vascular Pathologies A vast number of severe neuronal and vascular pathologies, as well as aging, are associated with abnormalities and aberrations to the vessel network [8], see Figure 4.2. One highly prevalent pathology, cerebral infarction, commonly known as a stroke, is a very severe condition. For example, a brain vessel occlusion, which is one type of stroke, blocks the blood flow at a specific location in the vascular network. Therefore, the oxygen supply of all the neurons which are supplied by the branching vascular network downstream of the occlusion is interrupted. This condition leads to so-called brain ischemia. If not treated rapidly and efficiently, the neurons, glial cells, and blood vessels are irreversibly damaged, which can lead to disability, a substantially lowered quality of life or death [58]. In Figure 4.2 such a stroke occlusion, specifically a bilateral common carotid artery occlusion (BCCAo) is shown [57]. Another common neurovascular pathology, Alzheimer's disease, is associated with the successive degeneration of microvessels and the associated degeneration of their supplied neurons. Alzheimer's patients often exhibit tauopathy, which leads to reshaped and reorganized capillaries, impairing their ability to efficiently supply oxygen [56], see Figure 4.2. Moreover, acute brain injuries are also associated with vascular degeneration. For example, in Figure 4.2 the severe reduction of capillary vessels after an acute brain injury can be observed [55]. Notably, at the smallest level of the vasculature, the capillaries are often most affected by such pathologies, motivating extended research for early diagnosis and prevention of diverse neurodegenerative diseases.

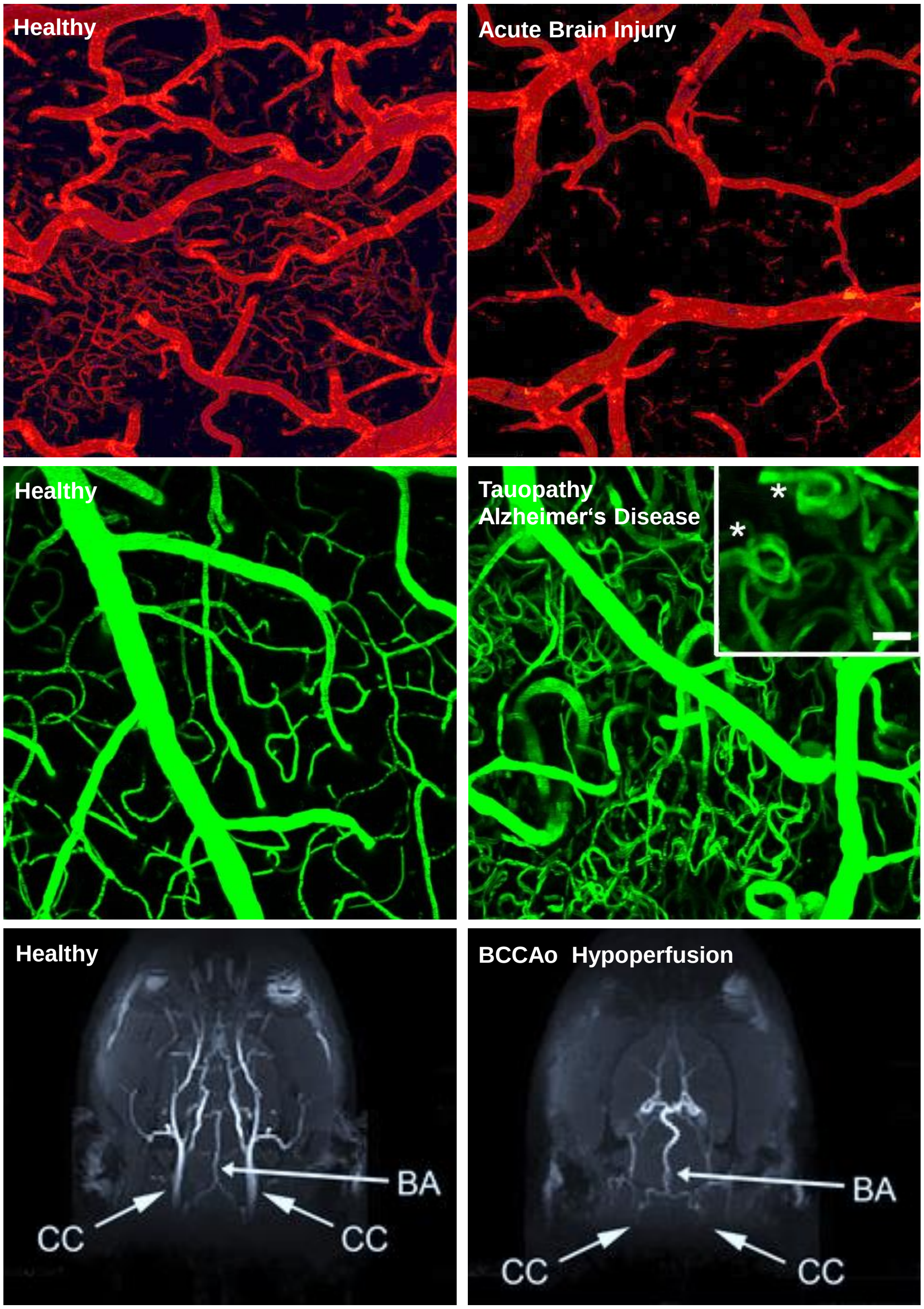

Figure 4.2: Common vessel pathologies: Top row, an acute, traumatic brain injury results in rarefication of the vascular network [55]; middle row, tauopathy [56] and in the last row, bilateral common carotid artery occlusion [57]; images licensed and taken from the respective publications, see Appendix E.

4.1 Whole-Brain Vessel Imaging

Light Sheet Microscopy Light-sheet microscopy (LSM) is a microscopic imaging technique where a single plane light-sheet laser images one plane of a 3D sample after another to generate a 3D image of the whole sample. In order to image whole specimens or organs such as the brain using LSM, the tissue sample has to be made transparent or cleared, and the cells of interest have to be marked. In recent years different protocols have been established to achieve a reliable clearing and staining of murine and human tissue, for example, 3D imaging of solvent-cleared organs (3DISCO) [4], CLARITY [59], and iDISCO which employs immunolabeling [60]. Nonetheless, the clearing protocols and staining techniques have to be tailored to the desired imaging foreground, often resulting in complicated and specific new experimental requirements, for example, in single-cell phenotyping [61], neuronal projections in whole mice [62], cancer metastases [7], or whole human organs [6].

Similar to other organs, brain vessels have been imaged using tissue clearing and microscopy. In 2018 Di Giovanna et al. combined CLARITY with a vascular staining approach to image the whole-brain vessels [5]. Next, the *VesSAP* work, presented as part of this thesis in Chapter 5 combined 3DISCO clearing and a dual dye staining to achieve a two-channel imaging of the whole mouse brain vasculature at a resolution of $1.625\ \mu m \times 1.625\ \mu m \times 3.0\ \mu m$ [11]. At a similar time, the Tubemap approach was also introduced [53] further solidifying tissue clearing and LSM as the state of the art in whole-brain vessel imaging.

Complete Datasets			
Name	Number of Nodes	Num of Edges	Node Degree
BALBc1 [11]	3,538,495	5,345,897	3.02
BALBc2	3,451,306	5,193,775	3.01
BALBc3	2,850,347	4,097,953	2.88
C57BL/6-1	3,820,133	5,614,677	2.94
C57BL/6-2	3,439,962	5,070,439	2.95
C57BL/6-3	3,318,212	4,819,208	2.90
CD1-E-1	3,645,963	5,791,309	3.18
CD1-E-2	1,664,811	2,150,326	2.58
CD1-E-3	2,295,360	3,130,650	2.73
C57BL/6-K18 [13]	4,284,051	6,525,881	3.05
C57BL/6-K19	3,948,612	5,999,958	3.04
C57BL/6-K20	4,165,085	6,317,179	3.03
Synth. Graph [63]	3159	3234	2.05

Table 4.1: Different whole-brain vessel datasets with their total number of edges, nodes, and average node degree according to the *VesselGraph* extraction approach. With a comparison to a synthetic dataset by Schneider et al. [63] which is frequently used for pre-training of segmentation networks. This table was first published in [15]. Please note that a standard bifurcation node has a degree of 3.

Other Imaging Methods Few performant alternatives to LSM for whole-brain imaging at micrometer resolution exist. Other methods, such as electron microscopy, two-photon microscopy, or confocal laser scanning, can provide even higher resolved images of diverse tissue but struggle with scanning the whole brain and the entire vasculature [64], [65]. Traditional medical imaging approaches such as magnetic resonance imaging (MRI), optical coherence tomography (OCT), and (X-ray microtomography) microCT can image whole brains but largely achieve substantially lower resolutions [66]–[68]. However, MRI and microCT constitute highly important research directions because of their potential to enable ultra-high resolution in-vivo imaging. Recently, Miettinen et al. achieved an 0.65 μm isotropic resolution image of the whole-brain vasculature using local synchrotron X-ray phase-contrast tomography [69]. A recent approach by Ji et al. employed serial sectional two-photon imaging with a resolution of 0.3 μm × 0.3 μm × 1 μm. Their results show a good agreement with the quantitative vascular features extracted in this thesis work [11], [13].

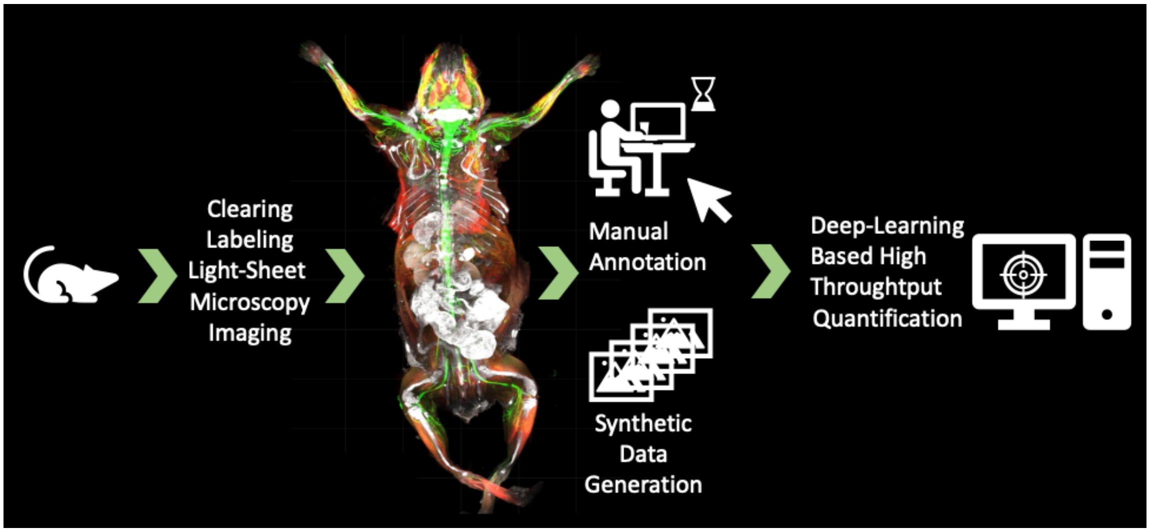

Figure 4.3: A typical pipeline for LSM imaging and deep learning enabled analysis.

4.2 Machine Learning on Vascular Structures

Considering the ultra-large size of LSM images in the terabyte range, machine learning based analysis plays a crucial role in biomarker extraction and quantification of the samples. In Figure 4.3 a typical workflow for LSM image analysis is depicted:

1. In the first step, the sample is prepared, tissue-cleared, and imaged using LSM.
2. Expert annotation or synthetic data generation techniques are required to produce high-quality image label pairs.
3. These image label pairs can then be used to develop supervised deep learning solutions to accomplish human-level analysis and high throughput quantification of biological samples, for example, vessel segmentation for capillary analysis.

Machine Learning Analysis of Whole Mouse Brain Vasculature

Mihail Ivilinov Todorov, **Johannes Christian Paetzold**, Oliver Schoppe, Giles Tetteh, Suprosanna Shit, Velizar Efremov, Katalin Todorov-Völgyi, Marco Düring, Martin Dichgans, Marie Piraud, Bjoern Menze & Ali Ertürk

Journal: Nature Methods, Volume 17, April 2020

Synopsis: Tissue clearing methods enable the imaging of biological specimens without sectioning. However, reliable and scalable analysis of large imaging datasets in three dimensions remains a challenge. Here we developed a deep learning-based framework to quantify and analyze brain vasculature, named Vessel Segmentation & Analysis Pipeline (VesSAP). Our pipeline uses a convolutional neural network (CNN) with a transfer learning approach for segmentation and achieves human-level accuracy. By using VesSAP, we analyzed the vascular features of whole C57BL/6J, CD1 and BALB/c mouse brains at the micrometer scale after registering them to the Allen mouse brain atlas. We report evidence of secondary intracranial collateral vascularization in CD1 mice and find reduced vascularization of the brainstem in comparison to the cerebrum. Thus, VesSAP enables unbiased and scalable quantifications of the angioarchitecture of cleared mouse brains and yields biological insights into the vascular function of the brain.

Contributions of thesis author: algorithm design and implementation, deep learning and feature extraction, other computational experiments, and leading role in composition and writing of the manuscript.

ARTICLES
https://doi.org/10.1038/s41592-020-0792-1

nature methods

Machine learning analysis of whole mouse brain vasculature

Mihail Ivilinov Todorov[1,2,3,10], Johannes Christian Paetzold[4,5,6,10], Oliver Schoppe[4,5], Giles Tetteh[4], Suprosanna Shit[4,5,6], Velizar Efremov[4,7], Katalin Todorov-Völgyi[2], Marco Düring[2,8], Martin Dichgans[2,8,9], Marie Piraud[4], Bjoern Menze[4,5,6,11] ✉ and Ali Ertürk[1,2,8,11] ✉

Tissue clearing methods enable the imaging of biological specimens without sectioning. However, reliable and scalable analysis of large imaging datasets in three dimensions remains a challenge. Here we developed a deep learning-based framework to quantify and analyze brain vasculature, named Vessel Segmentation & Analysis Pipeline (VesSAP). Our pipeline uses a convolutional neural network (CNN) with a transfer learning approach for segmentation and achieves human-level accuracy. By using VesSAP, we analyzed the vascular features of whole C57BL/6J, CD1 and BALB/c mouse brains at the micrometer scale after registering them to the Allen mouse brain atlas. We report evidence of secondary intracranial collateral vascularization in CD1 mice and find reduced vascularization of the brainstem in comparison to the cerebrum. Thus, VesSAP enables unbiased and scalable quantifications of the angioarchitecture of cleared mouse brains and yields biological insights into the vascular function of the brain.

Changes in cerebrovascular structures are key indicators for a large number of diseases affecting the brain. Primary angiopathies, vascular risk factors (for example, diabetes), traumatic brain injury, vascular occlusion and stroke all affect the function of the brain's vascular network[1–3]. The hallmarks of Alzheimer's disease, including tauopathy and amyloidopathy, can also lead to aberrant remodeling of blood vessels[1,4], allowing capillary rarefaction to be used as a marker for vascular damages[5]. Therefore, quantitative analysis of the entire brain vasculature is pivotal to developing a better understanding of brain function in physiological and pathological states. However, quantifying micrometer-scale changes in the cerebrovascular network of the brain has been difficult for two main reasons.

First, labeling and imaging of the complete mouse brain vasculature down to the smallest blood vessels has not yet been achieved. Magnetic resonance imaging (MRI), micro-computed tomography (micro-CT) and optical coherence tomography do not have sufficient resolution to capture capillaries in bulk tissue[6–8]. Fluorescent microscopy provides higher resolution, but can typically only be applied to tissue sections up to 200 µm in thickness[9]. Recent advances in tissue clearing could overcome this problem[10], but so far there has been no systematic description of all vessels of all sizes in an entire brain in three dimensions (3D).

The second challenge relates to the automated analysis of large 3D imaging datasets with substantial variance in signal intensity and signal-to-noise ratio (SNR) at different depths. Simple intensity- and shape-based filtering approaches such as Frangi's vesselness filters and more advanced image processing methods with local spatial adaptation cannot reliably differentiate vessels from background in whole-brain scans[11,12]. Finally, imaging of the complete vascular network of the brain at capillary resolution results in datasets of terabyte size. Established image processing methods do not scale well to terabyte-sized image volumes, as they do not generalize well to large images, and require intensive manual fine-tuning[13–15].

Here we present VesSAP (Vessel Segmentation & Analysis Pipeline), a deep learning-based method for automated analysis of the entire mouse brain vasculature, overcoming the above limitations. VesSAP encompasses three major steps: (1) staining, clearing and imaging of the mouse brain vasculature down to the capillary level with two different dyes: wheat germ agglutinin (WGA) and Evans blue (EB); (2) automatic segmentation and tracing of the whole-brain vasculature data via CNNs; and (3) extraction of vascular features for hundreds of brain regions after registration of the data to the Allen brain atlas (Fig. 1). Our deep learning-based approach for network extraction in cleared tissue is robust, despite variations in signal intensities and structures, outperforms previous filter-based methods and reaches the quality of segmentation achieved by human annotators. We applied VesSAP to the three commonly used mouse strains C57BL/6J, CD1 and BALB/c.

Results

Vascular staining, DISCO clearing and imaging. To reliably stain the entire vasculature, we used WGA and EB dyes, which can be visualized in different fluorescence channels. We injected EB dye into live mice 12 h before WGA perfusion, allowing its long-term circulation to mark vessels under physiological conditions[16], while we perfused mice with WGA during fixation. We then performed

---

[1]Institute for Tissue Engineering and Regenerative Medicine (iTERM), Helmholtz Zentrum München, Neuherberg, Germany. [2]Institute for Stroke and Dementia Research (ISD), Ludwig-Maximilians-Universität (LMU), Munich, Germany. [3]Graduate School of Neuroscience (GSN), Munich, Germany. [4]Department of Computer Science, Technical University of Munich (TUM), Munich, Germany. [5]Center for Translational Cancer Research of the TUM (TranslaTUM), Munich, Germany. [6]Munich School of Bioengineering, Technical University of Munich (TUM), Munich, Germany. [7]Institute of Pharmacology and Toxicology, University of Zurich (UZH), Zurich, Switzerland. [8]Munich Cluster for Systems Neurology (SyNergy), Munich, Germany. [9]German Center for Neurodegenerative Diseases (DZNE), Munich, Germany. [10]These authors contributed equally: Mihail Ivilinov Todorov, Johannes Christian Paetzold. [11]These authors jointly supervised this work: Bjoern Menze, Ali Ertürk. ✉e-mail: bjoern.menze@tum.de; erturk@helmholtz-muenchen.de

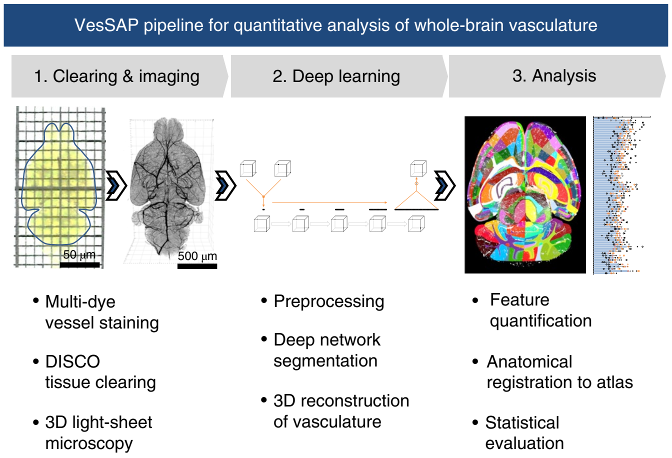

Fig. 1 | Summary of the VesSAP pipeline. The method consists of three modular steps: (1) multi-dye vessel staining and DISCO tissue clearing for high imaging quality using 3D light-sheet microscopy; (2) deep learning-based segmentation of blood vessels with 3D reconstruction; and (3) anatomical feature extraction and mapping of the entire vasculature to the Allen adult mouse brain atlas for statistical analysis.

3DISCO clearing[17] and light-sheet microscopy imaging of whole mouse brains (Fig. 2a–c and Supplementary Figs. 1 and 2). WGA highlighted microvessels, and EB predominantly stained major blood vessels, such as the middle cerebral artery and the circle of Willis (Fig. 2d–i and Supplementary Fig. 3). Merging the signals from the two dyes yielded more complete staining of the vasculature than relying on individual dyes alone (Fig. 2c,f and Supplementary Video 1). Staining with the two dyes was congruent in midsized vessels, with signals originating from the vessel wall layer (Fig. 2j–l and Supplementary Fig. 3a–c). When using WGA, we reached a higher SNR for microvessels than for bigger vessels. With EB, the SNR for small capillaries was lower but larger vessels reached a high SNR (Supplementary Fig. 4). Integrating the information from the two channels allowed acquisition of the entire vasculature and resulted in optimized SNR. We also compared the fluorescence signal quality of the WGA staining (targeting the complete endothelial glycocalyx lining[18]) to signal for a conventional vessel-specific antibody (anti-CD31, targeting endothelial cell–cell adhesion[19]) and found that WGA produced higher SNR for blood vessels in general (Supplementary Fig. 5).

Segmentation of volumetric images. To enable extraction of quantitative features of the vascular structure, vessels in acquired brain scans need to be segmented in 3D. Motivated by deep learning-based approaches in biomedical image data analysis[20–28], we used a five-layer CNN (Fig. 3a) to exploit the complementary signals of the two dyes to derive complete segmentation of the entire brain vasculature.

In the first step, the two input channels (WGA and EB) were concatenated. This yielded a matrix in which each voxel was characterized by two features. Then, each convolutional step integrated the information from a voxel's 3D neighborhood. We used full 3D convolutions[20] without further down- or upsampling and fewer trainable parameters than, for example, 3D U-Net and V-Net[29,30] to achieve high inference speeds. After the fourth convolution, the information from 50 features per voxel was combined with a convolutional layer with a kernel size of one and sigmoidal activation to estimate the likelihood that a given voxel represented a vessel. Subsequent binarization yielded the final segmentation. In both training and testing, the images were processed in subvolumes of 50 × 100 × 100 pixels.

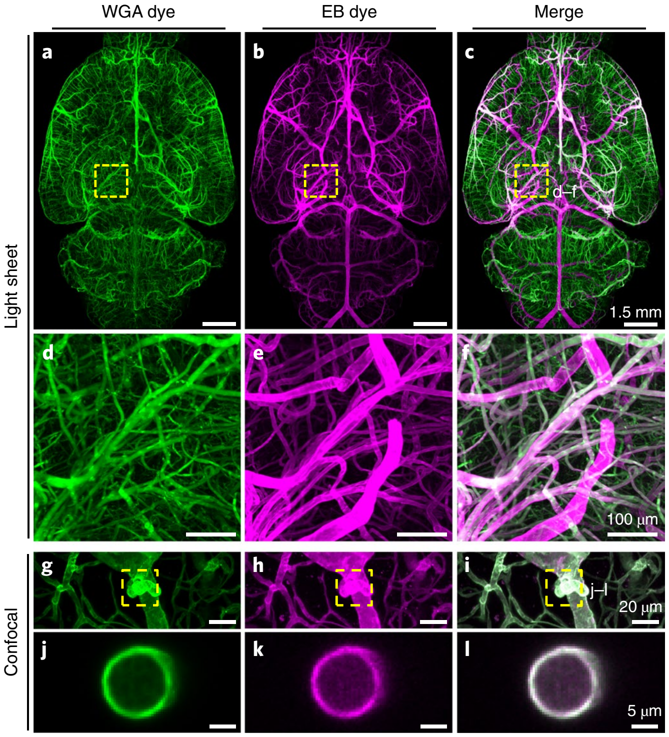

Fig. 2 | Enhancement of vascular staining using two complementary dyes. **a**–**c**, Maximum-intensity projections of automatically reconstructed tiling scans of WGA (**a**) and EB (**b**) signal in the same sample and the merged view (**c**). **d**–**f**, Magnified view of the boxed region in **c**. **g**–**l**, Confocal images of WGA- and EB-stained vessels and vascular wall (**g**–**i**, maximum-intensity projections at 112 µm; **j**–**l**, single slices of 1 µm corresponding to the boxed region in **i**). The experiment was performed on nine different mice with similar results.

Deep neural networks often require large amounts of annotated data or many iterations of training. Here we circumvented this requirement with a transfer learning approach[31]. In short, we first pretrained the network on a large, synthetically generated vessel-like dataset (Supplementary Fig. 6)[32] and then refined it on a small number of manually annotated parts of real brain vessel scans. This approach reduced the training iterations on manually annotated training data.

To assess the quality of the segmentation, we compared the VesSAP CNN predictions to manually labeled ground truth and the predictions from alternative computational approaches (Table 1). We report voxel-wise segmentation metrics, namely, accuracy, F1 score[33], Jaccard coefficient and cl-F1, which weights the centerlines and volumes of the vessels (detailed in the Methods). In comparison to the ground truth, our network achieved an accuracy of 0.94 ± 0.01 and an F1 score of 0.84 ± 0.05 (for additional scores, see Table 1; all values are given as the mean ± s.d.). As controls, we implemented alternative state-of-the-art deep learning and classical methods. Our network outperformed classical Frangi filters[11] (accuracy, 0.85 ± 0.03; F1 score, 0.47 ± 0.18), as well as recent methods based on local spatial context via Markov random fields[13,34] (accuracy, 0.85 ± 0.03; F1 score, 0.48 ± 0.04). VesSAP achieved similar performance in comparison to 3D U-Net and V-Net architectures, which require substantially more trainable parameters (3D U-Net: accuracy, 0.95 ± 0.01; F1 score, 0.85 ± 0.03; V-Net: accuracy, 0.95 ± 0.02; F1 score, 0.86 ± 0.07; no statistical difference in comparison to the VesSAP CNN: two-sided t test, all $P > 0.3$). However, the VesSAP CNN substantially outperformed the other architectures in terms of speed, being ~20 and ~50 times faster in the feedforward path than

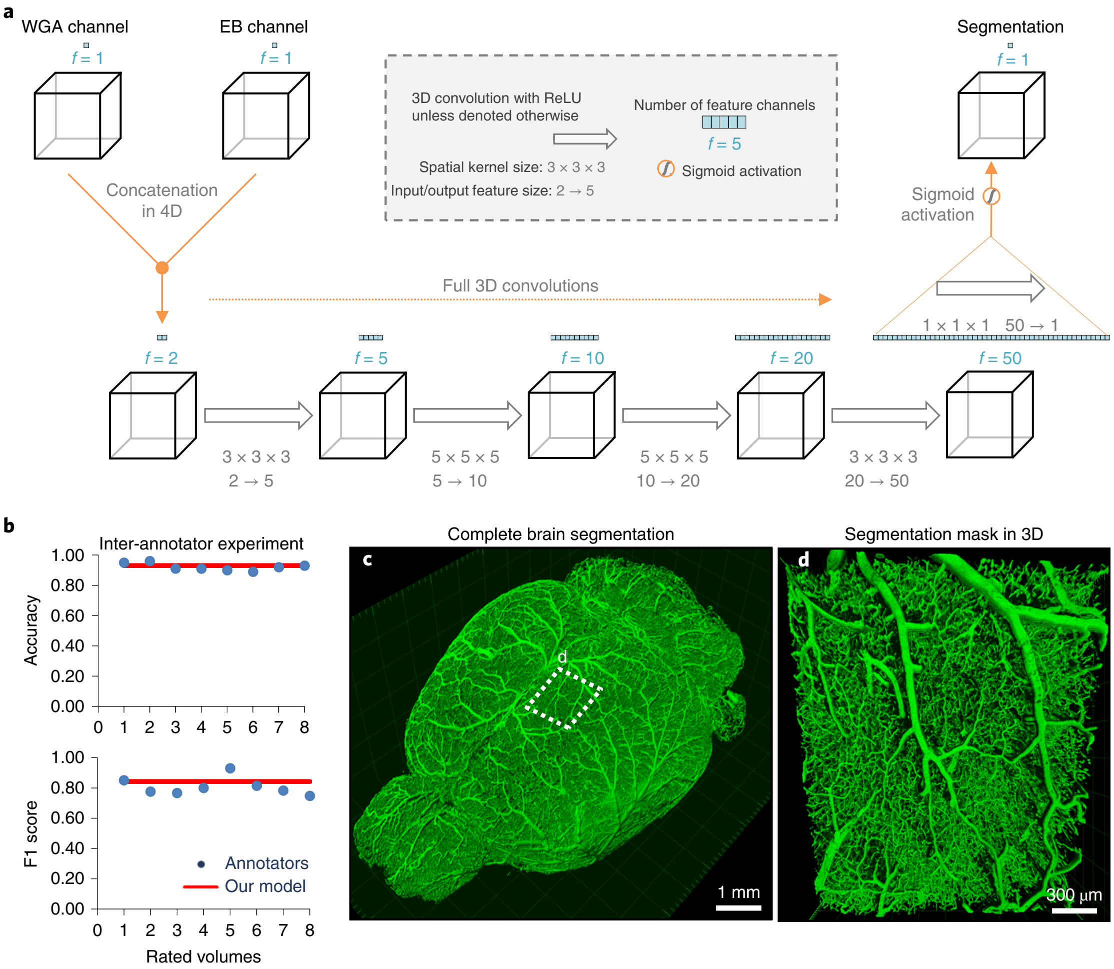

Fig. 3 | Deep learning architecture of VesSAP and performance on vessel segmentation. a, The 3D VesSAP network architecture consisting of five convolutional layers and sigmoid activation for the last layer, including the kernel size and feature size for the input/output. ReLU, rectified linear units. **b**, Accuracy and F1 score for the inter-annotator experiment (blue) as compared to VesSAP (red). **c**, 3D rendering of full brain segmentation from a CD1 mouse. **d**, 3D rendering of the small volume boxed in **c**. The experiment was performed on nine different mice with similar results.

Table 1 | Evaluation metrics of the different segmentation approaches for 75 volumes of 100 × 100 × 50 pixels

Segmentation model	cl-F1	Accuracy	F1 score	Jaccard	Parameters	Speed
VesSAP CNN	**0.93 ± 0.02***	**0.94 ± 0.01**	**0.84 ± 0.05**	**0.84 ± 0.04**	**0.0587 M***	**1.19 s***
VesSAP CNN, trained from scratch	**0.93 ± 0.02**	**0.94 ± 0.01**	**0.85 ± 0.04***	**0.85 ± 0.04**	**0.0587 M***	**1.19 s***
VesSAP CNN, synthetic training data	0.87 ± 0.02	0.90 ± 0.05	0.72 ± 0.07	0.70 ± 0.05	**0.0587 M***	**1.19 s***
3D U-Net	**0.93 ± 0.02**	**0.95 ± 0.01***	**0.85 ± 0.03***	**0.85 ± 0.03**	178.4537 M	61.22 s
V-Net	**0.94 ± 0.02***	**0.95 ± 0.02***	**0.86 ± 0.07***	**0.86 ± 0.07***	88.8556 M	26.87 s
Frangi vesselness	0.84 ± 0.03	0.85 ± 0.03	0.47 ± 0.19	–	–	117.00 s
Markov random field	0.86 ± 0.02	0.85 ± 0.03	0.48 ± 0.04	–	–	24.31 s

All values are given as the mean ± s.d. The best performing algorithms are in bold and highlighted with an asterisk; algorithms whose performance did not differ more than 2% from the best performing algorithms are in bold. The number of trainable parameters for deep learning architectures is given in millions (M).

V-Net and 3D U-Net, respectively. This is particularly important for our large datasets (hundreds of gigabytes). For example, the VesSAP CNN segmented a single brain in 4 h, whereas V-Net and 3D U-Net required 3.3 d and 8 d, respectively. The superior speed of the VesSAP CNN is due to the substantially fewer trainable parameters in its architecture (for example, our implementation of 3D U-Net had ~178 million parameters, whereas the VesSAP CNN had ~0.059 million parameters) (Table 1). Next, we compared the segmentation accuracy of our network to the accuracy of human annotations. A total of four human experts independently annotated two volumes. We found that the inter-annotator accuracy and F1 scores of the experts were comparable to those from the predicted segmentation of our network (human annotators: accuracy, 0.92 ± 0.02; F1 score, 0.81 ± 0.06; Fig. 3b). Notably, we extrapolate that human annotators

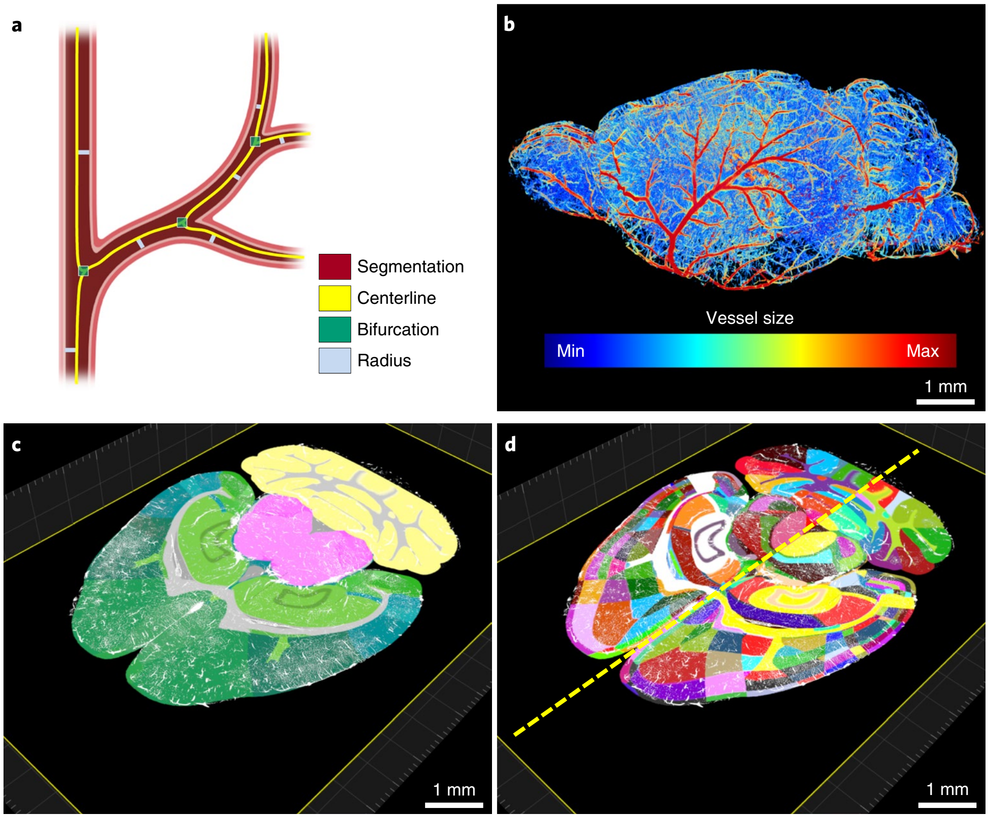

Fig. 4 | Pipeline showing the feature extraction and registration process. a, Representation of the features extracted from vessels. **b**, Radius illustration of the vasculature in a CD1 mouse brain. **c**,**d**, Vascular segmentation results overlaid on the hierarchically (**c**) and randomly (**d**) color-coded atlas to reveal all annotated regions available, including hemispheric difference (dashed line in **d**). The experiment was performed on nine different mice with similar results.

would need more than a year to process a whole brain instead of the 4 h required by our approach. Moreover, we observed differences in the human segmentations due to annotator bias. Thus, the VesSAP CNN can segment the complete brain vasculature consistently at human-level accuracy with a substantially higher speed than currently available methods, enabling high throughput for large-scale analysis.

We show an example of the vasculature from a brain segmented by VesSAP in 3D (Fig. 3c and Supplementary Videos 2 and 3). Zooming in on a smaller patch revealed that the connectivity of the vascular network was fully maintained (Fig. 3d and Supplementary Video 2). Comparing single slices of the imaging data with the predicted segmentation showed that vessels were accurately segmented regardless of absolute illumination or vessel diameter (Supplementary Fig. 7).

Feature extraction and atlas registration. Vessel lengths and radii and the number of bifurcation points are commonly used to describe the angioarchitecture[2]. Hence, we used our segmentation to quantify these features as distinct parameters to characterize the mouse brain vasculature (Fig. 4a and Supplementary Video 4). We evaluated the local vessel length (length normalized to the size of the brain region of interest), local bifurcation density (sum of the occurrences normalized to the size of the brain region of interest) and local vessel radius (average radius along the full length) of blood vessels in different brain regions.

We report the vascular features in three ways to enable comparison with various previous studies that differed in the measures used (Supplementary Fig. 8). More specifically, first, we provide the count of segmented voxels as compared to total voxels within a specific brain region (voxel space). Second, we provide the measurements by calculating the voxel size of our imaging system and accounting for the Euclidean length (microscopic space). Third, we corrected the microscopic measurements to account for tissue shrinkage caused by the clearing process (anatomical space)[35,36] (Supplementary Tables 2–10). We calculated this shrinkage rate by measuring the same mouse brain volume with MRI before clearing.

Here we use the anatomical space to report our specific biological findings, as it is closest to the physiological state. For the average blood vessel length of the whole brain, we found a value of 545.74 ± 94 mm per mm^3 (mean ± s.d.). Because our method quantifies brain regions separately, we could compare our results to the literature, which mostly reports either quantifications for specific brain regions or extrapolations to the whole brain from regional quantifications. For example, a vascular length of 922 ± 176 mm per mm^3 (mean ± s.d.) was previously reported for cortical regions (size of $508 \times 508 \times 1{,}500\ \mu m^3$)[10]. We found a similar vessel length for the same region in the mouse cortex (C57BL/6J mice: 913 ± 110 mm per mm^3), substantiating the accuracy of our method. We performed additional comparisons to other reports (Supplementary Table 11). Moreover, we compared the measurements acquired with our algorithms to manually labeled ground truth data and found deviations of 8.21% for centerlines, 13.18% for the number of bifurcation points and 16.33% for the average radius. These deviations were substantially lower than the average deviation among human annotators (Methods).

We quantified and visualized vessel radius along the entire vascular network (Fig. 4b). After extracting vascular features for the whole brain with VesSAP, we registered the volume to the Allen brain atlas (Supplementary Videos 5 and 6). This allowed us to map the segmented vasculature and corresponding features topographically to distinct anatomical brain regions (Fig. 4c). Each anatomical

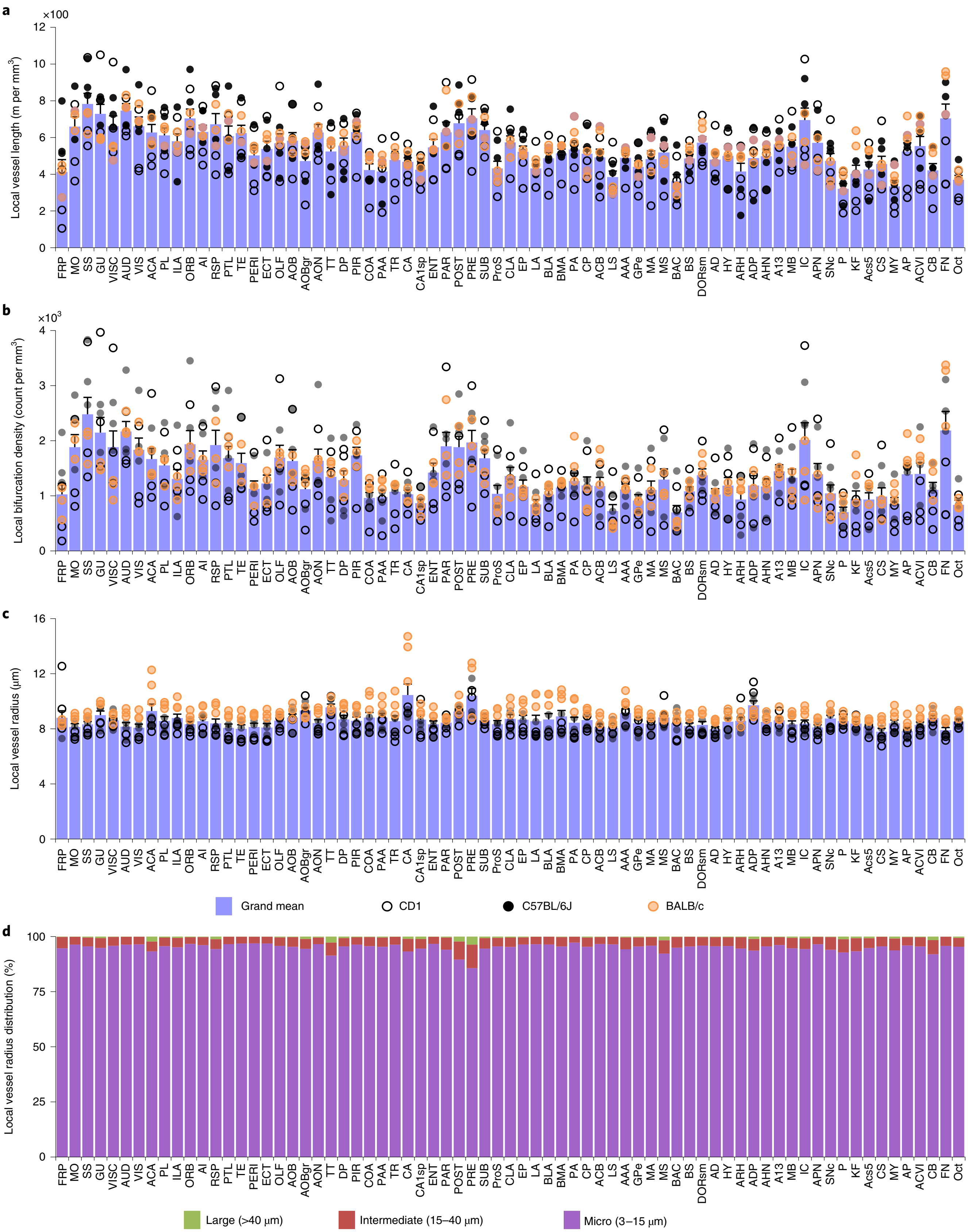

Fig. 5 | Anatomical properties of the neurovasculature in adult mouse brain mapped to the Allen brain atlas clusters. a–c, Representations of the local vessel length (**a**), density of bifurcations (**b**) and average radius (**c**) in each of the 71 main anatomical clusters of the Allen brain atlas. Open, black and orange circles denote measurements in the CD1, C57BL/6J and BALB/c strains, respectively; each circle represents a single mouse. Data are given as the mean ± s.e.m.; *n* = 3 mice per strain. **d**, Local distribution of large, intermediate and microvessels in the same anatomical clusters. Abbreviations are defined in Supplementary Table 1.

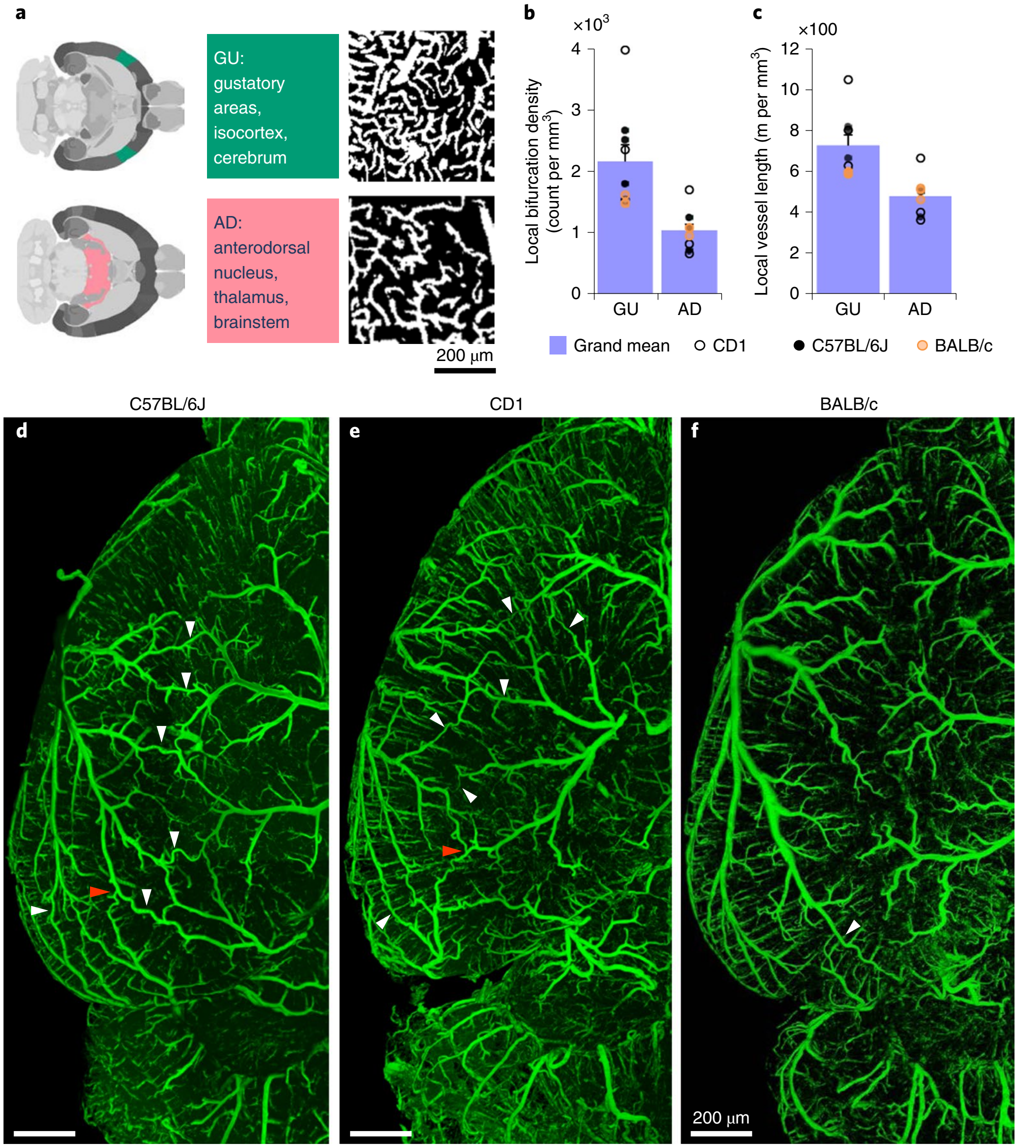

Fig. 6 | Exemplary quantitative analysis enabled by VesSAP. a, Respective locations of the anterodorsal nucleus (AD) and gustatory areas (GU) in the mouse brain (left) and maximum-intensity projections of representative volumes from segmentation of these areas (600 × 600 × 33 μm^3) (right). **b**,**c**, Quantification of the bifurcation density (**b**) and local vessel length (**c**) for the anterodorsal nucleus and gustatory area clusters. CD1 mice are shown by open circles, BALB/C mice by orange circles and C57BL/6J mice by black circles. Values are the mean ± s.e.m.; $n = 3$ mice per strain. **d**–**f**, Images of the vasculature in representative C57BL/6J (**d**), CD1 (**e**) and BALB/c (**f**) mice, where white arrowheads indicate anastomoses between major arteries. Direct vascular connections between the medial cerebral artery, the anterior cerebral artery and the posterior cerebral artery are indicated by red arrowheads. The experiment was performed three times with similar results.

region could be further divided into subregions, yielding a total of 1,238 anatomical structures (619 per hemisphere) for the entire mouse brain (Fig. 4d). This allowed analysis of each denoted brain region and grouping of regions into clusters such as left versus right hemisphere, gray versus white matter, or any hierarchical cluster of the Allen brain atlas ontology. For our subsequent statistical feature analysis, we grouped the labeled structures according to the 71 main anatomical clusters of the current Allen brain atlas ontology. We thus provide the whole mouse brain vascular map with extracted vessel lengths, bifurcation points and radii down to the capillary level.

VesSAP provides a reference map of the whole brain vasculature in mice. By studying whole brain vasculature in the C57BL/6J, CD1 and BALB/c strains ($n = 3$ mice for each strain), we found that the local vessel length and local bifurcation density differed in the same brain over different regions, while they were highly correlated among different mice for the same regions (Fig. 5a,b). Furthermore, the local bifurcation density was highly correlated with the local vessel length in most brain regions (Supplementary Fig. 9), and the average vessel radius was evenly distributed in different regions of the same brain (Fig. 5c). In addition, the extracted features showed no statistical difference (by Cohen's *d*; Supplementary Table 12) for the same anatomical cluster across the strains (Supplementary Fig. 9). Finally, microvessels made up the overwhelming majority of the total vascular composition in all brain regions (Fig. 5d). We visually inspected exemplary brain regions to validate the output of VesSAP. Both VesSAP and visual inspection revealed that the gustatory areas had a higher vascular length per volume than the anterodorsal nucleus (Fig. 6a–c). Visual inspection also suggested that the number of capillaries was the primary reason for regional feature variations within the same brain.

Finally, VesSAP offered insights into the neurovascular structure of the different mouse strains in our study. There were direct intracranial vascular anastomoses in the C57BL/6J, CD1 and BALB/c strains (white arrowheads in Fig. 6d–f). The anterior cerebral artery, middle cerebral artery and posterior cerebral artery were connected at the dorsal visual cortex in CD1 mice (red arrowheads in Fig. 6d,e) unlike in the BALB/c strain[33] (Fig. 6f).

Discussion

VesSAP can generate reference maps of the adult mouse brain vasculature, which can potentially be used to model synthetic cerebrovascular networks[37]. In addition to the metrics we obtain to describe the vasculature, advanced metrics, for example, Strahler values, network connectivity and bifurcation angles, can be extracted by using the data generated by VesSAP. Furthermore, the centerlines and bifurcation points can be interpreted as the edges and nodes for building a full vascular network graph, offering a means for studying local and global properties of the cerebrovascular network in the future.

The VesSAP workflow relies on staining of blood vessels by two different dyes. WGA binds to the glycocalyx of the endothelial lining of blood vessels[38] but may miss some segments of large vessels[18]. EB is a dye with a high affinity for serum albumin[35,36,39]; thus, it remains in the large vessels after a short perfusion protocol. In addition, EB labeling is not affected by subsequent DISCO clearing.

Vessels have long and thin tubular shapes. In our images, the radii of capillaries (about 3 μm) are in the range of our voxel size. Therefore, segmentation that yields the correct diameter down to single-pixel resolution poses a challenge, as we observed a 16% deviation for the radius. This subpixel deviation did not pose a problem for segmenting the whole vasculature network and extracting features because the vascular network can be defined by its centerlines and bifurcations.

The described segmentation concept is based on a transfer learning approach, where we pretrained the CNN and refined it on a small labeled dataset of 11% of the synthetic dataset and only 0.02% of one cleared brain. We consider this to be a major advantage in comparison to training from scratch. Thus, our CNN might generalize well to different types of imaging data (such as micro-CT angiography) or other curvilinear structures (for example, neurons), as only a small labeled dataset is needed to adjust our pretrained network.

On the basis of our vascular reference map, unknown vascular properties can be discovered and biological models can be confirmed. VesSAP showed a high number of collaterals in albino CD1 mice. Such collaterals between large vessels can substantially alter the outcome of ischemic stroke lesions: blood-deprived brain regions arising from occlusion of a large vessel can be compensated by blood supply from the collateral extensions of other large vessels[33,40]. Therefore, our VesSAP method can lead to the discovery of previously unknown anatomical details that could be functionally relevant.

In conclusion, VesSAP is a scalable, modular and automated machine learning-based method to analyze complex imaging data from cleared mouse brains. We foresee that our method will accelerate the applications of tissue clearing, in particular for studies assessing brain vasculature.

Online content

Any methods, additional references, Nature Research reporting summaries, source data, extended data, supplementary information, acknowledgements, peer review information; details of author contributions and competing interests; and statements of data and code availability are available at https://doi.org/10.1038/s41592-020-0792-1.

Received: 19 April 2019; Accepted: 14 February 2020;

References

1. Bennett, R. E. et al. Tau induces blood vessel abnormalities and angiogenesis-related gene expression in P301L transgenic mice and human Alzheimer's disease. *Proc. Natl Acad. Sci. USA* **115**, E1289–E1298 (2018).
2. Obenaus, A. et al. Traumatic brain injury results in acute rarefication of the vascular network. *Sci. Rep.* **7**, 239 (2017).
3. Völgyi, K. et al. Chronic cerebral hypoperfusion induced synaptic proteome changes in the rat cerebral cortex. *Mol. Neurobiol.* **55**, 4253–4266 (2018).
4. Klohs, J. et al. Contrast-enhanced magnetic resonance microangiography reveals remodeling of the cerebral microvasculature in transgenic ArcAbeta mice. *J. Neurosci.* **32**, 1705–1713 (2012).
5. Edwards-Richards, A. et al. Capillary rarefaction: an early marker of microvascular disease in young hemodialysis patients. *Clin. Kidney J.* **7**, 569–574 (2014).
6. Calabrese, E., Badea, A., Cofer, G., Qi, Y. & Johnson, G. A. A diffusion MRI tractography connectome of the mouse brain and comparison with neuronal tracer data. *Cereb. Cortex* **25**, 4628–4637 (2015).
7. Dyer, E. L. et al. Quantifying mesoscale neuroanatomy using X-ray microtomography. *eNeuro* **4**, ENEURO.0195-17.2017 (2017).
8. Li, T., Liu, C. J. & Akkin, T. Contrast-enhanced serial optical coherence scanner with deep learning network reveals vasculature and white matter organization of mouse brain. *Neurophotonics* **6**, 035004 (2019).
9. Tsai, P. S. et al. Correlations of neuronal and microvascular densities in murine cortex revealed by direct counting and colocalization of nuclei and vessels. *J. Neurosci.* **29**, 14553–14570 (2009).
10. Lugo-Hernandez, E. et al. 3D visualization and quantification of microvessels in the whole ischemic mouse brain using solvent-based clearing and light sheet microscopy. *J. Cereb. Blood Flow Metab.* **37**, 3355–3367 (2017).
11. Frangi, A. F., Niessen, W. J., Vincken, K. L. & Viergever, M. A. in *International Conference on Medical Image Computing and Computer-Assisted Intervention* 130–137 (Springer, 1998).
12. Sato, Y. et al. Three-dimensional multi-scale line filter for segmentation and visualization of curvilinear structures in medical images. *Med. Image Anal.* **2**, 143–168 (1998).
13. Di Giovanna, A. P. et al. Whole-brain vasculature reconstruction at the single capillary level. *Sci. Rep.* **8**, 12573 (2018).
14. Xiong, B. et al. Precise cerebral vascular atlas in stereotaxic coordinates of whole mouse brain. *Front. Neuroanat.* **11**, 128 (2017).
15. Clark, T. A. et al. Artery targeted photothrombosis widens the vascular penumbra, instigates peri-infarct neovascularization and models forelimb impairments. *Sci. Rep.* **9**, 2323 (2019).
16. Yao, J., Maslov, K., Hu, S. & Wang, L. V. Evans blue dye—enhanced capillary-resolution photoacoustic microscopy in vivo. *J. Biomed. Opt.* **14**, 054049 (2009).
17. Ertürk, A. et al. Three-dimensional imaging of solvent-cleared organs using 3DISCO. *Nat. Protoc.* **7**, 1983–1995 (2012).
18. Reitsma, S. et al. Endothelial glycocalyx structure in the intact carotid artery: a two-photon laser scanning microscopy study. *J. Vasc. Res.* **48**, 297–306 (2011).
19. Schimmenti, L. A., Yan, H. C., Madri, J. A. & Albelda, S. M. Platelet endothelial cell adhesion molecule, PECAM-1, modulates cell migration. *J. Cell. Physiol.* **153**, 417–428 (1992).
20. Tetteh, G. et al. DeepVesselNet: vessel segmentation, centerline prediction, and bifurcation detection in 3-D angiographic volumes. Preprint at https://arxiv.org/abs/1803.09340 (2018).
21. Weigert, M. et al. Content-aware image restoration: pushing the limits of fluorescence microscopy. *Nat. Methods* **15**, 1090–1097 (2018).
22. Wang, H. et al. Deep learning enables cross-modality super-resolution in fluorescence microscopy. *Nat. Methods* **16**, 103–110 (2019).
23. Falk, T. et al. U-Net: deep learning for cell counting, detection, and morphometry. *Nat. Methods* **16**, 67–70 (2019).
24. Caicedo, J. C. et al. Data-analysis strategies for image-based cell profiling. *Nat. Methods* **14**, 849–863 (2017).
25. Dorkenwald, S. et al. Automated synaptic connectivity inference for volume electron microscopy. *Nat. Methods* **14**, 435–442 (2017).
26. Liu, S., Zhang, D., Song, Y., Peng, H. & Cai, W. in *Machine Learning in Medical Imaging* (eds., Wang, Q. et al.) 185–193 (Springer International Publishing, 2017).
27. Long, J., Shelhamer, E. & Darrell, T. Fully convolutional networks for semantic segmentation. in *Proceedings of the IEEE Conference on Computer Vision and Pattern Recognition* 3431–3440 (IEEE, 2015).
28. Livne, M. et al. A U-Net deep learning framework for high performance vessel segmentation in patients with cerebrovascular disease. *Front. Neurosci.* **13**, 97 (2019).
29. Çiçek, Ö., Abdulkadir, A., Lienkamp, S. S., Brox, T. & Ronneberger, O. 3D U-Net: learning dense volumetric segmentation from sparse annotation. in *Medical Image Computing and Computer-Assisted Intervention* 424–432 (2016).
30. Milletari, F., Navab, N. & Ahmadi, S.A. V-Net: fully convolutional neural networks for volumetric medical image segmentation. in *2016 Fourth International Conference on 3D Vision* 565–571 (IEEE, 2016).

31. Litjens, G. et al. A survey on deep learning in medical image analysis. *Med. Image Anal.* **42**, 60–88 (2017).
32. Schneider, M., Reichold, J., Weber, B., Szekely, G. & Hirsch, S. Tissue metabolism driven arterial tree generation. *Med. Image Anal.* **16**, 1397–1414 (2012).
33. Chalothorn, D., Clayton, J. A., Zhang, H., Pomp, D. & Faber, J. E. Collateral density, remodeling, and VEGF-A expression differ widely between mouse strains. *Physiol. Genomics* **30**, 179–191 (2007).
34. Li, S. Z. In *Computer Vision—ECCV* (ed., Eklundh, J.-O.) 361–370 (Springer, 1994).
35. Pan, C. et al. Shrinkage-mediated imaging of entire organs and organisms using uDISCO. *Nat. Methods* **13**, 859–867 (2016).
36. Cai, R. et al. Panoptic imaging of transparent mice reveals whole-body neuronal projections and skull–meninges connections. *Nat. Neurosci.* **22**, 317–327 (2019).
37. Menti, E., Bonaldi, L., Ballerini, L., Ruggeri, A. & Trucco, E. In *International Workshop on Simulation and Synthesis in Medical Imaging* 167–176 (Springer, Year).
38. Kataoka, H. et al. Fluorescent imaging of endothelial glycocalyx layer with wheat germ agglutinin using intravital microscopy. *Microsc. Res. Tech.* **79**, 31–37 (2016).
39. Steinwall, O. & Klatzo, I. Selective vulnerability of the blood–brain barrier in chemically induced lesions. *J. Neuropathol. Exp. Neurol.* **25**, 542–559 (1966).
40. Zhang, H., Prabhakar, P., Sealock, R. & Faber, J. E. Wide genetic variation in the native pial collateral circulation is a major determinant of variation in severity of stroke. *J. Cereb. Blood Flow Metab.* **30**, 923–934 (2010).

Methods

Tissue preparation. Animal experiments were conducted according to institutional guidelines (Klinikum der Universität München/Ludwig Maximilian University of Munich), after approval of the ethical review board of the government of Upper Bavaria (Regierung von Oberbayern, Munich, Germany), and in accordance with European directive 2010/63/EU for animal research. Animals were housed under a 12-h light/12-h dark cycle. For this study, we injected 150 µl (2% (vol/vol) in saline) EB dye (Sigma-Aldrich, E2129) intraperitoneally into 3-month-old male mice from the C57BL/6J, CD1 and BALB/c strains (Charles River, strain codes 027, 482 and 028, respectively; $n = 3$ mice per strain). Twelve hours after injection of EB dye, we anesthetized the animals with a combination of midazolam, medetomidine and fentanyl (administered intraperitoneally; 1 ml per 100 g body weight containing 5 mg, 0.5 mg and 0.05 mg per kg body weight, respectively) and opened their chest for transcardial perfusion. Medium with WGA (0.25 mg WGA conjugated to Alexa Fluor 594 dye (Thermo Fisher Scientific, W11262) in 150 µl PBS, pH 7.2) was supplied by peristaltic pump set to deliver the medium at a rate of 8 ml min^{-1}, along with 15 ml of 1× PBS and 15 ml of 4% paraformaldehyde. This short perfusion protocol was established on the basis of preliminary experiments, where both WGA and EB staining were partially washed out (data not shown), with the goal of delivering fixative to brain tissue via the vessels to achieve a homogenous preservation effect[41].

After perfusion, brains were extracted from the neurocranium while severing some of the segments of the circle of Willis, which is an inevitable component of most retrieval processes aside from corrosion cast techniques. Next, the samples were incubated in 3DISCO clearing solutions as described[17]. Briefly, we immersed them in a gradient of tetrahydrofuran (Sigma-Aldrich, 186562): 50%, 70%, 80% and 90% (in distilled water) followed by 100%, at 25 °C for 12 h at each concentration. At this point, we modified the protocol by incubating the samples in *tert*-butanol for 12 h at 35 °C followed by immersion in dichloromethane (Sigma-Aldrich, 270997) for 12 h at room temperature and a final incubation with refractive index-matched BABB solution (benzyl alcohol + benzyl benzoate, 1:2; Sigma-Aldrich, 24122 and W213802), for at least 24 h at room temperature until transparency was achieved. Each incubation step was carried out on a laboratory shaker.

Imaging of cleared samples with light-sheet microscopy. We used a ×4 objective lens (Olympus XLFLUOR 340) equipped with an immersion-corrected dipping cap mounted on a LaVision UltraII microscope coupled to a white-light laser module (NKT SuperK Extreme EXW-12) for imaging. Images were taken with 16-bit depth and at a nominal resolution of 1.625 µm per voxel on the x and y axes. For ×12 imaging, we used a LaVision objective (×12/0.53 NA MI PLAN with an immersion-corrected dipping cap). Brain structures were visualized by Alexa Fluor 594 (using a 580/25-nm excitation filter and a 625/30-nm emission filter) and EB fluorescent dye (using a 640/40-nm excitation filter and a 690/50-nm emission filter) in sequential order. We maximized the SNR for each dye independently to avoid saturation of differently sized vessels when only a single channel was used. We achieved this by independently optimizing the excitation power so that the strongest signal in major vessels did not exceed the dynamic range of the camera. In the z dimension, we took sectional images in 3-µm steps while using left- and right-sided illumination. Our measured resolution was 2.83 µm × 2.83 µm × 4.99 µm for x, y and z, respectively (Supplementary Fig. 2). To reduce defocus, which derives from the Gaussian shape of the beam, we used 12-step sequential shifting of the focal position of the light sheet per plane and side. The thinnest point of the light sheet was 5 µm.

Imaging of cleared samples with confocal microscopy. Additionally, the cleared specimens were imaged with an inverted laser-scanning confocal microscope (Zeiss, LSM 880) for further analysis. Before imaging, samples were mounted by placing them onto the glass surface of a 35-mm glass-bottom Petri dish (MatTek, P35G-0-14-C) and immersed in BABB. A ×40 oil-immersion objective lens was used (Zeiss, ECPlan-NeoFluar ×40/1.30 NA Oil DIC M27, WD = 0.21 mm). Images were acquired with the settings for Alexa Fluor 594 (using excitation at 561 nm and an emission range of 585–733 nm) and EB fluorescent dye (using excitation at 633 nm and an emission range of 638–755 nm) in sequential order.

Magnetic resonance imaging. We used a nanoScan PET/MR device (3 Tesla, Mediso Medical Imaging Systems) equipped with a head coil for murine heads to acquire anatomical scans in the T1 modality.

Reconstruction of the datasets from tiling volumes. We stitched the acquired volumes by using TeraStitcher's automatic global optimization function (v1.10.3). We produced volumetric intensity images of the whole brain while considering each channel separately. To improve alignment to the Allen brain atlas, we downscaled our dataset in the xy plane to achieve pseudouniform voxel spacing matching the z plane.

Deep learning network architecture. We relied on a deep 3D CNN for segmentation of our blood vessel dataset. The network's general architecture consists of five convolutional layers, four with ReLU (rectified linear units) followed by one convolutional layer with sigmoid activation (Fig. 3a). The input layer is designed to take n images as input. In the implemented case, the input to the first layer of the network comprised $n = 2$ images of the same brain, which had been stained differently (Fig. 3a). To specifically account for the general class imbalance (much more tissue background than vessel signal) in our dataset and the potential for high false-positive rates associated with this, we chose the generalized soft-Dice as the loss function to our network. At all levels, we used full 3D convolutional kernels (Fig. 3a).

The network's training is driven by an Adam optimizer with a learning rate of 1×10^{-5} and an exponential decay rate of 0.9 for the first moment and 0.99 for the second moment[42]. A prediction or segmentation with a trained model takes volumetric images of arbitrary size as input and outputs a probabilistic segmentation map of identical size. To deal with volumes of arbitrary size and extension, we processed them in smaller subvolumes of 100 × 100 × 50 pixels in size. The algorithms were implemented by using the Tensorflow framework and KERAS[43]. They were trained and tested on two NVIDIA Quadro P5000 GPUs and on machines with 64 GB and 512 GB of RAM.

Transfer learning. Typically, supervised learning tasks in biomedical imaging are aggravated by the scarce availability of labeled training data. Our transfer learning approach aims to circumvent this problem by pretraining our models on synthetically generated data and refining them on a small set of real images[44]. Specifically, our approach pretrains the VesSAP CNN on 3D volumes of vascular image data, synthetically generated together with the corresponding training labels by using the approach of Schneider and colleagues[45]. The pretraining is carried out on a dataset of 20 volumes of 325 × 304 × 600 pixels in size for 38 epochs. During pretraining, we applied a learning rate of 1×10^{-4}. Afterward, the pretrained model was fine-tuned by retraining on a real microscopic dataset consisting of 11 volumes of 500 × 500 × 50 pixels in size. The image volumes were manually annotated by commissioned experts, including the expert who previously prepared the samples and operated the microscope. The labels were verified and further refined in consensus by two additional human raters. The data we used in this fine-tuning step amounted to 11% of the volume of the synthetic datasets and only 0.02% of the voxel volume of a single whole brain. For the fine-tuning step, we used a learning rate of 1×10^{-5}. The final model was obtained after training on the real dataset for six epochs. This training was substantially shorter than training from scratch, where we trained the same VesSAP CNN architecture for 72 epochs until we reached the best F1 score on the validation set. The labeled dataset consisted of 17 volumes of 500 × 500 × 50 pixels from five mouse brains. Three of these brains were from the CD1 strain, and two were from the C57BL/6J strain. The volumes were chosen from regions throughout the whole brain, to represent the variability in the vascular dataset in terms of both vessel shape and illumination. To ensure independence, volumes for the training set and test/validation set were chosen from independent brains. All datasets included brains from the two strains. Our training dataset consisted of 11 volumes, the validation dataset of 3 volumes and the test dataset of 3 volumes. We cross-tested on our test and validation datasets by rotating these. The volumes were processed during training and inference in 25 small subvolumes of 100 × 100 × 50 pixels.

We observed an average F1 score of 0.84 ± 0.02 (mean ± s.d.), an average accuracy of 0.94 ± 0.01 (mean ± s.d.) and an average Jaccard coefficient of 0.84 ± 0.04 (mean ± s.d.) on our test datasets (Fig. 3b). We tested the statistical significance of differences among the top three learning methods (the VesSAP CNN, V-Net and 3D U-Net) by using paired t tests. We found that the differences in F1 score were not statistically significant (all $P > 0.3$, rejecting the hypothesis of different distributions).

Because the F1 score, accuracy and Jaccard coefficient are all voxel-wise volumetric scores and can fall short in evaluating the connectedness of components, we developed the cl-F1 score. cl-F1 is calculated from the intersection of centerlines and vessel volumes and not from volumes only, as the traditional F1 score is[46]. To determine this score, we first calculated the intersection of the centerline of our prediction with the labeled volume and then calculated the intersection of the labeled volume's centerline with the predicted volume. Next, we treated the first intersection as recall, as it is susceptible to false negatives, and the second intersection as precision, as it is susceptible to false positives, and input this into the traditional F1 score formulation:

$$\mathrm{F1} = 2 \times \frac{\text{precision} \times \text{recall}}{\text{precision} + \text{recall}} \tag{1}$$

We report an average cl-F1 score of 0.93 ± 0.02 (mean ± s.d.) on the test set.

All scores are given as mean and s.d. Our model reached the best model selection point on the validation dataset after six epochs of training.

Comparison to 3D U-Net and V-Net. To compare our proposed architecture to different segmentation architectures, we implemented V-Net and 3D U-Net, both of which use more complex CNNs with substantially more trainable parameters, which further include down- and upsampling. While our experiments showed that 3D U-Net and V-Net reached marginally higher performance scores, the differences were not statistically significant (two-sided t test, $P > 0.3$). The amount of parameters for these tools makes them 51 and 23 times slower than VesSAP during the inference stage. For segmentation of one of our large whole-brain datasets, this translated to 4 h for VesSAP versus 8 d for 3D U-Net and 3.8 d for V-Net. This difference was also prevalent in the number of trainable parameters. The VesSAP CNN had 0.058 million parameters, whereas 3D U-Net consisted of more than 178 million and V-Net of more than 88 million parameters. Furthermore, the light VesSAP CNN already reached human-level performance. We therefore consider the problem of vessel segmentation as solved by the VesSAP CNN for our data. It should be mentioned that the segmentation network is a modular building block of the overall VesSAP pipeline and can be chosen by each user according to his or her own preferences and, importantly, according to the computational power available.

Preprocessing of segmentation. Preprocessing factors into the overall success of the training and segmentation. The intensity distribution among brains and among brain regions differs substantially. To account for intensity distributions, two preprocessing strategies were applied successively.

1. High-cut filter. In this step, the intensities x above a certain threshold c are set to c; c is defined by a global percentile. Next, they were normalized by $f(x)$.

$$g(x) = \begin{cases} c, & x > c \\ x, & x \leq c \end{cases} \tag{2}$$

2. Normalization of intensities. The original intensities were normalized to a range of 0 to 1, where x was the pixel intensity and X was all intensities for the volume.

$$f(x) = \frac{x - \min(X)}{\max(X) - \min(X)} \tag{3}$$

Inter-annotator experiment for segmentation. To compare VesSAP's segmentation to human-level annotations, we implemented an inter-annotator experiment. For this experiment, we determined a gold-standard label (ground truth) for two volumes of 500 × 500 × 50 pixels from a commissioned group of three experts, including the expert who imaged our data and was therefore most familiar with the images. Next, we gave the two volumes to four other experts to label the complete vasculature. The experts spent multiple hours labeling each patch in the ImageJ and ITK-snap environment and were allowed to use their favored approaches to generate what they considered to be the most accurate labeling. Finally, we calculated the accuracy and F1 scores for the different annotators, as compared to the gold standard, and compared them to the scores for our model (Table 1).

Feature extraction. To quantify the anatomy of the mouse brain vasculature, we extracted descriptive features on the basis of our segmentation. First, we calculated the features in voxel space. Later, we registered them to the Allen brain atlas.

As features we extracted the centerlines, the bifurcation points and the radii of the segmented blood vessels. We consider these features to be independent from the elongation of the light-sheet scans and the connectedness of the vessels due to staining, imaging and/or segmentation artifacts.

Our centerline extraction was based on a 3D thinning algorithm[47]. Before extracting the centerlines, we applied two cycles of binary erosion and dilation to remove false-negative pixels within the volume of segmented vessels, as these would induce false centerlines. On the basis of the centerlines, we extracted bifurcation points. A bifurcation was the branching point on a centerline where a larger vessel split into two or more smaller vessels (Fig. 4a). In a network analysis context, bifurcations are meaningful as they represent the nodes of a vascular network[48]. Furthermore, bifurcation points have relevance in a biological context. In neurodegenerative diseases, capillaries are known to degenerate[49], thereby substantially reducing the number of bifurcation points in an affected brain region as compared to healthy brain. Next, we implemented an algorithm to detect bifurcation points. We achieved this by calculating the surrounding pixels for every point on each centerline and determined whether a point was a centerline. The radius of a blood vessel is a key feature to describe vascular networks. The radius yields information about the flow and hierarchy of the vessel network. The proposed algorithm calculates the Euclidean distance transform for every segmented pixel v to the closest background pixel b_{closest}. Next, the distance transform matrix is multiplied by the 3D centerline mask, equaling the minimum radius of the vessel around the centerline.

$$d(v, b_{\text{closest}}) = \sqrt{\sum_{1}^{3} \left(v_i - b_{\text{closest},i}\right)^2} \tag{4}$$

Feature quantification. Here we describe in detail how we calculated the features between the three different spaces.

Voxel space to microscopic space. To quantify the length of our vessels in SI units instead of voxels, we calculated their Euclidean length, which depends on the direction of the connection of skeleton pixels (Supplementary Fig. 9). To calculate the Euclidean length of our centerlines, we carried out a connected component analysis, which transformed each pixel of the skeleton into an element of an undirected weighted graph, where zero weight means no connection and non-zero weights denote the Euclidean distance between two voxels (considering 26 connectivity). Thus, we obtained a large and sparse adjacency matrix. An element-wise summation of such a matrix provides the total Euclidean length of the vascular network along the extracted skeleton.

As measuring connected components is computationally very expensive, we calculated the Euclidean length of the centerlines for 12 representative volumes of 500 × 500 × 50 pixels and divided by the number of skeleton pixels. We calculated an average Euclidean length ε_{Cl} of 1.3234 ± 0.0063 voxels (mean ± s.d.) per centerline element. This corresponds to a length of 3.9701 ± 0.0188 μm (mean ± s.d.) in cleared tissue. Because the s.d. of this measurement was low, at less than 0.5% of the length, we applied this correction factor to the whole brain centerline measurements. This correction does not apply to the bifurcation points and our radius statistics, as bifurcations are independent of length and also radius extraction returns a Euclidean distance by default. Depending on the direction of the connection of skeleton pixels, the Euclidean length of a skeleton pixel is different (Supplementary Fig. 9).

Microscopic space to anatomical space. To account for tissue shrinkage (Supplementary Fig. 9), which is inherent to DISCO clearing, we carried out an experiment to measure the degree of shrinkage. Before clearing, we imaged the brains of three live BALB/c mice by MRI and calculated each brain's average volume, through precise manual segmentation by an expert. Next, we cleared three BALB/c brains, processed them with VesSAP and measured the total brain volume with atlas alignment. We report an average volume of 423.84 ± 2.04 mm^3 for the live mice and 255.62 ± 6.57 mm^3 for the cleared tissue. This corresponds to a total volume shrinkage of 39.69%. We applied this as a correction factor for the volumetric information (for example, for brain regions).

Similarly to previous studies, shrinkage was uniform in all three dimensions. This is important when considering shrinkage in one dimension, as needed to account for the shrinkage in centerlines and radii. The one-dimensional correction factor K_{L} then corresponds to the cube root of the volumetric correction factor K_{V}.

Accounting for these factors, we calculated the vessel length per volume (Z) in cleared (Z_{cleared}) and real (Z_{real}) tissue in equation (5), where $N_{\text{V,vox}}$ is the number of total voxels in the reference volume and $N_{\text{Cl,vox}}$ is the number of centerline voxels in the image volume:

$$Z_{\text{cleared}} = \frac{N_{\text{Cl,vox}}}{N_{\text{V,vox}}} \times \varepsilon_{\text{Cl}} \quad Z_{\text{real}} = \frac{N_{\text{Cl,vox}}}{N_{\text{V,vox}}} \times \varepsilon_{\text{Cl}} \times \frac{\kappa_{\text{L}}}{\kappa_{\text{V}}} \tag{5}$$

Similarly, we calculated the bifurcation density (B) in cleared and real tissue in equation (6), where $N_{\text{Bif,vox}}$ is the number of bifurcations in the reference volume:

$$B_{\text{cleared}} = \frac{N_{\text{Bif,vox}}}{N_{\text{V,vox}}} \quad B_{\text{real}} = \frac{N_{\text{Bif,vox}}}{N_{\text{V,vox}}} \times \frac{1}{\kappa_{\text{V}}} \tag{6}$$

Please note that the voxel spacing of 3 μm has to be taken into consideration when reporting features in SI units.

Inter-annotator experiment for features. To estimate the error in VesSAP's feature quantification, we extracted the features on a labeled test set of five volumes of 500 × 500 × 50 pixels. When comparing to the gold-standard label, we calculated errors (disagreements) of 8.21% for the centerlines, 13.18% for the number of bifurcation points and 16.33% for the average radius. To compare VesSAP's extracted features to human-level annotation, we implemented an inter-annotator experiment. For this experiment, we had four annotators label the vessels and radii in two volumes of 500 × 500 × 50 pixels by using ImageJ and ITK-snap. Finally, we calculated the agreement of the extracted features between all annotators and compared to the gold-standard labeling.

We calculated this for each of the volumes and found an average error (disagreement) of 34.62% for the radius, 25.20% for the bifurcation count and 12.55% for the centerline length.

The agreement between the VesSAP output and the gold standard was higher than the average agreement between the annotators and the gold standard. This difference underlines the quality and reproducibility of VesSAP's feature extraction.

Registration to the reference atlas. We used the average template, the annotation file and the latest ontology file (Ontology ID: 1) of the current Allen mouse brain atlas: CCFv3 201710. Then, we scaled the template and the annotation file up from 10 to 3 μm^3 to match our reconstructed brain scans and multiplied the left side of the (still symmetrical) annotation file by −1 so that the labels could be later assigned to the corresponding hemispheres. Next, the average template and 3D vascular datasets were downsampled to 10% of their original size in each dimension to achieve reasonably fast alignment with the elastix toolbox[50] (v4.9.0). For the sake of the integrity of the extracted features, we aligned the template to each of the brain scans individually by using a two-step rigid and deformable registration (B-spline; optimizer, AdaptiveStochasticGradientDescent; metric, AdvancedMattesMutualInformation; grid spacing in physical units, 90; in the VesSAP repository, we host the log and parameter files for each brain scan) and applied the transformation parameters to the full-resolution annotation volume

(3-µm resolution). Subsequently, we created masks for the anatomical clusters on the basis of the current Allen brain atlas ontology.

Statistical analysis of features. Data collection and analysis were not performed with blinding to the strains. Data distribution was assumed to be normal, although this was not formally tested. All data values of the descriptive statistics are given as mean ± s.e.m. unless stated otherwise. Data were analyzed with standardized effect size indices (Cohen's d)[51] to investigate differences in vessel length, number of bifurcation points and radii between brain areas across the three mouse strains ($n=3$ mice per strain). Descriptive statistics were evaluated across brain regions in the pooled ($n=9$) dataset.

Data visualization. All volumetric datasets were rendered with Imaris, Vision4D and ITK-snap.

Reporting Summary. Further information on research design is available in the Nature Research Reporting Summary linked to this article.

Data availability

VesSAP data are publicly hosted at http://DISCOtechnologies.org/VesSAP and include original scans and registered atlas data.

Code availability

VesSAP codes are publicly hosted at http://DISCOtechnologies.org/VesSAP and include the imaging protocol, trained algorithms, training data and a reference set of features describing the vascular network in all brain regions. Additionally, the source code is hosted on GitHub (https://github.com/vessap/vessap) and on the executable platform Code Ocean (https://doi.org/10.24433/CO.1402016.v1)[52]. Implementation of external libraries is available on request.

References

41. Breckwoldt, M. O. et al. Correlated magnetic resonance imaging and ultramicroscopy (MR-UM) is a tool kit to assess the dynamics of glioma angiogenesis. *eLife* **5**, e11712 (2016).
42. Kingma, D. P. & Ba, J. Adam: a method for stochastic optimization. Preprint at https://arxiv.org/abs/1412.6980 (2017).
43. Abadi, M. et al. in *12th USENIX Symposium on Operating Systems Design and Implementation* 265–283 (2016).
44. Hoo-Chang, S. et al. Deep convolutional neural networks for computer-aided detection: CNN architectures, dataset characteristics and transfer learning. *IEEE Trans. Med. Imaging* **35**, 1285–1298 (2016).
45. Schneider, M., Hirsch, S., Weber, B., Székely, G. & Menze, B. H. Joint 3-D vessel segmentation and centerline extraction using oblique Hough forests with steerable filters. *Med. Image Anal.* **19**, 220–249 (2015).
46. Paetzold, J. C. et al. clDice—a novel connectivity-preserving loss function for vessel segmentation. in *Medical Imaging Meets NeurIPS 2019 Workshop* (2019).
47. Lee, T. C., Kashyap, R. L. & Chu, C. N. Building skeleton models via 3-D medial surface axis thinning algorithms. *Graph. Models Image Process.* **56**, 462–478 (1994).
48. Rempfler, M. et al. Reconstructing cerebrovascular networks under local physiological constraints by integer programming. *Med. Image Anal.* **25**, 86–94 (2015).
49. Marchesi, V. T. Alzheimer's dementia begins as a disease of small blood vessels, damaged by oxidative-induced inflammation and dysregulated amyloid metabolism: implications for early detection and therapy. *FASEB J.* **25**, 5–13 (2011).
50. Klein, S., Staring, M., Murphy, K., Viergever, M. A. & Pluim, J. P. Elastix: a toolbox for intensity-based medical image registration. *IEEE Trans. Med. Imaging* **29**, 196–205 (2009).
51. Cohen, J. The effect size index: *d. Stat. Power Anal. Behav. Sci.* **2**, 284–288 (1988).
52. Paetzold, J. C. & Tetteh, G. VesSAP: machine learning analysis of whole mouse brain vasculature. *Code Ocean* https://doi.org/10.24433/CO.1402016.v1 (2020).

Acknowledgements

This work was supported by the Vascular Dementia Research Foundation, Deutsche Forschungsgemeinschaft (DFG, German Research Foundation) under Germany's Excellence Strategy within the framework of the Munich Cluster for Systems Neurology (EXC 2145 SyNergy, ID 390857198), ERA-Net Neuron (01EW1501A to A.E.), Fritz Thyssen Stiftung (to A.E.; reference no. 10.17.1.019MN), a DFG research grant (to A.E.; reference no. ER 810/2-1), the Helmholtz ICEMED Alliance (to A.E.), the NIH (to A.E.; reference no. AG057575) and the German Federal Ministry of Education and Research via the Software Campus initiative (to O.S.). S.S. is supported by the Translational Brain Imaging Training Network (TRABIT) under the European Union's Horizon 2020 research and innovation program (grant agreement ID 765148). Furthermore, NVIDIA supported this work via the GPU Grant Program. V.E. was funded by Human Brain Project (HBP SGA 2, 785907). M.I.T. is a member of the Graduate School of Systemic Neurosciences (GSN), Ludwig Maximilian University of Munich. We thank R. Cai, C. Pan, F. Voigt, I. Ezhov, A. Sekuboyina, M. Goergens, F. Hellal, R. Malik, U. Schillinger and T. Wang for technical advice and C. Heisen for critical reading of the manuscript.

Author contributions

M.I.T. performed the tissue processing, clearing and imaging experiments. M.I.T. and K.T.-V. developed the whole-brain staining protocol. M.I.T. stitched and assembled the whole-brain scans. V.E. and J.C.P. generated the synthetic vascular training dataset. J.C.P., G.T. and O.S. developed the deep learning architecture and trained the models. J.C.P. and S.S. performed the quantitative analyses. M.I.T. annotated the data. M. Düring and M. Dichgans helped with data interpretation. B.M., M.P. and G.T. provided guidance in developing the deep learning architecture and helped with data interpretation. A.E., M.I.T., B.M. and J.C.P. wrote the manuscript. All authors edited the manuscript. A.E. initiated and led all aspects of the project.

Competing interests

The authors declare no competing interests.

Additional information

Supplementary information is available for this paper at https://doi.org/10.1038/s41592-020-0792-1.

Correspondence and requests for materials should be addressed to B.M. or A.E.

Peer review information Nina Vogt was the primary editor on this article and managed its editorial process and peer review in collaboration with the rest of the editorial team.

Reprints and permissions information is available at www.nature.com/reprints.

nature research

Corresponding author(s): Ali Ertürk, Bjoern Menze

Last updated by author(s): Feb 14, 2020

Reporting Summary

Nature Research wishes to improve the reproducibility of the work that we publish. This form provides structure for consistency and transparency in reporting. For further information on Nature Research policies, see Authors & Referees and the Editorial Policy Checklist.

Statistics

For all statistical analyses, confirm that the following items are present in the figure legend, table legend, main text, or Methods section.

n/a	Confirmed	
☐	☒	The exact sample size (*n*) for each experimental group/condition, given as a discrete number and unit of measurement
☐	☒	A statement on whether measurements were taken from distinct samples or whether the same sample was measured repeatedly
☐	☒	The statistical test(s) used AND whether they are one- or two-sided *Only common tests should be described solely by name; describe more complex techniques in the Methods section.*
☒	☐	A description of all covariates tested
☐	☒	A description of any assumptions or corrections, such as tests of normality and adjustment for multiple comparisons
☐	☒	A full description of the statistical parameters including central tendency (e.g. means) or other basic estimates (e.g. regression coefficient) AND variation (e.g. standard deviation) or associated estimates of uncertainty (e.g. confidence intervals)
☒	☐	For null hypothesis testing, the test statistic (e.g. *F*, *t*, *r*) with confidence intervals, effect sizes, degrees of freedom and *P* value noted *Give P values as exact values whenever suitable.*
☒	☐	For Bayesian analysis, information on the choice of priors and Markov chain Monte Carlo settings
☒	☐	For hierarchical and complex designs, identification of the appropriate level for tests and full reporting of outcomes
☐	☒	Estimates of effect sizes (e.g. Cohen's *d*, Pearson's *r*), indicating how they were calculated

Our web collection on statistics for biologists contains articles on many of the points above.

Software and code

Policy information about availability of computer code

Data collection	ImspectorPro [v 5.1] was used for collecting light-sheet images, Zen black [v 10.0] for confocal images and Nucline [v 3.0] for MRI data.
Data analysis	Python [v 2.7 & 3.6], MATLAB [v 9.3], elastix [v 4.9], ITK-SNAP [v 3.6], ImageJ [v 1.52p], Imaris [v 9.3] and Vision4D [v 3.1] were used. Custom codes was used in the study were used for vascular segmentation, mapping and quantification. The description of the software is available in the Method section of the manuscript. The custom codes are publicly available on http://DISCOtechnologies.org/VesSAP

For manuscripts utilizing custom algorithms or software that are central to the research but not yet described in published literature, software must be made available to editors/reviewers. We strongly encourage code deposition in a community repository (e.g. GitHub). See the Nature Research guidelines for submitting code & software for further information.

Data

Policy information about availability of data

All manuscripts must include a data availability statement. This statement should provide the following information, where applicable:

- Accession codes, unique identifiers, or web links for publicly available datasets
- A list of figures that have associated raw data
- A description of any restrictions on data availability

The data that support the findings of this study are publicly available on http://DISCOtechnologies.org/VesSAP

Field-specific reporting

Please select the one below that is the best fit for your research. If you are not sure, read the appropriate sections before making your selection.

☒ Life sciences ☐ Behavioural & social sciences ☐ Ecological, evolutionary & environmental sciences

For a reference copy of the document with all sections, see nature.com/documents/nr-reporting-summary-flat.pdf

Life sciences study design

All studies must disclose on these points even when the disclosure is negative.

Sample size	Sample sizes for this reproducibility study were determined based on the literatures in the fields. Statistics were not used to predetermine sample sizes.
Data exclusions	No animals were excluded from the study. Specific brain regions in Figure 5a-d were excluded based on visual inspection (zero vascular length), because some regions were damaged and distorted during dissection so that vessels in these regions were not annotated.
Replication	The protocols in the study were replicated successfully more than 5 times in independent experiments. Tissue-clearing, imaging, vascular segmentation, mapping and quantification procedures were performed in nine mouse brains.
Randomization	Within each strain, animals were randomly selected.
Blinding	No blinding was done because knowledge of experimental conditions were required during data collection.

Reporting for specific materials, systems and methods

We require information from authors about some types of materials, experimental systems and methods used in many studies. Here, indicate whether each material, system or method listed is relevant to your study. If you are not sure if a list item applies to your research, read the appropriate section before selecting a response.

Materials & experimental systems

n/a	Involved in the study	
☒	☐	Antibodies
☒	☐	Eukaryotic cell lines
☒	☐	Palaeontology
☐	☒	Animals and other organisms
☒	☐	Human research participants
☒	☐	Clinical data

Methods

n/a	Involved in the study	
☒	☐	ChIP-seq
☒	☐	Flow cytometry
☐	☒	MRI-based neuroimaging

Animals and other organisms

Policy information about studies involving animals; ARRIVE guidelines recommended for reporting animal research

Laboratory animals	This study used male mice from the C57BL/6J, CD1 and BALB/c strains at the age of 3 months.
Wild animals	The study did not involve wild animals.
Field-collected samples	This study did not involve a field-collected samples.
Ethics oversight	The experiments were done after approval of the ethical review board of the government of Upper Bavaria (Regierung von Oberbayern, Munich, Germany), and in accordance with the European directive 2010/63/EU for animal research.

Note that full information on the approval of the study protocol must also be provided in the manuscript.

Magnetic resonance imaging

Experimental design

Design type	No functional MRI (fMRI) data were acquired.
Design specifications	None.
Behavioral performance measures	None.

Acquisition

Imaging type(s)	Structural MRI.
Field strength	3T
Sequence & imaging parameters	An average of six T1 scans (3D Gradient Echo sequence with TE/TR/flip angle=5.12/14.88/10, a slice thickness = 0.2 mm and 0.1667x0.1667 mm in plane resolution) was created to get a high resolution structural image of the brain.
Area of acquisition	Whole-brain in-vivo.

Diffusion MRI ☐ Used ☒ Not used

Preprocessing

Preprocessing software	None.
Normalization	No normalization was done to ensure the precise anatomical size measurements of the tissue.
Normalization template	None.
Noise and artifact removal	None.
Volume censoring	No volume censoring was performed.

Statistical modeling & inference

Model type and settings	None.
Effect(s) tested	None.

Specify type of analysis: ☒ Whole brain ☐ ROI-based ☐ Both

Statistic type for inference (See Eklund et al. 2016)	None.
Correction	None.

Models & analysis

n/a	Involved in the study
☒	☐ Functional and/or effective connectivity
☒	☐ Graph analysis
☒	☐ Multivariate modeling or predictive analysis

clDice - a Novel Topology-Preserving Loss Function for Tubular Structure Segmentation

Suprosanna Shit, **Johannes Christian Paetzold**, Anjany Sekuboyina, Ivan Ezhov, Alexander Unger, Andrey Zhylka, Josien P. W. Pluim, Ulrich Bauer & Bjoern Menze

Conference: 2021 IEEE/CVF Conference on Computer Vision and Pattern Recognition (CVPR), June 2021

Synopsis: Accurate segmentation of tubular, network-like structures, such as vessels, neurons, or roads, is relevant to many fields of research. For such structures, the topology is their most important characteristic; particularly preserving connectedness: in the case of vascular networks, missing a connected vessel entirely alters the blood-flow dynamics. We introduce a novel similarity measure termed centerlineDice (short *clDice*), which is calculated on the intersection of the segmentation masks and their (morphological) skeleta. We theoretically prove that *clDice* guarantees topology preservation up to homotopy equivalence for binary 2D and 3D segmentation. Extending this, we propose a computationally efficient, differentiable loss function (*soft-clDice*) for training arbitrary neural segmentation networks. We benchmark the *soft-clDice* loss on five public datasets, including vessels, roads and neurons (2D and 3D). Training on *soft-clDice* leads to segmentation with more accurate connectivity information, higher graph similarity, and better volumetric scores.

Contributions of thesis author: idea of the clDice formulation, theoretical formalization, 2D computational experiments, leading role in composition and writing of manuscript, project lead.

clDice - a Novel Topology-Preserving Loss Function for Tubular Structure Segmentation

Suprosanna Shit *[1] Johannes C. Paetzold *[1] Anjany Sekuboyina[1] Ivan Ezhov[1]
Alexander Unger[1] Andrey Zhylka[2] Josien P. W. Pluim[2] Ulrich Bauer[1] Bjoern H. Menze[1]
[1]Technical University of Munich [2] Eindhoven University of Technology

Abstract

Accurate segmentation of tubular, network-like structures, such as vessels, neurons, or roads, is relevant to many fields of research. For such structures, the topology is their most important characteristic; particularly preserving connectedness: in the case of vascular networks, missing a connected vessel entirely alters the blood-flow dynamics. We introduce a novel similarity measure termed centerlineDice (short clDice), which is calculated on the intersection of the segmentation masks and their (morphological) skeleta. We theoretically prove that clDice guarantees topology preservation up to homotopy equivalence for binary 2D and 3D segmentation. Extending this, we propose a computationally efficient, differentiable loss function (soft-clDice) for training arbitrary neural segmentation networks. We benchmark the soft-clDice loss on five public datasets, including vessels, roads and neurons (2D and 3D). Training on soft-clDice leads to segmentation with more accurate connectivity information, higher graph similarity, and better volumetric scores.

1. Introduction

Segmentation of *tubular* and *curvilinear* structures is an essential problem in numerous domains, such as clinical and biological applications (blood vessel and neuron segmentation from microscopic, optoacoustic, or radiology images), remote sensing applications (road network segmentation from satellite images) and industrial quality control, etc. In the aforementioned domains, a topologically accurate segmentation is necessary to guarantee error-free downstream tasks, such as computational hemodynamics, route planning, Alzheimer's disease prediction [18], or stroke modeling [20]. When optimizing computational algorithms for segmenting curvilinear structures, the two most commonly used categories of quantitative performance measures for evaluating segmentation accuracy of *tubular* structures, are 1) overlap based measures such as Dice, precision, recall, and Jaccard index; and 2) volumetric distance measures such as the Hausdorff and Mahalanobis distance [21, 40, 36, 16].

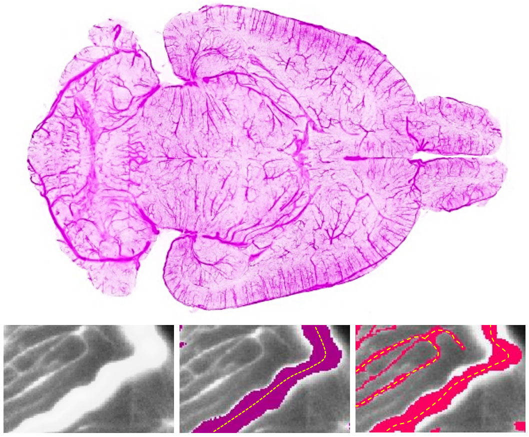

Figure 1. **Motivation:** The figure shows a 3D rendering of a complex, whole brain vascular dataset [48], where an exemplary 2D slice of the data is chosen and segmented by two different models, see purple (middle) and red (right), respectively. The two segmentation results achieve identical quality in terms of the traditional Dice score. Note that the purple segmentation does not capture the small vessels while segmenting the large vessel very accurately; on the other side, the red segmentation captures all vessels in the image while being less accurate on the radius of the large vessel. Skeleta are drawn in yellow. From a topology or network perspective, the red segmentation is evidently preferred.

However, in most segmentation problems, where the object of interest is 1) locally a *tubular* structure and 2) globally forms a *network*, the most important characteristic is the connectivity of the global network topology. Note that *network* in this context implies a physically connected structure, such as a vessel network, a road network, etc., which is also the primary structure of interest for the given

---

*The authors contributed equally to the work image data. As an example, one can refer to brain vasculature analysis, where a missed vessel segment in the segmentation mask can pathologically be interpreted as a stroke or may lead to dramatic changes in a global simulation of blood flow. On the other hand, limited over- or under-segmentation of vessel radius can be tolerated, because it does not affect clinical diagnosis.

For evaluating segmentations in such tubular-network structures, traditional volume-based performance indices are sub-optimal. For example, Dice and Jaccard rely on the average voxel-wise hit or miss prediction [46]. In a task like network-topology extraction, a spatially contiguous sequence of correct voxel prediction is more meaningful than a spurious correct prediction. This ambiguity is relevant for objects of interest, which are of the same thickness as the resolution of the signal. For them, it is evident that a single-voxel shift in the prediction can change the topology of the whole network. Further, a globally averaged metric does not equally weight tubular-structures with large, medium, and small radii (cf. Fig 1). In real vessel datasets, where vessels of wide radius ranges exist, e.g. 30 μm for arterioles and 5 μm for capillaries [48, 9], training on a globally averaged loss induces a strong bias towards the volumetric segmentation of large vessels. Both scenarios are pronounced in imaging modalities, such as fluorescence microscopy [48, 58] and optoacoustics, which focus on mapping small capillary structures.

To this end, we are interested in a topology-aware image segmentation, eventually enabling a correct network extraction. Therefore, we ask the following research questions:

Q1. What is a good pixelwise measure to benchmark segmentation algorithms for **tubular**, and related linear and curvilinear structure segmentation while guaranteeing the preservation of the **network-topology**?

Q2. Can we use this *improved measure* as a loss function for neural networks, which is a void in existing literature?

1.1. Related Literature

Achieving topology preservation can be crucial to obtain meaningful segmentation, particularly for elongated and connected shapes, e.g. vascular structures or roads. However, analyzing preservation of topology while simplifying geometries is a difficult analytical and computational problem [11, 10].

For binary geometries, various algorithms based on thinning and medial surfaces have been proven to be topology-preserving according to varying definitions of topology [23, 25, 26, 35]. For non-binary geometries, existing methods applied topology and connectivity constraints onto variational and Markov random field-based methods: tree shape priors for vessel segmentation [44], graph representation priors to natural images [2], higher-order cliques which connect superpixels [53] and adversarial learning for road segmentation [51], integer programming to general curvilinear structures [49], and proposed a tree-structured convolutional gated recurrent unit [22], morphological optimization [14], among others [3, 15, 32, 31, 33, 37, 41, 52, 57, 56]. Further, topological priors of containment were applied to histology scans [5], a 3D CNN with graph refinement was used to improve airway connectivity [19], and recently, Mosinska et al. trained networks which perform segmentation and path classification simultaneously [30]. Another approach enables the predefinition of Betti numbers and enforces them on the training[8].

The aforementioned literature has advanced the communities understanding of topology-preservation, but critically, they do not possess end-to-end loss functions that optimize topology-preservation. In this context, the literature remains sparse. Recently, Mosinska et al. suggested that pixel-wise loss-functions are unsuitable and used selected filter responses from a VGG19 network as an additional penalty [29]. Nonetheless, their approach does not prove topology preservation. Importantly, Hu et al. proposed the first continuous-valued loss function based on the Betti number and persistent homology [17]. However, this method is based on matching critical points, which, according to the authors makes the training very expensive and error-prone for real image-sized patches [17]. While this is already limiting for a translation to large real world data set, we find that none of these approaches have been extended to three dimensional (3D) data.

1.2. Our Contributions

The objective of this paper is to identify an efficient, general, and intuitive loss function that enables topology preservation while segmenting tubular objects. We introduce a novel connectivity-aware similarity measure named *clDice* for benchmarking tubular-segmentation algorithms. Importantly, we provide theoretical guarantees for the topological correctness of the *clDice* for binary 2D and 3D segmentation. As a consequence of its formulation based on morphological skeletons, our measure pronounces the network's topology instead of equally weighting every voxel. Using a differentiable soft-skeletonization, we show that the *clDice* measure can be used to train neural networks. We show experimental results for various 2D and 3D network segmentation tasks to demonstrate the practical applicability of our proposed similarity measure and loss function.

2. Let's Emphasize *Connectivity*

We propose a novel connectivity-preserving metric to evaluate tubular and linear structure segmentation based on intersecting skeletons with masks. We call this metric *centerlineDice* or ***clDice***.

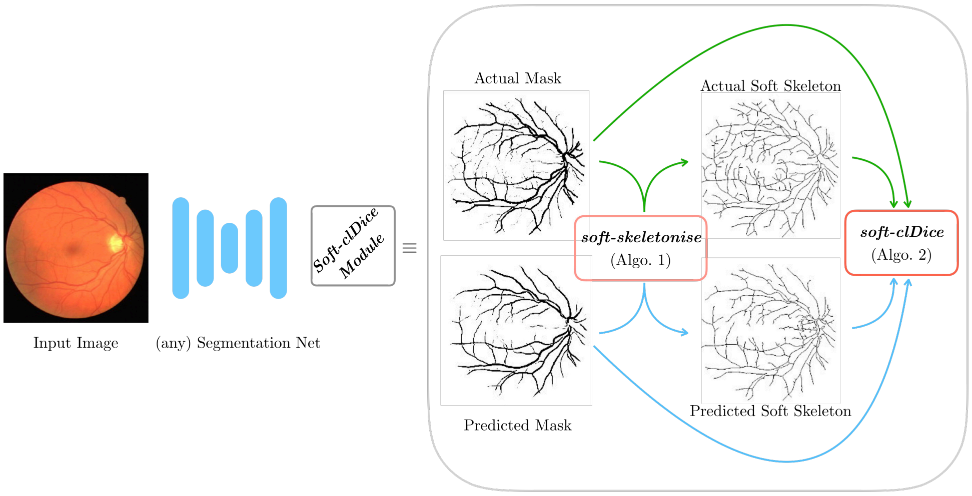

Figure 2. **Schematic overview of our proposed method:** Our proposed *clDice* loss can be applied to any arbitrary segmentation network. The soft-skeletonization can be easily implemented using pooling functions from any standard deep-learning toolbox.

We consider two binary masks: the ground truth mask (V_L) and the predicted segmentation masks (V_P). First, the skeletons S_P and S_L are extracted from V_P and V_L respectively. Subsequently, we compute the fraction of S_P that lies within V_L, which we call *Topology Precision* or $\mathrm{Tprec}(S_P, V_L)$, and vice-a-versa we obtain *Topology Sensitivity* or $\mathrm{Tsens}(S_L, V_P)$ as defined bellow;

$$\mathrm{Tprec}(S_P, V_L) = \frac{|S_P \cap V_L|}{|S_P|}; \quad \mathrm{Tsens}(S_L, V_P) = \frac{|S_L \cap V_P|}{|S_L|} \tag{1}$$

We observe that the measure $\mathrm{Tprec}(S_P, V_L)$ is susceptible to false positives in the prediction while the measure $\mathrm{Tsens}(S_L, V_P)$ is susceptible to false negatives. This explains our rationale behind referring to the $\mathrm{Tprec}(S_P, V_L)$ as topology's precision and to the $\mathrm{Tsens}(S_L, V_P)$ as its sensitivity. Since we want to maximize both precision and sensitivity (recall), we define *clDice* to be the harmonic mean (also known as F1 or Dice) of both the measures:

$$\mathrm{clDice}(V_P, V_L) = 2 \times \frac{\mathrm{Tprec}(S_P, V_L) \times \mathrm{Tsens}(S_L, V_P)}{\mathrm{Tprec}(S_P, V_L) + \mathrm{Tsens}(S_L, V_P)} \tag{2}$$

Note that our *clDice* formulation is not defined for $\mathrm{Tprec} = 0$ and $\mathrm{Tsens} = 0$, but can easily be extended continuously with the value 0.

3. Topological Guarantees for clDice

The following section provides general theoretical guarantees for the preservation of topological properties achieved by optimizing *clDice* under mild conditions on the input. Roughly, these conditions state that the object of interest is embedded in S^3 in a non-knotted way, as is typically the case for blood vessel and road structures.

Specifically, we assume that both ground truth and prediction *admit foreground and background skeleta*, which means that both foreground and background are homotopy-equivalent to topological graphs, which we assume to be embedded as *skeleta*. Here, the voxel grid is considered as a cubical complex, consisting of elementary cubes of dimensions 0, 1, 2, and 3. This is a special case of a *cell complex* (specifically, a *CW complex*), which is a space constructed inductively, starting with isolated points (0-cells), and gluing a collection of topological balls of dimension k (called k*-cells*) along their boundary spheres to a $k-1$-dimensional complex. The voxel grid, seen as a cell complex in this sense, can be completed to an ambient complex that is homeomorphic to the 3-sphere S^3 by attaching a single exterior cell to the boundary. In order to consider foreground and background of a binary image as complementary subspaces, the foreground is now assumed to be the union of closed unit cubes in the voxel grid, corresponding to voxels with value 1; and the background is the complement in the ambient complex. This convention is commonly used in digital topology [24, 23]. The assumption on the background can then be replaced by a convenient equivalent condition, stating that the foreground is also homotopy equivalent to a subcomplex obtained from the ambient complex by only removing 3-cells and 2-cells. Such a subcomplex is then clearly homotopy-equivalent to the complement of a 1-complex.

We will now observe that the above assumptions imply that the foreground and the background are connected and have a free fundamental group and vanishing higher fundamental groups. In particular, the homotopy type is already determined by the first Betti number [1]; moreover, a map inducing an isomorphism in homology is already a homotopy equivalence. To see this, first note that both foreground and background are assumed to have the homology of a graph, in particular, homology is trivial in degree 2. By Alexander duality [1], then, both foreground and background have trivial reduced cohomology in degree 0, meaning that they are connected. This implies that both have a free fundamental group (as any connected graph) and vanishing higher homotopy groups. In particular, since homology in degree 1 is the Abelianization of the fundamental group, these two groups are isomorphic. This in turn implies that in our setting a map that induces isomorphisms in homology already induces isomorphisms between all homotopy groups. By Whitehead's theorem [54], such a map is then a homotopy equivalence.

The following theorem shows that under our assumptions on the images admitting foreground and background skeleta, the existence of certain nested inclusions already implies the homotopy-equivalence of foreground and background, which we refer to as *topology preservation*.

Theorem 1. *Let $L_A \subseteq A \subseteq K_A$ and $L_B \subseteq B \subseteq K_B$ be connected subcomplexes of some cell complex. Assume that the above inclusions are homotopy equivalences. If the subcomplexes also are related by inclusions $L_A \subseteq B \subseteq K_A$ and $L_B \subseteq A \subseteq K_B$, then these inclusions must be homotopy equivalences as well. In particular, A and B are homotopy-equivalent.*

Proof. An inclusion of cell complexes map is a homotopy equivalence if and only if it induces isomorphisms on all homotopy groups. Since the inclusion $L_A \subseteq B \subseteq K_A$ induces an isomorphism, the inclusion $L_A \subseteq B$ induces a left-inverse, and since $B \subseteq K_B$ induces an isomorphism, the inclusion $L_A \subseteq K_B$ also induces a left-inverse. At the same time, since the inclusion $L_B \subseteq A \subseteq K_B$ induces an isomorphism, the inclusion $A \subseteq K_B$ induces a left-inverse, and since $L_A \subseteq A$ induces an isomorphism, the inclusion $L_A \subseteq K_B$ also induces a right-inverse. Together, this implies that the inclusion $L_A \subseteq K_B$ induces an isomorphism.

Together with the isomorphisms induced by $L_A \subseteq A$ and $B \subseteq K_B$, we obtain isomorphisms induced by $L_A \subseteq B$ and by $A \subseteq K_B$, which compose to an isomorphism between the homotopy groups of A and B. □

Corollary 1.1. *Let V_L and V_P be two binary masks admitting foreground and background skeleta, such that the foreground skeleton of V_L is included in the foreground of V_P and vice versa, and similarly for the background. Then the foregrounds of V_L and V_P are homotopy equivalent, and the same is true for their backgrounds.*

Note that the inclusion condition in this corollary is satisfied if and only if *clDice* evaluates to 1 on both foreground and background of (V_L, V_P).

This proof lays the ground for a general interpretation of *clDice* as a topology preserving metric. Additionally, we provide an elaborate explanation of *clDice* topological properties, using concepts of applied digital topology in the theory section of the Supplementary material [24, 23].

4. Training Neural Networks with *clDice*

In the previous section we provided general theoretic guarantees how *clDice* has topology preserving properties. The following chapter shows how we applied our theory to efficiently train topology preserving networks using the *clDice* formulation. [2]

4.1. *Soft-clDice* using *Soft-skeletonization*:

Extracting accurate skeletons is essential to our method. For this task, a multitude of approaches has been proposed. However, most of them are not fully differentiable and therefore unsuited to be used in a loss function. Popular approaches use the Euclidean distance transform or utilize repeated morphological thinning. Euclidean distance transform has been used on multiple occasions [42, 55], but remains a discrete operation and, to the best of our knowledge, an end-to-end differentiable approximation remains to be developed, preventing the use in a loss function for training neural networks. On the contrary, morphological thinning is a sequence of dilation and erosion operations [c.f. Fig. 3].

Importantly, thinning using morphological operations (skeletonization) on curvilinear structures can be topology-preserving [35]. Min- and max filters are commonly used as the grey-scale alternative of morphological dilation and erosion. Motivated by this, we propose 'soft-skeletonization', where an iterative min- and max-pooling is applied as a proxy for morphological erosion and dilation. The Algorithm 1 describes the iterative processes involved in its computation. The hyper-parameter k involved in its computation represents the iterations and has to be greater than or equal to the maximum observed radius. In our experiments, this parameter depends on the dataset. For example, it is $k = 5...25$ in our experiments, matching the pixel radius of the largest observed tubular structures. Choosing a larger k does not reduce performance but increases computation

---

[1] Betti numbers: β_0 represents the number of distinct *connected-components*, β_1 represents the number of *circular holes*, and β_2 represents the number of *cavities*, for depictions see Supplementary material

[2] `https://github.com/jocpae/clDice`

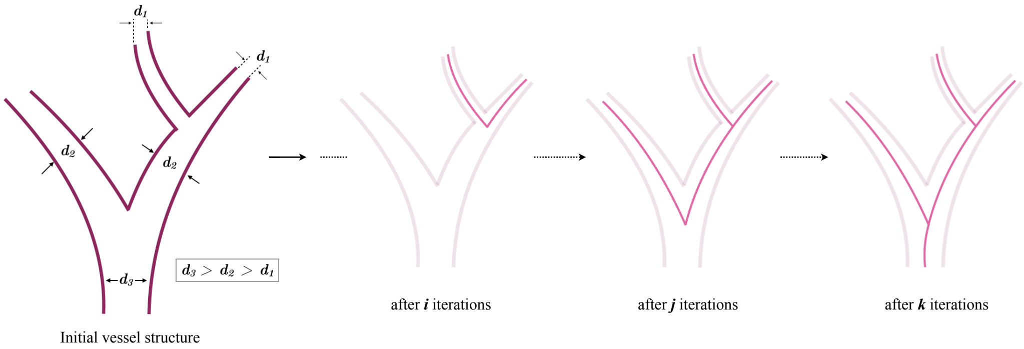

Figure 3. Based on the initial vessel structure (purple), sequential bagging of skeleton voxels (red) via iterative skeletonization leads to a complete skeletonization, where d denotes the diameter and $k > j > i$ iterations.

```
Algorithm 1: soft-skeleton
  Input: $I, k$
    $I' \leftarrow maxpool(minpool(I))$
    $S \leftarrow ReLU(I - I')$
  for $i \leftarrow 0$ to $k$ do
    $I \leftarrow minpool(I)$
    $I' \leftarrow maxpool(minpool(I))$
    $S \leftarrow S + (1 - S) \circ ReLU(I - I')$
  end
  Output: $S$
```

```
Algorithm 2: soft-clDice
  Input: $V_P, V_L$
    $S_P \leftarrow soft\text{-}skeleton(V_P)$
    $S_L \leftarrow soft\text{-}skeleton(V_L)$
    $Tprec(S_P, V_L) \leftarrow \frac{|S_P \circ V_L| + \epsilon}{|S_P| + \epsilon}$
    $Tsens(S_L, V_P) \leftarrow \frac{|S_L \circ V_P| + \epsilon}{|S_L| + \epsilon}$
    $clDice \leftarrow$
        $2 \times \frac{Tprec(S_P, V_L) \times Tsens(S_L, V_P)}{Tprec(S_P, V_L) + Tsens(S_L, V_P)}$
  Output: $clDice$
```

Figure 4. **Algorithm 1** calculates the proposed *soft-skeleton*, here I is the mask to be *soft-skeletonized* and k is the number of iterations for skeletonization. **Algorithm 2**, calculates the *soft-clDice* loss, where V_P is a real-valued probabilistic prediction from a segmentation network and V_L is the true mask. We denote Hadamard product using $\circ$.

time. On the other hand, a too low k leads to incomplete skeletonization.

In Figure 3, the successive steps of our skeletonization are intuitively represented. In the early iterations, the structures with a small radius are skeletonized and preserved until the later iterations when the thicker structures become skeletonized. This enables the extraction of a parameter-free, morphologically motivated soft-skeleton. The aforementioned soft-skeletonization enables us to use *clDice* as a fully differentiable, real-valued, optimizable measure. The Algorithm 2 describes its implementation. We refer to this as the *soft-clDice*.

For a single connected foreground component and in the absence of knots, the homotopy type is specified by the number of linked loops. Hence, if the reference and the predicted volumes are not homotopy equivalent, they do not have pairwise linked loops. To include these missing loops or exclude the extra loops, one has to add or discard deformation retracted skeleta of the solid foreground. This implies adding *new correctly predicted voxels*. In contrast to other volumetric losses such as Dice, cross-entropy, etc., *clDice* only considers the deformation-retracted graphs of the solid foreground structure. Thus, we claim that *clDice* requires the least amount of *new correctly predicted voxels* to guarantee the homotopy equivalence. Along these lines, Dice or cross-entropy can only guarantee homotopy equivalence if every single voxel is segmented correctly. On the other hand, *clDice* can guarantee homotopy equivalence for a broader combinations of connected-voxels. Intuitively, this is a very much desirable property as it makes *clDice* robust towards outliers and noisy segmentation labels.

4.2. Cost Function

Since our objective here is to preserve topology while achieving accurate segmentations, and not to learn skeleta, we combine our proposed *soft-clDice* with *soft-Dice* in the following manner:

$$\mathcal{L}_c = (1 - \alpha)(1 - soft\boldsymbol{Dice}) + \alpha(1 - soft\boldsymbol{clDice}) \quad (3)$$

where $\alpha \in [0, 0.5]$. In stark contrast to previous works, where segmentation and centerline prediction has been learned jointly as multi-task learning [50, 47], we are not interested in learning the centerline. We are interested in learning a topology-preserving segmentation. Therefore, we restrict our experimental choice of alpha to $\alpha \in [0, 0.5]$. We test *clDice* on two state-of-the-art network architectures: i) a 2D and 3D U-Net[38, 6], and ii) a 2D and 3D fully connected networks (FCN) [47, 13]. As baselines, we use the same architectures trained using *soft-Dice* [27, 45].

4.3. Adaption for Highly Imbalanced Data

Our theory (Section 3), describes a two-class problem where *clDice* should be computed on both the foreground and the background channels. In our experiments, we show that for complex and highly imbalanced dataset it is sufficient to calculate the **clDice** loss on the underrepresented foreground class. We attribute this to the distinct properties of tubularness, sparsity of foreground and the lack of cavities (Betti number 2) in our data. An intuitive interpretation how these assumptions are valid in terms of digital topology can be found in the supplementary material.

5. Experiments

5.1. Datasets

We employ five public datasets for validating *clDice* and *soft-clDice* as a measure and an objective function, respectively. In 2D, we evaluate on the DRIVE retina dataset [43], the Massachusetts Roads dataset [28] and the CREMI neuron dataset [12]. In 3D, a synthetic vessel dataset with an added Gaussian noise term [39] and the Vessap dataset of multi-channel volumetric scans of brain vessels is used [48, 34]. For the Vessap dataset we train different models for one and two input channels. For all of the datasets, we perform three fold cross-validation and test on held-out, large, and highly-variant test sets. Details concerning the experimental setup can be found in the supplementary material.

5.2. Evaluation Metrics

We compare the performance of various experimental setups using three types of metrics: volumetric, topology-based, and graph-based.

1. Volumetric: We compute volumetric scores such as Dice coefficient, Accuracy, and the proposed *clDice*.
2. Topology-based: We calculate the mean of absolute Betti Errors for the Betti Numbers β_0 and β_1 and the mean absolute error of Euler characteristic, $\chi = V - E + F$, where $V, E,$ and F denotes number of vertices, edges, and faces.
3. Graph-based: we extract random patch-wise graphs for the 2D/3D images. We uniformly sample fixed number of points from the graph and compute the StreetmoverDistance (SMD) [4]. SMD captures a Wasserstein distance between two graphs. Additionally we compute the F1 score of junction-based metric [7].

5.3. Results and Discussion

We trained two segmentation architectures, a U-Net and an FCN, for the various loss functions in our experimental setup. As a baseline, we trained the networks using *soft-dice* and compared it with the ones trained using the proposed loss (Eq. 3), by varying α from (0.1 to 0.5).

Quantitative: We observe that including *soft-clDice* in any proportion ($\alpha > 0$) leads to improved topological, volumetric and graph similarity for all 2D and 3D datasets, see Table 1. We conclude that α can be interpreted as a hyper parameter which can be tuned *per-dataset*. Intuitively, increasing the α improves the *clDice* measure for most experiments. Most often, *clDice* is high or highest when the graph and topology based measures are high or highest, particularly the β_1 Error, Streetmover distance and Opt-J F1 score; quantitatively indicating that topological properties are indeed represented in the *clDice* measure.

In spite of not optimizing for a high *soft-clDice* on the background class, all of our networks converge to superior segmentation results. This not only reinforces our assumptions on dataset-specific necessary conditions but also validates the practical applicability of our loss. Our findings hold for the different network architectures, for 2D or 3D, and for tubular or curvilinear structures, strongly indicating its generalizability to analogous binary segmentation tasks.

Observe that CREMI and the synthetic vessel dataset (see Supplementary material) appear to have the smallest increase in scores over the baseline. We attribute this to them being the least complex datasets in the collection, with CREMI having an almost uniform thickness of radii and the synthetic data having a high signal-to-noise ratio and insignificant illumination variation. More importantly, we observe larger improvements for all measures in case of the more complex Vessap and Roads data see Figure 5. In direct comparison to performance measures reported in two recent publications by Hu et al. and Mosinska et al. [17, 29], we find that our approach is on par or better in terms of Accuracy and Betti Error for the Roads and CREMI dataset. It is important to note that we used a smaller subset of training data for the Road dataset compared to both while using the same test set.

Hu et al. reported a Betti error for the DRIVE data, which exceeds ours; however, it is important to consider that their approach explicitly minimizes the mismatch of the persistence diagram, which has significantly higher computational complexity during training, see the section below. We find that our proposed loss performs superior to the baseline in almost every scenario. The improvement appears to be pronounced when evaluating the highly relevant graph and topology based measures, including the recently

Table 1. Quantitative experimental results for the Massachusetts road dataset (Roads), the CREMI dataset, the DRIVE retina dataset and the Vessap dataset (3D). Bold numbers indicate the best performance. The performance according to the *clDice* measure is highlighted in rose. For all experiments we observe that using *soft-clDice* in $\mathcal{L}_c$ results in improved scores compared to *soft-Dice*. This improvement holds for almost $\alpha > 0$; α can be interpreted as a dataset specific hyper-parameter.

Dataset	Network	Loss	Dice	Accuracy	*clDice*	β_0 Error	β_1 Error	SMD [4]	χ_{error}	Opt-J F1 [7]
Roads	FCN	*soft-dice*	64.84	95.16	70.79	1.474	1.408	0.1216	2.634	0.766
		$\mathcal{L}_c, \alpha = 0.1$	66.52	95.70	74.80	0.987	1.227	0.1002	2.625	0.768
		$\mathcal{L}_c, \alpha = 0.2$	**67.42**	**95.80**	76.25	**0.920**	1.280	**0.0954**	2.526	0.770
		$\mathcal{L}_c, \alpha = 0.3$	65.90	95.35	74.86	0.974	1.197	0.1003	2.448	0.775
		$\mathcal{L}_c, \alpha = 0.4$	67.18	95.46	**76.92**	0.934	**1.092**	0.0991	**2.183**	**0.803**
		$\mathcal{L}_c, \alpha = 0.5$	65.77	95.09	75.22	0.947	1.184	0.0991	2.361	0.782
	U-NET	*soft-dice*	76.23	96.75	86.83	0.491	1.256	0.0589	1.120	0.881
		$\mathcal{L}_c, \alpha = 0.1$	**76.66**	**96.77**	87.35	0.359	**0.938**	0.0457	0.980	0.878
		$\mathcal{L}_c, \alpha = 0.2$	76.25	96.76	87.29	**0.312**	1.031	**0.0415**	0.865	0.900
		$\mathcal{L}_c, \alpha = 0.3$	74.85	96.57	86.10	0.322	1.062	0.0504	0.827	0.913
		$\mathcal{L}_c, \alpha = 0.4$	75.38	96.60	86.16	0.344	1.016	0.0483	**0.755**	**0.916**
		$\mathcal{L}_c, \alpha = 0.5$	76.45	96.64	**88.17**	0.375	0.953	0.0527	1.080	0.894
	Mosinska et al.	[29, 17]	-	97.54	-	-	2.781	-	-	-
	Hu et al.	[17]	-	97.28	-	-	1.275	-	-	-
CREMI	U-NET	*soft-dice*	91.54	97.11	95.86	0.259	0.657	0.0461	1.087	0.904
		$\mathcal{L}_c, \alpha = 0.1$	91.76	**97.21**	96.05	0.222	0.556	**0.0395**	1.000	0.900
		$\mathcal{L}_c, \alpha = 0.2$	91.66	97.15	96.01	0.231	0.630	0.0419	0.991	0.902
		$\mathcal{L}_c, \alpha = 0.3$	**91.78**	97.18	**96.21**	**0.204**	**0.537**	0.0437	**0.919**	**0.913**
		$\mathcal{L}_c, \alpha = 0.4$	91.56	97.12	96.09	0.250	0.630	0.0444	0.995	0.902
		$\mathcal{L}_c, \alpha = 0.5$	91.66	97.16	96.16	0.231	0.620	0.0455	0.991	0.907
	Mosinska et al.	[29, 17]	82.30	94.67	-	-	1.973	-	-	-
	Hu et al.	[17]	-	94.56	-	-	1.113	-	-	-
DRIVE retina	FCN	*soft-Dice*	78.23	96.27	78.02	2.187	1.860	0.0429	3.275	0.773
		$\mathcal{L}_c, \alpha = 0.1$	78.36	96.25	79.02	2.100	1.610	0.0393	3.203	0.777
		$\mathcal{L}_c, \alpha = 0.2$	**78.75**	96.29	80.22	1.892	1.382	0.0383	2.895	0.793
		$\mathcal{L}_c, \alpha = 0.3$	78.29	96.20	80.28	1.888	**1.332**	**0.0318**	2.918	**0.798**
		$\mathcal{L}_c, \alpha = 0.4$	78.00	96.11	80.43	2.036	1.602	0.0423	3.141	0.764
		$\mathcal{L}_c, \alpha = 0.5$	77.76	96.04	**80.95**	**1.836**	1.408	0.0394	**2.848**	0.794
	U-Net	*soft-Dice*	74.25	95.63	75.71	1.745	1.455	0.0649	2.997	0.760
		$\mathcal{L}_c, \alpha = 0.5$	**75.21**	**95.82**	**76.86**	**1.538**	**1.389**	**0.0586**	**2.737**	**0.767**
	Mosinska et al.	[29, 17]	-	95.43	-	-	2.784	-	-	-
	Hu et al.	[17]	-	95.21	-	-	1.076	-	-	-
Vessap data	FCN, 1 ch	*soft-dice*	85.21	**96.03**	90.88	3.385	4.458	0.00459	5.850	0.862
		$\mathcal{L}_c, \alpha = 0.5$	**85.44**	95.91	**91.32**	**2.292**	**3.677**	**0.00417**	**5.620**	**0.864**
	FCN, 2 ch	*soft-dice*	85.31	95.82	90.10	2.833	4.771	0.00629	6.080	0.849
		$\mathcal{L}_c, \alpha = 0.1$	85.96	95.99	91.02	2.896	**4.156**	0.00447	5.980	0.860
		$\mathcal{L}_c, \alpha = 0.2$	**86.45**	**96.11**	91.22	2.656	4.385	0.00466	5.530	0.869
		$\mathcal{L}_c, \alpha = 0.3$	85.72	95.93	91.20	2.719	4.469	**0.00423**	5.470	0.866
		$\mathcal{L}_c, \alpha = 0.4$	85.65	95.95	**91.65**	2.719	4.469	**0.00423**	5.670	0.869
		$\mathcal{L}_c, \alpha = 0.5$	85.28	95.76	91.22	**2.615**	4.615	0.00433	**5.320**	**0.870**
	U-Net, 1 ch	*soft-dice*	87.46	96.35	91.18	3.094	5.042	0.00549	5.300	0.863
		$\mathcal{L}_c, \alpha = 0.5$	**87.82**	**96.52**	**93.03**	**2.656**	**4.615**	**0.00533**	**4.910**	**0.872**
	U-Net, 2 ch	*soft-dice*	87.98	96.56	90.16	2.344	4.323	0.00507	5.550	0.855
		$\mathcal{L}_c, \alpha = 0.1$	88.13	96.59	91.12	2.302	4.490	0.00465	5.180	**0.872**
		$\mathcal{L}_c, \alpha = 0.2$	87.96	96.74	92.52	2.208	**3.979**	0.00342	**4.830**	0.861
		$\mathcal{L}_c, \alpha = 0.3$	87.70	96.71	92.56	**2.115**	4.521	**0.00309**	5.260	0.858
		$\mathcal{L}_c, \alpha = 0.4$	**88.57**	**96.87**	**93.25**	2.281	4.302	0.00327	5.370	0.868
		$\mathcal{L}_c, \alpha = 0.5$	88.14	96.74	92.75	2.135	4.125	0.00328	5.390	0.864

introduced OPT-Junction F1 by Citraro et al. [7]. Our results are consistent across different network architectures, indicating that *soft-clDice* can be deployed to any network architecture.

Qualitative: In Figure 5, typical results for our datasets are depicted. Our networks trained on the proposed loss term recover connections, which were false negatives when trained with the soft-Dice loss. These missed connections appear to be particularly frequent in the complex road and DRIVE dataset. For the CREMI dataset, we observe these situations less frequently, which is in line with the very high quantitative scores on the CREMI data. Interestingly, in the real 3D vessel dataset, the soft-Dice loss oversegments vessels, leading to false positive connections. This is not the case when using our proposed loss function, which we attribute to its topology-preserving nature. Additional qualitative results can be inspected in the supplementary.

Computational Efficiency: Naturally, inference times of CNNs with the same architecture but different training losses are identical. However, during training, our soft-skeleton algorithm requires $O(kn^2)$ complexity for an $n \times n$ 2D image where k is the number of iterations. As a comparison, [17] needs $O(c^2 mlog(m))$ (see [15]) complexity to compute the 1d persistent homology where d is the number of points with zero gradients in the prediction and m is the number of simplices. Roughly, c is proportional to n^2, and m is of $O(n^2)$ for a 2D Euclidean grid. Thus, the worst complexity of [17] is $O(n^6 log(n))$. Additionally, their approach requires an $O(clog(c))$ complexity to find an optimal matching of the birth-death pairs. We note that the total run-time overhead for soft-clDice compared to soft-Dice is marginal, i.e., for batch-size of 4 and 1024x1024 image resolution, the former takes 1.35s while the latter takes 1.24s on average (<10% increase) on an RTX-8000.

Future Work: Although our proposed soft-skeleton approximation works well in practice, a better differentiable skeletonization can only improve performance, which we reserve for future research. Any such skeletonization can be readily plugged into our approach. Furthermore, theoretical and experimental multi-class studies would sensibly extend our study.

6. Conclusive Remarks

We introduce *clDice*, a novel topology-preserving similarity measure for tubular structure segmentation. Importantly, we present a theoretical guarantee that *clDice* enforces topology preservation up to homotopy equivalence. Next, we use a differentiable version of the *clDice*, *soft-clDice*, in a loss function, to train state-of-the-art 2D and 3D neural networks. We use *clDice* to benchmark segmentation quality from a topology-preserving perspective along with multiple volumetric, topological, and graph-based measures. We find that training on *soft-clDice* leads to segmentations with more accurate connectivity information, better graph-similarity, better Euler characteristics, and improved Dice and Accuracy. Our *soft-clDice* is computationally efficient and can be readily deployed to any other deep learning-based segmentation tasks such as neuron segmentation in biomedical imaging, crack detection in industrial quality control, or remote sensing.

Acknowledgement: J. C. Paetzold. and S. Shit. are supported by the GCB and Translatum, TU Munich. S.Shit., A. Zhylka. and I. Ezhov. are supported by TRABIT (EU Grant: 765148). We thank Ali Ertuerk, Mihail I. Todorov, Nils Börner and Giles Tetteh.

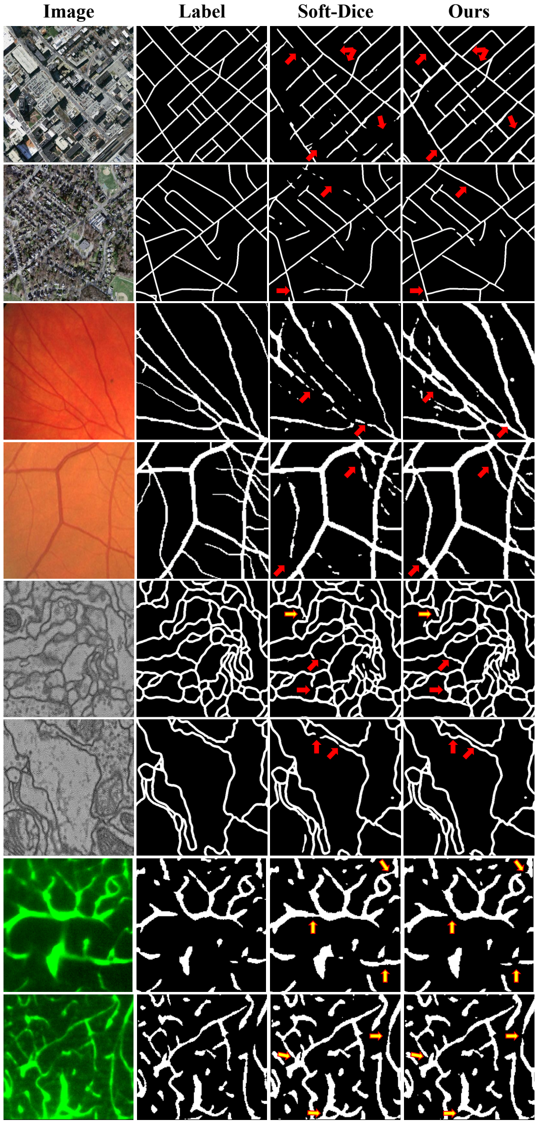

Figure 5. Qualitative results: from top to bottom we show two rows of results for: the Massachusetts road dataset, the DRIVE retina dataset, the CREMI neuron data and 2D slices from the 3D Vessap dataset. From left to right, the real image, the label, the prediction using soft-Dice and the U-Net predictions using $\mathcal{L}_c(\alpha = 0.5)$ are shown, respectively. The images indicate that *clDice* segments road, retina vessel connections and neuron connections which the soft-Dice loss misses, but also does not segment false-positive vessels in 3D. Some, but not all, missed connections are indicated with solid red arrows, false positives are indicated with red-yellow arrows. More qualitative results can be found in the Supplementary material.

References

[1] Pavel S Aleksandrov. *Combinatorial topology*, volume 1. Courier Corporation, 1998.

[2] Bjoern Andres et al. Probabilistic image segmentation with closedness constraints. In *ICCV*, pages 2611–2618. IEEE, 2011.

[3] Ricardo J Araújo, Jaime S Cardoso, and Hélder P Oliveira. A deep learning design for improving topology coherence in blood vessel segmentation. In *International Conference on Medical Image Computing and Computer-Assisted Intervention*, pages 93–101. Springer, 2019.

[4] Davide Belli and Thomas Kipf. Image-conditioned graph generation for road network extraction. *arXiv preprint arXiv:1910.14388*, 2019.

[5] Aïcha BenTaieb and Ghassan Hamarneh. Topology aware fully convolutional networks for histology gland segmentation. In *MICCAI*, pages 460–468. Springer, 2016.

[6] Özgün Çiçek and Aothers. 3D U-Net: learning dense volumetric segmentation from sparse annotation. In *MICCAI*, pages 424–432. Springer, 2016.

[7] Leonardo Citraro, Mateusz Koziński, and Pascal Fua. Towards reliable evaluation of algorithms for road network reconstruction from aerial images. In *European Conference on Computer Vision*, pages 703–719. Springer, 2020.

[8] James Clough, Nicholas Byrne, Ilkay Oksuz, Veronika A Zimmer, Julia A Schnabel, and Andrew King. A topological loss function for deep-learning based image segmentation using persistent homology. *IEEE Transactions on Pattern Analysis and Machine Intelligence*, 2020.

[9] Antonino Paolo Di Giovanna et al. Whole-brain vasculature reconstruction at the single capillary level. *Scientific reports*, 8(1):12573, 2018.

[10] Herbert Edelsbrunner et al. Topological persistence and simplification. In *FOCS*, pages 454–463. IEEE, 2000.

[11] Herbert Edelsbrunner and John Harer. *Computational topology: an introduction*. American Mathematical Soc., 2010.

[12] Jan Funke, Fabian Tschopp, William Grisaitis, Arlo Sheridan, Chandan Singh, Stephan Saalfeld, and Srinivas C. Turaga. Large scale image segmentation with structured loss based deep learning for connectome reconstruction. *IEEE Transactions on Pattern Analysis and Machine Intelligence*, 41(7):1669–1680, Jul 2019.

[13] Stefan Gerl et al. A distance-based loss for smooth and continuous skin layer segmentation in optoacoustic images. In *International Conference on Medical Image Computing and Computer-Assisted Intervention*, pages 309–319. Springer, 2020.

[14] Shir Gur, Lior Wolf, Lior Golgher, and Pablo Blinder. Unsupervised microvascular image segmentation using an active contours mimicking neural network. In *Proceedings of the IEEE/CVF International Conference on Computer Vision*, pages 10722–10731, 2019.

[15] Xiao Han et al. A topology preserving level set method for geometric deformable models. *IEEE TPAMI*, 25(6):755–768, 2003.

[16] Kai Hu et al. Retinal vessel segmentation of color fundus images using multiscale convolutional neural network with an improved cross-entropy loss function. *Neurocomputing*, 309:179–191, 2018.

[17] Xiaoling Hu et al. Topology-preserving deep image segmentation. In *NeurIPS*, pages 5658–5669, 2019.

[18] Jesse M Hunter et al. Morphological and pathological evolution of the brain microcirculation in aging and Alzheimer's disease. *PloS one*, 7(5):e36893, 2012.

[19] Dakai Jin, Ziyue Xu, Adam P Harrison, Kevin George, and Daniel J Mollura. 3d convolutional neural networks with graph refinement for airway segmentation using incomplete data labels. In *International Workshop on Machine Learning in Medical Imaging*, pages 141–149. Springer, 2017.

[20] Anne Joutel et al. Cerebrovascular dysfunction and microcirculation rarefaction precede white matter lesions in a mouse genetic model of cerebral ischemic small vessel disease. *JCI*, 120(2):433–445, 2010.

[21] Cemil Kirbas and Francis Quek. A review of vessel extraction techniques and algorithms. *CSUR*, 36(2):81–121, 2004.

[22] Bin Kong, Xin Wang, Junjie Bai, Yi Lu, Feng Gao, Kunlin Cao, Jun Xia, Qi Song, and Youbing Yin. Learning tree-structured representation for 3d coronary artery segmentation. *Computerized Medical Imaging and Graphics*, 80:101688, 2020.

[23] T. Yung Kong. On topology preservation in 2-D and 3-D thinning. *International journal of pattern recognition and artificial intelligence*, 9(05):813–844, 1995.

[24] T Yung Kong and Azriel Rosenfeld. Digital topology: Introduction and survey. *Computer Vision, Graphics, and Image Processing*, 48(3):357–393, 1989.

[25] Ta-Chih Lee et al. Building skeleton models via 3-D medial surface axis thinning algorithms. *CVGIP: Graphical Models and Image Processing*, 56(6):462–478, 1994.

[26] Cherng Min Ma. On topology preservation in 3D thinning. *CVGIP: Image understanding*, 59(3):328–339, 1994.

[27] Fausto Milletari et al. V-net: Fully convolutional neural networks for volumetric medical image segmentation. In *3DV*, pages 565–571. IEEE, 2016.

[28] Volodymyr Mnih. *Machine Learning for Aerial Image Labeling*. PhD thesis, University of Toronto, 2013.

[29] Agata Mosinska et al. Beyond the pixel-wise loss for topology-aware delineation. In *CVPR*, pages 3136–3145, 2018.

[30] Agata Mosinska, Mateusz Koziński, and Pascal Fua. Joint segmentation and path classification of curvilinear structures. *IEEE Transactions on Pattern Analysis and Machine Intelligence*, 42(6):1515–1521, 2019.

[31] Fernando Navarro, Suprosanna Shit, et al. Shape-aware complementary-task learning for multi-organ segmentation. In *International Workshop on MLMI*, pages 620–627. Springer, 2019.

[32] Sebastian Nowozin and Christoph H Lampert. Global connectivity potentials for random field models. In *CVPR*, pages 818–825. IEEE, 2009.

[33] Martin Ralf Oswald et al. Generalized connectivity constraints for spatio-temporal 3D reconstruction. In *ECCV*, pages 32–46. Springer, 2014.

[34] Johannes C Paetzold, Oliver Schoppe, et al. Transfer learning from synthetic data reduces need for labels to segment brain vasculature and neural pathways in 3d. In *International Conference on Medical Imaging with Deep Learning–Extended Abstract Track*, 2019.

[35] Kálmán Palágyi. A 3-subiteration 3D thinning algorithm for extracting medial surfaces. *Pattern Recognition Letters*, 23(6):663–675, 2002.

[36] Renzo Phellan et al. Vascular segmentation in TOF MRA images of the brain using a deep convolutional neural network. In *MICCAI Workshop*, pages 39–46. Springer, 2017.

[37] Markus Rempfler et al. Efficient algorithms for moral lineage tracing. In *ICCV*, pages 4695–4704, 2017.

[38] Olaf Ronneberger et al. U-net: Convolutional networks for biomedical image segmentation. In *MICCAI*, pages 234–241. Springer, 2015.

[39] Matthias Schneider et al. Tissue metabolism driven arterial tree generation. *Med Image Anal.*, 16(7):1397–1414, 2012.

[40] Matthias Schneider et al. Joint 3-D vessel segmentation and centerline extraction using oblique Hough forests with steerable filters. *Med Image Anal.*, 19(1):220–249, 2015.

[41] Florent Ségonne. Active contours under topology control—genus preserving level sets. *International Journal of Computer Vision*, 79(2):107–117, 2008.

[42] Frank Y Shih and Christopher C Pu. A skeletonization algorithm by maxima tracking on euclidean distance transform. *Pattern Recognition*, 28(3):331–341, 1995.

[43] Joes Staal, Michael D Abràmoff, Meindert Niemeijer, Max A Viergever, and Bram Van Ginneken. Ridge-based vessel segmentation in color images of the retina. *IEEE transactions on medical imaging*, 23(4):501–509, 2004.

[44] Jan Stuhmer et al. Tree shape priors with connectivity constraints using convex relaxation on general graphs. In *ICCV*, pages 2336–2343, 2013.

[45] Carole H Sudre et al. Generalised dice overlap as a deep learning loss function for highly unbalanced segmentations. In *MICCAI Workshop*, pages 240–248. Springer, 2017.

[46] Abdel Aziz Taha and Allan Hanbury. Metrics for evaluating 3D medical image segmentation: analysis, selection, and tool. *BMC Medical Imaging*, 15(1):29, 2015.

[47] Giles Tetteh et al. Deepvesselnet: Vessel segmentation, centerline prediction, and bifurcation detection in 3-d angiographic volumes. *arXiv preprint arXiv:1803.09340*, 2018.

[48] Mihail Ivilinov Todorov, Johannes C. Paetzold, et al. Automated analysis of whole brain vasculature using machine learning. *bioRxiv*, page 613257, 2019.

[49] Engin Türetken et al. Reconstructing curvilinear networks using path classifiers and integer programming. *IEEE TPAMI*, 38(12):2515–2530, 2016.

[50] Fatmatülzehra Uslu and Anil Anthony Bharath. A multi-task network to detect junctions in retinal vasculature. In *MICCAI*, pages 92–100. Springer, 2018.

[51] Subeesh Vasu, Mateusz Kozinski, Leonardo Citraro, and Pascal Fua. Topoal: An adversarial learning approach for topology-aware road segmentation. *arXiv preprint arXiv:2007.09084*, 2020.

[52] Sara Vicente et al. Graph cut based image segmentation with connectivity priors. In *CVPR*, pages 1–8. IEEE, 2008.

[53] Jan D Wegner et al. A higher-order CRF model for road network extraction. In *CVPR*, pages 1698–1705. IEEE, 2013.

[54] John HC Whitehead. Combinatorial homotopy. i. *Bulletin of the American Mathematical Society*, 55(3):213–245, 1949.

[55] Mark W Wright et al. Skeletonization using an extended euclidean distance transform. *Image and Vision Computing*, 13(5):367–375, 1995.

[56] Aaron Wu, Ziyue Xu, Mingchen Gao, Mario Buty, and Daniel J Mollura. Deep vessel tracking: A generalized probabilistic approach via deep learning. In *2016 IEEE 13th International Symposium on Biomedical Imaging (ISBI)*, pages 1363–1367. IEEE, 2016.

[57] Yun Zeng et al. Topology cuts: A novel min-cut/max-flow algorithm for topology preserving segmentation in n–d images. *CVIU*, 112(1):81–90, 2008.

[58] Shan Zhao et al. Cellular and molecular probing of intact human organs. *Cell*, 2020.

Whole Brain Vessel Graphs: A Dataset and Benchmark for Graph Learning and Neuroscience (VesselGraph)

Johannes Christian Paetzold, Julian McGinnis, Suprosanna Shit, Ivan Ezhov, Paul Büschl, Chinmay Prabhakar, Mihail I. Todorov, Anjany Sekuboyina, Georgios Kaissis, Ali Ertürk, Stephan Gn̈nemann & Bjoern Menze

Conference: 35th Conference on Neural Information Processing Systems (NeurIPS) Track on Datasets and Benchmarks, December 2021

Synopsis: Biological neural networks define the brain function and intelligence of humans and other mammals, and form ultra-large, spatial, structured graphs. Their neuronal organization is closely interconnected with the spatial organization of the brain's microvasculature, which supplies oxygen to the neurons and builds a complementary spatial graph. Recently, advances in tissue clearing have enabled whole brain imaging and segmentation of the entirety of the mouse brain's vasculature. Building on these advances, we are presenting an extendable dataset of whole-brain vessel graphs based on specific imaging protocols. Specifically, we extract vascular graphs using a refined graph extraction scheme and provide them in an accessible and adaptable form. We benchmark numerous state-of-the-art graph learning algorithms on the biologically relevant tasks of *vessel prediction* and *vessel classification* using the introduced vessel graph dataset. Our work paves a path towards advancing graph learning research into the field of neuroscience. Complementarily, the presented dataset raises challenging graph learning research questions for the machine learning community, in terms of incorporating biological priors into learning algorithms, or in scaling these algorithms to handle sparse, spatial graphs with millions of nodes and edges.

Contributions of thesis author: idea and conception of project, algorithm design, lead computational experiments, writing and composition of whole manuscript, led all aspects of the project.

Copyright: Attribution-NonCommercial 4.0 International (CC BY-NC 4.0).

Whole Brain Vessel Graphs: A Dataset and Benchmark for Graph Learning and Neuroscience (VesselGraph)

Johannes C. Paetzold†‡, Julian McGinnis†, Suprosanna Shit†, Ivan Ezhov†, Paul Büschl†, Chinmay Prabhakar*, Mihail I. Todorov‡, Anjany Sekuboyina*, Georgios Kaissis†, Ali Ertürk‡, Stephan Günnemann†, Bjoern H. Menze*
†Technical University of Munich, ‡Helmholtz Zentrum München, *University of Zürich
`johannes.paetzold@tum.de`

Abstract

Biological neural networks define the brain function and intelligence of humans and other mammals, and form ultra-large, spatial, structured graphs. Their neuronal organization is closely interconnected with the spatial organization of the brain's microvasculature, which supplies oxygen to the neurons and builds a complementary spatial graph. This vasculature (or the vessel structure) plays an important role in neuroscience; for example, the organization of (and changes to) vessel structure can represent early signs of various pathologies, e.g. Alzheimer's disease or stroke. Recently, advances in tissue clearing have enabled whole brain imaging and segmentation of the entirety of the mouse brain's vasculature. Building on these advances in imaging, we are presenting an extendable dataset of whole-brain vessel graphs based on specific imaging protocols. Specifically, we extract vascular graphs using a refined graph extraction scheme leveraging the volume rendering engine *Voreen* and provide them in an accessible and adaptable form through the *OGB* and *PyTorch Geometric* dataloaders. Moreover, we benchmark numerous state-of-the-art graph learning algorithms on the biologically relevant tasks of *vessel prediction* and *vessel classification* using the introduced vessel graph dataset. Our work paves a path towards advancing graph learning research into the field of neuroscience. Complementarily, the presented dataset raises challenging graph learning research questions for the machine learning community, in terms of incorporating biological priors into learning algorithms, or in scaling these algorithms to handle sparse,spatial graphs with millions of nodes and edges.[1]

1 Introduction

Human intelligence and brain function are defined by the cerebral biological neuronal network, the so-called *connectome*. The entirety of all single neurons forms an ultra-large, spatial, hierarchical and structured graph. Imaging and reconstructing these whole-brain graphs on a single-neuron level is one of the key problems in neuroscience. Neuronal organization is closely linked to the vascular network, as vessels supply the neurons with nutrients (e.g. oxygen). Specifically, the vessel topology determines the maximum metabolic load and determines neural growth patterns [1]. Vascular organisation, particularly in regards to vessel sizes and numbers of capillary links, varies substantially between brain regions, see Supplementary Figure 5 and 6. Moreover, its organization and changes to its structure are early signs for the development of specific diseases, e.g. Alzheimer's disease [2, 3]

---

[1] All datasets and code are available for download at `https://github.com/jocpae/VesselGraph`.
Ali Ertük, Stephan Günnemann and Bjoern H. Menze share last authorship.

35th Conference on Neural Information Processing Systems (NeurIPS 2021) Track on Datasets and Benchmarks.

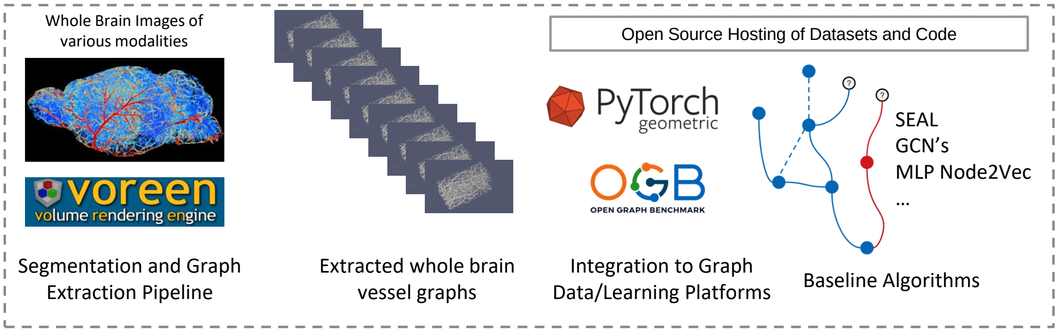

Figure 1: Graphical Abstract of *VesselGraph*.

or even COVID-19 encephalopathy [4]. As an initial step towards understanding the neuronal and vascular connectome (also known as the *angiome* [5]), reliable imaging and segmentation methods are required. To this day, whole-brain imaging and segmentation of all neurons in the brain remains elusive. On the other hand, advances in tissue clearing and deep learning have enabled imaging and segmentation of the whole murine brain vasculature down to the microcapillary level [6, 7].

Nonetheless, a binary segmentation of the vasculature is insufficient for a full, abstract description of the vascular connectome. To enable a comprehensive hierarchical description of the spatial vessel structure and anatomy, a graph representation of the brain with detailed features is required. This work provides the first large-scale, reproducible graph dataset thereof.

We believe that such a graph representation can facilitate research and understanding in many fields. The correction of imperfect vascular imaging and segmentation based on such an enhanced vascular graph, could one day enable the simulation of blood-flow (hemodynamic modeling), the study of vessel anatomy, connectivity, collateralization/anastomosis and structural abnormalities. Future studies using enhanced datasets could find our approach useful to study pathologies associated with neurovascular disorders, such as stroke and dementia, given that obstacles such as plaques would be accounted for.

Evidently, the study of such spatial graphs with millions of nodes requires its own set of methods; we believe that the recent rise of advanced machine learning methods for graphs will provide suitable approaches to efficiently and accurately permit drawing deep insight from vascular graphs. This, in turn, will foster the development of methods capable of dealing with massive, but sparsely connected circular graphs, for inference on these graphs, and inference under structural and functional prior constraints that are present in such spatial physical 3D networks.

In this work we benchmark two exemplary and biologically relevant tasks using both traditional approaches and advanced graph learning. First, in order to improve the structure and anatomical fidelity of the extracted graphs, we benchmark vessel (link) prediction. As a second task, we benchmark vessel (node) classification into the three main classes (capillaries, arterioles/venules, and arteries/veins), which represent biologically meaningful classifications by vessel size, and whose relevance for hemodynamics has been demonstrated in stroke and oxygenation modeling [8].

1.1 Whole brain vascular imaging and segmentation

Novel imaging methods, e.g. tissue-clearing-based methods [9–12], VesSAP [6], Tubemap [7] and the work by diGiovanna et al. [13] have enabled the imaging of the full vascular structure on a whole-brain scale [1].

The segmentation of the resulting ultra-large and unbalanced images with thousands of pixels in each dimension (e.g. $3096 \times 4719 \times 1867$ pixels [6]) is a challenging computer vision task which is strongly affected by technical imaging imperfections. The best-performing segmentation approaches rely on deep learning, e.g. using the U-Net architecture, and are only trained on selected, manually annotated sub-volumes of the whole brain images [6, 7, 1], leading to further imperfections in the segmentation masks.

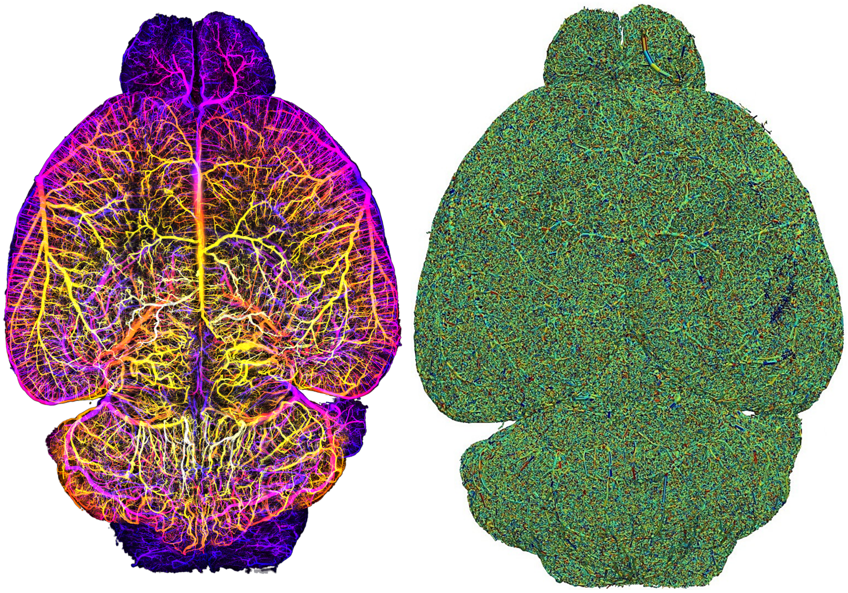

Figure 2: Left: 3D imaging of the whole mouse brain vasculature [6] and right; the corresponding rendering of our whole brain spatial vessel graphs; the edges (vessels) are rendered with the average radius feature.

The process presented in our work commences with segmentations of whole-brain vessel images, for which we use publicly available data from lightsheet microscopy (VesSAP), two-photon microscopy and a synthetic blood vessel dataset. For details refer to Appendix B.4. In the future, we will continuously increase the dataset with whole-brain images and segmentation as they become publicly available.

1.2 Graph learning

Machine learning on graphs is a highly relevant research field which aims to develop efficient machine learning algorithms exploiting the unique properties of graphs, such as structure neighborhoods and the sparse representation of complex systems. Our work concerns a particularly challenging domain - spatial, structured and ultra large biological graphs. In this paper we utilize and benchmark two fundamental graph learning tasks: node classification and link prediction to study the biological properties of the vascular connectome.

A widely recognized concept for node classification is the adaption of deep learning techniques to graphs via graph convolutional networks (GCN) [14], a concept which was adapted and extended for many of the algorithms that we implemented, such as such as GNNs, GCNs, and GAEs [15–23]. A key approach for link prediction is a so-called *labeling trick* [24], which is a concept to generate sensible training data. The SEAL labeling trick used in our work constructs a subgraph for two candidate nodes (enclosing subgraph) and aims to learn a functional mapping on the subgraph to predict link existence [25].

1.3 Our contribution

Our main contributions are:

1. We extract a set of standardized whole-brain vessel graphs based on whole, segmented murine brain images.
2. We publicly release said dataset in an easily accessible and adaptable format for use in graph learning benchmarking by implementing the *open graph benchmark* (OGB) [26] and *PyTorch Geometric* data loaders [27].
3. In addition to our standard vessel graph, in which bifurcation points are nodes and vessels are edges, we propose an alternative representation of the vascular connectome as a line

graph (where vessels become nodes), enabling the use of a multitude of advanced *node classification algorithms* for vessel property prediction.

4. We extensively benchmark graph algorithms for the biologically important tasks of **link prediction** and **node classification**, which can serve as baselines for further research efforts in graph learning and neuroscience.

The rest of the paper is organized as follows: In Section 2, we describe our refined graph generation process and provide implementation details for the used *voreen* framework and compare to other graph generation methods. We introduce the structure of our 3D brain vessel graph and provide statistics on the different extracted graphs from different brains in Section 3.1. We describe how we generated an alternative line graph representation in Section 3.2. In Section 4, we benchmark the link prediction task and in Section 5, we benchmark the node classification task on a multitude of baseline algorithms. We conclude with a focused discussion of our contribution and outline future perspectives and topics related to dataset maintenance.

2 Graph extraction from segmentations

Our graph extraction protocol begins with a given segmented whole-brain vascular dataset. Independent of segmentation method used (deep learning or filter-based), we tested the following state-of-the-art graph extraction algorithms: 1) the TubeMap method [7] which uses pruning on a 27-neighborhood skeletonization after a deep learning based tube-filling algorithm, based on a modified DeepVesselNet architecture [28]; 2) the metric graph reconstruction algorithm by Aanjaneya et al. [29] which reduces linear connections of a skeleton to form a more compact and topologically correct graph and 3) the *Voreen* vessel graph extraction method [30, 31]. We tested the graph extraction algorithms on different imaging modalities, varying brain areas, and the synthetically generated vascular trees [32].

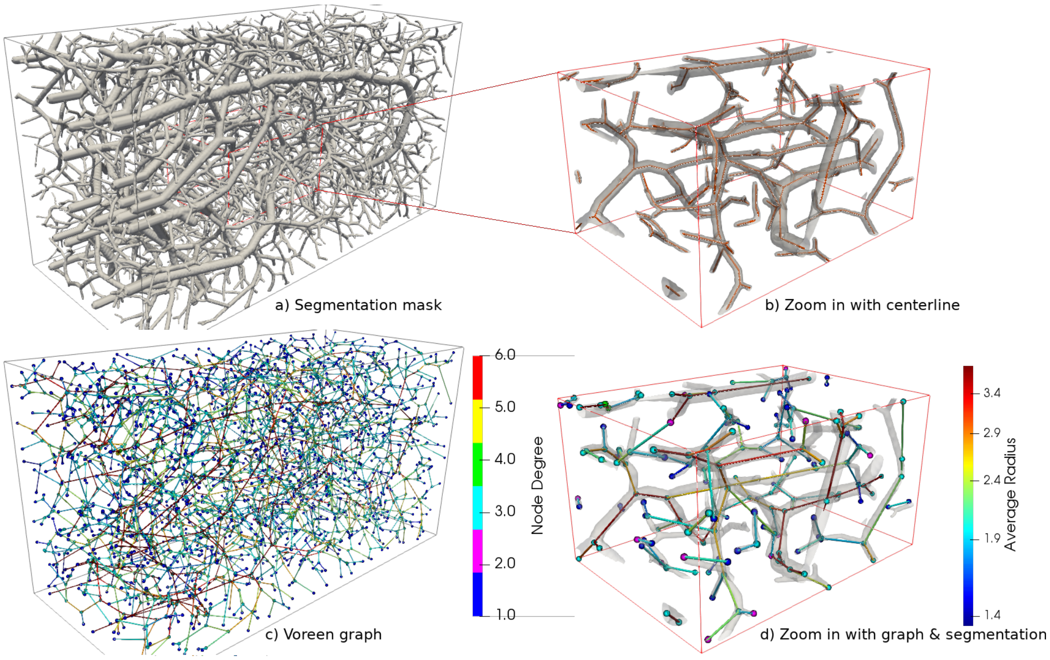

Figure 3: Extracted spatial vessel graph on a synthetic vessel volume [32]; the graph is extracted using the *Voreen* software [30]; a) the original vascular segmentation rendered in rendered in grey; b) depiction of the centerlines in red for a zoomed-in section; c) the nodes with a discrete colorbar encoding their degree; d) depiction of the segmentation with the edges and a continuous colorbar encoding the radius.

After expert-level evaluation of the extracted graphs in terms of feature quality, graph robustness and pipeline parameters, and of the algorithms in terms of scalability, runtime and resource constraints, we selected *Voreen* [31] for our graph generation. For details and comparisons we refer to Supplementary section C.1.

Voreen (Volume Rendering Engine) is a general framework for multi-modal volumetric dataset visualization and analysis purposes. One key advantage of *Voreen* compared to other graph generation algorithms, is that its graph extraction process is deterministic, robust and scalable. It has successfully been applied to cosmological visualization [33], visualization of large volumetric multi-channel microscopy data [34], 3D visualization of the lymphatic vasculature [35], 3D histopathology of lymphatic malformations [36] and velocity mapping of the aortic flow in mice [37].

Our graph extraction follows a four-stage protocol:

1. Skeletonization: The binary segmentation volume is reduced to a skeleton based representation by applying a standard topological thinning algorithm by Lee et al. [38].
2. Topology Extraction: memory efficient algorithms extract the vessel centerlines [39]. *Voreen* allows to store this intermediate representation in a combination with the graph.
3. Voxel-Branch Assignment: Computing of mapping between the so-called protograph (i.e. the initial graph) and the voxels of the binary segmentation.
4. Feature Extraction: On basis of the protograph and the mapping, several features can be computed from the foreground segmentation.

Multiple iterations of the four-stage protocol refine and improve the graph quality and prune small, spurious branches. The key optimization parameter for the graph structure in terms of node representation, and node statistics is the *bulge size*. Expert neuroscientists determined the parameter (bulge size = 3, a parameter choice in line with previous work [31]) by statistically comparing the resulting graphs, and visually interpreting the vascular connections in varying brain regions (compare Supplementary Figure 6). Still, known limitations of topological thinning-based methods for graph extraction exist [31], motivating our first baseline task, presented in Section 4.

3 3D vessel graph dataset

Complete Datasets			
Name	Number of Nodes	Num of Edges	Node Degree
BALBc1 [6]	3,538,495	5,345,897	3.02
BALBc2	3,451,306	5,193,775	3.01
BALBc3	2,850,347	4,097,953	2.88
C57BL/6-1	3,820,133	5,614,677	2.94
C57BL/6-2	3,439,962	5,070,439	2.95
C57BL/6-3	3,318,212	4,819,208	2.90
CD1-E-1	3,645,963	5,791,309	3.18
CD1-E-2	1,664,811	2,150,326	2.58
CD1-E-3	2,295,360	3,130,650	2.73
C57BL/6-K18 [1]	4,284,051	6,525,881	3.05
C57BL/6-K19	3,948,612	5,999,958	3.04
C57BL/6-K20	4,165,085	6,317,179	3.03
Synth. Graph 1 [32]	3159	3234	2.05
Synth. Graph 2	3349	3421	2.04
Synth. Graph 3	3227	3310	2.05
Synth. Graph 4	3178	3251	2.05
Synth. Graph 5	3294	3376	2.05

Table 1: Total number of edges, nodes and average node degree for the different whole brain graphs.

Our 3D vessel dataset features 17 graphs from 2 different imaging modalities as well as 5 sets of synthetic vascular graphs. We found the smaller synthetic graphs useful for prototyping since they are smaller in size and cover all three classes of vessels (arteries, arterioles and capillaries). For all real vessel graphs, the full 3D images and binary segmentations are also publicly available. An overview of the notation used throughout the following sections alongside typical values can be found in Table 2.

3.1 Vessel graph G

The output of the *Voreen* graph extraction pipeline represents our primary unweighted and undirected graph or “intuitive” vessel graph. Let this graph be denoted as $\mathcal{G} = (\mathcal{V}, \mathcal{E})$, where $\mathcal{V}$ is the set of nodes and $\mathcal{E}$ is the set of all the edges of the graph.

Nodes: From a biological perspective, each node $n \in \mathcal{V}$ in our graph either represents end points of the vessel branches or the bifurcation of vessel branches, (see Figure 4). Bifurcation points are the points where a larger vessel branches into two or more smaller vessels (in case of an artery) or smaller vessels merge into a large vessel (in case of a vein). The number of vessels branching from a bifurcation point defines the degree of that particular node. Bifurcation points have node degree of 3 or higher. In some cases, our graphs also have vessel endpoints, which are encoded as nodes of degree 1. Further, degree 2 nodes are generated by the graph extraction in cases when vessels exhibit a large curvature. These nodes are important to preserve the vessel curvature in its graph representation. For a statistical evaluation of the node degree please see Supplementary Figure 9.

Feature Overview			
Name	Feature Type	Value	Description
x_n	node feature	$[178, 3096]$ *	x-coordinate
y_n	node feature	$[808, 4719]$ *	y-coordinate
z_n	node feature	$[0, 1866]$ *	z-coordinate
a_n	node feature	$\{0, 1\}^{71}$	Allen mouse brain atlas region
μ_{ij}^{r}	edge feature	$[0.5, 38.65]$	mean of minimum radii
σ_{ij}^{r}	edge feature	$[0.0, 12.49]$	std. of minimum radii
$\mu_{ij}^{\bar{r}}$	edge feature	$[0.79, 38.65]$	mean of average radii
$\sigma_{ij}^{\bar{r}}$	edge feature	$[0.0, 11.99]$	std. of minimum radii
μ_{ij}^{R}	edge feature	$[0.91, 44.12]$	mean of maximum radii
σ_{ij}^{R}	edge feature	$[0.0, 23.64]$	std. of minimum radii
μ_{ij}^{o}	edge feature	$[0.04, 1.99]$	mean of roundness
σ_{ij}^{o}	edge feature	$[0.0, 1.0]$	std. of roundness
l_{ij}	edge feature	$[2, 322.81]$	vessel length
d_{ij}	edge feature	$[1.77, 300.36]$	shortest distance
ρ_{ij}	edge feature	$[0.18, 27.43]$	curvature
α_{ij}	edge feature	$[0.29, 1587.49]$	mean crosssection area
v_{ij}	edge feature	$[1.0, 119459]$	Volume of vessel
nv_{ij}	edge feature	$[0.0, 256] \cap \mathbb{N}$	no. of voxel in vessel
ν_{ij}^{1}	edge feature	$[1, 14] \cap \mathbb{N}$	degree of n_i of edge e_{ij}
ν_{ij}^{2}	edge feature	$[1, 14] \cap \mathbb{N}$	degree of n_j of edge e_{ij}

Table 2: Systematic overview of the notation of the existing node and edge features in our spatial vessel graphs. All features besides the Allen brain atlas region and the node degree are spatial and extracted using Voreen, discrete ranges are given for the *Balbc1* brain (* subject to imaging resolution).

Node features: We extract two important features for the nodes of graph $\mathcal{G}$. For each node, the key features are the physical location in the coordinate space and the anatomical location in reference to the Allen brain atlas [40]. For the physical location feature, we denote real valued coordinates $[x_n, y_n, z_n] \in \mathbb{R}^3 \; \forall n \in \mathcal{V}$ where $[x_n, y_n, z_n]$ is the location of node n in 3D space. Further, multiple prior works have shown that regional differences in vessel geometry can be observed in different brain regions [1, 41, 6]. This motivates us to include anatomical location features for the nodes. Hence, we register the whole segmentation volume to the Allen brain atlas. Our reference Atlas uses the ontology the Allen mouse brain atlas (CCFv3 201710). We use the average template. After appropriate downsampling of the Allen brain atlas and the images, we apply a two-step-rigid and deformable registration using *elastix*. Our protocol is thus identical to the Vessap paper[6]. Subsequently, we assign the brain region where a particular node is located in the brain atlas as anatomical node location feature, see Supplementary Figure 7. Formally, the anatomical location feature $a_n = c \; \forall n \in \mathcal{V}$ if $[x_n, y_n, z_n] \in \; A_c$, where A_c is the c^{th} region of the brain atlas. The atlas includes 71 brain regions which are hierarchically clustered from > 2000 subregions. The anatomical location feature is embedded as a one-hot encoded vector.

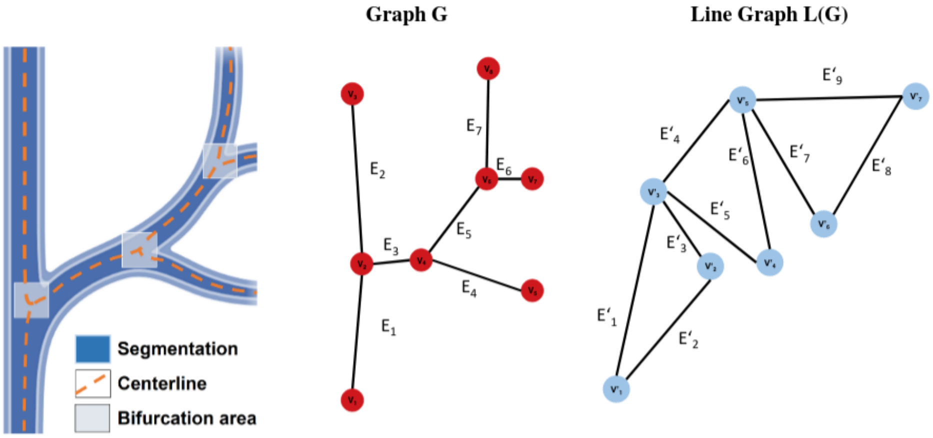

Figure 4: Depiction of an exemplary vessel tree with the the spatial vessel Graph $\mathcal{G}(\mathcal{V}, \mathcal{E})$ with nodes $(\mathcal{V})$ and edges $(\mathcal{E})$; additionally, a line graph $L(\mathcal{G})$ of the spatial vessel graph $\mathcal{G}$; where each node (bifurcation point) becomes an edge; two nodes of $L(\mathcal{G})$ are adjacent if and only if their edges are incident in $\mathcal{G}$.

Edges: Each edge $e_{ij} \in \mathcal{E}$ in our graph represents vessels or vessel segments which connect two nodes $\mathcal{V}$, see Figure 4. These edges (vessels) determine the structure of the whole brain network and represent the core aspect of our research questions. The edges exhibit the following rich set of features, which are extracted based on the shape and topology of the given segmented images.

Edge features: We extract geometric properties for each of the edges. For that, we determine the maximum diameter inscribed circle, least square reference circle, and minimum circumscribed circle on the discretized cross-section of a vessel branch and compute their radius as $\{r_{ij}^k\}$, $\{\bar{r}_{ij}^k\}$ and $\{R_{ij}^k\}$ where $k = 1 : K$ for K number of cross section of the edge e_{ij}, respectively. From this, we compute the mean and standard deviation of the minimum, average and maximum radius for each edge e_{ij} as follows. Specifically, $\mu_{ij}^r, \sigma_{ij}^r$ denotes the mean and standard deviation of minimum radius of edge e_{ij}. We extend the same notation for mean and standard deviation for $\{\bar{r}_{ij}^k\}$ and $\{R_{ij}^k\}$ as $\mu_{ij}^{\bar{r}}, \sigma_{ij}^{\bar{r}}, \mu_{ij}^R, \mu_{ij}^R$ respectively. We compute the roundness of each cross section as $o_{ij}^k = \frac{r_{ij}^k}{R_{ij}^k}$. We denote the mean and standard deviation of roundness as μ_{ij}^o and σ_{ij}^o, respectively. Further, we extract the vessel length l_{ij}, shortest distance between two nodes of an edge d_{ij}, curvature $\rho_{ij} = \frac{l_{ij}}{d_{ij}}$, mean cross section are α_{ij}. Moreover, we use the degree of the nodes n_i and n_j for an edge e_{ij} as ν_i and ν_j, respectively. The complete set of edge features can be found in Table 2.

3.2 Line vessel graph L(G)

As an alternative representation of whole brain vessel graphs, we convert our vessel graphs $\mathcal{G}$ to a corresponding line-graph representation, $L(\mathcal{G})$[42]. A line graph (depicted in Figure 4) is a graph where the edges of the base graph $\mathcal{G}$ become nodes and an edge between the new nodes is created if and only if their edges are incident in $\mathcal{E}$. Edges are the most important aspects in our graph $\mathcal{E}$ because of their one-to-one correspondence to the vessels. Therefore, we wish to apply another set of graph-learning algorithms, namely node classification algorithms, to study their biological properties based on the rich set of vessel features. Hence, we construct an alternative representation with the help of line graph $L(\mathcal{G})$. We formally define $L(\mathcal{G}) := (\mathcal{V}', \mathcal{E}')$ where $\mathcal{V}' = \mathcal{E}$ and $\mathcal{E}' = \{\{e_{ij}, e_{ik}\}$ if $\exists\ (e_{ij}, e_{ik}) \in \mathcal{E}\}$.

Nodes: Now, the nodes in the line graph $\mathcal{V}'$ represent vessels or vessel segments, see Figure 4.

Node features: Thus, all edge features of $\mathcal{G}$ can now be used as node features for $L(\mathcal{G})$, see Table 2. One of the key advantages of constructing the line graph is that we can now leverage a large number of prior techniques presented in node classification literature such as the use of vessel features in message passing.

Edges: Edges are defined as pairwise adjacencies of two nodes (vessels) *if and only if* the corresponding edges in $\mathcal{G}$ are connected to a node $\mathcal{V}$. In practice, this means that nodes in $\mathcal{G}$ which are of degree 1 disappear in $L(\mathcal{G})$ and that each node in $\mathcal{G}$ with a degree ≥ 2 will create multiple edges in $L(\mathcal{G})$.

Edge features: The spatial location given as node features in $\mathcal{G}$ can now be added as an edge feature.

4 Benchmarking link prediction

The formal goal of link prediction is to train a classifier $\mathcal{F}$ which predicts links in $\mathcal{E}_{pred}$ as positive and negative labels, it can be formalized as follows $\mathcal{F} : \mathcal{E}_{pred} \rightarrow \{0, 1\}$.

From a biological perspective this task is relevant to correct missing and imperfect vessel graph connections, because the extracted graph may be over- or under-connected, due to artifacts and shortcoming of the segmentation and network extraction.

In order to provide initial baselines for vessel (link) prediction, we implemented 10 models. The following graph learning baselines were trained without edge features: the GCN by Kipf et al. [14], a GNN using the GraphSAGE operator [17] and the SEAL GNN, a network aiming to learn general graph structure features from the local subgraph [25]. Furthermore, we trained a multilayer perceptron (MLP) on full batches based on Node2Vec features [43]. Apart from these, more traditional, heuristic-based methods were implemented for the task of link prediction, which include the Katz index [44], Common Neighbour, Page Rank and Adamic Adar [45], a measure which computes the closeness of nodes. These traditional methods make predictions based on the graph structure itself.

4.1 Dataset curation - SEAL

Link sampling strategy: The curation of a balanced training dataset requires the introduction of two types of edges. Similar to the SEAL paper [25], we use the notion of *positive edges* and *negative edges*. Generally, positive edges are random samples of existing links and negative edges are samples of non-existent links between randomly chosen nodes of the dataset (which are included in the adjacency matrix). For positive edges, we utilize random samples of the existing edges of each graph. However, since our dataset includes 3D coordinates as the node features, their spatial nature makes selecting negative samples more challenging. A trivial random selection, which has been used in other state-of-the-art methods such as SEAL, would lead to biologically implausible edges, e.g. an edge between two nodes in different brain hemispheres. These can be easily distinguished based on the coordinates and thus would not provide useful information to the model. As such, models trained with trivial random sampling struggle with the link prediction task. To address this issue, we restrict negative edge sampling to a coordinate space which spatially surrounds the source node, and choose the target node by randomly selecting nodes that are located within the following cubic space around the source node: $\delta = \overline{l_{i,j}} + 2\sigma$, where $\overline{l_{i,j}}$ denotes the average vessel length in $\mathcal{G}$. We note that this link sampling strategy is a first baseline and could be improved upon in future work.

Experiment: For our GCN based architectures we did an extensive grid-search of hyper-parameter combinations on a subset of the whole brain graph. We subsequently trained on the whole brain graphs. This intermediate step was necessary because exploring thousands of hyper-parameter combinations on the whole brain dataset is computationally infeasible. Implementation details and details on the hyperparameter search are indicated in supplementary Table 5.

For the main experiment we sample all edges from one whole brain graph as positive edges $\mathcal{G}(\mathcal{V}, \mathcal{E})$ (BALBc-1, Vessap, see Table 1)and randomly assign these to the training, validation and test set (80/10/10 split). Moreover, we sample an identical number of negative edges, i.e. non-existent but theoretically probable links according to the curation criterion described above. Next, we randomly shuffle all negative edges. Thus, we mitigate any bias in the negative train, validation and test splits and ensure a region-independent distribution. Subsequently, we randomly assign the negative edges to the train, validation and test set (80/10/10 split). This provides us with a balanced datast in regards to positive and negative edges.

We choose to only use the spatial node features for our experiment: x_n, y_n, z_n. This task is very hard because the algorithm essentially has to learn the vascular graph hierarchy purely on undirected relational and spatial information.

Table 3: Results for the link prediction baselines.

Algorithm	ROC AUC	
	validation	test
Adamic Adar	48.49	48.49
Common Neighbors	48.50	48.49
Resource Allocation	48.49	48.50
Matrix Factorization	50.07	50.08
MLP	57.98	58.02
GCN GCN	50.69	50.72
GCN GCN + embeddings	51.32	51.13
GCN SAGE + embeddings	52.81	52.88
GCN SAGE	59.37	59.23
SEAL	**91.01**	**90.96**

Generally, traditional methods and simple GCN models performed poorly. Among the traditional methods tested, the MLP performed best. On the other hand, the SEAL implementation reached a superior performance and a strong inductive bias (ROC AUC $> 90\%$). This improvement is in line with recent literature [24], which found a considerable performance improvement as a result of the employed labeling trick. This highlights that complex, dedicated graph-learning concepts need to be developed to address biologically inspired spatial graph challenges. A detailed experimental description and interpretation can be found in the Supplementary material, section D.1.

5 Benchmarking vessel attribute classification

Our formal goal of node classification is to train a classifier $\mathcal{F}$ which predicts a class label $\mathcal{Y}$ out of a set of possible classes $\mathcal{N}_n$ of a node $\mathcal{V}$, it can be formalized as follows $\mathcal{F} : \mathcal{V} \rightarrow \mathcal{Y} \in \mathcal{N}_n$.

Biologically, this task is relevant because the vessel radius is one of the most important parameters for blood flow; any task associated with flow modelling (such as stroke diagnosis and treatment) is heavily dependent on the diameter of the affected vessel. For example in stroke, a different treatment option is chosen based on the size of the vessel in the context of its local network topology. Therefore, reliably classifying vessel segments into categories such as arteries/veins, arterioles/venules and capillaries is relevant.

For the secondary task of vessel radius (node) classification we implemented 7 graph and non-graph learning baselines discussed in the OGB paper [26]. Among them node classification using an MLP initialized on N2Vec [43], a simple GCN [14], a GNN using the GraphSAGE operator [17], the GraphSAINT algorithm which includes a mini-batch GCN[16], the Scalable Inception Graph Neural Networks (SIGN)[18] and the Cluster-GCN algorithm[20]. Furthermore we implemented SpecMLP-W + C&S and SpecMLP-W + C&S + N2Vec, which use shallow models ignoring graph structure and standard label propagation techniques from semi-supervised learning methods [22].

Experiment: We split our three classes according to the minimum radius feature μ_{ij}^r into classes of $\mu_{ij}^r < 15\mu m; 15-40\mu m$ and $> 40\mu m$. Defined by the anatomy and properties of oxygen distribution these three classes are highly imbalanced. E.g. for the *Vessap* datasets the distribution is roughly 95%, 4% and 1%. Similarly to the link prediction task we carried out a grid search for optimal hyper-parameters, see Supplementary Table 6. We randomly split the nodes into train, validation and test sets of (80/10/10) of one whole mouse brain (BALBc-1, Vessap, see Table 1). We choose to use the following node features for our experiment: l_{ij} , d_{ij} and ρ_{ij}.

For node classification, we find acceptable to high performance in our baselines by all the methods we tested. More complex graph models such as GraphSAGE and Cluster-GCN outperform simple GCNs on average over all metrics. According to the metrics which account for class imbalance i.e.

Table 4: Results of the implemented node classification baselines. The performance scores are the weighted F1 score, one versus rest ROC AUC, class balanced accuracy and total accuracy (ACC).

	F1 Score		ROC AUC		Balanced ACC		ACC	
	valid	test	valid	test	valid	test	valid	test
GCN	75.74	75.75	67.23	66.46	58.38	56.83	62.94	62.92
GraphSAGE	81.98	81.98	**77.35**	**77.18**	**71.82**	**71.33**	72.02	71.98
GraphSAINT	77.46	77.40	71.38	70.71	63.74	62.51	64.88	64.84
SIGN	74.46	74.49	67.26	66.04	57.90	55.88	61.25	61.27
Cluster-GCN	**86.10**	**86.06**	**77.91**	**77.43**	**72.23**	**71.87**	**77.47**	**77.41**
MLP	76.11	76.11	58.08	57.79	42.36	41.72	63.65	63.61
SpecMLP-W + C&S	84.48	84.55	58.12	58.54	42.20	42.93	75.84	75.91
SpecMLP-W + + N2Vec	80.53	80.63	66.69	66.20	59.04	57.90	69.99	70.10

ROC AUC and balanced ACC, graph neural networks outperform non-graph learning methods, for a detailed interpretation see Supplementary D.2.

6 Discussion

In this work, we introduce and make publicly available a large dataset of vessel graphs representing the most comprehensive and highest resolution representation of the whole vascular connectome to-date. We provide this set of graphs as a new "baseline dataset" for machine learning on graphs and make it re-usable and easily accessible by leveraging widely employed open standards, such as the *OGB* and *PyTorch Geometric* dataloaders.

To provide an example for the utilization of our dataset and to promote graph machine learning research in neuroscience, we provide two benchmarks: First, we benchmark vessel (link) prediction to improve the vascular connectome; second, we implement vessel (node) classification into three main anatomical categories on the line graph. We thus show that graph learning-based methods outperform traditional methods for vessel (node) classification. Moreover, we demonstrate that link prediction based solely on the spatial organization is a difficult task for most algorithms. However, we provide evidence that the combination of an appropriately chosen, complex GNN model (SEAL) with a labeling trick can achieve high accuracy on this task, paving the way for dedicated machine learning research on spatial (biological) graphs as a key to unlocking biological insight.

Dataset bias: While the dataset and the evaluation we provide are thorough, we note the following bias in our work: Our vascular graphs are constrained by the technical bias and limitations inherent to experimental imaging, such as artifacts in the clearing protocol and physical limitations concerning the resolution and isotropy of the microscopy. All specimen imaged in this study are males. Moreover, even state-of-the-art deep learning methods for segmentation presented in literature are only trained on incomplete sets of labeled data, leading to a model bias in segmentation. Further problems can occur from the known limitations of topological thinning-based methods for graph extraction [31].

Limitations: The sum of these effects and bias can impair the usefulness of our dataset for certain, highly specialised tasks, such as flow simulations using the Navier-Stokes equations, which are strongly dependent on accurate radius measurements.

Moreover, benchmarking all available features, data and concepts was beyond the scope of our work. For instance, an extension to heterogeneous graph representations [46, 47], the utilization of more features, the inclusion of more than one graph or of weighted graphs, where e.g. all edges (vessels) are weighted depending on an embedding of their radius, may facilitate an improved interpretation. In summary, we are convinced that both the machine learning concepts and the biological insight arising from our work can be translated to other tasks, such as graph extraction and refinement on different vascular or neuronal imaging techniques, artery and vein classification, and even vessel classification in inherently different medical imaging protocols such as angiography for stroke diagnosis. We are thus hopeful that our provision of high-quality data and strong baselines will stimulate future research in this area.

Acknowledgments and Disclosure of Funding

We thank Dominik Drees for his advice and help with setting up the *Voreen* pipeline, and Muhan Zhang for his advice on enhancing SEAL. Moreover, we would like to thank Mattias Fey, Weihua Hu and the OGB Team for providing PyTorch geometric and baseline implementations.

References

[1] Xiang Ji, Tiago Ferreira, Beth Friedman, Rui Liu, Hannah Liechty, Erhan Bas, Jayaram Chandrashekar, and David Kleinfeld. Brain microvasculature has a common topology with local differences in geometry that match metabolic load. *Neuron*, 109(7):1168–1187, 2021.

[2] Eszter Farkas, Gineke I De Jong, Rob AI de Vos, ENH Jansen Steur, and Paul GM Luiten. Pathological features of cerebral cortical capillaries are doubled in alzheimer's disease and parkinson's disease. *Acta neuropathologica*, 100(4):395–402, 2000.

[3] Rachel E Bennett, Ashley B Robbins, Miwei Hu, Xinrui Cao, Rebecca A Betensky, Tim Clark, Sudeshna Das, and Bradley T Hyman. Tau induces blood vessel abnormalities and angiogenesis-related gene expression in p301l transgenic mice and human alzheimer's disease. *Proceedings of the National Academy of Sciences*, 115(6):E1289–E1298, 2018.

[4] Marjolaine Uginet, Gautier Breville, Jérémy Hofmeister, Paolo Machi, Patrice H Lalive, Andrea Rosi, Aikaterini Fitsiori, Maria Isabel Vargas, Frederic Assal, Gilles Allali, et al. Cerebrovascular complications and vessel wall imaging in covid-19 encephalopathy—a pilot study. *Clinical neuroradiology*, pages 1–7, 2021.

[5] Pablo Blinder, Philbert S Tsai, John P Kaufhold, Per M Knutsen, Harry Suhl, and David Kleinfeld. The cortical angiome: an interconnected vascular network with noncolumnar patterns of blood flow. *Nature neuroscience*, 16(7):889–897, 2013.

[6] Mihail Ivilinov Todorov, Johannes Christian Paetzold, Oliver Schoppe, Giles Tetteh, Suprosanna Shit, Velizar Efremov, Katalin Todorov-Völgyi, Marco Düring, Martin Dichgans, Marie Piraud, et al. Machine learning analysis of whole mouse brain vasculature. *Nature methods*, 17(4):442–449, 2020.

[7] Christoph Kirst, Sophie Skriabine, Alba Vieites-Prado, Thomas Topilko, Paul Bertin, Gaspard Gerschenfeld, Florine Verny, Piotr Topilko, Nicolas Michalski, Marc Tessier-Lavigne, et al. Mapping the fine-scale organization and plasticity of the brain vasculature. *Cell*, 180(4):780–795, 2020.

[8] Franca Schmid, Giulia Conti, Patrick Jenny, and Bruno Weber. The severity of microstrokes depends on local vascular topology and baseline perfusion. *Elife*, 10:e60208, 2021.

[9] Hiroki R Ueda, Ali Ertürk, Kwanghun Chung, Viviana Gradinaru, Alain Chédotal, Pavel Tomancak, and Philipp J Keller. Tissue clearing and its applications in neuroscience. *Nature Reviews Neuroscience*, 21(2):61–79, 2020.

[10] Ali Ertürk et al. Three-dimensional imaging of solvent-cleared organs using 3DISCO. *Nature Protocols*, 7(11):1983, 2012.

[11] Kwanghun Chung and Karl Deisseroth. Clarity for mapping the nervous system. *Nature methods*, 10(6):508–513, 2013.

[12] Nicolas Renier, Zhuhao Wu, David J Simon, Jing Yang, Pablo Ariel, and Marc Tessier-Lavigne. idisco: a simple, rapid method to immunolabel large tissue samples for volume imaging. *Cell*, 159(4):896–910, 2014.

[13] Antonino Paolo Di Giovanna et al. Whole-brain vasculature reconstruction at the single capillary level. *Scientific reports*, 8(1):12573, 2018.

[14] Thomas N Kipf and Max Welling. Semi-supervised classification with graph convolutional networks. *arXiv preprint arXiv:1609.02907*, 2016.

[15] Thomas N. Kipf and Max Welling. Variational graph auto-encoders, 2016.

[16] Hanqing Zeng, Hongkuan Zhou, Ajitesh Srivastava, Rajgopal Kannan, and Viktor Prasanna. Graphsaint: Graph sampling based inductive learning method. *arXiv preprint arXiv:1907.04931*, 2019.

[17] William L Hamilton, Rex Ying, and Jure Leskovec. Inductive representation learning on large graphs. In *Proceedings of the 31st International Conference on Neural Information Processing Systems*, pages 1025–1035, 2017.

[18] Fabrizio Frasca, Emanuele Rossi, Davide Eynard, Ben Chamberlain, Michael Bronstein, and Federico Monti. Sign: Scalable inception graph neural networks. *arXiv preprint arXiv:2004.11198*, 2020.

[19] Johannes Klicpera, Aleksandar Bojchevski, and Stephan Günnemann. Predict then propagate: Graph neural networks meet personalized pagerank. *arXiv preprint arXiv:1810.05997*, 2018.

[20] Wei-Lin Chiang, Xuanqing Liu, Si Si, Yang Li, Samy Bengio, and Cho-Jui Hsieh. Cluster-gcn: An efficient algorithm for training deep and large graph convolutional networks. In *Proceedings of the 25th ACM SIGKDD International Conference on Knowledge Discovery & Data Mining*, pages 257–266, 2019.

[21] Kezhi Kong, Guohao Li, Mucong Ding, Zuxuan Wu, Chen Zhu, Bernard Ghanem, Gavin Taylor, and Tom Goldstein. Flag: Adversarial data augmentation for graph neural networks, 2020.

[22] Qian Huang, Horace He, Abhay Singh, Ser-Nam Lim, and Austin R Benson. Combining label propagation and simple models out-performs graph neural networks. *arXiv preprint arXiv:2010.13993*, 2020.

[23] Johannes Klicpera, Janek Groß, and Stephan Günnemann. Directional message passing for molecular graphs. In *International Conference on Learning Representations*, 2019.

[24] Muhan Zhang, Pan Li, Yinglong Xia, Kai Wang, and Long Jin. Revisiting graph neural networks for link prediction, 2021.

[25] Muhan Zhang and Yixin Chen. Link prediction based on graph neural networks, 2018.

[26] Weihua Hu, Matthias Fey, Marinka Zitnik, Yuxiao Dong, Hongyu Ren, Bowen Liu, Michele Catasta, and Jure Leskovec. Open graph benchmark: Datasets for machine learning on graphs. *arXiv preprint arXiv:2005.00687*, 2020.

[27] Matthias Fey and Jan Eric Lenssen. Fast graph representation learning with pytorch geometric. *arXiv preprint arXiv:1903.02428*, 2019.

[28] Giles Tetteh et al. Deepvesselnet: Vessel segmentation, centerline prediction, and bifurcation detection in 3-d angiographic volumes. *arXiv preprint arXiv:1803.09340*, 2018.

[29] Mridul Aanjaneya, Frederic Chazal, Daniel Chen, Marc Glisse, Leonidas J Guibas, and Dmitriy Morozov. Metric graph reconstruction from noisy data. In *Proceedings of the twenty-seventh annual symposium on Computational geometry*, pages 37–46, 2011.

[30] Jennis Meyer-Spradow, Timo Ropinski, Jörg Mensmann, and Klaus Hinrichs. Voreen: A rapid-prototyping environment for ray-casting-based volume visualizations. *IEEE Computer Graphics and Applications*, 29(6):6–13, 2009.

[31] Dominik Drees, Aaron Scherzinger, René Hägerling, Friedemann Kiefer, and Xiaoyi Jiang. Scalable robust graph and feature extraction for arbitrary vessel networks in large volumetric datasets. *arXiv preprint arXiv:2102.03444*, 2021.

[32] Matthias Schneider et al. Tissue metabolism driven arterial tree generation. *Med Image Anal.*, 16(7):1397–1414, 2012.

[33] Aaron Scherzinger, Tobias Brix, Dominik Drees, Andreas Völker, Kiril Radkov, Niko Santalidis, Alexander Fieguth, and Klaus H Hinrichs. Interactive exploration of cosmological dark-matter simulation data. *IEEE computer graphics and applications*, 37(2):80–89, 2017.

[34] Tobias Brix, Jörg-Stefan Praßni, and Klaus Hinrichs. Visualization of large volumetric multi-channel microscopy data streams on standard pcs. *arXiv preprint arXiv:1407.2074*, 2014.

[35] Cathrin Dierkes, Aaron Scherzinger, and Friedemann Kiefer. Three-dimensional visualization of the lymphatic vasculature. In *Lymphangiogenesis*, pages 1–18. Springer, 2018.

[36] René Hägerling, Dominik Drees, Aaron Scherzinger, Cathrin Dierkes, Silvia Martin-Almedina, Stefan Butz, Kristiana Gordon, Michael Schäfers, Klaus Hinrichs, Pia Ostergaard, et al. Vipar, a quantitative approach to 3d histopathology applied to lymphatic malformations. *JCI insight*, 2(16), 2017.

[37] Philipp Rene Bovenkamp, Tobias Brix, Florian Lindemann, Richard Holtmeier, Desiree Abdurrachim, Michael T Kuhlmann, Gustav J Strijkers, Jörg Stypmann, Klaus H Hinrichs, and Verena Hoerr. Velocity mapping of the aortic flow at 9.4 t in healthy mice and mice with induced heart failure using time-resolved three-dimensional phase-contrast mri (4d pc mri). *Magnetic Resonance Materials in Physics, Biology and Medicine*, 28(4):315–327, 2015.

[38] Ta-Chih Lee et al. Building skeleton models via 3-D medial surface axis thinning algorithms. *CVGIP: Graphical Models and Image Processing*, 56(6):462–478, 1994.

[39] Martin Isenburg and Jonathan Shewchuk. Streaming connected component computation for trillion voxel images. In *Workshop on Massive Data Algorithmics*, volume 2, 2009.

[40] Susan M Sunkin, Lydia Ng, Chris Lau, Tim Dolbeare, Terri L Gilbert, Carol L Thompson, Michael Hawrylycz, and Chinh Dang. Allen brain atlas: an integrated spatio-temporal portal for exploring the central nervous system. *Nucleic acids research*, 41(D1):D996–D1008, 2012.

[41] Artur Hahn, Julia Bode, Allen Alexander, Kianush Karimian-Jazi, Katharina Schregel, Daniel Schwarz, Alexander C Sommerkamp, Thomas Krüwel, Amir Abdollahi, Wolfgang Wick, et al. Large-scale characterization of the microvascular geometry in development and disease by tissue clearing and quantitative ultramicroscopy. *Journal of Cerebral Blood Flow & Metabolism*, 41(7):1536–1546, 2021.

[42] Jonathan L Gross, Jay Yellen, and Mark Anderson. *Graph theory and its applications*. Chapman and Hall/CRC, 2018.

[43] Aditya Grover and Jure Leskovec. node2vec: Scalable feature learning for networks. In *Proceedings of the 22nd ACM SIGKDD international conference on Knowledge discovery and data mining*, pages 855–864, 2016.

[44] Leo Katz. A new status index derived from sociometric analysis. *Psychometrika*, 18(1):39–43, 1953.

[45] Lada A Adamic and Eytan Adar. Friends and neighbors on the web. *Social networks*, 25(3):211–230, 2003.

[46] Michael Schlichtkrull, Thomas N Kipf, Peter Bloem, Rianne Van Den Berg, Ivan Titov, and Max Welling. Modeling relational data with graph convolutional networks. In *European semantic web conference*, pages 593–607. Springer, 2018.

[47] Shikhar Vashishth, Soumya Sanyal, Vikram Nitin, and Partha Talukdar. Composition-based multi-relational graph convolutional networks. *arXiv preprint arXiv:1911.03082*, 2019.

[48] Eva L Dyer, William Gray Roncal, Judy A Prasad, Hugo L Fernandes, Doga Gürsoy, Vincent De Andrade, Kamel Fezzaa, Xianghui Xiao, Joshua T Vogelstein, Chris Jacobsen, et al. Quantifying mesoscale neuroanatomy using x-ray microtomography. *Eneuro*, 4(5), 2017.

[49] Jingpeng Wu, Yong He, Zhongqin Yang, Congdi Guo, Qingming Luo, Wei Zhou, Shangbin Chen, Anan Li, Benyi Xiong, Tao Jiang, et al. 3d braincv: simultaneous visualization and analysis of cells and capillaries in a whole mouse brain with one-micron voxel resolution. *Neuroimage*, 87:199–208, 2014.

[50] Evan Calabrese, Alexandra Badea, Gary Cofer, Yi Qi, and G Allan Johnson. A diffusion mri tractography connectome of the mouse brain and comparison with neuronal tracer data. *Cerebral cortex*, 25(11):4628–4637, 2015.

[51] Tianqi Li, Chao J Liu, and Taner Akkin. Contrast-enhanced serial optical coherence scanner with deep learning network reveals vasculature and white matter organization of mouse brain. *Neurophotonics*, 6(3):035004, 2019.

[52] Arttu Miettinen, Antonio Zippo, Alessandra Patera, Anne Bonnin, Sarah Shahmoradian, Gabriele Biella, and Marco Stampanoni. Micrometer-resolution reconstruction and analysis of whole mouse brain vasculature by synchrotron-based phase-contrast tomographic microscopy. *bioRxiv*, 2021.

[53] Solomon Kullback and Richard A Leibler. On information and sufficiency. *The annals of mathematical statistics*, 22(1):79–86, 1951.

[54] Rex Ying, Dylan Bourgeois, Jiaxuan You, Marinka Zitnik, and Jure Leskovec. Gnnexplainer: Generating explanations for graph neural networks. *Advances in neural information processing systems*, 32:9240, 2019.

Concluding Remarks

The brain, its functionality, capacity, and efficiency have for long been regarded a captivating research direction. The controlled firing of neurons and their precise interaction with the smallest vessels constitute an ultra-complex system. Historically, the origins of computational neural networks and machine learning are closely related to –and inspired by– neuroscience. It, therefore, is no surprise that his work has also immensely benefited from the cross-pollination between machine learning theory and vascular neuroscience. As this work is a cumulative thesis, the main Chapters 5 - 7 are self-contained, full research articles including a discussion and concluding remarks on their content. In consideration of the cumulative nature of this thesis, I will constrain myself to discussing specific challenges in the context of the literature and providing a general outlook, subject to my personal opinion, on machine learning for brain vessel analysis in the future.

Discussion

Chapter 5 - Machine Learning Analysis of Whole Mouse Brain Vasculature (***VesSAP***)

VesSAP constitutes an automated, deep-learning-based method to efficiently analyze tissue-cleared images of the mouse brain vasculature, a modality that has generated substantial attention in neuroscience and biology [5], [13], [53]. While the method constitutes the first-ever solution to the problem, its performance is influenced by various factors inherent to the imaging technology. For example, the anisotropic resolution of the given images, which is determined by the system's point spread function and the precision of the z-step in image acquisition [11]. Further, the thermal noise of the camera, aberration of the lenses of the microscope, and imperfect clearing of the tissue samples can frequently lead to minor image artifacts. From a segmentation perspective, the main limitation concerns the small vessels, which are sometimes overlooked because traditional loss functions optimize toward the total number of correctly classified pixels and do not account for the highly relevant network structure and topology of vessels. Similar to vessel segmentation, the topology is the most important property in segmentations of other (biological) structures, such as neurons or even roads. Inspired by this observation, we developed the *clDice*-loss for vessel segmentation to optimize the network output towards a biologically optimal goal that is beyond pixelwise accuracy.

Chapter 6 - clDice - a Novel Topology-Preserving Loss Function for Tubular Structure Segmentation

Since the topological correctness of vessel networks is their most important property, we propose the *clDice*-Loss which calculates the union of the binary mask and their skeleta to optimize the network structure preservation in segmentation. Further, we provide theoretical guarantees for the topology preservation of the *clDice* loss function. Moreover, experiments show an improvement in traditional segmentation metrics and topological scores on a vast set of data, for example, vessels, roads, and neurons. Importantly, our approach is the first topology-preserving loss function that efficiently operates in 3D as compared to previous 2D approaches in the literature [39]–[41]. The theoretical limit is that the proposed soft skeletonization is only an approximation of the skeleton. Moreover, memory demands increase with every pooling iteration. Therefore, an optimized skeletonization approach, which is easy to plug into the existing *clDice* formulation, would improve performance. The skeleton of a vessel is a compact representation of the vascular network. Considering this, the interpretation of vessels as a graph, which is an even more compact representation, appears instinctive [70], a concept which is studied in the next chapter.

Chapter 7 - Whole Brain Vessel Graphs: A Dataset and Benchmark for Graph Learning and Neuroscience (VesselGraph)

Representing the whole brain vessels as a spatial graph provides a drastically more compact representation of the neuronal oxygen supply network that is the brain's vasculature. In the *VesselGraph* paper, such representation is generated for a variety of publicly available whole-brain vessel representations, such as our *VesSAP* paper [11] or the work by Ji et al. [13]. We achieve the graph extraction using a refined approach based on the *Voreen* software [54] and make all graphs publicly available as a baseline dataset in a dedicated Github repository [1]. The efficiency and relevance for

---

[1] https://github.com/jocpae/VesselGraph

neuroscience is demonstrated in two benchmark experiments on the dataset. First, we study how the graph learning task of link prediction can be used to improve the vascular connectome. Second, we benchmark the classification of vessels into three hierarchical classes. In the experimentation, we show that standard GCN approaches outperform traditional non-GCN methods, which indicates the potential for dedicated research on graph learning concepts for spatial vascular graphs, similar to the more researched domain of graph learning on molecular graphs [71]. While our link prediction concept aims to improve the overall graph structure, the inherent bias and limitations of the individual dataset's imaging and segmentation techniques persist, affecting the overall structure of the graph. For a more detailed description of the limitations, refer to the Discussion Section in Chapter 7.

Additional Comments on the Transfer Learning Publication in Appendix A - Transfer Learning from Synthetic Data Reduces Need for Labels to Segment Brain Vasculature and Neural Pathways in 3D

The additional Chapter A on Transfer Learning evaluates how synthetically generated tubular data can be efficiently used to speed up model convergence and tackle the labeling bottleneck in biological and medical imaging. The results demonstrate the efficiency of transfer learning across modalities and even across different anatomical structures such as vascular data and neural pathways. This chapter can be placed into the overall context of Transfer Learning for vessel segmentation which is also used in the *VesSAP* project. Moreover, the same synthetic data from Schneider et al. [63] is used to benchmark the *clDice* performance, see Chapter 6 and is also provided as a graph in the *VesselGraph* Chapter 7. Therefore, this work is relevant to the three main publications of this thesis.

Outlook

This thesis studies brain vessels, three forms of their representation, and how their properties inspire machine learning research. Chronologically, the work in this thesis first considers images, then their binary segmentation, and finally studies a compact, spatial graph representation of the brain vessels. Considering this chronology, I conclude that future discoveries in neuroscience and advancements in machine learning will eventuate on the graph representations of the vasculature. The orders of magnitude sparser representation of relations in a graph enable a more rapid analysis, straightforward visualization, and faster prototyping of machine learning models. Considering the ever-growing memory and computational requirements of modern computer vision models such as transformers [50], [72], I foresee a requirement for compact machine learning models to infer knowledge, for example, on graphs. Ultimately, when used for similar tasks, such models not only enable more rapid training and inference but eventually reduce power consumption and the carbon footprint of machine learning models. In the future, dedicated machine learning concepts inspired by the physiological constraints and physical knowledge of vessels are likely to advance neuroscience discoveries on vessels and neurons. Similar feats have already been achieved for molecular graphs [73], [74] and protein prediction [75], where complex graph learning methods outperform experimental methods [76]. Moreover, I see considerable research potential in joint representations and analysis of brain vessels, neurons, and other cells, for example, in a heterogeneous graph representation [77], [78], which promises to enhance the representative power of the graphs and will thus lead to significant findings. Naturally, an extension not only to the brain but the whole murine vascular system or the human brain will further deepen biological understanding. Furthermore, heterogeneous graph embeddings could be used to combine spatial imaging data with graph representations originating from RNA sequence analysis in single-cell biology [79], [80], which would pave the way towards a holistic analysis of whole-body cell information and sub-cellular RNA or protein information in a single model. Ultimately, I consider a spatial graph representation of the connectivity of all neurons in the human brain to be a blueprint for understanding human intelligence. I foresee that once a whole-brain imaging of all neurons, including all dendrites, axons, and all their connections, is achieved, machine learning will be the principal technology to extract functional connectivity data from the neural image information. So far, works on the vascular connectome represent the first step toward such developments, and the technology developed herein will guide future studies of the whole cerebral neural network.

Appendices

Bibliography

[1] A. Krizhevsky, I. Sutskever, and G. E. Hinton. “Imagenet classification with deep convolutional neural networks.” In: *Advances in neural information processing systems* 25 (2012).

[2] J. Deng, W. Dong, R. Socher, L.-J. Li, K. Li, and L. Fei-Fei. “Imagenet: A large-scale hierarchical image database.” In: *2009 IEEE conference on computer vision and pattern recognition*. Ieee. 2009, pp. 248–255.

[3] W. T. Clarke, O. Mougin, I. D. Driver, C. Rua, A. T. Morgan, M. Asghar, S. Clare, S. Francis, R. G. Wise, C. T. Rodgers, et al. “Multi-site harmonization of 7 tesla MRI neuroimaging protocols.” In: *NeuroImage* 206 (2020), p. 116335.

[4] A. Ertürk et al. “Three-dimensional imaging of solvent-cleared organs using 3DISCO.” In: *Nature Protocols* 7.11 (2012), p. 1983.

[5] A. P. Di Giovanna et al. “Whole-brain vasculature reconstruction at the single capillary level.” In: *Scientific reports* 8.1 (2018), p. 12573.

[6] S. Zhao, M. I. Todorov, R. Cai, A.-M. Rami, H. Steinke, E. Kemter, H. Mai, Z. Rong, M. Warmer, K. Stanic, O. Schoppe, J. C. **Paetzold**, et al. “Cellular and molecular probing of intact human organs.” In: *Cell* 180.4 (2020), pp. 796–812.

[7] C. Pan, O. Schoppe, A. Parra-Damas, R. Cai, M. I. Todorov, G. Gondi, B. von Neubeck, N. Böğürcü-Seidel, S. Seidel, K. Sleiman, et al. “Deep learning reveals cancer metastasis and therapeutic antibody targeting in the entire body.” In: *Cell* 179.7 (2019), pp. 1661–1676.

[8] M. D. Sweeney, K. Kisler, A. Montagne, A. W. Toga, and B. V. Zlokovic. “The role of brain vasculature in neurodegenerative disorders.” In: *Nature neuroscience* 21.10 (2018), pp. 1318–1331.

[9] E. T. Rolls, A. Treves, and E. T. Rolls. *Neural networks and brain function*. Vol. 572. Oxford university press Oxford, 1998.

[10] C. Iadecola. “The neurovascular unit coming of age: a journey through neurovascular coupling in health and disease.” In: *Neuron* 96.1 (2017), pp. 17–42.

[11] M. I. Todorov*, J. C. **Paetzold***, O. Schoppe, G. Tetteh, S. Shit, V. Efremov, K. Todorov-Völgyi, M. Düring, M. Dichgans, M. Piraud, et al. "Machine learning analysis of whole mouse brain vasculature." In: *Nature Methods* 17.4 (2020), pp. 442–449.

[12] M. I. Todorov. "Systematic analysis of whole mouse brain vasculature and intact human organs using machine learning." PhD thesis. lmu, 2020.

[13] X. Ji, T. Ferreira, B. Friedman, R. Liu, H. Liechty, E. Bas, J. Chandrashekar, and D. Kleinfeld. "Brain microvasculature has a common topology with local differences in geometry that match metabolic load." In: *Neuron* 109.7 (2021), pp. 1168–1187.

[14] W. L. Hamilton, R. Ying, and J. Leskovec. "Representation learning on graphs: Methods and applications." In: *arXiv preprint arXiv:1709.05584* (2017).

[15] J. C. **Paetzold**, J. McGinnis, S. Shit, I. Ezhov, P. Büschl, C. Prabhakar, A. Sekuboyina, M. Todorov, G. Kaissis, A. Ertürk, et al. "Whole Brain Vessel Graphs: A Dataset and Benchmark for Graph Learning and Neuroscience." In: *Thirty-fifth Conference on Neural Information Processing Systems Datasets and Benchmarks Track (Round 2)*. 2021.

[16] M. M. Bronstein, J. Bruna, Y. LeCun, A. Szlam, and P. Vandergheynst. "Geometric deep learning: going beyond euclidean data." In: *IEEE Signal Processing Magazine* 34.4 (2017), pp. 18–42.

[17] S. Shit*, J. C. **Paetzold***, A. Sekuboyina, I. Ezhov, A. Unger, A. Zhylka, J. P. Pluim, U. Bauer, and B. H. Menze. "clDice-a Novel Topology-Preserving Loss Function for Tubular Structure Segmentation." In: *Proceedings of the IEEE/CVF Conference on Computer Vision and Pattern Recognition*. 2021, pp. 16560–16569.

[18] D. Ciresan, A. Giusti, L. Gambardella, and J. Schmidhuber. "Deep neural networks segment neuronal membranes in electron microscopy images." In: *Advances in neural information processing systems* 25 (2012).

[19] J. Long, E. Shelhamer, and T. Darrell. "Fully convolutional networks for semantic segmentation." In: *Proceedings of the IEEE conference on computer vision and pattern recognition*. 2015, pp. 3431–3440.

[20] O. Ronneberger et al. "U-net: Convolutional networks for biomedical image segmentation." In: *MICCAI*. Springer. 2015, pp. 234–241.

[21] F. Milletari et al. "V-net: Fully convolutional neural networks for volumetric medical image segmentation." In: *3DV*. IEEE. 2016, pp. 565–571.

[22] Ö. Çiçek and Aothers. "3D U-Net: learning dense volumetric segmentation from sparse annotation." In: *MICCAI*. Springer. 2016, pp. 424–432.

[23] F. Isensee, P. F. Jaeger, S. A. Kohl, J. Petersen, and K. H. Maier-Hein. "nnU-Net: a self-configuring method for deep learning-based biomedical image segmentation." In: *Nature methods* 18.2 (2021), pp. 203–211.

[24] A. L. Maas, A. Y. Hannun, A. Y. Ng, et al. "Rectifier nonlinearities improve neural network acoustic models." In: *Proc. icml*. Vol. 30. 1. Citeseer. 2013, p. 3.

[25] D. E. Rumelhart, P. Smolensky, J. L. McClelland, and G. Hinton. "Sequential thought processes in PDP models." In: *Parallel distributed processing: explorations in the microstructures of cognition* 2 (1986), pp. 3–57.

[26] S. Ruder. "An overview of gradient descent optimization algorithms." In: *arXiv preprint arXiv:1609.04747* (2016).

[27] Y. LeCun, F. J. Huang, and L. Bottou. "Learning methods for generic object recognition with invariance to pose and lighting." In: *Proceedings of the 2004 IEEE Computer Society Conference on Computer Vision and Pattern Recognition, 2004. CVPR 2004.* Vol. 2. IEEE. 2004, pp. II–104.

[28] S. Albawi, T. A. Mohammed, and S. Al-Zawi. "Understanding of a convolutional neural network." In: *2017 international conference on engineering and technology (ICET)*. Ieee. 2017, pp. 1–6.

[29] K. He, X. Zhang, S. Ren, and J. Sun. "Deep residual learning for image recognition." In: *Proceedings of the IEEE conference on computer vision and pattern recognition*. 2016, pp. 770–778.

[30] B. H. Menze, A. Jakab, S. Bauer, J. Kalpathy-Cramer, K. Farahani, J. Kirby, Y. Burren, N. Porz, J. Slotboom, R. Wiest, et al. "The multimodal brain tumor image segmentation benchmark (BRATS)." In: *IEEE transactions on medical imaging* 34.10 (2014), pp. 1993–2024.

[31] P. Bilic, P. F. Christ, E. Vorontsov, G. Chlebus, H. Chen, Q. Dou, C.-W. Fu, X. Han, P.-A. Heng, J. Hesser, et al. "The liver tumor segmentation benchmark (lits)." In: *arXiv preprint arXiv:1901.04056* (2019).

[32] E. Gibson, F. Giganti, Y. Hu, E. Bonmati, S. Bandula, K. Gurusamy, B. Davidson, S. P. Pereira, M. J. Clarkson, and D. C. Barratt. "Automatic multi-organ segmentation on abdominal CT with dense v-networks." In: *IEEE transactions on medical imaging* 37.8 (2018), pp. 1822–1834.

[33] Y. Zhao, H. Li, S. Wan, A. Sekuboyina, X. Hu, G. Tetteh, M. Piraud, and B. Menze. "Knowledge-aided convolutional neural network for small organ segmentation." In: *IEEE journal of biomedical and health informatics* 23.4 (2019), pp. 1363–1373.

[34] A. Sekuboyina, M. E. Husseini, A. Bayat, M. Löffler, H. Liebl, H. Li, G. Tetteh, J. Kukačka, C. Payer, D. Štern, et al. "VerSe: A Vertebrae labelling and segmentation benchmark for multi-detector CT images." In: *Medical image analysis* 73 (2021), p. 102166.

[35] F. Isensee, P. F. Jäger, P. M. Full, P. Vollmuth, and K. H. Maier-Hein. "nnU-net for brain tumor segmentation." In: *International MICCAI Brainlesion Workshop*. Springer. 2020, pp. 118–132.

[36] V. Mnih. "Machine Learning for Aerial Image Labeling." PhD thesis. University of Toronto, 2013.

[37] J. Staal, M. D. Abràmoff, M. Niemeijer, M. A. Viergever, and B. Van Ginneken. "Ridge-based vessel segmentation in color images of the retina." In: *IEEE transactions on medical imaging* 23.4 (2004), pp. 501–509.

[38] J. Funke, F. Tschopp, W. Grisaitis, A. Sheridan, C. Singh, S. Saalfeld, and S. C. Turaga. "Large Scale Image Segmentation with Structured Loss Based Deep Learning for Connectome Reconstruction." In: *IEEE Transactions on Pattern Analysis and Machine Intelligence* 41.7 (2019), pp. 1669–1680.

[39] X. Hu et al. "Topology-preserving deep image segmentation." In: *NeurIPS*. 2019, pp. 5658–5669.

[40] A. Mosinska et al. "Beyond the pixel-wise loss for topology-aware delineation." In: *CVPR*. 2018, pp. 3136–3145.

[41] A. Mosinska, M. Koziński, and P. Fua. "Joint Segmentation and Path Classification of Curvilinear Structures." In: *IEEE Transactions on Pattern Analysis and Machine Intelligence* 42.6 (2019), pp. 1515–1521.

[42] W. Hu, M. Fey, M. Zitnik, Y. Dong, H. Ren, B. Liu, M. Catasta, and J. Leskovec. "Open graph benchmark: Datasets for machine learning on graphs." In: *arXiv preprint arXiv:2005.00687* (2020).

[43] T. N. Kipf and M. Welling. “Semi-supervised classification with graph convolutional networks.” In: *arXiv preprint arXiv:1609.02907* (2016).

[44] A. Bojchevski, O. Shchur, D. Zügner, and S. Günnemann. “Netgan: Generating graphs via random walks.” In: *International Conference on Machine Learning*. PMLR. 2018, pp. 610–619.

[45] D. Zügner, A. Akbarnejad, and S. Günnemann. “Adversarial attacks on neural networks for graph data.” In: *Proceedings of the 24th ACM SIGKDD International Conference on Knowledge Discovery & Data Mining*. 2018, pp. 2847–2856.

[46] F. Chen, Y.-C. Wang, B. Wang, and C.-C. J. Kuo. “Graph representation learning: a survey.” In: *APSIPA Transactions on Signal and Information Processing* 9 (2020).

[47] M. Fey and J. E. Lenssen. “Fast graph representation learning with PyTorch Geometric.” In: *arXiv preprint arXiv:1903.02428* (2019).

[48] J. L. Gross, J. Yellen, and M. Anderson. *Graph theory and its applications*. Chapman and Hall/CRC, 2018.

[49] J. Gilmer, S. S. Schoenholz, P. F. Riley, O. Vinyals, and G. E. Dahl. “Neural message passing for quantum chemistry.” In: *International conference on machine learning*. PMLR. 2017, pp. 1263–1272.

[50] A. Vaswani, N. Shazeer, N. Parmar, J. Uszkoreit, L. Jones, A. N. Gomez, Ł. Kaiser, and I. Polosukhin. “Attention is all you need.” In: *Advances in neural information processing systems* 30 (2017).

[51] P. Veličković, G. Cucurull, A. Casanova, A. Romero, P. Lio, and Y. Bengio. “Graph attention networks.” In: *arXiv preprint arXiv:1710.10903* (2017).

[52] J. Zhang, X. Shi, J. Xie, H. Ma, I. King, and D.-Y. Yeung. “Gaan: Gated attention networks for learning on large and spatiotemporal graphs.” In: *arXiv preprint arXiv:1803.07294* (2018).

[53] C. Kirst, S. Skriabine, A. Vieites-Prado, T. Topilko, P. Bertin, G. Gerschenfeld, F. Verny, P. Topilko, N. Michalski, M. Tessier-Lavigne, et al. “Mapping the fine-scale organization and plasticity of the brain vasculature.” In: *Cell* 180.4 (2020), pp. 780–795.

[54] D. Drees, A. Scherzinger, R. Hägerling, F. Kiefer, and X. Jiang. “Scalable Robust Graph and Feature Extraction for Arbitrary Vessel Networks in Large Volumetric Datasets.” In: *arXiv preprint arXiv:2102.03444* (2021).

[55] A. Obenaus, M. Ng, A. M. Orantes, E. Kinney-Lang, F. Rashid, M. Hamer, R. A. DeFazio, J. Tang, J. H. Zhang, and W. J. Pearce. “Traumatic brain injury results in acute rarefication of the vascular network.” In: *Scientific reports* 7.1 (2017), pp. 1–14.

[56] R. E. Bennett, A. B. Robbins, M. Hu, X. Cao, R. A. Betensky, T. Clark, S. Das, and B. T. Hyman. “Tau induces blood vessel abnormalities and angiogenesis-related gene expression in P301L transgenic mice and human Alzheimer’s disease.” In: *Proceedings of the National Academy of Sciences* 115.6 (2018), E1289–E1298.

[57] K. Völgyi, P. Gulyássy, M. I. Todorov, G. Puska, K. Badics, D. Hlatky, K. A. Kékesi, G. Nyitrai, A. Czurkó, L. Drahos, et al. “Chronic cerebral hypoperfusion induced synaptic proteome changes in the rat cerebral cortex.” In: *Molecular Neurobiology* 55.5 (2018), pp. 4253–4266.

[58] E. Farkas, P. G. Luiten, and F. Bari. “Permanent, bilateral common carotid artery occlusion in the rat: a model for chronic cerebral hypoperfusion-related neurodegenerative diseases.” In: *Brain research reviews* 54.1 (2007), pp. 162–180.

[59] K. Chung and K. Deisseroth. “CLARITY for mapping the nervous system.” In: *Nature methods* 10.6 (2013), pp. 508–513.

[60] N. Renier, Z. Wu, D. J. Simon, J. Yang, P. Ariel, and M. Tessier-Lavigne. “iDISCO: a simple, rapid method to immunolabel large tissue samples for volume imaging.” In: *Cell* 159.4 (2014), pp. 896–910.

[61] B. Yang, J. B. Treweek, R. P. Kulkarni, B. E. Deverman, C.-K. Chen, E. Lubeck, S. Shah, L. Cai, and V. Gradinaru. “Single-cell phenotyping within transparent intact tissue through whole-body clearing.” In: *Cell* 158.4 (2014), pp. 945–958.

[62] R. Cai et al. *Panoptic imaging of transparent mice reveals whole-body neuronal projections and skull–meninges connections*. Tech. rep. Nature Publishing Group, 2018.

[63] M. Schneider et al. “Tissue metabolism driven arterial tree generation.” In: *Med Image Anal.* 16.7 (2012), pp. 1397–1414.

[64] M. Zaccaria, F. Di Tommaso, A. Brancaccio, P. Paggi, and T. Petrucci. “Dystroglycan distribution in adult mouse brain: a light and electron microscopy study.” In: *Neuroscience* 104.2 (2001), pp. 311–324.

[65] S. P. Amato, F. Pan, J. Schwartz, and T. M. Ragan. “Whole brain imaging with serial two-photon tomography.” In: *Frontiers in neuroanatomy* 10 (2016), p. 31.

[66] E. Calabrese, A. Badea, G. Cofer, Y. Qi, and G. A. Johnson. “A diffusion MRI tractography connectome of the mouse brain and comparison with neuronal tracer data.” In: *Cerebral cortex* 25.11 (2015), pp. 4628–4637.

[67] T. Li, C. J. Liu, and T. Akkin. “Contrast-enhanced serial optical coherence scanner with deep learning network reveals vasculature and white matter organization of mouse brain.” In: *Neurophotonics* 6.3 (2019), p. 035004.

[68] E. L. Dyer, W. G. Roncal, J. A. Prasad, H. L. Fernandes, D. Gürsoy, V. De Andrade, K. Fezzaa, X. Xiao, J. T. Vogelstein, C. Jacobsen, et al. “Quantifying mesoscale neuroanatomy using X-ray microtomography.” In: *Eneuro* 4.5 (2017).

[69] A. Miettinen, A. Zippo, A. Patera, A. Bonnin, S. Shahmoradian, G. Biella, and M. Stampanoni. “Micrometer-resolution reconstruction and analysis of whole mouse brain vasculature by synchrotron-based phase-contrast tomographic microscopy.” In: *bioRxiv* (2021).

[70] J. Reichold, M. Stampanoni, A. L. Keller, A. Buck, P. Jenny, and B. Weber. “Vascular graph model to simulate the cerebral blood flow in realistic vascular networks.” In: *Journal of Cerebral Blood Flow & Metabolism* 29.8 (2009), pp. 1429–1443.

[71] J. Klicpera, J. Groß, and S. Günnemann. “Directional Message Passing for Molecular Graphs.” In: *International Conference on Learning Representations*. 2019.

[72] N. Carion, F. Massa, G. Synnaeve, N. Usunier, A. Kirillov, and S. Zagoruyko. “End-to-end object detection with transformers.” In: *European conference on computer vision*. Springer. 2020, pp. 213–229.

[73] Y. Liu, L. Wang, M. Liu, Y. Lin, X. Zhang, B. Oztekin, and S. Ji. “Spherical message passing for 3d molecular graphs.” In: *International Conference on Learning Representations*. 2021.

[74] J. Klicpera, F. Becker, and S. Günnemann. “Gemnet: Universal directional graph neural networks for molecules.” In: *arXiv preprint arXiv:2106.08903* (2021).

[75] J. Jumper, R. Evans, A. Pritzel, T. Green, M. Figurnov, O. Ronneberger, K. Tunyasuvunakool, R. Bates, A. Žıdek, A. Potapenko, et al. “Highly accurate protein structure prediction with AlphaFold.” In: *Nature* (2021), pp. 1–11.

[76] K. Tunyasuvunakool, J. Adler, Z. Wu, T. Green, M. Zielinski, A. Žıdek, A. Bridgland, A. Cowie, C. Meyer, A. Laydon, et al. “Highly accurate protein structure prediction for the human proteome.” In: *Nature* 596.7873 (2021), pp. 590–596.

[77] S. Vashishth, S. Sanyal, V. Nitin, and P. Talukdar. “Composition-based multi-relational graph convolutional networks.” In: *arXiv preprint arXiv:1911.03082* (2019).

[78] M. Schlichtkrull, T. N. Kipf, P. Bloem, R. Van Den Berg, I. Titov, and M. Welling. “Modeling relational data with graph convolutional networks.” In: *European semantic web conference*. Springer. 2018, pp. 593–607.

[79] L. Hetzel, D. S. Fischer, S. Günnemann, and F. J. Theis. “Graph representation learning for single-cell biology.” In: *Current Opinion in Systems Biology* 28 (2021), p. 100347.

[80] D. Buterez, I. Bica, I. Tariq, H. Andrés-Terré, and P. Liò. “CellVGAE: an unsupervised scRNA-seq analysis workflow with graph attention networks.” In: *Bioinformatics* 38.5 (2022), pp. 1277–1286.

Transfer Learning from Synthetic Data Reduces Need for Labels to Segment Brain Vasculature and Neural Pathways in 3D

Johannes Christian Paetzold, **Oliver Schoppe**, Rami Al-Maskari, Giles Tetteh, Velizar Efremov, Mihail Ivilinov Todorov, Ruiyao Cai, Hongcheng Mai, Zhouyi Rong, Ali Ertürk & Bjoern Menze

Conference: Medical Imaging with Deep Learning 2019 (MIDL), July 2019

Synopsis: Novel microscopic techniques yield high-resolution volumetric scans of complex anatomical structures such as the blood vasculature or the nervous system. Here, we show how transfer learning and synthetic data generation can be used to train deep neural networks to segment these structures successfully in the absence of or with very limited training data.

Contributions of thesis author: algorithm design and implementation, deep learning and feature extraction, other computational experiments, and leading role in composition and writing of the manuscript.

Transfer learning from synthetic data reduces need for labels to segment brain vasculature and neural pathways in 3D

Johannes C. Paetzold[*1,†], **Oliver Schoppe**[*1,†], **Rami Al-Maskari**[1], **Giles Tetteh**[1], **Velizar Efremov**[1], **Mihail I. Todorov**[2], **Ruiyao Cai**[2], **Hongcheng Mai**[2], **Zhouyi Rong**[2], **Ali Ertuerk**[2], **Bjoern H. Menze**[1]
[1] *TranslaTUM and Department of Computer Science, Technical University of Munich, Germany*
[2] *Institute for Stroke and Dementia Research, Ludwig Maximilian University of Munich, Germany*
[†] *Correspondence to johannes.paetzold@tum.de and oliver.schoppe@tum.de*

Abstract

Novel microscopic techniques yield high-resolution volumetric scans of complex anatomical structures such as the blood vasculature or the nervous system. Here, we show how transfer learning and synthetic data generation can be used to train deep neural networks to segment these structures successfully in the absence of or with very limited training data.

Keywords: Deep learning, transfer learning, synthetic data, vasculature, neural pathways.

1. Introduction

Recent advances in tissue-clearing (Ertürk et al., 2012; Chung and Deisseroth, 2013) combined with 3D light-sheet microscopy (*3D LSM*) overcome previous imaging limitations: they enable volumetric acquisition at cellular resolution of entire organisms (Cai et al., 2018; Pan et al., 2019; Stefaniuk et al., 2016; Mano et al., 2018). This yields unprecedented insight into the micro-anatomy at the macro-scale, e.g., to study highly connected structures like the brain vasculature or the peripheral nervous system. Differences in these structures have been associated with a wide range of disorders (Joutel et al., 2010; Li et al., 2010). Thus, segmentation and characterization of these anatomical structures is crucial to study causes and effects of such pathologies. However, manual segmentation of complex structures is very time-consuming, especially in high-resolution volumetric scans. While this motivates the need for deep learning it also implies a high cost of labeling. Here, we substantially reduce the need for manually labeled training data using transfer learning, an approach gaining attention (Van Opbroek et al., 2015; Khan et al., 2019). In short, we show that training deep networks on synthetic data is already sufficient to learn the basic underlying task across different anatomical structures, species, and imaging modalities.

2. Methods

Here, we present results from three widely different applications: human brain vessels (MRI), mouse brain vessels and the mouse peripheral nervous system (both *3D LSM*). The same network was trained either on a small labeled set from the respective application

---

[*] Joint first authors

(”real data”), on synthetically generated data, or on a combination of both. The synthetic data used is identical for all three applications. We chose DeepVesselNet as our architecture; the schedule for pre-training on synthetic data and refinement on real data match the methods of (Tetteh et al., 2018). The methods for generation of synthetic training data is described in (Schneider et al., 2012). MRI scans from human brain vasculature are taken from (Tetteh et al., 2018) (voxel size: $300\mu m$ x $300\mu m$ x $600\mu m$). Volumetric scans of the brain vasculature (voxel size: $(3\mu m)^3$) and the peripheral nervous system (voxel size: $(10\mu m)^3$) were obtained using DISCO tissue clearing and fluorescent light-sheet microscopy as described in (Cai et al., 2018). Representative 2D cross-sections of the synthetic data and segmentations of all three applications are shown in Figure 1.

3. Results

Transfer learning from synthetic data (Table 1, Part 1). For segmenting the human vasculature from MRI scans, training the net on the synthetic data alone yields very good results, 81% in F1-score (note: the synthetic data set had been designed for this application). Training on the real data for this application yields a higher F1-score of 86%. The best result (87%), however, is achieved by a combination of both: pre-training on synthetic data and fine-tuning on real data. Interestingly, the network also converges about 50% faster in this case (data not shown). Motivated by this observation, we repeated this experiment for *3D LSM* scans of the mouse brain vasculature. Again, the same pattern can be observed and the combination of synthetic with real data (F1-score of 76%) outperforms synthetic data (71%) or real data alone (73%). Taking the approach yet further, we applied the approach to *3D LSM* full body scans of the peripheral nervous system of a mouse. While training on synthetic data alone was not very successful (16%) as compared to real data (49%), the gain from combining both was almost completely additive (64%).

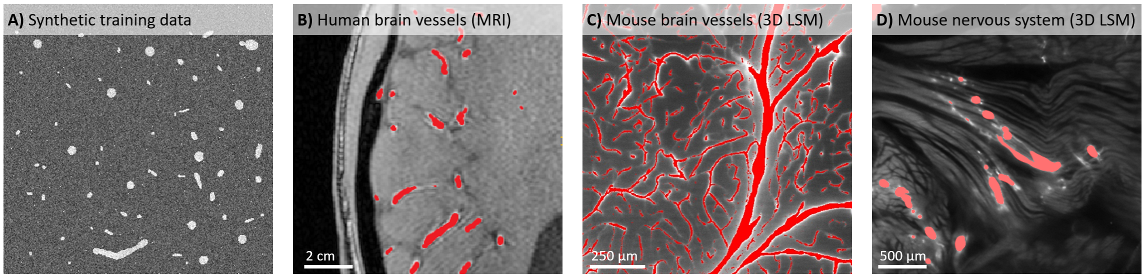

Figure 1: A) Synthetic training data was designed to resemble vasculature of human brain in MRI scans. B-D) Predicted segmentations of 3 different applications: MRI scans of human brain vasculature (B), *3D LSM* of mouse brain vasculature (C), and peripheral nervous system (D; shown here: innervated muscle fibres)

Transfer learning across domains (Table 1, Part 2). Here, we trained the network on a combination of synthetic data and the real data from a given application and then predicted on data from another application. When predicting on human vasculatures from MRI scans, the refinement step on real data from another application after pre-training on synthetic data leads to worse results (left column: 43% and 36%) compared to training on synthetic data alone (81%, see Part 1). However, when training the model on synthetic data and real data of human vessels in MRI scans (first row of Part 2), the performance on *3D LSM* scans of mouse brain vessels (72%) or the mouse peripheral nervous system (49%) is about as good as when trained on the respective real data alone. Also, while the domain transfer from mouse vasculature to mouse nervous system only yields mediocre results (35%), it works well the other way around: refining a model trained on synthetic data with real data from the nervous system to segment brain vessels almost works as well (75%) as if it had been refined on data within the same domain (76%, see Part 1).

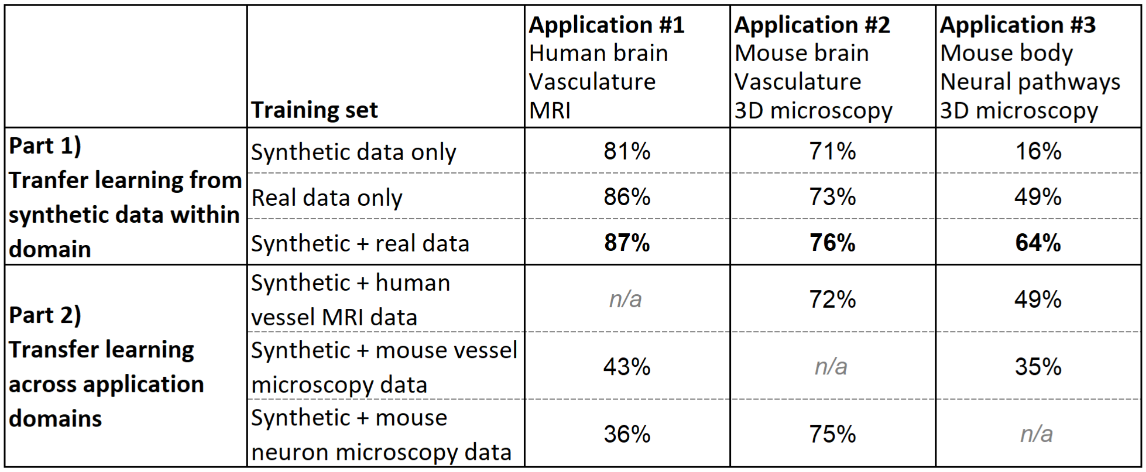

	Training set	**Application #1** Human brain Vasculature MRI	**Application #2** Mouse brain Vasculature 3D microscopy	**Application #3** Mouse body Neural pathways 3D microscopy
Part 1) **Tranfer learning from synthetic data within domain**	Synthetic data only	81%	71%	16%
	Real data only	86%	73%	49%
	Synthetic + real data	**87%**	**76%**	**64%**
Part 2) **Transfer learning across application domains**	Synthetic + human vessel MRI data	*n/a*	72%	49%
	Synthetic + mouse vessel microscopy data	43%	*n/a*	35%
	Synthetic + mouse neuron microscopy data	36%	75%	*n/a*

Table 1: Quality of predicted segmentations (F1-score) for 3 different applications

4. Discussion

Our results demonstrate how pre-training on synthetically generated data can accelerate model convergence and boost the overall segmentation performance. For a given desired performance, this thus means a reduced need for manually labeled training data, which is very expensive for complex structures in 3D scans. Importantly, a single synthetic data set that was originally designed to represent human vessels also works well for applications from different species, anatomical structures, and imaging modalities. This suggests that the features learned from the synthetic data are of general use for the abstract segmentation tasks, highlighting the generalizability of the approach. Thus, the expensively labeled data for a given application does not have to be used to learn a basic task but rather can be preserved for refining the pre-trained model to the specifics of the application (such as contrast, noise, background structures). Interestingly, this approach may also be of use in cases where no training data is available at all. For instance, we could show that a model trained on synthetic data and real data from another application can match the performance of a model trained from scratch on real data from the application of interest. Together, these results highlight the importance of transfer learning towards the goal of resolving a key bottleneck in adoption of deep learning: the high cost of data annotation.

Acknowledgments

This work was supported the German Federal Ministry of Education and Research via the Software Campus initiative (to O.S.), the Vascular Dementia Research Foundation, Synergy Excellence Cluster Munich (SyNergy), ERA-Net Neuron (01EW1501A to A.E.). Furthermore, NVIDIA supported this work with a Titan XP GPU via the GPU Grant Program.

References

Ruiyao Cai, Chenchen Pan, Alireza Ghasemigharagoz, Mihail Ivilinov Todorov, Benjamin Förstera, Shan Zhao, Harsharan S Bhatia, Arnaldo Parra-Damas, Leander Mrowka, Delphine Theodorou, et al. Panoptic imaging of transparent mice reveals whole-body neuronal projections and skull–meninges connections. Technical report, Nature Publishing Group, 2018.

Kwanghun Chung and Karl Deisseroth. Clarity for mapping the nervous system. *Nature methods*, 10(6):508, 2013.

Ali Ertürk, Klaus Becker, Nina Jährling, Christoph P Mauch, Caroline D Hojer, Jackson G Egen, Farida Hellal, Frank Bradke, Morgan Sheng, and Hans-Ulrich Dodt. Three-dimensional imaging of solvent-cleared organs using 3disco. *Nature protocols*, 7(11):1983, 2012.

Anne Joutel, Marie Monet-Leprêtre, Claudia Gosele, Céline Baron-Menguy, Annette Hammes, Sabine Schmidt, Barbara Lemaire-Carrette, Valérie Domenga, Andreas Schedl, Pierre Lacombe, et al. Cerebrovascular dysfunction and microcirculation rarefaction precede white matter lesions in a mouse genetic model of cerebral ischemic small vessel disease. *The Journal of clinical investigation*, 120(2):433–445, 2010.

SanaUllah Khan, Naveed Islam, Zahoor Jan, Ikram Ud Din, and Joel JP C Rodrigues. A novel deep learning based framework for the detection and classification of breast cancer using transfer learning. *Pattern Recognition Letters*, 2019.

Weiguo Li, Roshini Prakash, Aisha I Kelly-Cobbs, Safia Ogbi, Anna Kozak, Azza B El-Remessy, Derek A Schreihofer, Susan C Fagan, and Adviye Ergul. Adaptive cerebral neovascularization in a model of type 2 diabetes: relevance to focal cerebral ischemia. *Diabetes*, 59(1):228–235, 2010.

Tomoyuki Mano, Alexandre Albanese, Hans-Ulrich Dodt, Ali Erturk, Viviana Gradinaru, Jennifer B Treweek, Atsushi Miyawaki, Kwanghun Chung, and Hiroki R Ueda. Whole-brain analysis of cells and circuits by tissue clearing and light-sheet microscopy. *Journal of Neuroscience*, 38(44):9330–9337, 2018.

Chenchen Pan, Oliver Schoppe, Arnaldo Parra-Damas, Ruiyao Cai, Mihail Ivilinov Todorov, Gabor Gondi, Bettina von Neubeck, Alireza Ghasemi, Madita Alice Reimer, Javier Coronel, et al. Deep learning reveals cancer metastasis and therapeutic antibody targeting in whole body. *bioRxiv*, page 541862, 2019.

Matthias Schneider, Johannes Reichold, Bruno Weber, Gábor Székely, and Sven Hirsch. Tissue metabolism driven arterial tree generation. *Medical image analysis*, 16(7):1397–1414, 2012.

Marzena Stefaniuk, Emilio J Gualda, Monika Pawlowska, Diana Legutko, Paweł Matryba, Paulina Koza, Witold Konopka, Dorota Owczarek, Marcin Wawrzyniak, Pablo Loza-Alvarez, et al. Light-sheet microscopy imaging of a whole cleared rat brain with thy1-gfp transgene. *Scientific reports*, 6:28209, 2016.

Giles Tetteh, Velizar Efremov, Nils D Forkert, Matthias Schneider, Jan Kirschke, Bruno Weber, Claus Zimmer, Marie Piraud, and Bjoern H Menze. Deepvesselnet: Vessel segmentation, centerline prediction, and bifurcation detection in 3-d angiographic volumes. *arXiv preprint arXiv:1803.09340*, 2018.

Annegreet Van Opbroek, M Arfan Ikram, Meike W Vernooij, and Marleen De Bruijne. Transfer learning improves supervised image segmentation across imaging protocols. *IEEE transactions on medical imaging*, 34(5):1018–1030, 2015.

Supplementary Material: Machine Learning Analysis of Whole Mouse Brain Vasculature

nature methods

SUPPLEMENTARY INFORMATION

https://doi.org/10.1038/s41592-020-0792-1

In the format provided by the authors and unedited.

Machine learning analysis of whole mouse brain vasculature

Mihail Ivilinov Todorov[1,2,3,10], **Johannes Christian Paetzold**[4,5,6,10], **Oliver Schoppe**[4,5], **Giles Tetteh**[4], **Suprosanna Shit**[4,5,6], **Velizar Efremov**[4,7], **Katalin Todorov-Völgyi**[2], **Marco Düring**[2,8], **Martin Dichgans**[2,8,9], **Marie Piraud**[4], **Bjoern Menze**[4,5,6,11] ✉ and **Ali Ertürk**[1,2,8,11] ✉

---

[1]Institute for Tissue Engineering and Regenerative Medicine (iTERM), Helmholtz Zentrum München, Neuherberg, Germany. [2]Institute for Stroke and Dementia Research (ISD), Ludwig-Maximilians-Universität (LMU), Munich, Germany. [3]Graduate School of Neuroscience (GSN), Munich, Germany. [4]Department of Computer Science, Technical University of Munich (TUM), Munich, Germany. [5]Center for Translational Cancer Research of the TUM (TranslaTUM), Munich, Germany. [6]Munich School of Bioengineering, Technical University of Munich (TUM), Munich, Germany. [7]Institute of Pharmacology and Toxicology, University of Zurich (UZH), Zurich, Switzerland. [8]Munich Cluster for Systems Neurology (SyNergy), Munich, Germany. [9]German Center for Neurodegenerative Diseases (DZNE), Munich, Germany. [10]These authors contributed equally: Mihail Ivilinov Todorov, Johannes Christian Paetzold. [11]These authors jointly supervised this work: Bjoern Menze, Ali Ertürk. ✉e-mail: bjoern.menze@tum.de; erturk@helmholtz-muenchen.de

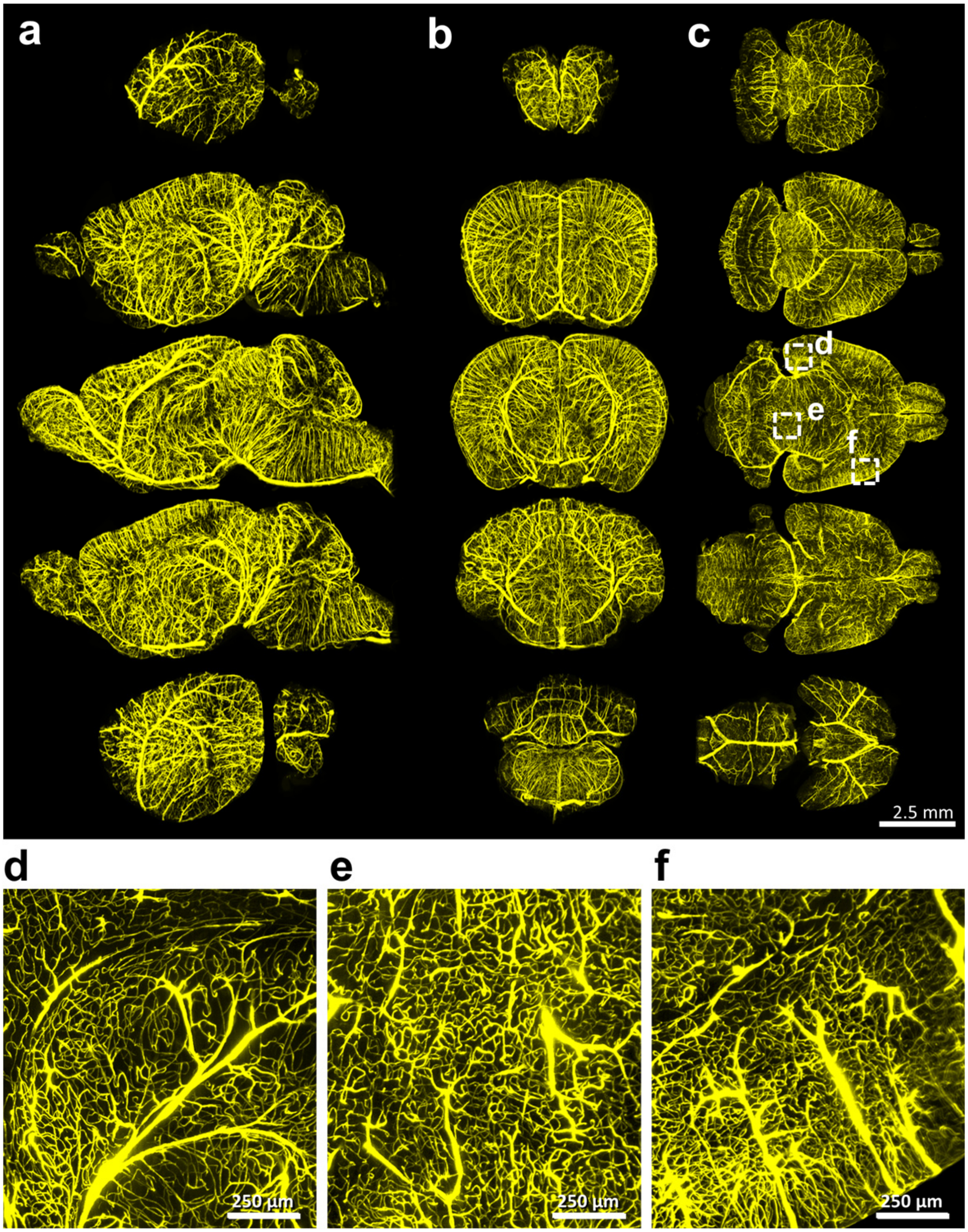

Supplementary Figure 1
Vasculature of a CD1 mouse, stained with WGA and EB.

a, Sagittal maximum intensity projections. **b,** Coronal maximum intensity projections. **c,** Axial maximum projections. **d-f**, Close-ups where capillary level staining is evident. The experiment was performed 9 times with similar results.

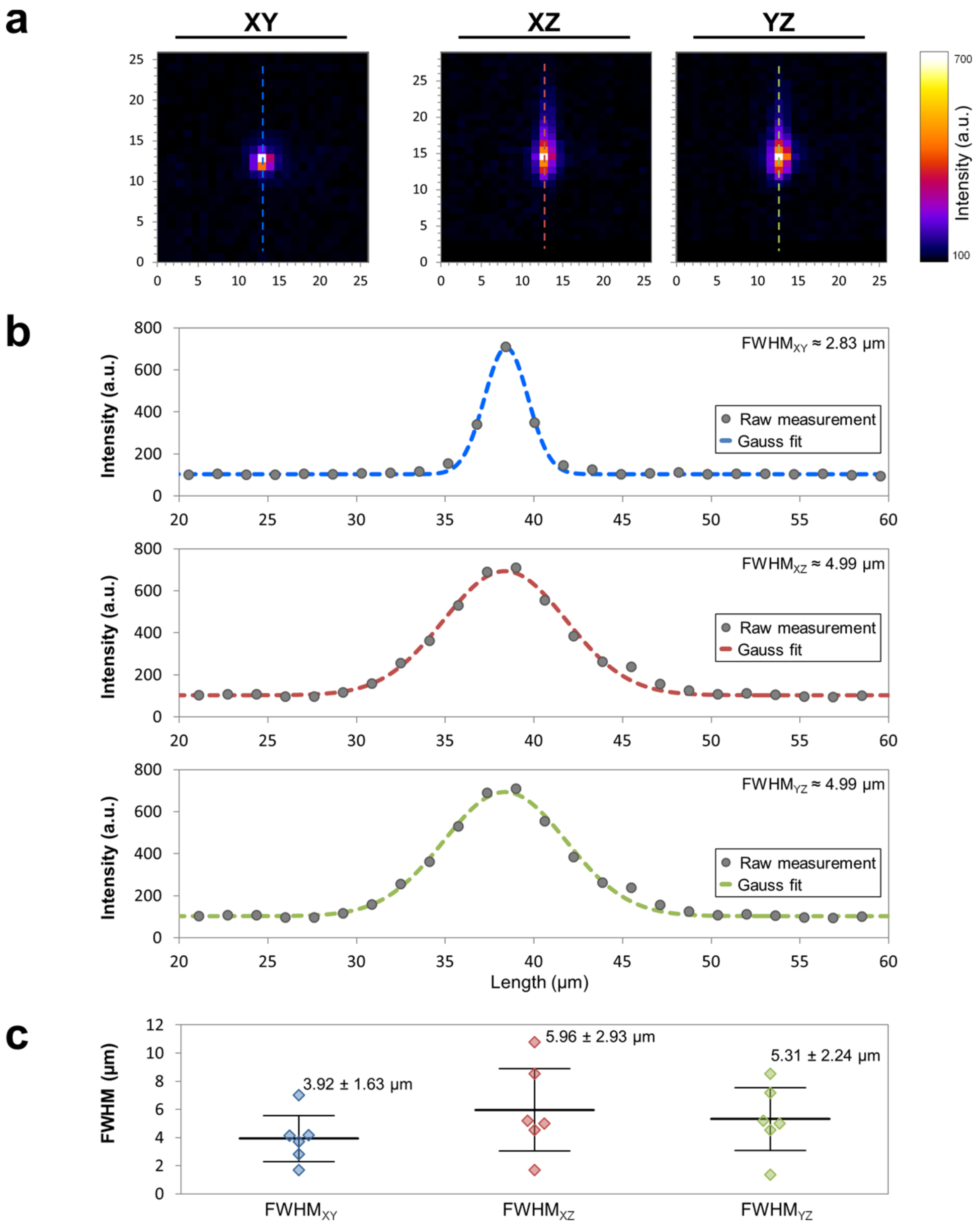

Supplementary Figure 2
Experimental measurement of the point spread function (PSF) of the LaVision light-sheet Ultramicroscope II.

a, Red fluorescent beads (diameter 0.1 µm) were embedded in 1% agarose gel and cleared using 3DISCO. The beads were then imaged in BABB medium (RI = 1.56) using 4× objective lens (Olympus XLFLUOR 340), at 580/25 nm excitation and with a 625/30 nm emission filter by sampling at 1.625 × 1.625 × 1 µm. **b,** Full width half maximum (FWHM) measure derived from the Gaussian fit to the intensity profile, along the indicated cross-sections in the center of the diffraction pattern (a) of an exemplary bead. **c,** Quantification of the PSF distribution (n = 6) derived from the Gaussian fittings. All data values are given as mean ± SEM.

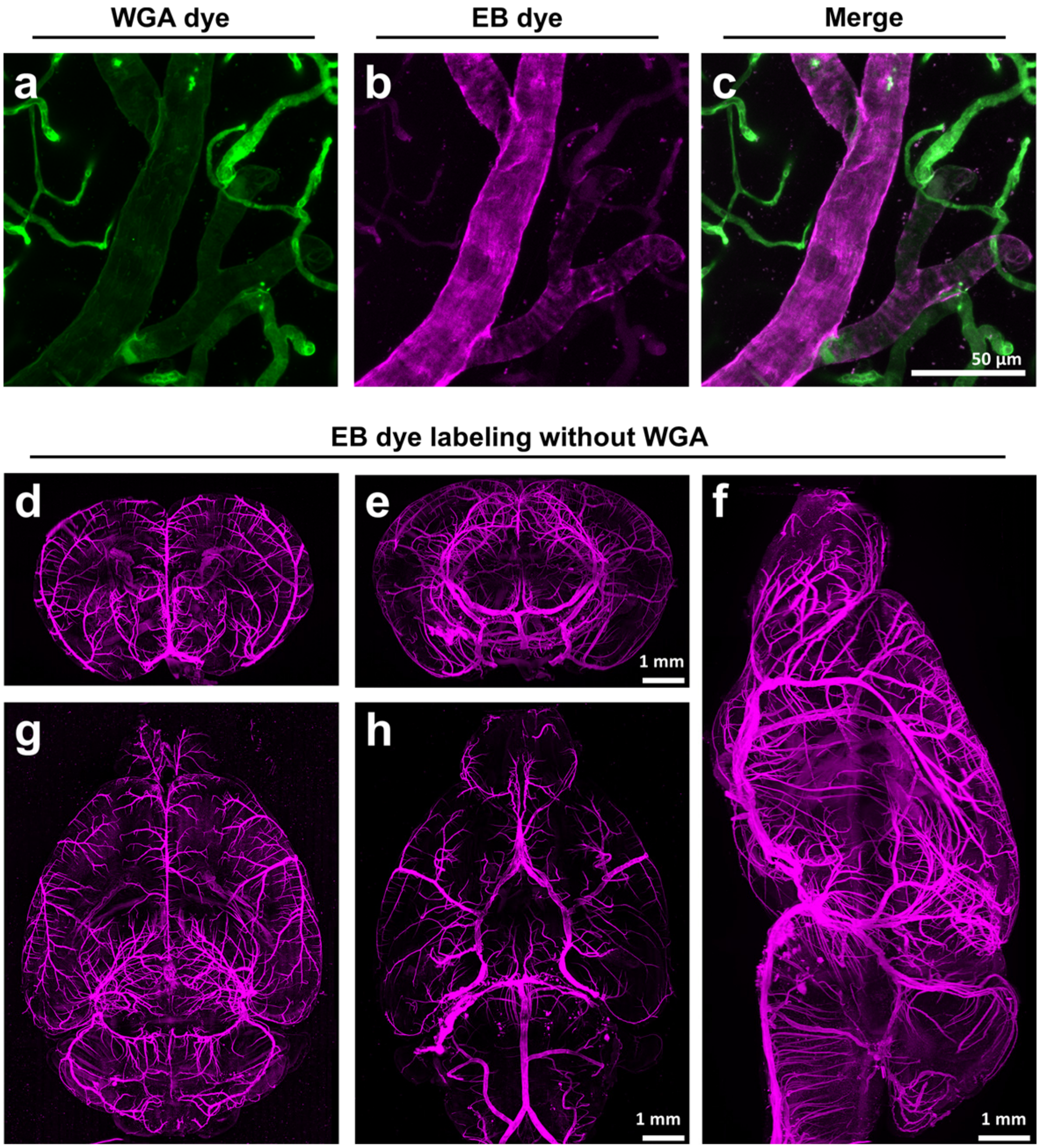

Supplementary Figure 3

Validation of complimentary staining of the neurovasculature.
a,b, Maximum intensity projection of confocal microscopy imaging of WGA and EB signal respectively. **c,** Merging of the two signals. **d-h,** Maximum intensity projections of the light-sheet microscopy imaging of a representative C57BL/6J specimen stained with EB, showing the major vascular segments in different planes. The experiment was performed 3 times with similar results.

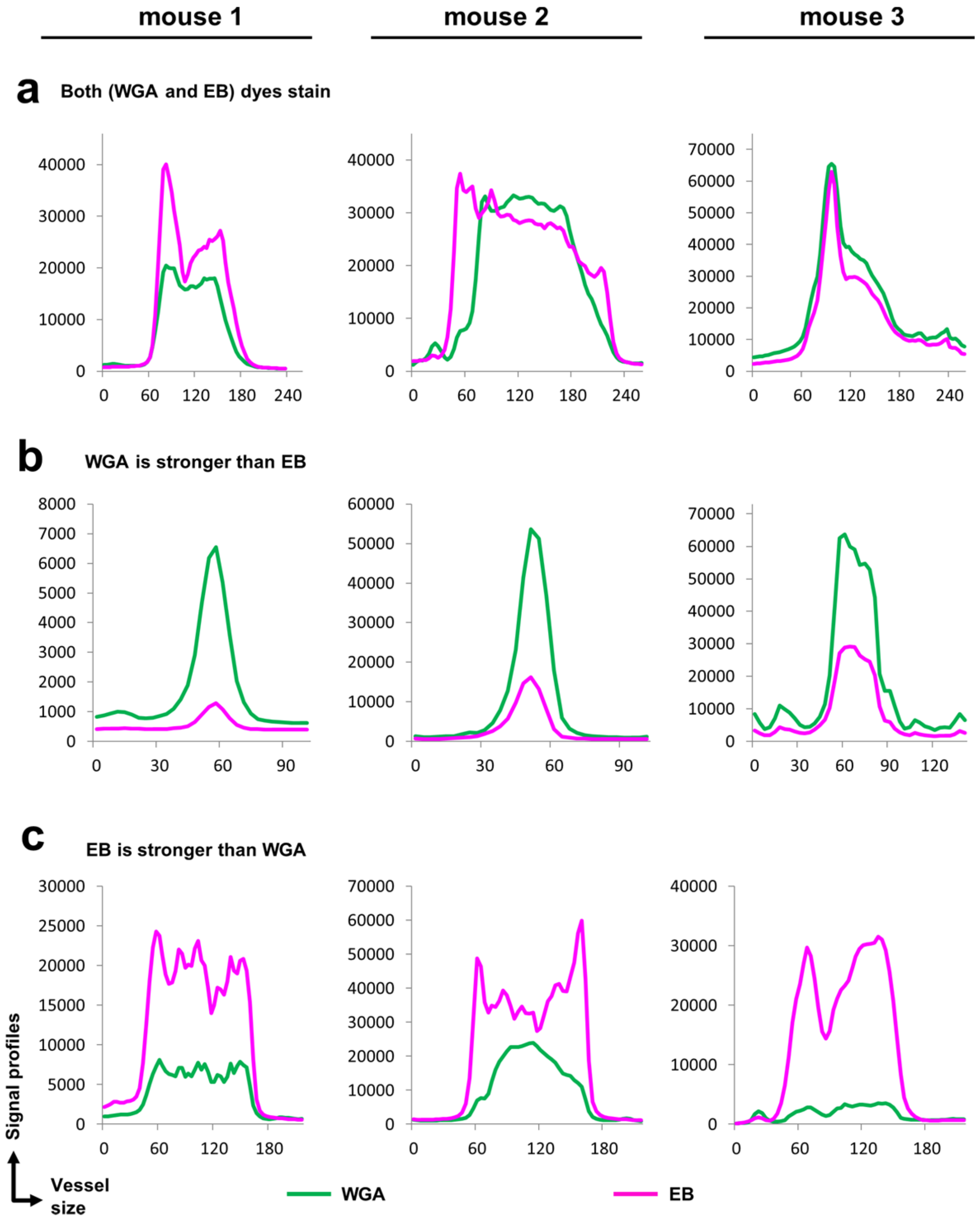

Supplementary Figure 4

Raw signal intensity distribution along line profiles across stained vessels for three animals.
Fluorescence signal profiles for WGA and EB plotted based on vessel size. Data are separated based on WGA and EB signal intensity: a) comparable WGA and EB signal intensity, b) Signal intensity is stronger for WGA than for EB, c) Signal intensity is stronger for EB than for WGA.

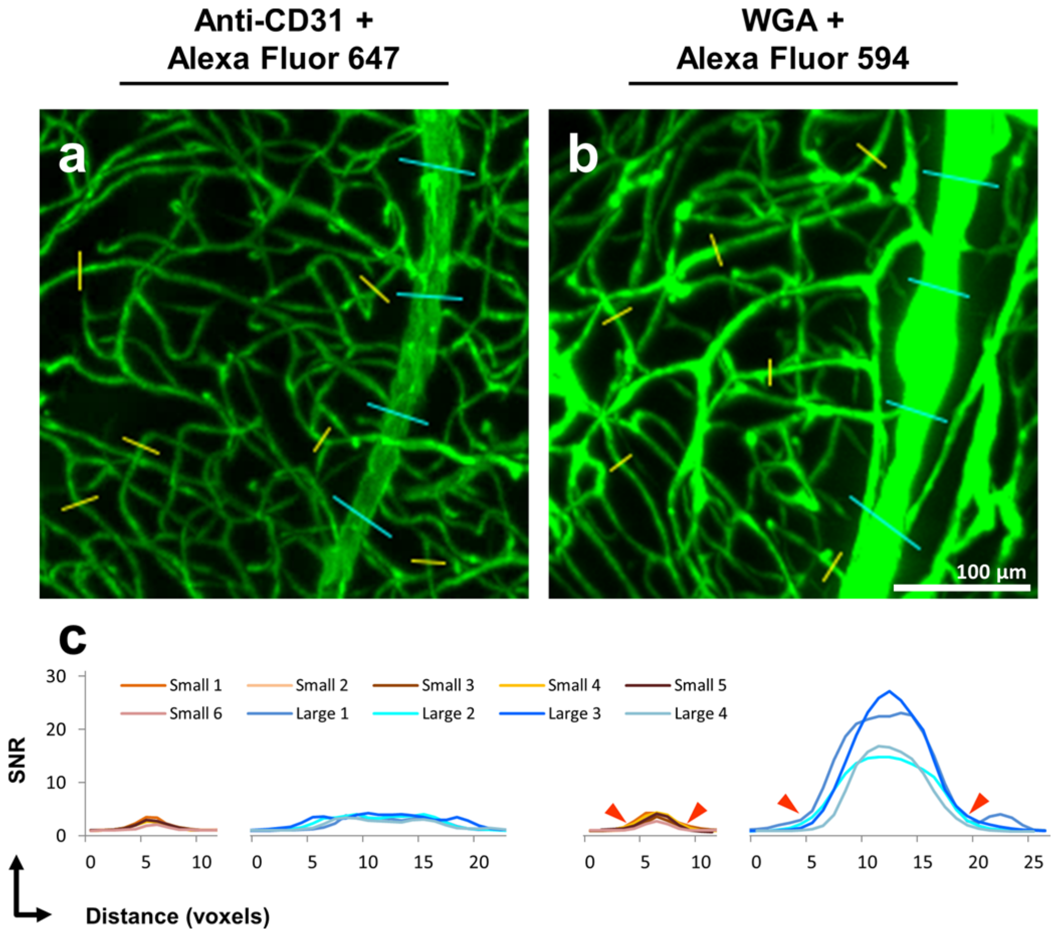

Supplementary Figure 5

Comparison of the signal strength of anti-CD31 and lectin dyes.
a-b, Axial maximum intensity projection of 150 µm thick tissue, stained as indicated. **c,** SNR quantifications on the line profiles indicated in (a) and (b) with warm and cold colored lines for small and large sized segments, respectively. The red arrowheads indicate where the signal of the vasculature gets higher. The experiments were performed on one mouse per condition.

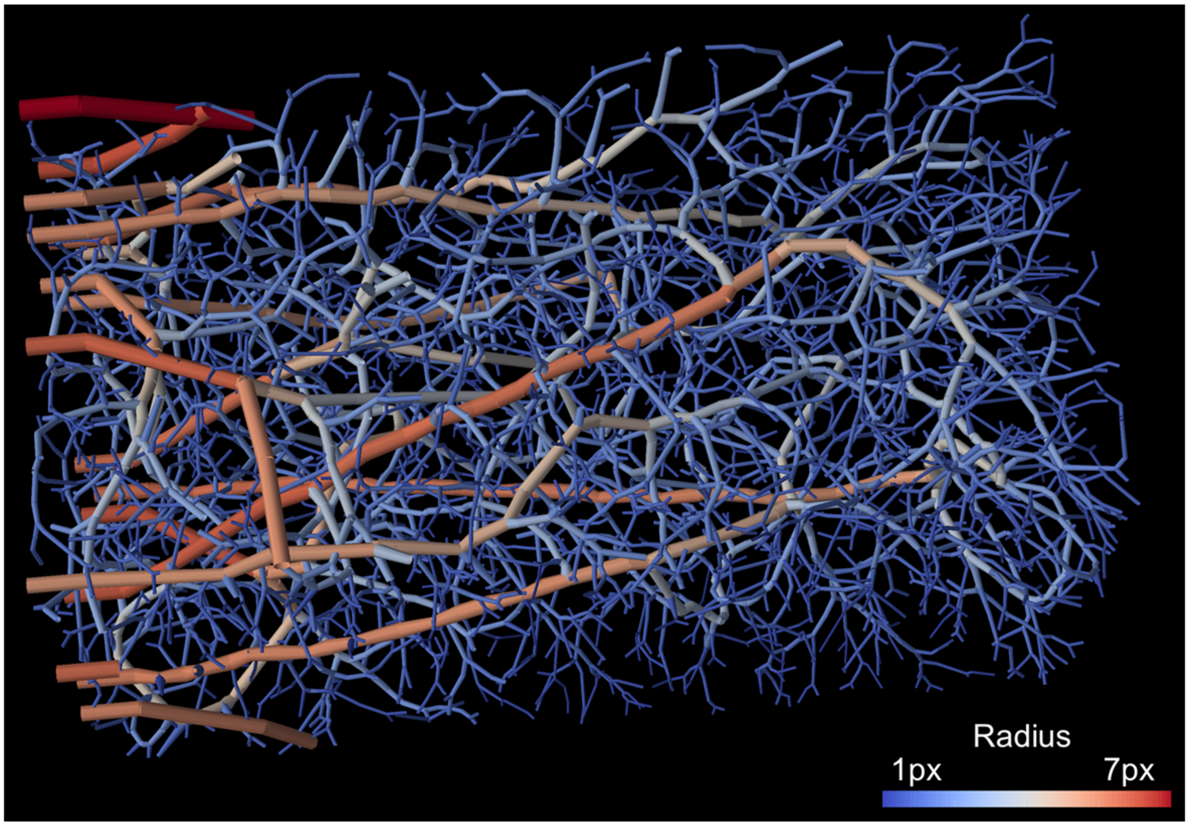

Supplementary Figure 6

Demonstration of the synthetic data used for VesSAP.
3D visualization including radius information in pixels (px) for one exemplary volume of synthetic data, which was used for pre-training our model in our transfer learning approach.

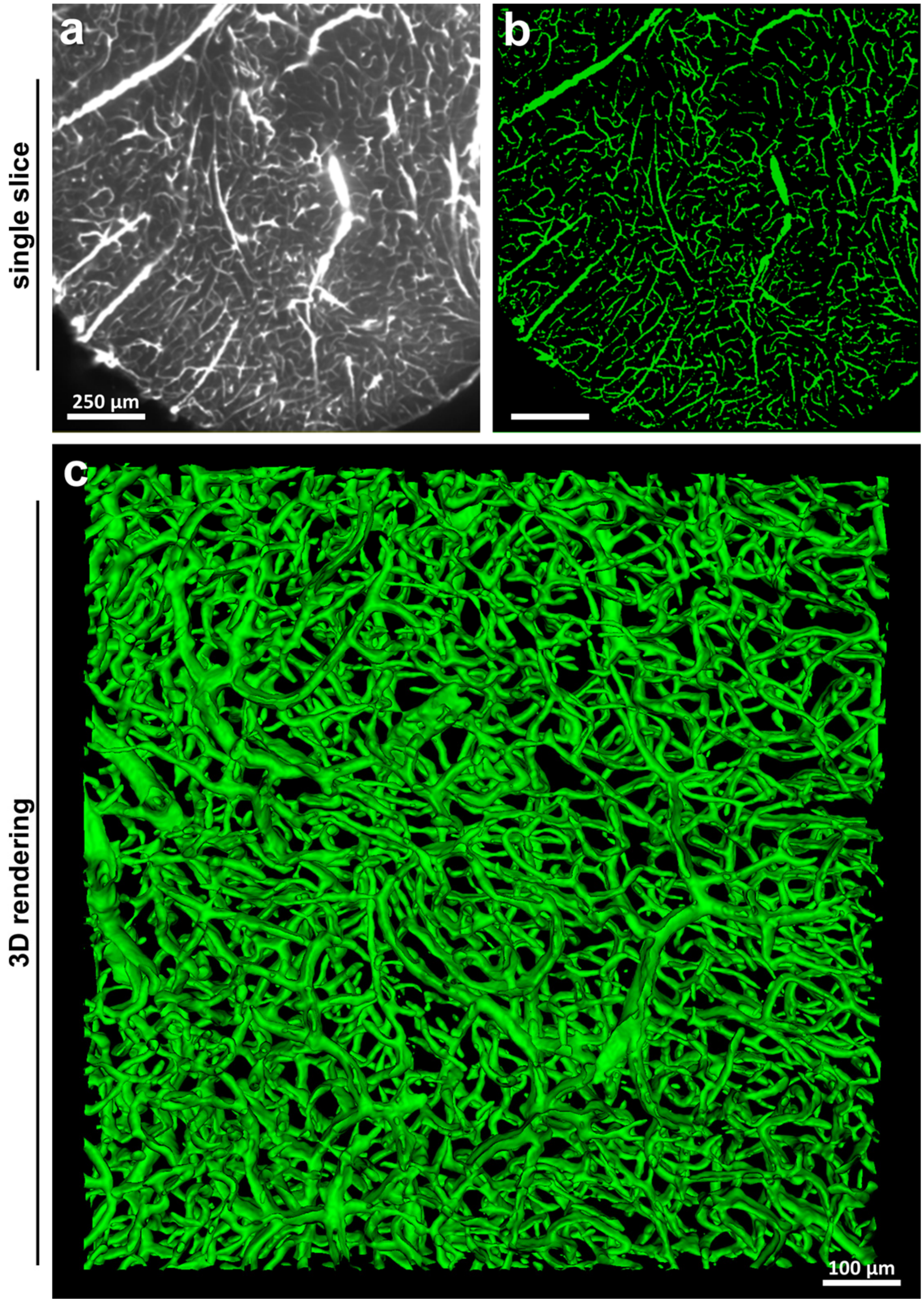

Supplementary Figure 7

Details of the segmentation quality by VesSAP.
a,b, Side by side slices of the raw WGA channel image (a) and the segmentation (b). **c,** 3D rendering of a small brain volume. The experiment was performed on 9 different mice with similar results.

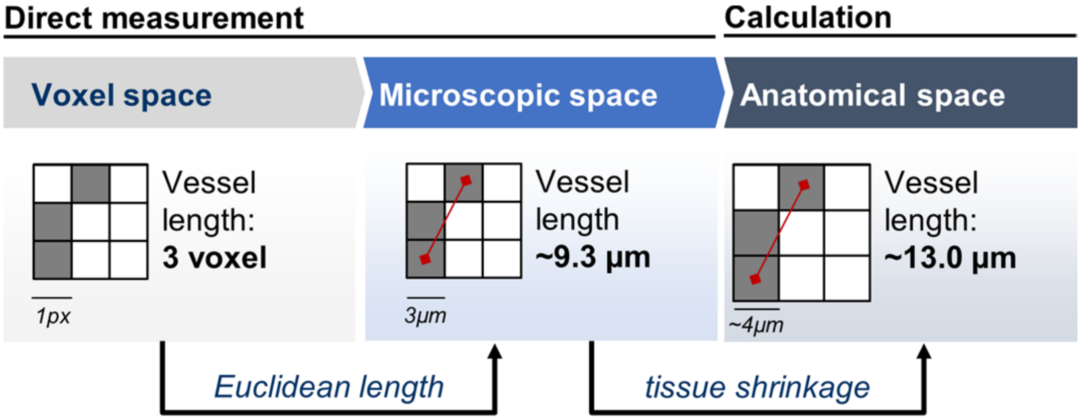

Supplementary figure 8

Three spaces of reported features.
Visualization of the three distinct spaces, in which we report the extracted features. The steps to account for the Euclidean length and the tissue shrinkage are visualized with an exemplary calculation of the vessel length of three vessel pixels in a 2D plane.

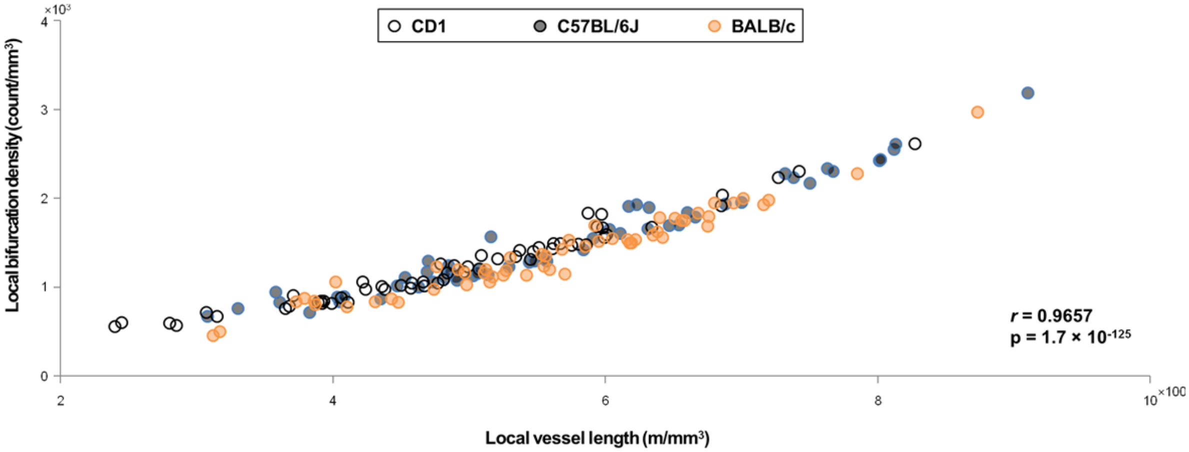

Supplementary Figure 9

Regression analysis of the neurovasculature in mouse strains.
Scatter plot of the local vessel length against the local bifurcation density (Pearson's *r* = 0.9657; p = 1.7 × 10^{-125}). Each point represents the mean of three animals per strain.

Cluster	All regions in the cluster	Name of cluster
FRP	FRP, FRP1, FRP2/3, FRP5, FRP6a, FRP6b	Frontal pole
MO	MO, MO1, MO2/3, MO5, MO6a, MO6b, MOp, MOp1, MOp2/3, MOp5, MOp6a, MOp6b, MOs, MOs1, MOs2/3, MOs5, MOs6a, MOs6b	Somatomotor areas
SS	SS, SS1, SS2/3, SS4, SS5, SS6a, SS6b, SSp, SSp1, SSp2/3, SSp4, SSp5, SSp6a, SSp6b, SSp-bfd, SSp-bfd1, SSp-bfd2/3, SSp-bfd4, SSp-bfd5, SSp-bfd6a, SSp-bfd6b, SSp-ll, SSp-ll1, SSp-ll2/3, SSp-ll4, SSp-ll5, SSp-ll6a, SSp-ll6b, SSp-m, SSp-m1, SSp-m2/3, SSp-m4, SSp-m5, SSp-m6a, SSp-m6b, SSp-n, SSp-n1, SSp-n2/3, SSp-n4, SSp-n5, SSp-n6a, SSp-n6b, SSp-tr, SSp-tr1, SSp-tr2/3, SSp-tr4, SSp-tr5, SSp-tr6a, SSp-tr6b, SSp-ul, SSp-ul1, SSp-ul2/3, SSp-ul4, SSp-ul5, SSp-ul6a, SSp-ul6b, SSp-un, SSp-un1, SSp-un2/3, SSp-un4, SSp-un5, SSp-un6a, SSp-un6b, SSs, SSs1, SSs2/3, SSs4, SSs5, SSs6a, SSs6b, VISrll, VISrll1, VISrll2/3, VISrll4, VISrll5, VISrll6a, VISrll6b	Somatosensory areas
GU	GU, GU1, GU2/3, GU4, GU5, GU6a, GU6b	Gustatory areas
VISC	VISC, VISC1, VISC2/3, VISC4, VISC5, VISC6a, VISC6b	Visceral area
AUD	AUD, AUDd, AUDd1, AUDd2/3, AUDd4, AUDd5, AUDd6a, AUDd6b, AUDp, AUDp1, AUDp2/3, AUDp4, AUDp5, AUDp6a, AUDp6b, AUDpo, AUDpo1, AUDpo2/3, AUDpo4, AUDpo5, AUDpo6a, AUDpo6b, AUDv, AUDv1, AUDv2/3, AUDv4, AUDv5, AUDv6a, AUDv6b, VISlla, VISlla1, VISlla2/3, VISlla4, VISlla5, VISlla6a, VISlla6b	Auditory areas
VIS	VIS, VIS1, VIS2/3, VIS4, VIS5, VIS6a, VIS6b, VISal, VISal1, VISal2/3, VISal4, VISal5, VISal6a, VISal6b, VISam, VISam1, VISam2/3, VISam4, VISam5, VISam6a, VISam6b, VISl, VISl1, VISl2/3, VISl4, VISl5, VISl6a, VISl6b, VISli, VISli1, VISli2/3, VISli4, VISli5, VISli6a, VISli6b, VISp, VISp1, VISp2/3, VISp4, VISp5, VISp6a, VISp6b, VISpl, VISpl1, VISpl2/3, VISpl4, VISpl5, VISpl6a, VISpl6b, VISpm, VISpm1, VISpm2/3, VISpm4, VISpm5, VISpm6a, VISpm6b, VISpor, VISpor1, VISpor2/3, VISpor4, VISpor5, VISpor6a, VISpor6b	Visual areas
ACA	ACA, ACA1, ACA2/3, ACA5, ACA6a, ACA6b, ACAd, ACAd1, ACAd2/3, ACAd5, ACAd6a, ACAd6b, ACAv, ACAv1, ACAv2/3, ACAv5, ACAv6a, ACAv6b	Anterior cingulate area
PL	PL, PL1, PL2, PL2/3, PL5, PL6a, PL6b	Prelimbic area
ILA	ILA, ILA1, ILA2, ILA2/3, ILA5, ILA6a, ILA6b	Infralimbic area
ORB	ORB, ORB1, ORB2/3, ORB5, ORB6a, ORB6b, ORBl, ORBl1, ORBl2/3, ORBl5, ORBl6a, ORBl6b, ORBm, ORBm1, ORBm2, ORBm2/3, ORBm5, ORBm6a, ORBm6b, ORBv, ORBvl, ORBvl1, ORBvl2/3, ORBvl5, ORBvl6a, ORBvl6b	Orbital area
AI	AI, AId, AId1, AId2/3, AId5, AId6a, AId6b, AIp, AIp1, AIp2/3, AIp5, AIp6a, AIp6b, AIv, AIv1, AIv2/3, AIv5, AIv6a, AIv6b	Agranular insular area
RSP	RSP, RSPagl, RSPagl1, RSPagl2/3, RSPagl5, RSPagl6a, RSPagl6b, RSPd, RSPd1, RSPd2/3, RSPd4, RSPd5, RSPd6a, RSPd6b, RSPv, RSPv1, RSPv2, RSPv2/3, RSPv5, RSPv6a, RSPv6b, VISm, VISm1, VISm2/3, VISm4, VISm5, VISm6a, VISm6b, VISmma, VISmma1, VISmma2/3, VISmma4, VISmma5, VISmma6a, VISmma6b, VISmmp, VISmmp1, VISmmp2/3, VISmmp4, VISmmp5, VISmmp6a, VISmmp6b	Retrosplenial area
PTL	PTLp, PTLp1, PTLp2/3, PTLp4, PTLp5, PTLp6a, PTLp6b, VISa, VISa1, VISa2/3, VISa4, VISa5, VISa6a, VISa6b, VISrl, VISrl1, VISrl2/3, VISrl4, VISrl5, VISrl6a, VISrl6b	Posterior parietal association areas

TE	TEa, TEa1, TEa2/3, TEa4, TEa5, TEa6a, TEa6b	Temporal association areas
PERI	PERI, PERI1, PERI2/3, PERI5, PERI6a, PERI6b	Perirhinal area
ECT	ECT, ECT1, ECT2/3, ECT5, ECT6a, ECT6b	Ectorhinal area
OLF	OLF, MOB, MOBipl, MOBopl	Olfactory areas
AOB	AOB, AOBgl, AOBmi	Accessory olfactory bulb
AOBgr	AOBgr, NLOT, NLOT1, NLOT1-3, NLOT2, NLOT3	AOBgr & NLOT
AON	AON, AON1, AON2, AONd, AONe, AONl, AONm, AONpv	Anterior olfactory nucleus
TT	TT, TTd, TTd1, TTd1-4, TTd2, TTd3, TTd4, TTv, TTv1, TTv1-3, TTv2, TTv3	Taenia tecta
DP	DP, DP1, DP2, DP2/3, DP5, DP6a	Dorsal peduncular area
PIR	PIR, PIR1, PIR1-3, PIR2, PIR3	Piriform area
COA	COA, COAa, COAa1, COAa2, COAa3, COAp, COApl, COApl1, COApl1-2, COApl1-3, COApl2, COApl3, COApm, COApm1, COApm1-2, COApm1-3, COApm2, COApm3	Cortical amygdalar area
PAA	PAA, PAA1, PAA1-3, PAA2, PAA3	Piriform-amygdalar area
TR	TR, TR1, TR1-3, TR2, TR3	Postpiriform transition area
CA	CA, CA1, CA1slm, CA1so, CA1sr, CA2, CA2slm, CA2so, CA2sr, CA3, CA3slm, CA3slu, CA3so, CA3sr, DG, DGcr, DGcr-mo, DGcr-po, DGcr-sg, DGlb, DGlb-mo, DGlb-po, DGlb-sg, DGmb, DGmb-mo, DGmb-po, DGmb-sg, DG-mo, DG-po, DG-sgz, FC, HIP, HPF, IG	Hippocampal formation
CA1sp	CA1sp, CA2sp, CA3sp, DG-sg	
ENT	ENT, ENTl, ENTl1, ENTl2, ENTl2/3, ENTl2a, ENTl2b, ENTl3, ENTl4, ENTl4/5, ENTl5, ENTl5/6, ENTl6a, ENTl6b, ENTm, ENTm1, ENTm2, ENTm2a, ENTm2b, ENTm3, ENTm4, ENTm5, ENTm5/6, ENTm6, ENTmv, ENTmv1, ENTmv2, ENTmv3, ENTmv4, ENTmv5/6, RHP	Retrohippocampal region
PAR	PAR, PAR1, PAR2, PAR3	Parasubiculum
POST	POST, POST1, POST2, POST3	Postsubiculum
PRE	PRE, PRE1, PRE2, PRE3	Presubiculum
SUB	SUB, SUBd, SUBd-m, SUBd-sr, SUBv, SUBv-m, SUBv-sr	Subiculum
ProS	ProS, ProSd, ProSd-m, ProSd-sr, ProSv, ProSv-m, Prosv-sr	Prosubiculum
CLA	CLA, CTXsp, 6b	Claustrum
EP	EP, EPd, EPv	Endopiriform nucleus
LA	LA	Lateral amygdalar nucleus
BLA	BLA, BLAa, BLAp, BLAv	Basolateral amygdalar nucleus
BMA	BMA, BMAa, BMAp	Basomedial amygdalar nucleus
PA	PA	Posterior amygdalar nucleus
CP	CP, CNU, STR, STRd	Caudoputamen

ACB	ACB, FS, isl, islm, LSS, OT, OT1, OT1-3, OT2, OT3, STRv	Nucleus accumbens
LS	LS, LSc, LSr, LSv, LSX, SF, SH	Lateral septal complex
AAA	AAA, BA, CEA, CEAc, CEAl, CEAm, IA, MEA, MEAad, MEAav, MEApd, MEApd-a, MEApd-b, MEApd-c, MEApv, sAMY	Anterior amygdalar area
GPe	GPe, GPi, PAL, PALd	Pallidum
MA	MA, PALv, SI	Magnocellular nucleus
MS	MS, MSC, NDB, PALm, TRS	Medial septal nucleus
BAC	BAC, BST, BSTa, BSTal, BSTam, BSTd, BSTdm, BSTfu, BSTif, BSTju, BSTmg, BSTov, BSTp, BSTpr, BSTrh, BSTse, BSTtr, BSTv, PALc	Bed nucleus of the anterior commissure
BS	BS, TH	Brain stem
DORsm	DORsm, GENd, LGd, LGd-co, LGd-ip, LGd-sh, MG, MGd, MGm, MGv, PoT, PP, SPA, SPF, SPFm, SPFp, VAL, VENT, VM, VP, VPL, VPLpc, VPM, VPMpc	Thalamus, sensory-motor cortex related
AD	AD, AM, AMd, AMv, ATN, AV, CL, CM, DORpm, EPI, Eth, GENv, IAD, IAM, IGL, ILM, IMD, IntG, LAT, LD, LGv, LGvl, LGvm, LH, LP, MD, MDc, MDl, MDm, MED, MH, MTN, PCN, PF, PIL, PIN, PO, POL, PR, PT, PVT, RE, REth, RH, RT, SGN, SMT, SubG, Xi	Anterodorsal nucleus
HY	HY	Hypothalamus
ARH	ARH, ASO, NC, PVa, PVH, PVHam, PVHap, PVHm, PVHmm, PVHmpd, PVHp, PVHpm, PVHpml, PVHpmm, PVHpv, PVi, PVZ, SO	Arcuate hypothalamic nucleus
ADP	ADP, AHA, AVP, AVPV, DMH, DMHa, DMHp, DMHv, MEPO, MPO, OV, PD, PS, PSCH, PVp, PVpo, PVR, SBPV, SCH, SFO, VLPO, VMPO	Anterodorsal preoptic nucleus
AHN	AHN, AHNa, AHNc, AHNd, AHNp, LM, MBO, MEZ, MM, MMd, MMl, MMm, MMme, MMp, MPN, MPNc, MPNl, MPNm, PH, PMd, PMv, PVHd, PVHdp, PVHf, PVHlp, PVHmpv, SUM, SUMl, SUMm, TM, TMd, TMv, VMH, VMHa, VMHc, VMHdm, VMHvl	Anterior hypothalamic nucleus
A13	A13, FF, LHA, LPO, LZ, ME,PeF, PST, PSTN, RCH, STN, TU, ZI	
MB	MB	Midbrain
IC	IC, ICc, ICd, ICe, MBsen, MEV, NB, PBG, SAG, SCO, SCop, SCs, SCsg, SCzo	Inferior colliculus
APN	APN, AT, CUN, DT, EW, III, INC, InCo, IV, LT, MA3, MBmot, MBsta, MPT, MRN, MRNm, MRNmg, MRNp, MT, ND, NOT, NPC, OP, Pa4, PAG, PN, PPT, PRC, PRT, RN, RPF, RR, SCdg, SCdw, SCig, SCig-a, SCig-b, SCig-c, SCiw, SCm, SNl, SNr, Su3, VTA, VTN	Anterior pretectal nucleus
SNc	SNc, CLI, DR, IF, IPA, IPC, IPDL, IPDM, IPI, IPL, IPN, IPR, IPRL, PPN, RAmb, RL	Substantia nigra
P	P, HB	Pons
KF	KF, NLL, NLLd, NLLh, NLLv, PB, PBl, PBlc, PBld, PBle, PBls, PBlv, PBm, PBme, PBmm, PBmv, POR, P-sen, PSV, SOC, SOCl, SOCm	Koelliker-Fuse subnucleus
Acs5	Acs5, B, DTN, I5, LTN, P5, PC5, PCG, PDTg, PG, P-mot, PRNc, PRNv, SG, SSN, SUT, TRN, V	Accessory trigeminal nucleus
CS	CS, CSl, CSm, LC, LDT, NI, PRNr, P-sat, RPO, SLC, SLD	Superior central nucleus raphe
MY	MY	Medulla

AP	AP, CN, CNlam, CNspg, CU, DCN, DCO, ECU, GR, MY-sen, NTB, NTS, NTSce, NTSco, NTSge, NTSl, NTSm, Pa5, SPVC, SPVI, SPVO, SPVOcdm, SPVOmdmd, SPVOmdmv, SPVOrdm, SPVOvl, VCO, z	Area postrema
ACVI	ACVI, ACVII, AMB, AMBd, AMBv, DMX, ECO, EV, GRN, ICB, INV, IO, IRN, ISN, LAV, LIN, LRN, LRNm, LRNp, MARN, MDRN, MDRNd, MDRNv, MV, MY-mot, NIS, NR, PARN, PAS, PGRN, PGRNd, PGRNl, PHY, PMR, PPY, PPYd, PPYs, PRP, SPIV, SUV, VI, VII, VNC, x, XII, y	Accessory facial motor nucleus
CB	CB, CBX, CBN	Cerebellum
FN	FN, IP, DN, VeCB	Fastigial nucleus
oct	oct, ab, aco, act, alv, amc, aolt, aot, apd, ar, arb, bct, bic, bsc, cbc, cbf, cbp, cbt, cc, ccb, ccg, ccr, ccs, cct, cett, cic, cing, cm, cpd, cpt, crt, csc, cst, cstc, cstu, ctb, cte, cuf, cvb, cVIIIn, das, db, dc, dcm, df, dhc, dl, dlf, drt, dscp, dtd, dtt, ec, ee, em, eps, epsc, fa, fi, fp, fpr, fr, fx, fxpo, fxprg, fxs, grf, gVIIn, hbc, hc, hht, iaf, ias, icp, IIIn, IIn, im, In, int, IVd, iVIIn, IVn, IXn, jrb, lab, lfbs, lfbst, ll, lot, lotd, lotg, mcp, mct, mfb, mfbc, mfbs, mfbse, mfbsm, mfbsma, mfbst, mfsbshy, ml, mlf, moV, mp, mtc, mtg, mtt, mtV, nst, ntt, och, onl, opt, or, pap, pc, per, php, phpd, phpl, phpm, phpv, PIS, pm, pmx, poc, ptf, pvbh, pvbt, py, pyd, rct, rrt, rst, rstl, rstm, rust, scp, scrt, sct, sctd, sctv, scwm, shp, sm, smd, snp, sop, sptV, srp, sst, st, stc, step, stf, stp, sttl, sttv, sup, supa, supd, supv, sV, svp, tb, tct, tn, tp, ts, tsp, tspc, tspd, ttp, uf, vc, vhc, VIIIn, VIIn, VIn, vlt, Vn, von, vrt, vsp, vtd, vVIIIn, XIIn, XIn, Xn	fiber tracts

Supplementary table 1

List of anatomical clusters and all the brain regions that they represent according to the current Allen adult mouse brain atlas ontology.

Cluster	BL6#1	BL6#2	BL6#3	CD1#1	CD1#2	CD1#3	BALBC #1	BALBC #2	BALBC #3
FRP	0.00490	0.00761	0.00499	0.00196	0.00405	0.00100	0.00261	0.00397	0.00428
MO	0.00713	0.00838	0.00561	0.00447	0.00743	0.00346	0.00708	0.00689	0.00606
SS	0.00831	0.00981	0.00791	0.00528	0.00987	0.00607	0.00694	0.00701	0.00589
GU	0.00782	0.00767	0.00635	0.00599	0.01000	0.00766	0.00572	0.00569	0.00560
VISC	0.00691	0.00778	0.00625	0.00496	0.00963	0.00619	0.00453	0.00520	0.00527
AUD	0.00632	0.00924	0.00637	0.00605	0.00776	0.00579	0.00725	0.00791	0.00730
VIS	0.00632	0.00845	0.00603	0.00399	0.00717	0.00412	0.00659	0.00747	0.00654
ACA	0.00700	0.00671	0.00534	0.00425	0.00814	0.00471	0.00554	0.00676	0.00533
PL	0.00727	0.00680	0.00503	0.00383	0.00704	0.00479	0.00528	0.00627	0.00614
ILA	0.00730	0.00497	0.00342	0.00495	0.00676	0.00600	0.00498	0.00601	0.00531
ORB	0.00925	0.00756	0.00613	0.00481	0.00823	0.00510	0.00591	0.00700	0.00640
AI	0.00710	0.00711	0.00546	0.00429	0.00734	0.00496	0.00624	0.00578	0.00578
RSP	0.00825	0.00794	0.00562	0.00378	0.00841	0.00478	0.00528	0.00744	0.00610
PTL	0.00401	0.00838	0.00570	0.00419	0.00687	0.00383	0.00658	0.00696	0.00557
TE	0.00474	0.00777	0.00554	0.00490	0.00758	0.00466	0.00548	0.00686	0.00604
PERI	0.00428	0.00637	0.00520	0.00296	0.00622	0.00331	0.00441	0.00507	0.00527
ECT	0.00419	0.00662	0.00514	0.00367	0.00682	0.00371	0.00449	0.00587	0.00562
OLF	0.00625	0.00360	0.00491	0.00343	0.00838	0.00526	0.00565	0.00595	0.00533
AOB	0.00745	0.00574	0.00464	0.00356	0.00744	0.00506	0.00551	0.00489	0.00565
AOBgr	0.00475	0.00345	0.00526	0.00222	0.00523	0.00375	0.00540	0.00551	0.00493
AON	0.00848	0.00529	0.00510	0.00453	0.00731	0.00493	0.00602	0.00629	0.00584
TT	0.00648	0.00275	0.00419	0.00350	0.00625	0.00533	0.00553	0.00532	0.00555
DP	0.00669	0.00395	0.00355	0.00437	0.00644	0.00643	0.00498	0.00596	0.00533
PIR	0.00690	0.00608	0.00613	0.00364	0.00699	0.00559	0.00653	0.00631	0.00578
COA	0.00353	0.00346	0.00468	0.00206	0.00494	0.00352	0.00474	0.00454	0.00480
PAA	0.00353	0.00225	0.00455	0.00183	0.00566	0.00412	0.00449	0.00481	0.00432
TR	0.00485	0.00493	0.00492	0.00248	0.00578	0.00335	0.00468	0.00477	0.00520
CA	0.00469	0.00485	0.00448	0.00340	0.00538	0.00376	0.00423	0.00501	0.00433
CA1sp	0.00447	0.00411	0.00430	0.00302	0.00478	0.00341	0.00352	0.00467	0.00414
ENT	0.00503	0.00733	0.00488	0.00351	0.00664	0.00354	0.00510	0.00575	0.00506
PAR	0.00598	0.00644	0.00524	0.00413	0.00857	0.00409	0.00602	0.00817	0.00525
POST	0.00702	0.00844	0.00744	0.00484	0.00684	0.00475	0.00592	0.00747	0.00539
PRE	0.00587	0.00785	0.00773	0.00396	0.00873	0.00583	0.00665	0.00783	0.00601
SUB	0.00646	0.00708	0.00648	0.00470	0.00723	0.00527	0.00569	0.00677	0.00524
ProS	0.00558	0.00466	0.00363	0.00340	0.00604	0.00264	0.00366	0.00399	0.00341
CLA	0.00718	0.00599	0.00533	0.00358	0.00615	0.00535	0.00533	0.00559	0.00468
EP	0.00613	0.00562	0.00495	0.00308	0.00585	0.00442	0.00488	0.00507	0.00478
LA	0.00423	0.00443	0.00379	0.00313	0.00551	0.00313	0.00395	0.00457	0.00429
BLA	0.00454	0.00460	0.00465	0.00272	0.00583	0.00391	0.00517	0.00532	0.00501
BMA	0.00483	0.00471	0.00487	0.00330	0.00561	0.00486	0.00529	0.00528	0.00530
PA	0.00511	0.00480	0.00510	0.00302	0.00536	0.00416	0.00681	0.00598	0.00547
CP	0.00634	0.00513	0.00524	0.00358	0.00642	0.00451	0.00400	0.00500	0.00368

ACB	0.00494	0.00319	0.00465	0.00263	0.00571	0.00375	0.00629	0.00608	0.00494
LS	0.00435	0.00274	0.00388	0.00313	0.00547	0.00448	0.00279	0.00316	0.00297
AAA	0.00513	0.00412	0.00453	0.00309	0.00498	0.00504	0.00519	0.00487	0.00501
GPe	0.00544	0.00394	0.00466	0.00267	0.00544	0.00330	0.00368	0.00434	0.00430
MA	0.00608	0.00373	0.00473	0.00218	0.00594	0.00421	0.00571	0.00490	0.00394
MS	0.00655	0.00345	0.00560	0.00267	0.00671	0.00519	0.00530	0.00456	0.00435
BAC	0.00532	0.00250	0.00377	0.00221	0.00475	0.00348	0.00314	0.00320	0.00273
BS	0.00479	0.00388	0.00485	0.00352	0.00556	0.00426	0.00452	0.00525	0.00503
DORsm	0.00503	0.00493	0.00517	0.00426	0.00688	0.00445	0.00564	0.00650	0.00618
AD	0.00483	0.00361	0.00481	0.00346	0.00635	0.00383	0.00442	0.00489	0.00494
HY	0.00620	0.00305	0.00465	0.00303	0.00602	0.00521	0.00519	0.00482	0.00470
ARH	0.00474	0.00167	0.00304	0.00268	0.00528	0.00358	0.00521	0.00465	0.00476
ADP	0.00623	0.00244	0.00430	0.00279	0.00616	0.00503	0.00559	0.00492	0.00441
AHN	0.00611	0.00303	0.00442	0.00300	0.00598	0.00487	0.00535	0.00511	0.00483
A13	0.00605	0.00452	0.00567	0.00391	0.00666	0.00519	0.00561	0.00533	0.00531
MB	0.00626	0.00540	0.00536	0.00401	0.00708	0.00418	0.00438	0.00575	0.00478
IC	0.00700	0.00877	0.00746	0.00511	0.00979	0.00472	0.00429	0.00697	0.00549
APN	0.00714	0.00566	0.00590	0.00465	0.00742	0.00397	0.00400	0.00570	0.00453
SNc	0.00541	0.00517	0.00500	0.00390	0.00664	0.00326	0.00318	0.00448	0.00347
P	0.00336	0.00217	0.00328	0.00179	0.00394	0.00227	0.00294	0.00374	0.00400
KF	0.00345	0.00328	0.00450	0.00192	0.00383	0.00241	0.00382	0.00528	0.00606
Acs5	0.00433	0.00243	0.00476	0.00257	0.00543	0.00313	0.00379	0.00502	0.00507
CS	0.00553	0.00381	0.00513	0.00304	0.00658	0.00324	0.00324	0.00417	0.00434
MY	0.00449	0.00248	0.00328	0.00178	0.00297	0.00214	0.00430	0.00373	0.00346
AP	0.00520	0.00541	0.00540	0.00304	0.00499	0.00260	0.00583	0.00683	0.00565
ACVI	0.00681	0.00412	0.00597	0.00303	0.00493	0.00328	0.00641	0.00683	0.00609
CB	0.00518	0.00414	0.00412	0.00202	0.00375	0.00303	0.00374	0.00493	0.00521
FN	0.00685	0.00784	0.00858	0.00330	0.00329	0.00554	0.00691	0.00913	0.00892
oct	0.00457	0.00356	0.00355	0.00243	0.00400	0.00259	0.00343	0.00403	0.00357

Supplementary table 2

Quantification of the local vascular length per volume in the C57BL/6J, CD1 and BALB/c samples in the voxel-corrected space. Units are in vx/vx3.

Cluster	BL6#1	BL6#2	BL6#3	CD1#1	CD1#2	CD1#3	BALBC #1	BALBC #2	BALBC #3
FRP	0,00064	0,00096	0,00056	0,00020	0,00053	0,00008	0,00025	0,00041	0,00051
MO	0,00107	0,00127	0,00066	0,00047	0,00107	0,00036	0,00104	0,00090	0,00075
SS	0,00138	0,00172	0,00119	0,00060	0,00170	0,00080	0,00094	0,00097	0,00071
GU	0,00119	0,00112	0,00080	0,00069	0,00178	0,00105	0,00066	0,00072	0,00066
VISC	0,00104	0,00121	0,00082	0,00055	0,00165	0,00080	0,00041	0,00057	0,00054
AUD	0,00083	0,00147	0,00080	0,00071	0,00113	0,00074	0,00097	0,00114	0,00095
VIS	0,00085	0,00131	0,00073	0,00039	0,00102	0,00044	0,00081	0,00105	0,00081
ACA	0,00100	0,00081	0,00061	0,00044	0,00128	0,00053	0,00063	0,00082	0,00061
PL	0,00104	0,00080	0,00052	0,00036	0,00097	0,00055	0,00053	0,00075	0,00074
ILA	0,00102	0,00044	0,00028	0,00049	0,00082	0,00069	0,00041	0,00061	0,00052
ORB	0,00155	0,00100	0,00073	0,00048	0,00119	0,00058	0,00065	0,00085	0,00078
AI	0,00104	0,00095	0,00061	0,00042	0,00101	0,00057	0,00075	0,00067	0,00064
RSP	0,00130	0,00116	0,00068	0,00037	0,00133	0,00055	0,00055	0,00106	0,00075
PTL	0,00049	0,00130	0,00075	0,00044	0,00093	0,00041	0,00085	0,00093	0,00068
TE	0,00053	0,00108	0,00061	0,00051	0,00109	0,00050	0,00056	0,00087	0,00067
PERI	0,00047	0,00078	0,00054	0,00024	0,00080	0,00031	0,00037	0,00053	0,00052
ECT	0,00042	0,00080	0,00053	0,00032	0,00090	0,00035	0,00039	0,00065	0,00058
OLF	0,00098	0,00048	0,00065	0,00037	0,00140	0,00067	0,00077	0,00080	0,00071
AOB	0,00115	0,00082	0,00062	0,00033	0,00115	0,00052	0,00063	0,00056	0,00078
AOBgr	0,00061	0,00034	0,00060	0,00017	0,00058	0,00038	0,00066	0,00063	0,00055
AON	0,00135	0,00057	0,00055	0,00045	0,00099	0,00055	0,00074	0,00072	0,00067
TT	0,00092	0,00025	0,00042	0,00034	0,00081	0,00064	0,00071	0,00062	0,00073
DP	0,00092	0,00033	0,00029	0,00041	0,00083	0,00077	0,00044	0,00064	0,00056
PIR	0,00103	0,00078	0,00077	0,00035	0,00098	0,00068	0,00090	0,00080	0,00069
COA	0,00040	0,00035	0,00045	0,00015	0,00055	0,00035	0,00059	0,00052	0,00051
PAA	0,00040	0,00024	0,00048	0,00012	0,00063	0,00042	0,00058	0,00057	0,00051
TR	0,00054	0,00051	0,00049	0,00018	0,00070	0,00030	0,00053	0,00054	0,00054
CA	0,00056	0,00049	0,00045	0,00030	0,00064	0,00039	0,00040	0,00051	0,00040
CA1sp	0,00053	0,00038	0,00041	0,00025	0,00052	0,00033	0,00028	0,00043	0,00036
ENT	0,00063	0,00101	0,00058	0,00034	0,00097	0,00039	0,00055	0,00072	0,00055
PAR	0,00091	0,00095	0,00071	0,00044	0,00150	0,00053	0,00078	0,00123	0,00061
POST	0,00097	0,00128	0,00101	0,00050	0,00094	0,00055	0,00072	0,00101	0,00062
PRE	0,00075	0,00112	0,00106	0,00036	0,00134	0,00071	0,00085	0,00107	0,00067
SUB	0,00089	0,00093	0,00081	0,00047	0,00106	0,00061	0,00064	0,00083	0,00054
ProS	0,00078	0,00052	0,00037	0,00036	0,00082	0,00024	0,00036	0,00041	0,00031
CLA	0,00104	0,00067	0,00056	0,00028	0,00077	0,00059	0,00054	0,00059	0,00044
EP	0,00082	0,00060	0,00050	0,00024	0,00069	0,00044	0,00047	0,00050	0,00044
LA	0,00048	0,00037	0,00032	0,00023	0,00063	0,00026	0,00032	0,00043	0,00036
BLA	0,00053	0,00042	0,00044	0,00020	0,00067	0,00035	0,00052	0,00054	0,00047
BMA	0,00057	0,00045	0,00050	0,00028	0,00065	0,00052	0,00057	0,00056	0,00054
PA	0,00063	0,00047	0,00052	0,00024	0,00063	0,00045	0,00093	0,00069	0,00057
CP	0,00090	0,00053	0,00058	0,00032	0,00081	0,00048	0,00034	0,00050	0,00032

ACB	0,00062	0,00028	0,00046	0,00021	0,00070	0,00039	0,00083	0,00072	0,00054
LS	0,00046	0,00018	0,00032	0,00024	0,00065	0,00044	0,00018	0,00022	0,00021
AAA	0,00069	0,00037	0,00044	0,00026	0,00057	0,00059	0,00058	0,00050	0,00051
GPe	0,00067	0,00033	0,00045	0,00021	0,00060	0,00029	0,00032	0,00041	0,00040
MA	0,00083	0,00031	0,00047	0,00016	0,00073	0,00044	0,00067	0,00049	0,00036
MS	0,00091	0,00028	0,00064	0,00021	0,00098	0,00063	0,00064	0,00045	0,00047
BAC	0,00065	0,00015	0,00032	0,00016	0,00052	0,00034	0,00024	0,00024	0,00020
BS	0,00057	0,00035	0,00050	0,00032	0,00067	0,00045	0,00043	0,00057	0,00051
DORsm	0,00060	0,00049	0,00056	0,00041	0,00089	0,00046	0,00062	0,00079	0,00070
AD	0,00055	0,00031	0,00048	0,00029	0,00076	0,00036	0,00042	0,00048	0,00048
HY	0,00083	0,00026	0,00049	0,00026	0,00077	0,00063	0,00056	0,00050	0,00048
ARH	0,00061	0,00013	0,00028	0,00021	0,00061	0,00037	0,00056	0,00050	0,00049
ADP	0,00087	0,00019	0,00044	0,00022	0,00083	0,00062	0,00065	0,00051	0,00046
AHN	0,00082	0,00026	0,00044	0,00024	0,00076	0,00055	0,00058	0,00054	0,00050
A13	0,00081	0,00047	0,00069	0,00040	0,00092	0,00063	0,00068	0,00064	0,00060
MB	0,00084	0,00058	0,00057	0,00037	0,00100	0,00044	0,00041	0,00064	0,00049
IC	0,00102	0,00137	0,00104	0,00053	0,00167	0,00054	0,00041	0,00090	0,00065
APN	0,00101	0,00060	0,00068	0,00045	0,00107	0,00040	0,00035	0,00062	0,00043
SNc	0,00068	0,00054	0,00051	0,00035	0,00087	0,00028	0,00025	0,00044	0,00029
P	0,00039	0,00019	0,00033	0,00014	0,00047	0,00019	0,00028	0,00040	0,00045
KF	0,00038	0,00033	0,00053	0,00015	0,00042	0,00020	0,00039	0,00062	0,00078
Acs5	0,00051	0,00018	0,00051	0,00020	0,00063	0,00029	0,00038	0,00052	0,00055
CS	0,00069	0,00032	0,00053	0,00025	0,00086	0,00026	0,00025	0,00038	0,00042
MY	0,00062	0,00026	0,00039	0,00016	0,00037	0,00022	0,00055	0,00047	0,00041
AP	0,00068	0,00064	0,00068	0,00028	0,00069	0,00025	0,00074	0,00095	0,00071
ACVI	0,00101	0,00037	0,00070	0,00025	0,00057	0,00032	0,00077	0,00091	0,00073
CB	0,00072	0,00049	0,00053	0,00017	0,00046	0,00032	0,00041	0,00065	0,00071
FN	0,00097	0,00114	0,00139	0,00029	0,00030	0,00072	0,00101	0,00151	0,00147
oct	0,00059	0,00037	0,00038	0,00020	0,00046	0,00025	0,00035	0,00043	0,00036

Supplementary table 3

Quantification of the number of bifurcation points in the C57BL/6J, CD1 and BALB/c samples in the voxel-corrected space, units are in counts/vx3.

Cluster	BL6#1	BL6#2	BL6#3	CD1#1	CD1#2	CD1#3	BALBC #1	BALBC #2	BALBC #3
FRP	2.06	2.35	2.33	3.53	2.26	2.66	2.44	2.32	2.36
MO	2.07	2.40	2.29	2.08	2.04	2.19	2.45	2.57	2.51
SS	2.14	2.47	2.38	2.12	2.17	2.25	2.47	2.59	2.50
GU	2.21	2.68	2.68	2.14	2.37	2.38	2.82	2.76	2.75
VISC	2.23	2.66	2.43	2.30	2.33	2.45	2.53	2.57	2.34
AUD	2.02	2.38	2.27	2.14	1.97	2.14	2.58	2.67	2.50
VIS	2.07	2.34	2.27	2.08	2.03	2.08	2.48	2.64	2.47
ACA	2.34	2.35	2.49	2.20	2.32	2.45	3.15	3.46	2.79
PL	2.17	2.48	2.29	2.14	2.12	2.34	2.66	2.79	2.75
ILA	2.32	2.43	2.42	2.31	2.15	2.35	2.68	2.91	2.69
ORB	2.27	2.41	2.34	2.24	2.10	2.18	2.50	2.43	2.64
AI	2.14	2.52	2.48	2.15	2.15	2.27	2.72	2.73	2.53
RSP	2.10	2.30	2.30	2.12	2.13	2.23	2.57	2.74	2.78
PTL	2.04	2.34	2.27	2.03	2.04	2.10	2.53	2.62	2.49
TE	2.04	2.41	2.27	2.04	1.98	1.99	2.49	2.63	2.42
PERI	2.13	2.42	2.33	2.02	2.07	2.03	2.54	2.57	2.51
ECT	2.13	2.38	2.28	2.03	2.02	1.99	2.55	2.65	2.47
OLF	2.29	2.44	2.47	2.26	2.20	2.48	2.54	2.59	2.52
AOB	2.15	2.70	2.58	2.16	2.46	2.44	2.64	2.78	2.45
AOBgr	2.62	2.67	2.81	2.58	2.35	2.93	2.70	2.50	2.47
AON	2.15	2.28	2.42	2.14	2.20	2.25	2.57	2.63	2.68
TT	2.86	2.53	2.86	2.54	2.31	2.92	2.91	2.67	2.61
DP	2.21	2.35	2.48	2.13	2.11	2.54	2.77	2.66	2.74
PIR	2.18	2.38	2.56	2.14	2.18	2.34	2.73	2.69	2.55
COA	2.16	2.33	2.49	2.30	2.18	2.29	3.02	2.94	2.64
PAA	2.22	2.26	2.59	2.43	2.16	2.45	2.92	2.74	2.57
TR	2.16	2.48	2.46	2.10	2.19	1.99	2.73	3.02	2.54
CA	2.56	2.49	2.65	2.57	2.24	2.70	3.93	4.14	3.22
CA1sp	2.34	2.23	2.42	2.12	2.07	2.86	2.60	2.55	2.76
ENT	2.09	2.41	2.32	2.08	2.25	2.22	2.52	2.70	2.51
PAR	2.44	2.31	2.33	2.16	2.27	2.54	2.46	2.49	2.42
POST	2.43	2.61	2.73	2.64	2.31	2.54	2.72	2.55	2.94
PRE	3.28	2.60	2.53	3.04	2.42	2.90	3.49	2.48	3.60
SUB	2.34	2.50	2.52	2.34	2.40	2.25	2.51	2.56	2.46
ProS	2.10	2.35	2.38	2.14	2.10	2.19	2.53	2.66	2.67
CLA	2.22	2.41	2.62	2.12	2.29	2.33	2.88	2.72	2.54
EP	2.17	2.42	2.56	2.12	2.20	2.28	2.85	2.78	2.60
LA	2.08	2.13	2.40	2.10	2.14	2.19	2.96	2.96	2.70
BLA	2.08	2.25	2.54	2.10	2.19	2.18	2.96	2.96	2.73
BMA	2.13	2.20	2.55	2.18	2.25	2.38	3.05	2.96	2.87
PA	2.06	2.24	2.47	2.06	2.08	2.17	2.86	2.87	2.60
CP	2.30	2.23	2.54	2.26	2.20	2.51	2.63	2.67	2.55

ACB	2.16	2.05	2.37	2.22	2.06	2.29	2.58	2.51	2.34
LS	2.05	2.13	2.44	2.15	2.29	2.15	2.34	2.49	2.38
AAA	2.30	2.27	2.51	2.60	2.31	2.63	3.03	2.75	2.79
GPe	2.19	2.07	2.46	2.18	2.22	2.43	2.58	2.65	2.52
MA	2.28	2.10	2.51	2.31	2.12	2.41	2.56	2.47	2.47
MS	2.30	2.28	2.55	2.52	2.36	2.93	2.43	2.55	2.46
BAC	2.23	2.53	2.68	2.00	2.39	2.03	2.42	2.59	2.45
BS	2.12	2.19	2.39	2.15	2.16	2.23	2.57	2.55	2.46
DORsm	2.14	2.23	2.43	2.14	2.13	2.17	2.63	2.55	2.56
AD	2.07	2.14	2.31	2.14	2.07	2.22	2.45	2.42	2.38
HY	2.22	2.11	2.48	2.23	2.23	2.60	2.59	2.66	2.48
ARH	2.17	2.29	2.50	2.28	2.29	2.88	2.45	2.61	2.29
ADP	2.52	2.82	2.94	3.21	2.43	3.00	2.56	2.64	2.50
AHN	2.27	2.23	2.58	2.25	2.20	2.49	2.50	2.60	2.44
A13	2.26	2.17	2.44	2.32	2.45	2.62	2.70	2.45	2.44
MB	2.12	2.31	2.56	2.06	2.20	2.17	2.54	2.61	2.52
IC	2.15	2.24	2.27	2.11	2.34	2.24	2.63	2.73	2.54
APN	2.14	2.28	2.40	2.03	2.19	2.13	2.48	2.48	2.40
SNc	2.31	2.53	2.63	2.26	2.22	2.29	2.60	2.75	2.60
P	2.33	2.31	2.43	2.32	2.24	2.55	2.42	2.61	2.49
KF	2.18	2.24	2.26	2.43	2.25	2.54	2.52	2.43	2.40
Acs5	2.19	2.12	2.31	2.31	2.07	2.41	2.46	2.42	2.40
CS	2.12	2.04	2.27	1.90	2.04	2.10	2.35	2.50	2.44
MY	2.20	2.16	2.36	2.17	2.28	2.29	2.59	2.74	2.50
AP	2.05	2.12	2.21	2.08	2.22	1.97	2.37	2.56	2.30
ACVI	2.30	2.12	2.35	2.27	2.22	2.12	2.50	2.66	2.46
CB	2.18	2.36	2.67	2.55	2.31	2.40	2.49	2.71	2.56
FN	2.10	2.15	2.34	2.13	2.02	2.09	2.46	2.38	2.38
oct	2.31	2.30	2.45	2.27	2.26	2.37	2.59	2.63	2.46

Supplementary table 4

Quantification of the radii in the C57BL/6J, CD1 and BALB/c samples in the voxel-corrected space, units are in vx.

Cluster	BL6#1	BL6#2	BL6#3	CD1#1	CD1#2	CD1#3	BALBC #1	BALBC #2	BALBC #3
FRP	719.81	1118.68	733.15	287.84	596.06	146.94	383.64	583.69	629.29
MO	1048.25	1232.20	825.23	656.95	1093.14	508.53	1040.80	1013.67	891.79
SS	1222.57	1441.97	1162.48	776.57	1451.00	892.96	1021.11	1031.19	866.42
GU	1149.30	1127.14	933.31	881.49	1470.88	1126.30	841.42	836.62	823.94
VISC	1016.51	1143.88	919.24	729.46	1415.35	910.67	666.37	765.01	775.18
AUD	929.26	1358.36	936.36	889.46	1141.52	851.74	1065.89	1163.60	1073.18
VIS	928.94	1242.70	886.48	586.44	1054.50	606.48	968.61	1097.99	962.29
ACA	1028.65	986.51	785.10	625.14	1197.54	693.00	814.56	994.05	783.90
PL	1069.15	1000.28	740.29	563.85	1035.32	703.89	776.62	921.60	902.68
ILA	1072.84	730.91	502.99	728.36	994.08	882.39	731.92	883.94	780.31
ORB	1359.66	1111.72	901.02	706.82	1210.53	749.79	869.66	1029.35	940.88
AI	1044.59	1045.48	802.82	630.52	1079.05	729.32	916.89	850.15	849.33
RSP	1213.69	1167.69	826.12	556.53	1236.67	703.25	776.24	1093.96	896.48
PTL	589.85	1232.58	837.70	615.78	1010.92	563.72	967.03	1023.68	818.77
TE	696.56	1142.78	814.66	720.03	1114.58	685.05	805.32	1008.26	887.77
PERI	628.88	936.89	764.54	434.56	915.32	486.02	648.91	745.63	774.86
ECT	615.54	973.08	756.32	539.22	1002.36	544.91	660.33	863.42	826.04
OLF	918.29	528.93	721.69	503.74	1232.31	773.96	831.16	874.80	784.00
AOB	1095.15	844.41	682.01	523.93	1094.73	744.21	810.80	719.11	830.29
AOBgr	698.45	506.86	772.76	326.25	769.50	551.26	793.40	809.63	725.02
AON	1246.96	777.66	750.09	665.89	1075.61	724.66	885.26	925.20	858.75
TT	952.74	404.86	616.27	514.86	919.39	783.44	812.56	782.74	815.38
DP	984.41	580.32	521.76	643.00	946.98	946.02	731.76	875.84	783.36
PIR	1014.22	893.75	902.01	535.96	1027.76	822.62	960.81	928.15	849.46
COA	519.31	508.62	688.35	302.72	726.67	517.43	697.20	668.07	705.16
PAA	519.67	331.52	669.07	268.43	832.27	605.50	660.83	707.58	635.27
TR	713.29	725.55	722.80	365.16	850.23	492.55	688.54	701.81	765.26
CA	689.09	712.58	659.15	500.22	790.85	552.59	621.69	736.13	636.36
CA1sp	657.85	604.65	632.59	443.61	703.31	500.71	517.49	686.62	608.19
ENT	739.55	1078.29	717.63	516.81	976.19	520.25	749.89	844.99	744.69
PAR	879.62	946.67	770.00	607.20	1260.23	601.76	885.30	1201.17	772.23
POST	1032.48	1241.02	1094.03	712.26	1006.41	698.99	870.70	1098.09	791.99
PRE	863.57	1153.73	1137.18	581.74	1283.05	856.64	978.21	1150.62	883.73
SUB	949.30	1041.07	953.54	690.63	1063.20	774.25	836.39	996.21	770.36
ProS	819.91	684.89	534.20	500.48	887.92	388.53	538.65	587.25	501.86
CLA	1056.38	881.31	783.01	526.75	904.03	786.12	783.96	821.79	687.97
EP	901.38	825.73	728.23	452.45	859.75	650.63	716.91	745.74	702.97
LA	622.41	651.07	557.65	460.41	810.48	459.70	580.43	671.64	631.47
BLA	667.57	675.91	683.98	399.58	857.36	575.35	760.15	782.80	736.35
BMA	709.76	692.22	715.82	485.51	824.96	714.55	777.27	776.70	779.55
PA	750.73	706.11	749.80	443.59	788.33	611.11	1001.29	879.84	804.16
CP	931.54	754.27	769.97	526.23	943.65	663.07	587.46	734.87	541.26

ACB	726.78	468.84	683.56	386.39	840.11	550.87	924.94	894.13	726.36
LS	639.18	403.36	569.81	459.94	804.94	658.75	410.96	464.19	436.64
AAA	754.54	606.42	665.74	453.88	732.46	740.79	762.91	716.18	736.72
GPe	800.59	579.02	685.23	393.02	800.25	485.55	541.33	638.24	631.98
MA	894.22	548.66	695.15	319.83	873.57	619.46	839.26	720.59	579.14
MS	963.30	506.92	823.94	393.19	987.01	762.96	779.51	670.04	639.58
BAC	782.50	367.08	554.83	325.31	698.31	511.71	461.13	470.45	401.36
BS	704.80	569.94	713.50	518.26	817.19	626.73	664.73	771.37	739.95
DORsm	739.20	724.49	759.70	625.93	1010.94	654.18	829.20	955.45	908.10
AD	710.52	530.64	707.36	509.14	933.33	562.48	650.16	718.36	726.77
HY	912.22	449.00	684.05	445.60	885.77	766.83	763.63	708.17	691.49
ARH	697.02	246.12	446.55	394.21	776.16	526.03	765.37	684.29	699.34
ADP	916.67	358.25	632.37	410.92	905.57	739.81	821.80	723.03	648.11
AHN	898.72	445.45	650.43	440.86	879.34	716.36	786.07	751.71	710.06
A13	889.18	664.83	833.02	574.50	980.00	763.20	824.92	783.77	781.41
MB	920.67	793.93	788.32	590.22	1041.19	615.08	644.43	845.51	702.16
IC	1029.18	1289.43	1096.39	751.61	1438.99	694.66	630.47	1024.37	806.88
APN	1049.56	832.80	867.45	683.94	1090.88	584.14	588.78	837.74	666.08
SNc	795.22	759.98	734.68	573.06	976.72	478.87	468.03	658.41	510.82
P	493.76	318.81	482.09	263.62	579.83	333.32	431.94	550.02	587.69
KF	507.24	482.30	661.72	282.48	563.46	354.57	561.88	776.05	891.69
Acs5	636.43	357.36	700.60	377.53	798.93	459.86	557.17	738.23	745.40
CS	812.85	560.07	754.40	447.45	967.60	476.53	476.94	612.59	637.48
MY	660.51	364.51	482.57	261.65	436.11	314.62	632.36	548.89	508.50
AP	764.94	794.94	793.32	447.33	733.75	381.68	857.35	1004.94	830.18
ACVI	1001.85	606.15	878.32	445.09	724.62	482.96	942.05	1004.80	894.96
CB	761.08	609.37	606.03	297.01	551.35	445.34	549.30	724.44	766.69
FN	1007.05	1152.18	1261.14	485.80	483.46	814.84	1016.73	1343.19	1311.83
oct	671.42	523.78	522.04	357.37	587.50	381.05	504.58	592.97	525.37

Supplementary table 5

Quantification of the local vascular length per volume in the C57BL/6J, CD1 and BALB/c samples in the microscopy space. Units are in mm/mm3.

Cluster	BL6#1	BL6#2	BL6#3	CD1#1	CD1#2	CD1#3	BALBC #1	BALBC #2	BALBC #3
FRP	23524	35671	20593	7322	19611	2991	9357	15228	19019
MO	39776	46880	24446	17511	39601	13432	38467	33505	27601
SS	50955	63539	43967	22296	62891	29549	34831	35821	26155
GU	44052	41461	29646	25455	65769	38823	24384	26636	24383
VISC	38342	44642	30287	20389	61105	29690	15299	21212	20002
AUD	30604	54404	29622	26250	41971	27252	35903	42101	35349
VIS	31402	48335	27079	14373	37617	16370	29846	38792	29951
ACA	36955	29816	22417	16131	47382	19575	23352	30328	22768
PL	38603	29477	19432	13501	35750	20427	19472	27722	27366
ILA	37816	16328	10361	17993	30320	25411	15359	22456	19290
ORB	57233	37077	27086	17922	44024	21437	23985	31380	28755
AI	38586	35276	22411	15510	37532	21014	27625	24993	23888
RSP	48191	42920	25043	13611	49439	20492	20279	39112	27817
PTL	18202	48296	27920	16219	34279	15116	31532	34435	25245
TE	19758	40058	22684	18874	40247	18696	20737	32153	24805
PERI	17292	28715	19853	8909	29664	11527	13559	19521	19375
ECT	15504	29570	19494	11924	33371	13125	14312	24089	21435
OLF	36378	17766	23892	13782	51825	24895	28538	29626	26177
AOB	42498	30535	23087	12246	42653	19413	23379	20805	28818
AOBgr	22467	12598	22046	6260	21666	14139	24596	23304	20363
AON	50084	21192	20271	16628	36730	20329	27574	26851	24663
TT	33906	9083	15401	12692	29852	23552	26186	23141	26906
DP	34126	12167	10567	15050	30600	28553	16172	23805	20569
PIR	38037	29002	28671	12779	36128	25360	33170	29812	25456
COA	14709	13070	16841	5710	20309	13039	21850	19152	18728
PAA	14677	9006	17760	4614	23225	15644	21464	21229	18715
TR	20034	18850	17977	6664	26085	11179	19672	19929	20081
CA	20639	18296	16823	11043	23758	14272	14845	18935	14943
CA1sp	19524	13929	15313	9210	19295	12350	10362	15826	13496
ENT	23338	37302	21371	12602	35910	14294	20336	26644	20433
PAR	33758	35125	26234	16274	55377	19536	28754	45529	22765
POST	35759	47237	37547	18518	34643	20191	26600	37512	22960
PRE	27593	41367	39199	13187	49737	26456	31537	39650	24860
SUB	32851	34550	29948	17240	39242	22657	23730	30609	20162
ProS	28791	19378	13664	13342	30513	8940	13334	15221	11472
CLA	38557	24851	20872	10496	28508	21857	19897	21760	16148
EP	30218	22047	18339	8850	25408	16373	17539	18654	16472
LA	17633	13708	11816	8513	23186	9707	11928	15858	13448
BLA	19702	15504	16330	7315	24692	13087	19321	19902	17472
BMA	21083	16502	18569	10279	24232	19367	20990	20558	20019
PA	23221	17257	19099	8729	23440	16623	34509	25428	20982
CP	33159	19558	21393	11784	30174	17953	12657	18690	11997

ACB	23144	10253	17072	7649	26037	14381	30581	26629	19925
LS	17041	6650	11918	9003	23904	16428	6785	8262	7815
AAA	25446	13541	16447	9484	20930	21667	21657	18400	18885
GPe	24976	12139	16739	7940	22108	10753	11803	15073	14772
MA	30875	11542	17445	5815	27084	16355	24868	18066	13439
MS	33886	10198	23886	7692	36461	23346	23606	16646	17413
BAC	24068	5733	11756	5953	19364	12447	8833	8980	7237
BS	21273	13001	18448	11699	24688	16487	15851	21019	18710
DORsm	22144	18236	20772	15104	33095	17050	23086	29349	26033
AD	20509	11571	17748	10779	28015	13326	15526	17775	17721
HY	30920	9484	18077	9572	28510	23337	20581	18623	17708
ARH	22573	4768	10441	7879	22499	13528	20835	18703	18226
ADP	32210	6960	16226	8228	30795	22818	24216	18872	16923
AHN	30442	9800	16367	9025	28260	20526	21359	20148	18619
A13	30072	17325	25442	14771	33976	23269	25072	23658	22269
MB	31271	21590	21256	13718	37148	16118	15306	23874	17994
IC	37799	50760	38351	19526	61811	19891	15307	33208	23985
APN	37315	22166	25184	16654	39738	14876	12846	23064	16041
SNc	25162	19831	18732	12978	32327	10200	9374	16264	10874
P	14324	6858	12292	5169	17488	7196	10549	14639	16594
KF	13943	12055	19606	5494	15559	7478	14543	22827	28922
Acs5	18747	6484	19025	7513	23303	10724	13977	19301	20227
CS	25654	11964	19787	9253	31869	9706	9184	14091	15509
MY	23133	9594	14425	5800	13704	8325	20281	17362	15108
AP	25007	23692	25283	10523	25399	9100	27271	35320	26199
ACVI	37345	13709	25953	9118	21117	11687	28554	33776	27172
CB	26645	18278	19501	6460	17132	12011	15181	23935	26402
FN	36062	42105	51586	10895	10967	26773	37518	55981	54320
oct	21725	13587	13891	7346	16906	9292	12936	15907	13310

Supplementary table 6

Quantification of the number of bifurcation points in the C57BL/6J, CD1 and BALB/c samples in the microscopy space, units are in counts/mm3.

Cluster	BL6#1	BL6#2	BL6#3	CD1#1	CD1#2	CD1#3	BALBC #1	BALBC #2	BALBC #3
FRP	6.17	7.04	7.00	10.60	6.79	7.98	7.33	6.95	7.09
MO	6.21	7.21	6.88	6.25	6.11	6.58	7.35	7.71	7.52
SS	6.43	7.40	7.14	6.37	6.50	6.76	7.40	7.78	7.51
GU	6.63	8.05	8.03	6.43	7.10	7.15	8.45	8.27	8.26
VISC	6.68	7.97	7.28	6.89	6.98	7.35	7.60	7.72	7.02
AUD	6.06	7.13	6.80	6.41	5.90	6.42	7.74	8.00	7.51
VIS	6.21	7.03	6.80	6.25	6.10	6.25	7.44	7.93	7.42
ACA	7.01	7.06	7.48	6.59	6.95	7.36	9.44	10.37	8.38
PL	6.52	7.44	6.87	6.41	6.35	7.01	7.99	8.38	8.24
ILA	6.95	7.28	7.26	6.93	6.45	7.05	8.05	8.73	8.08
ORB	6.81	7.24	7.01	6.71	6.31	6.55	7.51	7.30	7.92
AI	6.42	7.55	7.43	6.44	6.46	6.82	8.15	8.18	7.58
RSP	6.31	6.90	6.89	6.35	6.40	6.70	7.72	8.21	8.35
PTL	6.11	7.03	6.81	6.08	6.13	6.29	7.58	7.87	7.47
TE	6.12	7.24	6.81	6.13	5.94	5.98	7.47	7.90	7.25
PERI	6.39	7.26	6.99	6.06	6.21	6.08	7.62	7.71	7.52
ECT	6.38	7.13	6.85	6.10	6.07	5.98	7.64	7.96	7.42
OLF	6.88	7.31	7.41	6.79	6.60	7.43	7.62	7.76	7.55
AOB	6.45	8.09	7.74	6.49	7.39	7.31	7.91	8.34	7.34
AOBgr	7.87	8.01	8.44	7.75	7.05	8.80	8.11	7.49	7.42
AON	6.46	6.83	7.25	6.43	6.61	6.74	7.71	7.89	8.05
TT	8.57	7.59	8.58	7.61	6.92	8.76	8.73	8.01	7.83
DP	6.64	7.04	7.44	6.39	6.33	7.61	8.32	7.98	8.22
PIR	6.54	7.14	7.67	6.43	6.53	7.03	8.20	8.08	7.66
COA	6.48	6.99	7.47	6.90	6.53	6.86	9.06	8.81	7.93
PAA	6.67	6.77	7.76	7.28	6.47	7.36	8.76	8.23	7.72
TR	6.49	7.43	7.39	6.31	6.57	5.98	8.20	9.07	7.62
CA	7.68	7.46	7.94	7.71	6.72	8.11	11.78	12.43	9.66
CA1sp	7.02	6.69	7.25	6.37	6.22	8.57	7.80	7.65	8.29
ENT	6.26	7.24	6.95	6.24	6.74	6.67	7.55	8.11	7.53
PAR	7.32	6.92	7.00	6.48	6.81	7.61	7.39	7.46	7.26
POST	7.29	7.83	8.19	7.91	6.93	7.63	8.17	7.66	8.83
PRE	9.85	7.81	7.60	9.12	7.27	8.70	10.48	7.45	10.80
SUB	7.01	7.50	7.57	7.01	7.19	6.76	7.54	7.69	7.37
ProS	6.31	7.04	7.13	6.41	6.30	6.58	7.58	7.99	8.00
CLA	6.65	7.22	7.85	6.36	6.88	7.00	8.64	8.15	7.62
EP	6.50	7.25	7.68	6.37	6.59	6.83	8.54	8.33	7.81
LA	6.24	6.39	7.19	6.31	6.41	6.57	8.89	8.89	8.11
BLA	6.25	6.75	7.62	6.31	6.57	6.54	8.89	8.88	8.19
BMA	6.38	6.61	7.66	6.53	6.74	7.14	9.16	8.87	8.61
PA	6.18	6.72	7.42	6.18	6.25	6.50	8.57	8.62	7.79
CP	6.90	6.70	7.62	6.77	6.61	7.54	7.90	8.02	7.66

ACB	6.48	6.14	7.11	6.65	6.17	6.87	7.74	7.52	7.03
LS	6.15	6.40	7.33	6.46	6.87	6.44	7.02	7.47	7.14
AAA	6.89	6.81	7.54	7.79	6.94	7.88	9.10	8.24	8.37
GPe	6.57	6.21	7.39	6.54	6.66	7.29	7.75	7.95	7.55
MA	6.83	6.31	7.53	6.93	6.36	7.22	7.68	7.41	7.42
MS	6.90	6.83	7.66	7.57	7.07	8.80	7.28	7.65	7.38
BAC	6.69	7.60	8.04	6.00	7.16	6.09	7.27	7.78	7.34
BS	6.36	6.57	7.16	6.45	6.47	6.69	7.70	7.66	7.37
DORsm	6.42	6.68	7.30	6.43	6.40	6.52	7.90	7.64	7.67
AD	6.21	6.41	6.93	6.41	6.21	6.67	7.35	7.26	7.15
HY	6.65	6.33	7.43	6.70	6.70	7.79	7.77	7.98	7.43
ARH	6.51	6.88	7.51	6.85	6.87	8.65	7.34	7.82	6.86
ADP	7.55	8.47	8.82	9.63	7.28	8.99	7.67	7.92	7.49
AHN	6.81	6.69	7.73	6.74	6.59	7.47	7.49	7.81	7.32
A13	6.78	6.51	7.31	6.97	7.36	7.86	8.11	7.36	7.31
MB	6.37	6.92	7.68	6.17	6.60	6.51	7.62	7.82	7.56
IC	6.45	6.71	6.82	6.32	7.02	6.71	7.90	8.18	7.62
APN	6.43	6.84	7.20	6.08	6.58	6.39	7.43	7.43	7.19
SNc	6.92	7.59	7.89	6.78	6.65	6.88	7.79	8.26	7.81
P	6.99	6.92	7.30	6.96	6.72	7.65	7.27	7.83	7.46
KF	6.54	6.71	6.77	7.28	6.76	7.61	7.56	7.30	7.19
Acs5	6.58	6.37	6.94	6.92	6.21	7.24	7.38	7.26	7.21
CS	6.37	6.11	6.80	5.70	6.13	6.29	7.04	7.51	7.32
MY	6.59	6.49	7.08	6.52	6.85	6.86	7.76	8.21	7.51
AP	6.15	6.37	6.62	6.25	6.67	5.90	7.11	7.67	6.89
ACVI	6.89	6.37	7.05	6.80	6.65	6.36	7.50	7.98	7.38
CB	6.53	7.09	8.01	7.66	6.94	7.20	7.47	8.13	7.67
FN	6.30	6.44	7.01	6.40	6.05	6.27	7.37	7.13	7.14
oct	6.93	6.90	7.36	6.80	6.77	7.12	7.77	7.89	7.37

Supplementary table 7

Quantification of the radii in the C57BL/6J, CD1 and BALB/c samples in the microscopy space, units are in µm.

Cluster	BL6#1	BL6#2	BL6#3	CD1#1	CD1#2	CD1#3	BALBC #1	BALBC #2	BALBC #3
FRP	513.82	798.55	523.34	205.47	425.49	104.89	273.85	416.65	449.20
MO	748.27	879.58	589.07	468.95	780.32	363.00	742.96	723.58	636.58
SS	872.71	1029.32	829.81	554.34	1035.76	637.42	728.90	736.09	618.47
GU	820.40	804.59	666.22	629.23	1049.95	803.98	600.63	597.20	588.15
VISC	725.61	816.54	656.18	520.71	1010.32	650.06	475.67	546.08	553.35
AUD	663.33	969.64	668.40	634.92	814.85	608.00	760.86	830.61	766.07
VIS	663.10	887.08	632.79	418.62	752.73	432.92	691.42	783.77	686.91
ACA	734.28	704.20	560.42	446.24	854.84	494.68	581.45	709.58	559.57
PL	763.19	714.03	528.44	402.49	739.04	502.46	554.37	657.87	644.36
ILA	765.83	521.75	359.05	519.92	709.60	629.88	522.47	630.98	557.01
ORB	970.56	793.58	643.17	504.55	864.11	535.22	620.79	734.78	671.63
AI	745.66	746.30	573.08	450.08	770.26	520.61	654.50	606.86	606.28
RSP	866.37	833.53	589.71	397.26	882.77	502.00	554.10	780.90	639.93
PTL	421.05	879.85	597.98	439.56	721.62	402.40	690.29	730.74	584.46
TE	497.22	815.75	581.53	513.97	795.62	489.01	574.86	719.72	633.72
PERI	448.91	668.78	545.75	310.20	653.38	346.93	463.21	532.25	553.12
ECT	439.39	694.61	539.88	384.91	715.51	388.97	471.36	616.33	589.65
OLF	655.50	377.57	515.16	359.59	879.66	552.47	593.31	624.46	559.64
AOB	781.75	602.76	486.84	374.00	781.45	531.24	578.77	513.32	592.68
AOBgr	498.57	361.81	551.62	232.89	549.29	393.51	566.35	577.94	517.54
AON	890.12	555.11	535.43	475.33	767.80	517.29	631.93	660.44	613.00
TT	680.10	289.00	439.91	367.52	656.28	559.24	580.03	558.74	582.04
DP	702.70	414.25	372.45	458.99	675.98	675.29	522.35	625.20	559.19
PIR	723.98	637.98	643.88	382.58	733.64	587.21	685.85	662.54	606.37
COA	370.70	363.07	491.36	216.09	518.72	369.35	497.68	476.89	503.36
PAA	370.96	236.65	477.60	191.62	594.10	432.22	471.72	505.09	453.47
TR	509.17	517.92	515.96	260.66	606.92	351.59	491.50	500.97	546.27
CA	491.89	508.66	470.52	357.07	564.53	394.46	443.78	525.47	454.25
CA1sp	469.59	431.62	451.56	316.66	502.04	357.42	369.40	490.13	434.14
ENT	527.91	769.72	512.26	368.92	696.84	371.37	535.30	603.18	531.58
PAR	627.90	675.76	549.65	433.44	899.59	429.56	631.95	857.43	551.24
POST	737.01	885.88	780.95	508.43	718.40	498.96	621.53	783.85	565.34
PRE	616.44	823.57	811.75	415.26	915.88	611.49	698.27	821.34	630.84
SUB	677.64	743.15	680.67	492.99	758.94	552.69	597.04	711.13	549.90
ProS	585.27	488.89	381.33	357.25	633.82	277.35	384.50	419.20	358.24
CLA	754.07	629.10	558.94	376.01	645.32	561.16	559.61	586.62	491.09
EP	643.43	589.43	519.83	322.98	613.71	464.44	511.75	532.33	501.80
LA	444.29	464.75	398.06	328.65	578.55	328.14	414.32	479.44	450.76
BLA	476.53	482.49	488.25	285.23	612.01	410.70	542.62	558.78	525.62
BMA	506.65	494.13	510.97	346.57	588.88	510.07	554.84	554.43	556.47
PA	535.89	504.04	535.23	316.64	562.73	436.23	714.75	628.06	574.03
CP	664.96	538.42	549.63	375.64	673.60	473.32	419.35	524.57	386.37

ACB	518.80	334.67	487.95	275.81	599.69	393.23	660.25	638.26	518.50
LS	456.27	287.93	406.75	328.32	574.59	470.23	293.36	331.35	311.69
AAA	538.61	432.88	475.22	323.99	522.85	528.80	544.59	511.23	525.89
GPe	571.48	413.32	489.14	280.55	571.24	346.60	386.42	455.60	451.12
MA	638.32	391.65	496.22	228.30	623.58	442.19	599.09	514.38	413.41
MS	687.63	361.85	588.15	280.67	704.56	544.62	556.44	478.30	456.55
BAC	558.57	262.03	396.06	232.21	498.48	365.27	329.17	335.82	286.51
BS	503.11	406.84	509.32	369.95	583.33	447.38	474.51	550.62	528.20
DORsm	527.66	517.16	542.30	446.81	721.64	466.98	591.91	682.03	648.23
AD	507.19	378.78	504.93	363.44	666.24	401.52	464.10	512.79	518.79
HY	651.17	320.51	488.30	318.08	632.29	547.38	545.10	505.51	493.61
ARH	497.55	175.69	318.76	281.40	554.05	375.50	546.34	488.47	499.21
ADP	654.35	255.73	451.40	293.33	646.42	528.10	586.63	516.12	462.64
AHN	641.53	317.97	464.29	314.70	627.70	511.36	561.12	536.59	506.86
A13	634.72	474.57	594.64	410.09	699.55	544.80	588.85	559.48	557.79
MB	657.20	566.73	562.73	421.31	743.23	439.06	460.01	603.55	501.22
IC	734.66	920.44	782.63	536.52	1027.19	495.87	450.05	731.22	575.98
APN	749.21	594.48	619.21	488.21	778.70	416.98	420.29	598.00	475.46
SNc	567.65	542.50	524.44	409.07	697.21	341.83	334.09	469.99	364.64
P	352.46	227.58	344.13	188.18	413.90	237.93	308.33	392.62	419.51
KF	362.08	344.28	472.36	201.65	402.21	253.10	401.08	553.97	636.51
Acs5	454.30	255.09	500.11	269.49	570.30	328.26	397.73	526.97	532.09
CS	580.24	399.79	538.51	319.40	690.70	340.16	340.45	437.28	455.05
MY	471.49	260.20	344.47	186.78	311.31	224.59	451.40	391.81	362.98
AP	546.03	567.45	566.29	319.32	523.77	272.45	612.00	717.35	592.61
ACVI	715.15	432.69	626.97	317.72	517.25	344.75	672.46	717.26	638.85
CB	543.28	434.98	432.60	212.02	393.57	317.89	392.11	517.13	547.28
FN	718.86	822.46	900.24	346.78	345.11	581.66	725.77	958.80	936.42
oct	479.28	373.89	372.65	255.10	419.38	272.00	360.18	423.28	375.03

Supplementary table 8

Quantification of the local vascular length (per volume) in the C57BL/6J, CD1 and BALB/c samples in the anatomical space. Units are in mm/mm3.

Cluster	BL6#1	BL6#2	BL6#3	CD1#1	CD1#2	CD1#3	BALBC #1	BALBC #2	BALBC #3
FRP	14188	21513	12420	4416	11827	1804	5643	9184	11470
MO	23989	28273	14743	10561	23884	8101	23199	20207	16646
SS	30731	38321	26517	13447	37930	17821	21007	21604	15774
GU	26568	25005	17880	15352	39666	23414	14706	16064	14706
VISC	23124	26924	18266	12296	36853	17906	9227	12793	12063
AUD	18457	32811	17865	15831	25313	16436	21653	25391	21319
VIS	18939	29151	16331	8668	22687	9873	18000	23396	18064
ACA	22288	17982	13520	9729	28576	11806	14084	18291	13732
PL	23282	17778	11719	8143	21561	12320	11744	16719	16504
ILA	22807	9847	6249	10852	18286	15325	9263	13544	11634
ORB	34517	22361	16336	10809	26551	12929	14465	18925	17342
AI	23271	21275	13516	9354	22635	12673	16661	15073	14407
RSP	29064	25885	15103	8209	29817	12359	12230	23588	16777
PTL	10978	29128	16839	9782	20674	9116	19017	20768	15225
TE	11916	24159	13681	11383	24273	11275	12507	19391	14960
PERI	10429	17318	11973	5373	17891	6952	8177	11773	11685
ECT	9350	17833	11757	7191	20126	7916	8632	14528	12927
OLF	21940	10715	14410	8312	31256	15014	17211	17867	15787
AOB	25631	18415	13924	7386	25724	11708	14100	12548	17380
AOBgr	13550	7598	13296	3775	13067	8527	14834	14055	12281
AON	30206	12781	12226	10028	22152	12261	16630	16194	14875
TT	20449	5478	9288	7655	18004	14204	15793	13956	16227
DP	20581	7338	6373	9077	18455	17221	9754	14357	12405
PIR	22940	17491	17291	7707	21789	15295	20005	17980	15353
COA	8871	7883	10157	3444	12249	7864	13178	11551	11295
PAA	8852	5432	10711	2783	14007	9435	12945	12803	11287
TR	12082	11368	10842	4019	15732	6742	11864	12020	12111
CA	12447	11034	10146	6660	14329	8608	8953	11420	9012
CA1sp	11775	8401	9236	5555	11637	7448	6250	9545	8139
ENT	14075	22497	12889	7601	21657	8621	12264	16069	12323
PAR	20360	21184	15822	9815	33398	11782	17342	27459	13729
POST	21566	28489	22645	11168	20893	12177	16043	22624	13847
PRE	16641	24949	23641	7953	29997	15956	19020	23913	14993
SUB	19812	20837	18062	10398	23667	13664	14311	18460	12160
ProS	17364	11687	8241	8047	18403	5392	8042	9180	6919
CLA	23254	14988	12588	6330	17193	13182	12000	13124	9739
EP	18225	13296	11060	5338	15324	9875	10578	11250	9934
LA	10635	8267	7126	5134	13984	5854	7194	9564	8110
BLA	11882	9351	9849	4412	14892	7893	11652	12003	10537
BMA	12715	9952	11199	6199	14615	11681	12659	12399	12074
PA	14005	10408	11519	5265	14137	10026	20813	15336	12654
CP	19999	11795	12902	7107	18198	10827	7634	11272	7236

ACB	13958	6184	10296	4613	15703	8673	18443	16060	12017
LS	10278	4011	7188	5430	14416	9908	4092	4983	4713
AAA	15347	8166	9919	5720	12623	13067	13062	11097	11389
GPe	15063	7321	10095	4789	13333	6485	7119	9091	8909
MA	18621	6961	10521	3507	16335	9864	14998	10896	8105
MS	20437	6150	14405	4639	21990	14080	14237	10039	10502
BAC	14516	3457	7090	3590	11678	7507	5327	5416	4365
BS	12830	7841	11126	7056	14889	9943	9560	12676	11284
DORsm	13355	10998	12527	9109	19960	10283	13923	17700	15700
AD	12369	6978	10704	6501	16896	8037	9363	10720	10688
HY	18648	5720	10902	5773	17194	14075	12413	11232	10680
ARH	13614	2876	6297	4752	13569	8159	12565	11280	10992
ADP	19426	4198	9786	4962	18572	13762	14605	11382	10206
AHN	18360	5911	9871	5443	17044	12379	12882	12151	11229
A13	18137	10449	15344	8908	20491	14033	15121	14268	13430
MB	18860	13021	12820	8274	22404	9721	9231	14399	10852
IC	22796	30614	23129	11776	37278	11996	9232	20028	14466
APN	22505	13368	15188	10044	23966	8972	7747	13910	9674
SNc	15175	11960	11297	7827	19497	6152	5654	9809	6558
P	8639	4136	7413	3118	10547	4340	6362	8829	10008
KF	8409	7270	11824	3313	9383	4510	8771	13767	17443
Acs5	11307	3911	11474	4531	14054	6468	8429	11640	12199
CS	15472	7215	11933	5581	19220	5854	5539	8498	9354
MY	13952	5786	8700	3498	8265	5021	12231	10471	9112
AP	15082	14288	15248	6347	15318	5488	16447	21302	15801
ACVI	22523	8268	15652	5499	12736	7048	17221	20370	16387
CB	16070	11024	11761	3896	10333	7244	9155	14435	15923
FN	21749	25394	31112	6571	6614	16147	22627	33762	32761
oct	13102	8194	8378	4431	10196	5604	7802	9594	8028

Supplementary table 9

Quantification of the number of bifurcation points in the C57BL/6J, CD1 and BALB/c samples in the anatomical space, units are in counts/mm^3.

Cluster	BL6#1	BL6#2	BL6#3	CD1#1	CD1#2	CD1#3	BALBC #1	BALBC #2	BALBC #3
FRP	7.30	8.33	8.28	12.55	8.03	9.44	8.68	8.22	8.39
MO	7.35	8.54	8.15	7.40	7.23	7.79	8.69	9.13	8.90
SS	7.61	8.75	8.45	7.54	7.69	8.00	8.76	9.21	8.89
GU	7.85	9.52	9.50	7.61	8.40	8.46	10.00	9.78	9.77
VISC	7.90	9.43	8.62	8.15	8.26	8.69	9.00	9.14	8.31
AUD	7.18	8.44	8.05	7.59	6.99	7.60	9.17	9.47	8.88
VIS	7.35	8.32	8.04	7.40	7.22	7.39	8.81	9.39	8.78
ACA	8.29	8.35	8.86	7.79	8.23	8.71	11.18	12.27	9.92
PL	7.72	8.81	8.13	7.58	7.51	8.30	9.46	9.92	9.75
ILA	8.22	8.61	8.60	8.21	7.63	8.34	9.53	10.33	9.57
ORB	8.06	8.57	8.29	7.94	7.46	7.76	8.88	8.64	9.37
AI	7.60	8.93	8.79	7.63	7.64	8.07	9.64	9.69	8.97
RSP	7.47	8.17	8.15	7.52	7.57	7.93	9.14	9.72	9.88
PTL	7.23	8.32	8.06	7.19	7.25	7.45	8.97	9.32	8.84
TE	7.25	8.57	8.06	7.26	7.03	7.08	8.85	9.36	8.59
PERI	7.57	8.59	8.28	7.17	7.35	7.20	9.01	9.13	8.90
ECT	7.55	8.43	8.11	7.22	7.18	7.08	9.05	9.42	8.78
OLF	8.15	8.65	8.77	8.04	7.81	8.79	9.01	9.19	8.93
AOB	7.63	9.57	9.16	7.68	8.75	8.66	9.36	9.87	8.69
AOBgr	9.32	9.48	9.99	9.18	8.35	10.41	9.60	8.87	8.78
AON	7.64	8.08	8.58	7.61	7.82	7.98	9.13	9.34	9.53
TT	10.14	8.98	10.15	9.01	8.19	10.37	10.33	9.48	9.26
DP	7.86	8.33	8.80	7.57	7.49	9.01	9.85	9.44	9.73
PIR	7.74	8.45	9.08	7.61	7.73	8.32	9.70	9.57	9.07
COA	7.67	8.28	8.84	8.16	7.72	8.11	10.72	10.43	9.39
PAA	7.90	8.01	9.19	8.62	7.66	8.71	10.36	9.74	9.14
TR	7.68	8.79	8.75	7.47	7.77	7.07	9.71	10.74	9.01
CA	9.09	8.84	9.40	9.13	7.95	9.59	13.94	14.71	11.43
CA1sp	8.30	7.92	8.59	7.54	7.36	10.15	9.23	9.06	9.81
ENT	7.41	8.57	8.22	7.39	7.98	7.90	8.94	9.60	8.91
PAR	8.66	8.20	8.28	7.67	8.06	9.01	8.75	8.84	8.59
POST	8.63	9.27	9.69	9.36	8.20	9.03	9.67	9.07	10.45
PRE	11.66	9.24	9.00	10.79	8.61	10.30	12.41	8.82	12.78
SUB	8.30	8.87	8.97	8.30	8.51	8.00	8.93	9.11	8.72
ProS	7.47	8.33	8.43	7.59	7.46	7.79	8.97	9.46	9.47
CLA	7.87	8.54	9.29	7.53	8.14	8.29	10.23	9.65	9.02
EP	7.69	8.58	9.09	7.54	7.80	8.08	10.11	9.86	9.24
LA	7.39	7.57	8.51	7.47	7.58	7.78	10.52	10.52	9.60
BLA	7.40	7.98	9.02	7.47	7.77	7.75	10.52	10.51	9.70
BMA	7.56	7.83	9.07	7.73	7.97	8.45	10.84	10.50	10.19
PA	7.32	7.95	8.78	7.31	7.40	7.70	10.14	10.20	9.22
CP	8.17	7.93	9.02	8.01	7.82	8.92	9.35	9.50	9.06

ACB	7.68	7.26	8.42	7.88	7.31	8.13	9.16	8.90	8.32
LS	7.28	7.58	8.67	7.65	8.14	7.62	8.31	8.84	8.45
AAA	8.16	8.06	8.93	9.23	8.21	9.33	10.77	9.75	9.91
GPe	7.78	7.35	8.75	7.74	7.88	8.63	9.17	9.41	8.93
MA	8.08	7.47	8.91	8.21	7.53	8.55	9.09	8.77	8.79
MS	8.17	8.09	9.07	8.96	8.37	10.42	8.62	9.06	8.74
BAC	7.92	8.99	9.52	7.11	8.47	7.20	8.61	9.21	8.69
BS	7.53	7.77	8.47	7.64	7.65	7.92	9.11	9.07	8.73
DORsm	7.60	7.91	8.64	7.61	7.57	7.72	9.35	9.04	9.08
AD	7.35	7.58	8.20	7.59	7.35	7.90	8.70	8.59	8.46
HY	7.88	7.49	8.79	7.93	7.93	9.22	9.20	9.44	8.79
ARH	7.71	8.14	8.89	8.11	8.13	10.23	8.69	9.25	8.12
ADP	8.94	10.03	10.44	11.40	8.62	10.64	9.08	9.38	8.87
AHN	8.06	7.92	9.15	7.98	7.80	8.84	8.86	9.24	8.66
A13	8.02	7.71	8.65	8.25	8.71	9.31	9.60	8.72	8.66
MB	7.53	8.19	9.09	7.31	7.81	7.70	9.02	9.26	8.95
IC	7.63	7.94	8.07	7.48	8.31	7.95	9.35	9.68	9.02
APN	7.61	8.10	8.53	7.19	7.79	7.56	8.80	8.79	8.51
SNc	8.19	8.98	9.33	8.03	7.88	8.14	9.21	9.78	9.25
P	8.28	8.19	8.65	8.24	7.96	9.06	8.61	9.27	8.83
KF	7.74	7.94	8.02	8.62	8.00	9.01	8.95	8.65	8.51
Acs5	7.79	7.54	8.22	8.19	7.35	8.57	8.74	8.59	8.53
CS	7.54	7.23	8.05	6.74	7.25	7.45	8.34	8.89	8.67
MY	7.80	7.68	8.37	7.72	8.11	8.12	9.19	9.72	8.89
AP	7.28	7.54	7.83	7.40	7.90	6.98	8.42	9.08	8.16
ACVI	8.16	7.54	8.34	8.04	7.87	7.53	8.87	9.45	8.73
CB	7.73	8.40	9.49	9.07	8.21	8.52	8.85	9.62	9.08
FN	7.46	7.62	8.30	7.57	7.16	7.43	8.72	8.44	8.45
oct	8.20	8.17	8.71	8.05	8.02	8.42	9.20	9.34	8.73

Supplementary table 10

Quantification of the radii in the C57BL/6J, CD1 and BALB/c samples in the anatomical space, units are in µm.

Brain region	**References**	***Normalized vascular length***			**Region-match**	**Quantified volume (µm)**
		Reported (m/mm^3)	Measured by VesSAP			
			microscopic space (m/mm^3)	anatomical space (m/mm^3)		
Cortex	Lugo-Hernandez et al.*	0.92 ± 0.17	1.28 ± 0.16	0.91 ± 0.11	yes	508×508×1500
Cortex	Tsai et al. **,[1]	0.88 ± 0.17	0.87 ± 0.13	0.63 ± 0.09	yes	256×1656×700
Cortex	Di Giovanna et al. ***	0.46 - 0.47	0.67 ± 0.03	0.48 ± 0.02	yes	361×361×350
Cortex	Zhang et al. ***, [α]	0.44 ± 0.04	1.47 ± 0.05	1.05 ± 0.04	no	504×504×886

*: 3DISCO technique, image acquisition in low (3.2x) and in high resolution (12.6x)

**: sucrose clearing of dissected dorsal cortex pieces

***: CLARITY technique

[α]: This study did not exactly define the quantified cortex regions and did not indicate a numerical correction for any potential volume change due to clearing[2], which can explain the difference compared to our results.

1 Tsai, P. S. et al. Correlations of neuronal and microvascular densities in murine cortex revealed by direct counting and colocalization of nuclei and vessels. Journal of Neuroscience 29, 14553-14570 (2009).

2 Kim, J. H. et al. Optimizing tissue-clearing conditions based on analysis of the critical factors affecting tissue-clearing procedures. Scientific reports 8, 12815 (2018).

Supplementary table 11

Comparison of VesSAP measurements with those in existing literature. Each comparison is calculated from n=3 C57BL/6J animals and two ROIs per animal. Data is shown as mean ± SD.

Cluster	**BL6 vs. CD1**	**BL6 vs. BALBC**	**CD1 vs. BLABC**	**BL6 vs. CD1**	**BL6 vs. BALBC**	**CD1 vs. BLABC**	**BL6 vs. CD1**	**BL6 vs. BALBC**	**CD1 vs. BLABC**
Average:	**Local length**	**Local length**	**Local length**	**Local bifurc.**	**Local bifurc.**	**Local bifurc.**	**Local radius**	**Local radius**	**Local radius**
FRP	0.41	0.09	-0.38	0.36	0.26	-0.17	0.31	-1.30	-1.49
MO	0.39	0.07	-0.37	0.35	0.24	-0.16	0.37	-1.31	-1.59
SS	0.38	0.07	-0.36	0.34	0.24	-0.15	0.36	-1.31	-1.59
GU	0.38	0.05	-0.38	0.34	0.22	-0.17	0.36	-1.31	-1.58
VISC	0.40	0.03	-0.41	0.36	0.21	-0.20	0.34	-1.31	-1.56
AUD	0.41	0.01	-0.45	0.37	0.18	-0.24	0.34	-1.33	-1.57
VIS	0.41	0.01	-0.45	0.37	0.19	-0.24	0.34	-1.32	-1.56
ACA	0.40	0.01	-0.44	0.36	0.19	-0.22	0.33	-1.31	-1.54
PL	0.40	0.00	-0.44	0.36	0.18	-0.23	0.33	-1.30	-1.54
ILA	0.39	0.00	-0.44	0.36	0.18	-0.23	0.32	-1.29	-1.52
ORB	0.41	0.00	-0.45	0.37	0.17	-0.25	0.32	-1.27	-1.50
AI	0.40	-0.02	-0.46	0.36	0.16	-0.25	0.31	-1.27	-1.49
RSP	0.40	-0.02	-0.46	0.36	0.15	-0.25	0.30	-1.27	-1.47
PTL	0.39	-0.04	-0.46	0.35	0.13	-0.26	0.29	-1.25	-1.45
TE	0.39	-0.04	-0.46	0.34	0.14	-0.25	0.29	-1.24	-1.43
PERI	0.39	-0.03	-0.46	0.35	0.13	-0.25	0.27	-1.23	-1.42
ECT	0.38	-0.04	-0.46	0.34	0.13	-0.25	0.25	-1.22	-1.40
OLF	0.38	-0.04	-0.45	0.34	0.12	-0.26	0.24	-1.22	-1.38
AOB	0.40	-0.03	-0.47	0.36	0.13	-0.27	0.23	-1.22	-1.38
AOBgr	0.40	-0.04	-0.48	0.36	0.12	-0.28	0.23	-1.23	-1.38
AON	0.40	-0.03	-0.46	0.35	0.13	-0.26	0.23	-1.27	-1.42
TT	0.40	-0.03	-0.46	0.35	0.12	-0.26	0.22	-1.25	-1.40
DP	0.42	-0.02	-0.46	0.36	0.14	-0.26	0.22	-1.29	-1.42
PIR	0.44	-0.01	-0.48	0.38	0.14	-0.27	0.21	-1.28	-1.40
COA	0.44	-0.01	-0.48	0.38	0.14	-0.27	0.20	-1.27	-1.38
PAA	0.44	0.01	-0.47	0.38	0.16	-0.26	0.20	-1.24	-1.35
TR	0.46	0.03	-0.47	0.39	0.17	-0.25	0.20	-1.23	-1.34
CA	0.45	0.03	-0.46	0.39	0.18	-0.24	0.18	-1.21	-1.31
CA1sp	0.45	0.02	-0.46	0.39	0.18	-0.24	0.17	-1.34	-1.43
ENT	0.45	0.02	-0.46	0.39	0.17	-0.25	0.18	-1.33	-1.44
PAR	0.44	0.01	-0.46	0.38	0.16	-0.25	0.17	-1.31	-1.42
POST	0.45	0.02	-0.46	0.40	0.17	-0.26	0.17	-1.32	-1.43
PRE	0.43	0.00	-0.46	0.37	0.15	-0.26	0.17	-1.35	-1.44
SUB	0.44	-0.01	-0.47	0.38	0.14	-0.26	0.19	-1.58	-1.65
ProS	0.43	-0.03	-0.48	0.37	0.12	-0.28	0.17	-1.60	-1.65
CLA	0.43	-0.05	-0.51	0.37	0.10	-0.30	0.16	-1.58	-1.61
EP	0.42	-0.07	-0.51	0.36	0.07	-0.31	0.14	-1.58	-1.58

LA	0.41	-0.09	-0.51	0.35	0.05	-0.31	0.11	-1.57	-1.53
BLA	0.41	-0.09	-0.52	0.35	0.05	-0.32	0.11	-1.53	-1.48
BMA	0.41	-0.08	-0.51	0.35	0.06	-0.31	0.09	-1.52	-1.43
PA	0.41	-0.07	-0.50	0.36	0.07	-0.31	0.09	-1.51	-1.40
CP	0.40	-0.04	-0.47	0.35	0.10	-0.28	0.06	-1.48	-1.33
ACB	0.40	-0.08	-0.50	0.34	0.06	-0.31	0.06	-1.46	-1.31
LS	0.40	-0.04	-0.47	0.35	0.09	-0.28	0.06	-1.45	-1.29
AAA	0.43	-0.06	-0.52	0.38	0.08	-0.33	0.06	-1.46	-1.28
GPe	0.44	-0.05	-0.52	0.38	0.09	-0.32	0.09	-1.45	-1.31
MA	0.43	-0.07	-0.52	0.38	0.07	-0.33	0.10	-1.41	-1.27
MS	0.42	-0.07	-0.52	0.38	0.07	-0.33	0.10	-1.40	-1.26
BAC	0.43	-0.09	-0.55	0.40	0.06	-0.36	0.16	-1.42	-1.39
BS	0.44	-0.12	-0.59	0.41	0.03	-0.40	0.09	-1.51	-1.36
DORsm	0.45	-0.11	-0.59	0.42	0.04	-0.41	0.08	-1.46	-1.31
AD	0.47	-0.07	-0.59	0.44	0.07	-0.40	0.05	-1.41	-1.23
HY	0.49	-0.06	-0.60	0.46	0.08	-0.42	0.05	-1.40	-1.20
ARH	0.52	-0.05	-0.62	0.49	0.08	-0.44	0.07	-1.35	-1.19
ADP	0.58	0.01	-0.60	0.52	0.12	-0.43	0.12	-1.38	-1.31
AHN	0.63	0.04	-0.62	0.57	0.13	-0.45	0.23	-1.82	-1.97
A13	0.66	0.07	-0.63	0.60	0.15	-0.47	0.22	-1.87	-1.99
MB	0.70	0.07	-0.66	0.64	0.15	-0.50	0.33	-1.85	-2.19
IC	0.72	0.04	-0.71	0.66	0.12	-0.55	0.26	-1.87	-2.07
APN	0.83	-0.07	-0.89	0.79	-0.01	-0.75	0.28	-1.75	-1.98
SNc	0.89	-0.17	-1.03	0.86	-0.11	-0.90	0.20	-1.74	-1.91
P	0.94	-0.28	-1.22	0.91	-0.20	-1.07	0.08	-1.98	-1.79
KF	1.04	-0.26	-1.29	0.99	-0.19	-1.12	0.10	-2.03	-1.89
Acs5	1.05	-0.19	-1.20	1.01	-0.13	-1.06	0.26	-1.96	-2.14
CS	1.19	-0.14	-1.24	1.13	-0.11	-1.11	0.34	-1.91	-2.25
MY	1.34	-0.24	-1.53	1.29	-0.21	-1.41	0.27	-1.86	-2.21
AP	1.51	-0.25	-1.65	1.40	-0.22	-1.48	0.31	-1.64	-2.03
ACVI	1.42	-0.18	-1.49	1.37	-0.15	-1.38	0.34	-1.61	-2.08
CB	1.34	-0.08	-1.26	1.34	-0.09	-1.19	0.30	-1.35	-1.74
FN	1.31	-0.07	-1.21	1.32	-0.10	-1.18	0.65	-1.74	-2.43
oct	1.21	0.46	-1.04	1.08	0.68	-0.77	0.73	-2.34	-3.32

Supplementary table 12

Statistical estimation of the difference between the local properties of the neurovasculature in the C57BL/6J, CD1 and BALB/c samples using Cohen's *d.* Each comparison is calculated from n=3 animals per strain.

Supplementary Material: clDice - a Novel Topology-Preserving Loss Function for Tubular Structure Segmentation

Supplementary Material for clDice - a Novel Topology-Preserving Loss Function for Tubular Structure Segmentation

Suprosanna Shit *[1] Johannes C. Paetzold *[1] Ivan Ezhov[1] Anjany Sekuboyina[1]
Alexander Unger[1] Andrey Zhylka[2] Josien P. W. Pluim[2] Ulrich Bauer[1] Bjoern H. Menze[1]
[1]Technical University of Munich [2] Eindhoven University of Technology

1. Theory - *clDice* in Digital Topology

In addition to our Theorem 1 in the main paper, we are providing intuitive interpretations of *clDice* from the digital topology perspective. Betti numbers describe and quantify topological differences in algebraic topology. The first three Betti numbers (β_0, β_1, and β_2) comprehensively capture the manifolds appearing in 2D and 3D topological space. Specifically,

- β_0 represents the number of *connected-components*,
- β_1 represents the number of *circular holes*, and
- β_2 represents the number of *cavities* (Only in 3D)

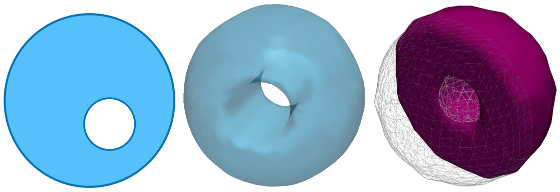

Figure 1. Examples of the topology properties. Left, a hole in 2D, in the middle a hole in 3D and right a cavity inside a sphere in 3D.

Using the concepts of Betti numbers and digital topology by Kong et al. [3, 6], we formulate the effect of topological changes between a true binary mask (V_L) and a predicted binary mask (V_P) in Fig. 2. We will use the following definition of **ghosts** and **misses**, see Figure 2.

1. **Ghosts in skeleton:** We define ghosts in the predicted skeleton (S_P) when $S_P \not\subset V_L$. This means the predicted skeleton is not completely included in the true mask. In other words, there exist false-positives in the prediction, which survive after skeletonization.

2. **Misses in skeleton:** We define misses in the predicted skeleton (S_P) when $S_L \not\subset V_P$. This means the true skeleton is not completely included in the predicted mask. In other words, there are false-negatives in the prediction, which survive after skeletonization.

The false positives and false negatives are denoted by $V_P \setminus V_L$ and $V_L \setminus V_P$, respectively, where $\setminus$ denotes a set difference operation. The loss function aims to minimize both errors. We call an error correction to happen when the value of a previously false-negative or false-positive voxel flips to a correct value. Commonly used voxel-wise loss functions, such as Dice-loss, treat every false-positive and false-negative equally, irrespective of the improvement in regards to topological differences upon their individual error correction. Thus, they cannot guarantee homotopy equivalence until and unless every single voxel is correctly classified. In stark contrast, we show in the following proposition that *clDice* guarantees homotopy equivalence under *a minimum error correction.*

Proposition 1. *For any topological differences between V_P and V_L, achieving optimal clDice to guarantee homotopy equivalence requires a minimum error correction of V_P.*

Proof. From Fig 2, any topological differences between V_P and V_L will result in ghosts or misses in the foreground or background skeleton. Therefore, removing ghosts and misses are sufficient conditions to remove topological differences. Without the loss of generalizability, we consider the case of ghosts and misses separately:

For a **ghost** $g \subset S_P, \exists$ a set of predicted voxels $E1 \subset \{V_P \setminus V_L\}$ such that $V_P \setminus E1$ does not create any misses and removes g. Without the loss of generalizability, let's assume that there is only one ghost g. Now, to remove g, under a minimum error correction of V_P, we have to minimize $|E1|$. Let's say an optimum solution $E1_{min}$ exists. By construction, this implies that $V_P \setminus E1_{min}$ removes g.

For a **miss** $m \subset V_P^{\complement}, \exists$ a set of predicted voxels $E2 \subset \{V_L \setminus V_P\}$ such that $V_P \cup E2$ does not create any ghosts and removes m. Without the loss of generalizability, let's assume that there is only one miss m. Now, to remove m, under a minimum error correction of V_P, we have to minimize $|E2|$. Let's say an optimum solution $E2_{min}$ exists. By construction, this implies that $V_P \cup E2_{min}$ removes m.

Thus, in the absence of any ghosts and misses, from Lemma 1.1, *clDice*=1 for both foreground and background. Finally, Therefore, Theorem 1 (from the main paper) guarantees homotopy equivalence. □

Lemma 1.1. *In the absence of any ghosts and misses clDice=1.*

---

*The authors contributed equally to the work

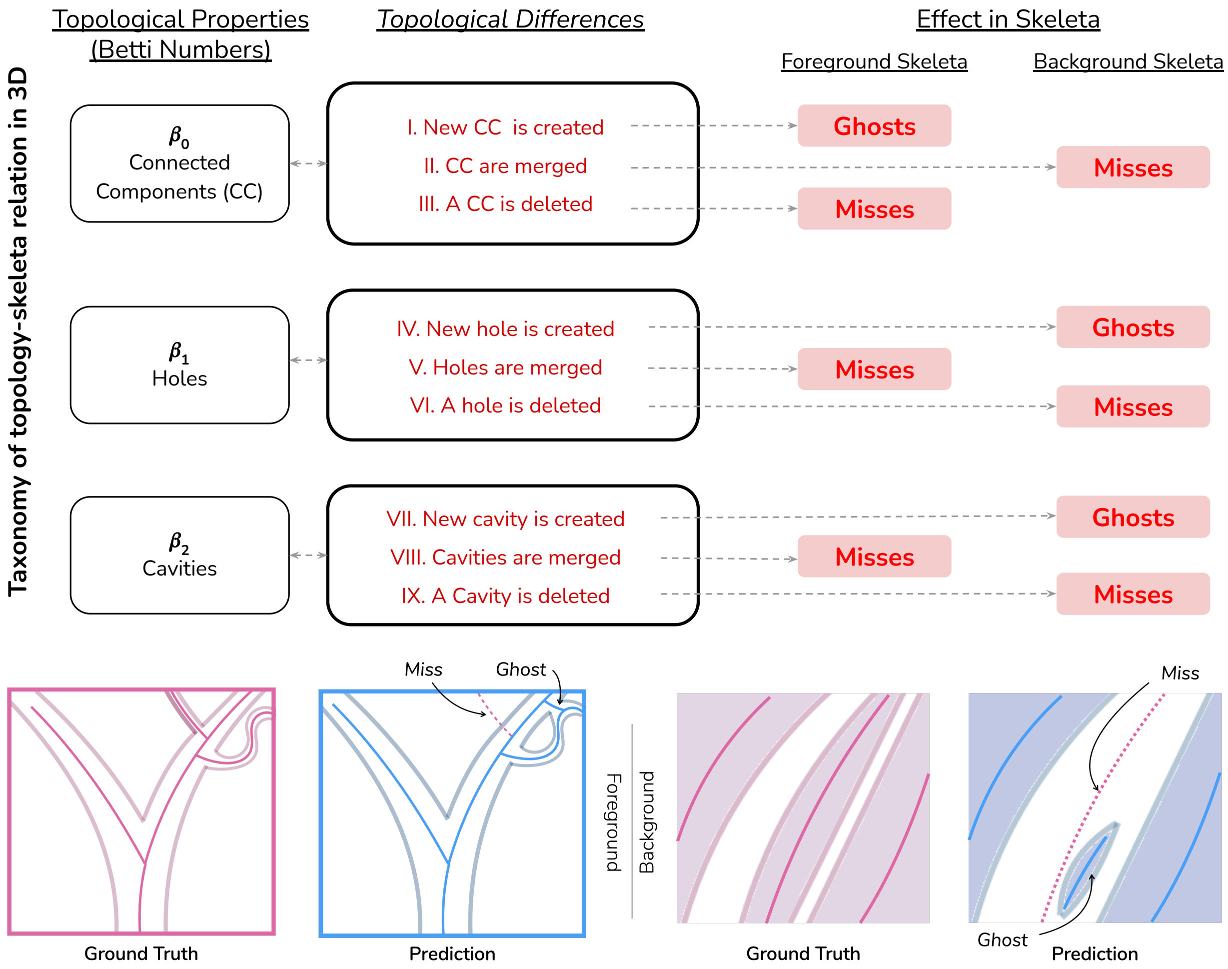

Figure 2. Upper part, left, taxonomy of the iff conditions to preserve topology in 3D using the concept of Betti numbers [3, 4]; interpreted as the necessary violation of skeleton properties for any possible topological change in the terminology of ghosts and misses (upper part right) . Lower part, intuitive depictions of ghosts and misses in the prediction; for the skeleton of the foreground (left) and the skeleton of the background (right).

Proof. The absence of any ghosts $S_P \in V_L$ implies $Tprec = 1$; and the absence of any misses $S_L \in V_P$ implies $Tsens = 1$. Hence, *clDice*=1. □

1.1. Interpretation of the Adaption to Highly Unbalanced Data According to Digital Topology:

Considering the adaptions we described in the main text, the following provides analysis on how these assumptions and adaptions are funded in the concept of ghosts and misses, described in the previous proofs. Importantly, the described adaptions are not detrimental to the performance of *clDice* for our datasets. We attribute this to the non-applicability of the necessary conditions specific to the background (i.e. II, IV, VI, VII, and IX in Figure 1), as explained below:

- II. → In tubular structures, all foreground objects are eccentric (or anisotropic). Therefore isotropic skeletonization will highly likely produce a ghost in the foreground.
- IV. → Creating a hole outside the labeled mask means adding a ghost in the foreground. Creating a hole inside the labeled mask is extremely unlikely because no such holes exist in our training data.
- VI. → The deletion of a hole without creating a miss is extremely unlikely because of the sparsity of the data.
- VII.and IX. (only for 3D) → Creating or removing a cavity is very unlikely because no cavities exist in our training data.

2. Additional Qualitative Results

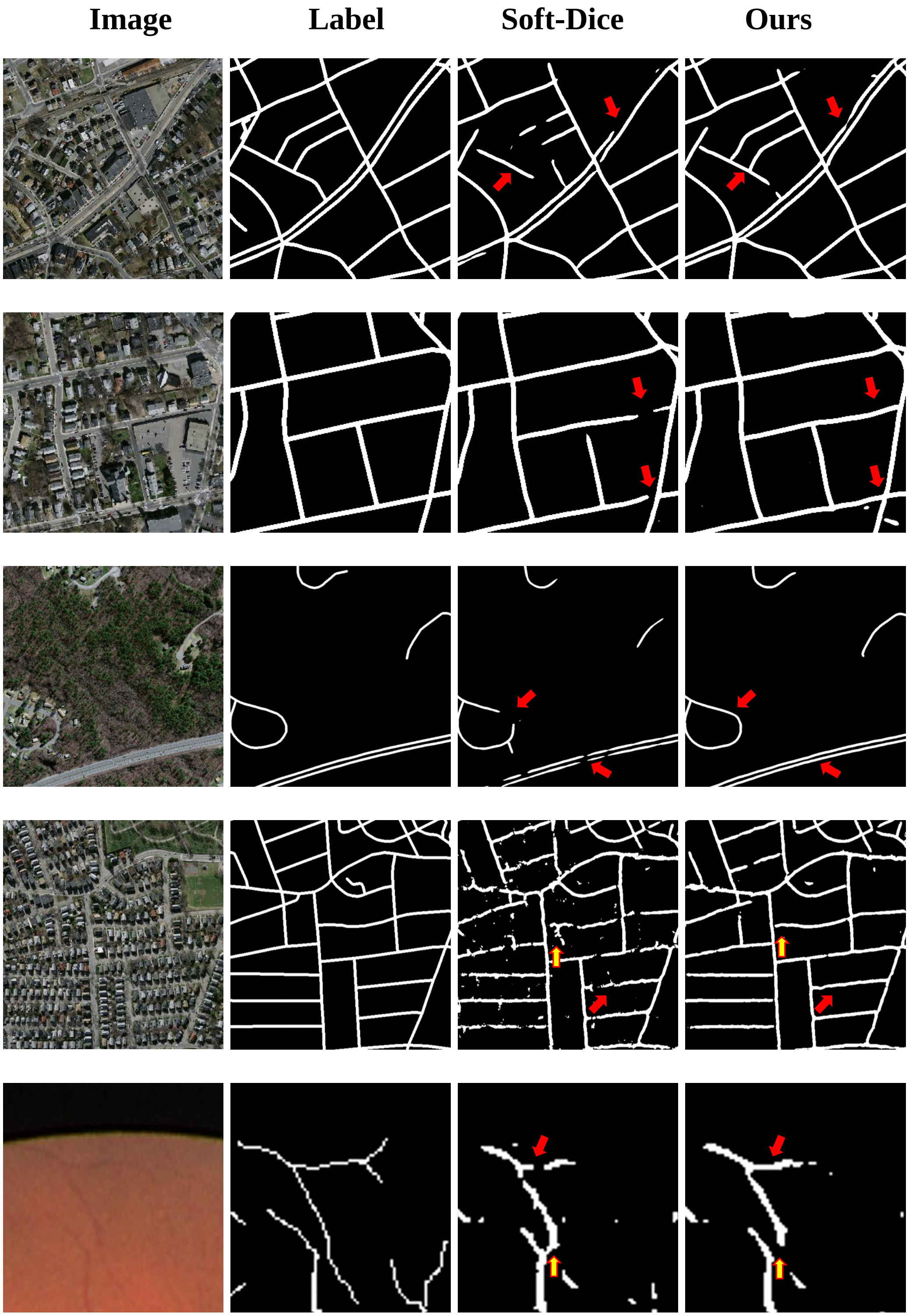

Figure 3. Qualitative results: for the Massachusetts Road dataset and for the DRIVE retina dataset (last row). From left to right, the real image, the label, the prediction using soft-dice and the predictions using the proposed $\mathcal{L}_c(\alpha = 0.5)$, respectively. The first three rows are U-Net results and the fourth row is an FCN result. This indicates that *soft-clDice* segments road connections which the soft-dice loss misses. Some, but not all, missed connections are indicated with solid red arrows, false positives are indicated with red-yellow arrows.

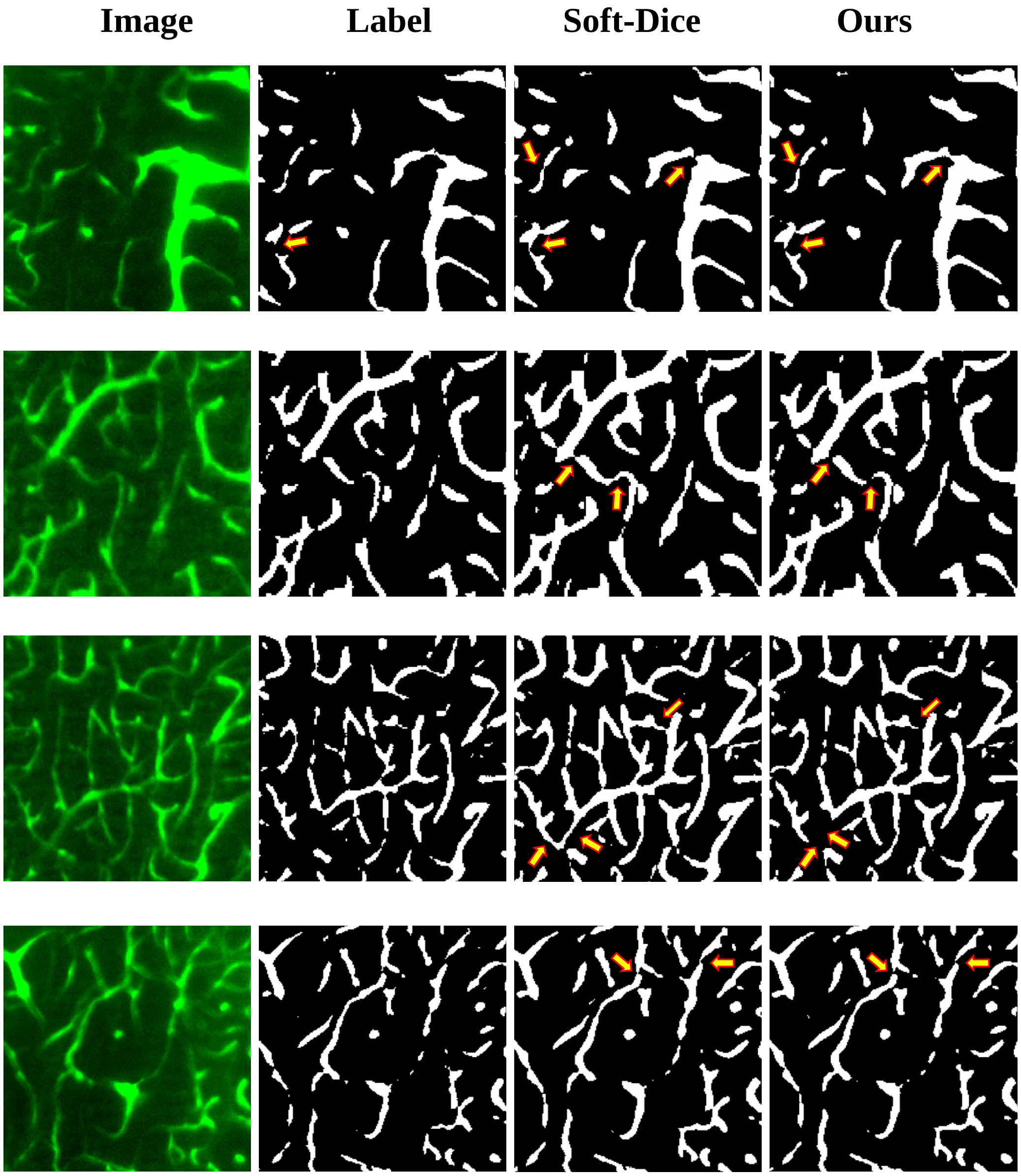

Figure 4. Qualitative results: 2D slices of the 3D vessel dataset for different sized field of views. From left to right, the real image, the label, the prediction using soft-dice and the U-Net predictions using $\mathcal{L}_c(\alpha = 0.4)$, respectively. These images show that *soft-clDice* helps to better segment the vessel connections. Importantly the networks trained using soft-dice over-segment the vessel radius and segments incorrect connections. Both of these errors are not present when we train including *soft-clDice* in the loss. Some, but not all, false positive connections are indicated with red-yellow arrows.

3. Comparison to Other Literature:

A recent pre-print proposed a region-separation approach, which aims to tackle the issue by analysing disconnected foreground elements [5]. Starting with the predicted distance map, a network learns to close ambiguous gaps by referring to a ground truth map which is dilated by a five-pixel kernel, which is used to cover the ambiguity. However, this does not generalize to scenarios with a close or highly varying proximity of the foreground elements (as is the case for e.g. capillary vessels, synaptic gaps or irregular road intersections). Any two foreground objects which are placed at a twice-of-kernel-size distance or closer to each other will potentially be connected by the trained network. This is facilitated by the loss function considering the gap as a foreground due to performing dilation in the training stage. Generalizing their approach to smaller kernels has been described as infeasible in their paper [5].

4. Datasets and Training Routine

For the DRIVE vessel segmentation dataset, we perform three-fold cross-validation with 30 images and deploy the best performing model on the test set with 10 images. For the Massachusetts Roads dataset, we choose a subset of 120 images (ignoring imaged without a network of roads) for three-fold cross-validation and test the models on the 13 official test images. For CREMI, we perform three-fold cross-validation on 324 images and test on 51 images. For the 3D synthetic dataset. we perform experiments using 15 volumes for training, 2 for validation, and 5 for testing. For the Vessap dataset, we use 11 volumes for training, 2 for validation and 4 for testing. In each of these cases, we report the performance of the model with the highest clDice score on the validation set.

5. Network Architectures

We use the following notation: $In(input\ channels)$, $Out(output\ channels)$,
$B(output\ channels)$ present input, output, and bottleneck information(for U-Net); $C(filter\ size, output\ channels)$ denote a convolutional layer followed by $ReLU$ and batch-normalization; $U(filter\ size, output\ channels)$ denote a trans-posed convolutional layer followed by $ReLU$ and batch-normalization; $\downarrow 2$ denotes maxpooling; $\oplus$ indicates concatenation of information from an encoder block. We had to choose a different FCN architecture for the Massachusetts road dataset because we realize that a larger model is needed to learn useful features for this complex task.

5.1. Drive Dataset

5.1.1 FCN :

$IN(3\text{ ch}) \rightarrow C(3,5) \rightarrow C(5,10) \rightarrow C(5,20) \rightarrow C(3,50) \rightarrow C(1,1) \rightarrow Out(1)$

5.1.2 Unet :

ConvBlock : $C_B(3, out\ size) \equiv C(3, out\ size) \rightarrow C(3, out\ size) \rightarrow \downarrow 2$

UpConvBlock: $U_B(3, out\ size) \equiv U(3, out\ size) \rightarrow \oplus \rightarrow C(3, out\ size)$

Encoder : $IN(3\text{ ch}) \rightarrow C_B(3,64) \rightarrow C_B(3,128) \rightarrow C_B(3,256) \rightarrow C_B(3,512) \rightarrow C_B(3,1024) \rightarrow B(1024)$

Decoder : $B(1024) \rightarrow U_B(3,1024) \rightarrow U_B(3,512) \rightarrow U_B(3,256) \rightarrow U_B(3,128) \rightarrow U_B(3,64) \rightarrow Out(1)$

5.2. Road Dataset

5.2.1 FCN :

$IN(3\text{ ch}) \rightarrow C(3,10) \rightarrow C(5,20) \rightarrow C(7,30) \rightarrow C(11,30) \rightarrow C(7,40) \rightarrow C(5,50) \rightarrow C(3,60) \rightarrow C(1,1) \rightarrow Out(1)$

5.2.2 Unet :

Same as Drive Dataset, except we used 2x2 up-convolutions instead of bilinear up-sampling followed by a 2D-convolution with kernel size 1.

5.3. Cremi Dataset

5.3.1 Unet :

Same as Road Dataset.

5.4. 3D Dataset

5.4.1 3D FCN :

$IN(1\text{ or }2\text{ ch}) \rightarrow C(3,5) \rightarrow C(5,10) \rightarrow C(5,20) \rightarrow C(3,50) \rightarrow C(1,1) \rightarrow Out(1)$

5.4.2 3D Unet :

ConvBlock : $C_B(3, out\ size) \equiv C(3, out\ size) \rightarrow C(3, out\ size) \rightarrow \downarrow 2$

UpConvBlock: $U_B(3, out\ size) \equiv U(3, out\ size) \rightarrow \oplus \rightarrow C(3, out\ size)$

Encoder : $IN(1\text{ or }2\text{ ch}) \rightarrow C_B(3,32) \rightarrow C_B(3,64) \rightarrow C_B(3,128) \rightarrow C_B(5,256) \rightarrow C_B(5,512) \rightarrow B(512)$

Decoder : $B(512) \rightarrow U_B(3,512) \rightarrow U_B(3,256) \rightarrow U_B(3,128) \rightarrow U_B(3,64) \rightarrow U_B(3,32) \rightarrow Out(1)$

Table 1. Total number of parameters for each of the architectures used in our experiment.

Dataset	Network	Number of parameters
Drive	FCN	15.52K
	UNet	28.94M
Road	FCN	279.67K
Cremi	UNet	31.03M
3D	FCN 2ch	58.66K
	Unet 2ch	19.21M

6. Soft Skeletonization Algorithm

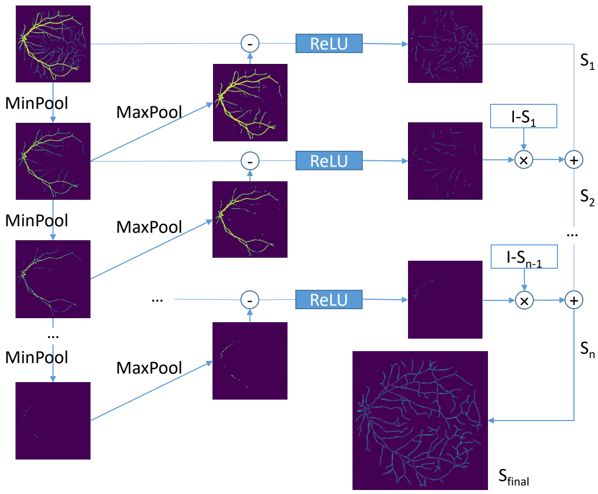

Figure 5. Scheme of our proposed differentiable skeletonization. On the top left the mask input is fed. Next, the input is reatedly eroded and dilated. The resulting erosions and dilations are compared to the image before dilation. The difference between thise images is part of the skeleton and will be added iteratively to obtain a full skeletonization. The ReLu operation eliminates pixels that were generated by the dilation but are not part of the oirginal or eroded image.

7. Code for the *clDice* similarity measure and the *soft-clDice* loss (PyTorch):

7.1. *clDice* measure

```
from skimage.morphology import skeletonize
import numpy as np
def cl_score(v, s):
    return np.sum(v*s)/np.sum(s)
def clDice(v_p, v_l):
    tprec = cl_score(v_p,skeletonize(v_l))
    tsens = cl_score(v_l,skeletonize(v_p))
    return 2*tprec*tsens/(tprec+tsens)
```

7.2. *soft-skeletonization* in 2D

```
import torch.nn.functional as F
def soft_erode(img):
    p1 = -F.max_pool2d(-img, (3,1), (1,1), (1,0))
    p2 = -F.max_pool2d(-img, (1,3), (1,1), (0,1))
    return torch.min(p1,p2)

def soft_dilate(img):
    return F.max_pool2d(img, (3,3), (1,1), (1,1))

def soft_open(img):
    return soft_dilate(soft_erode(img))
```

```
def soft_skel(img, iter):
    img1 = soft_open(img)
    skel = F.relu(img-img1)
    for j in range(iter):
        img = soft_erode(img)
        img1 = soft_open(img)
        delta = F.relu(img-img1)
        skel = skel + F.relu(delta-skel*delta)
    return skel
```

7.3. *soft-skeletonization* in 3D

```
import torch.nn.functional as F

def soft_erode(img):
    p1 = -F.max_pool3d(-img,(3,1,1),(1,1,1),(1,0,0))
    p2 = -F.max_pool3d(-img,(1,3,1),(1,1,1),(0,1,0))
    p3 = -F.max_pool3d(-img,(1,1,3),(1,1,1),(0,0,1))

    return torch.min(torch.min(p1, p2), p3)

def soft_dilate(img):
    return F.max_pool3d(img,(3,3,3),(1,1,1),(1,1,1))

def soft_open(img):
    return soft_dilate(soft_erode(img))

def soft_skel(img, iter_):
    img1  =  soft_open(img)
    skel  =  F.relu(img-img1)
    for j in range(iter_):
        img  =  soft_erode(img)
        img1  =  soft_open(img)
        delta  =  F.relu(img-img1)
        skel  =  skel +  F.relu(delta-skel*delta)
    return skel
```

8. Evaluation Metrics

As discused in the text, we compare the performance of various experimental setups using three types of metrics: volumetric, graph-based and topology-based.

8.1. Overlap-based:

Dice coefficient, Accuracy and *clDice*, we calculate these scores on the whole 2D/3D volumes. *clDice* is calculated using a morphological skeleton (skeletonize3D from the skimage library).

8.2. Graph-based:

We extract graphs from random patches of 64×64 pixels in 2D and $48 \times 48 \times 48$ in 3D images.

For the StreetmoverDistance (SMD) [1] we uniformly sample a fixed number of points from the graph of the prediction and label, match them and calculate the Wasserstein-distance between these graphs. For the junction-based metric (Opt-J) we compute the F1 score of junction-based metrics, recently proposed by [2]. According to their paper this metric is advantageous over all previous junction-based metrics as it can account for nodes with an arbitrary number of incident edges, making this metric more sensitive to end-points and missed connections in predicted networks. For more information please refor to their paper.

8.3. Topology-based:

For topology-based scores we calculate the Betti Errors for the Betti Numbers β_0 and β_1. Also, we calculate the Euler characteristic, $\chi = V - E + F$, where E is the number of edges, F is the number of faces and V is the number of vertices. We report the relative Euler characteristic error (χ_{ratio}), as the ratio of the χ of the predicted mask and that of the ground truth. Note that a χ_{ratio} closer to one is preferred. All three topology-based scores are calculated on random patches of 64×64 pixels in 2D and $48 \times 48 \times 48$ in 3D images.

9. Additional Quantitative Results

Table 2. Quantitative experimental results for the 3D synthetic vessel dataset. Bold numbers indicate the best performance. We trained baseline models of binary-cross-entropy (BCE), softDice and mean-squared-error loss (MSE) and combined them with our *soft-clDice* and varied the $\alpha > 0$. For all experiments we observe that using *soft-clDice* in $\mathcal{L}_c$ results in improved scores compared to *soft-Dice*. This improvement holds for almost $\alpha > 0$. We observe that *soft-clDice* can be efficiently combined with all three frequently used loss functions.

Loss	Dice	clDice
BCE	99.81	98.24
L_c, $\alpha = 0.5$	99.76	98.25
L_c, $\alpha = 0.4$	99.77	98.29
L_c, $\alpha = 0.3$	99.76	98.20
L_c, $\alpha = 0.2$	99.78	98.29
L_c, $\alpha = 0.1$	99.82	98.39
L_c, $\alpha = 0.01$	99.83	98.46
L_c, $\alpha = 0.001$	**99.85**	**98.42**
soft-Dice	99.74	97.07
L_c, $\alpha = 0.5$	99.74	97.53
L_c, $\alpha = 0.4$	99.74	97.07
L_c, $\alpha = 0.3$	**99.80**	**98.13**
L_c, $\alpha = 0.2$	99.74	97.08
L_c, $\alpha = 0.1$	99.74	97.08
L_c, $\alpha = 0.01$	99.74	97.07
L_c, $\alpha = 0.001$	99.74	97.12
MSE	99.71	97.03
L_c, $\alpha = 0.5$	99.62	98.22
L_c, $\alpha = 0.4$	99.65	97.04
L_c, $\alpha = 0.3$	99.67	98.16
L_c, $\alpha = 0.2$	99.70	97.10
L_c, $\alpha = 0.1$	99.74	98.21
L_c, $\alpha = 0.01$	99.82	98.32
L_c, $\alpha = 0.001$	**99.84**	**98.37**

References

[1] Davide Belli and Thomas Kipf. Image-conditioned graph generation for road network extraction. *arXiv preprint arXiv:1910.14388*, 2019. 4326

[2] Leonardo Citraro, Mateusz Koziński, and Pascal Fua. Towards reliable evaluation of algorithms for road network reconstruction from aerial images. In *European Conference on Computer Vision*, pages 703–719. Springer, 2020. 4326

[3] T. Yung Kong. On topology preservation in 2-D and 3-D thinning. *International journal of pattern recognition and artificial intelligence*, 9(05):813–844, 1995. 4321, 4322

[4] T Yung Kong and Azriel Rosenfeld. Digital topology: Introduction and survey. *Computer Vision, Graphics, and Image Processing*, 48(3):357–393, 1989. 4322

[5] Doruk Oner, Mateusz Koziński, Leonardo Citraro, Nathan C Dadap, Alexandra G Konings, and Pascal Fua. Promoting connectivity of network-like structures by enforcing region separation. *arXiv preprint arXiv:2009.07011*, 2020. 4324

[6] Azriel Rosenfeld. Digital topology. *The American Mathematical Monthly*, 86(8):621–630, 1979. 4321

Supplementary Material: Whole Brain Vessel Graphs: A Dataset and Benchmark for Graph Learning and Neuroscience (VesselGraph)

Supplementary material

A Additional graph visualisations

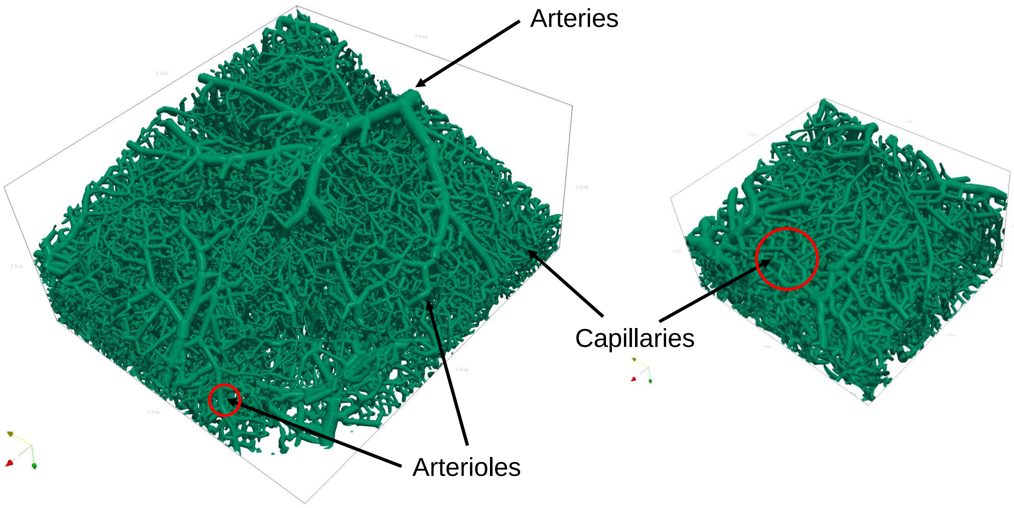

Figure 5: Graphical visualisations of the vessel graph and three different vessel types distinguishable by diameter.

B Code and dataset documentation

B.1 Hosting, licensing and author statement

All of our codes and baselines are available in a public github repository `https://github.com/jocpae/VesselGraph` licensed under an MIT License. All of our data is also freely available and can be downloaded from a university server following the links in `https://github.com/jocpae/VesselGraph#datasets`. The dataset is provided in CSV format. The dataset has the following DOI: `10.5281/zenodo.5301621`. All of our released data is licensed under an *Attribution-NonCommercial 4.0 International (CC BY-NC 4.0) license*. The authors confirm the CC licenses for the included datasets and declare to bear all responsibility in case of violation of rights. The authors declare no competing financial interests

B.2 Long term maintenance plan

The dataset and code has been permanently archived at Zenodo, guaranteeing long-term availability. We will update the dataset when novel segmentations of the whole brain vasculature become publicly available. Contributions will be solicited via GitHub pull request. Regarding maintenance, we will update the code repository for loading and processing the data; the links to the university server where the data is stored will also be kept up-to-date.

Additionally, we plan to incorporate our dataset into the Open Graph Benchmark[2]. Our dataset and dataloader are already compatible with the OGB data loader and platform. We believe that an integration into the OGB framework will further facilitate and simplify the usage of our data. We also provide an alternative dataloader for use with Pytorch Geometric.

B.3 Whole brain vessel imaging and segmentation

As discussed in the introduction, whole brain vascular imaging is an emerging field spanning different imaging techniques, among the first technologies were tissue clearing-based methods [9–12] which enable the fluorescent staining and clearing (that is, a chemical process which renders the organ transparent) of intact, whole

---

[2] `https://ogb.stanford.edu/`

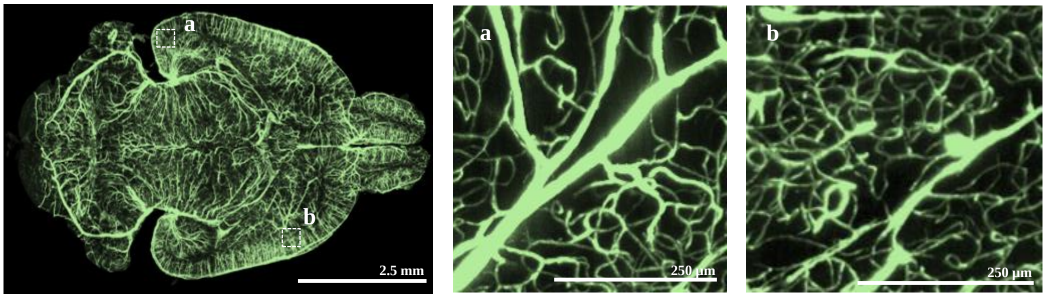

Figure 6: Local differences in vessel structure can be observed in different brain regions in a dataset of Todorov and Paetzold et al. [6].

brains with a subsequent imaging of the vessels with a 3D lightsheet microscope. Among the first imaging protocols were VesSAP [6], Tubemap [7] and the work by diGiovanna et al. [13]. Alternative imaging techniques are microCT[48, 49], magnetic resonance imaging [50] and optical coherence tomography [51], which however fail to achieve the spatial resolution to reliably image microcapillaries. Recently, a method based on synchrotron-based phase-contrast tomographic microscopy was developed, achieving an isotropic voxel size of 0.65 micrometers [52]. Other technologies, such as serial serial two-photon microscopic imaging are also developing rapidly with similar or even better resolution compared to the tissue clearing methods (e.g. $0.303 \times 0.303 \times 1.0$ resolution [1]), promising a widespread use/adoption of whole brain vascular imaging approaches in the future.

B.4 Individual datasets, licenses and animal experiments

The nine base datasets from the VesSAP paper [6] are available here: `http://discotechnologies.org/VesSAP/`. They are licensed under a Attribution-NonCommercial 4.0 International (CC BY-NC 4.0). The animal experiments were carried out under approval of the institutional ethics review board of the Government of Upper Bavaria (Regierung von Oberbayern, Munich, Germany), and in accordance with European directive 2010/63/EU for animal research, details can be read here `https://doi.org/10.1038/s41592-020-0792-1`.

The base datasets from Ji et al. [1] are licensed under an open source (BSD 3-Clause) license. They are available upon email request from the authors, their code is available at `https://neurophysics.ucsd.edu/software.php`. The animal experiments followed the Guide for the Care and Use of Laboratory Animals and have been approved by the Institutional Animal Care and Use Committee, details can be found in the original paper: `https://doi.org/10.1016/j.neuron.2021.02.006`

The synthetic data was generated by the authors themselves following the approach by Schneider et al. [32], the same license applies as for the graph datasets presented here. The synthetic base data can be downloaded here `https://github.com/giesekow/deepvesselnet/wiki/Datasets`.

C Graph documentation

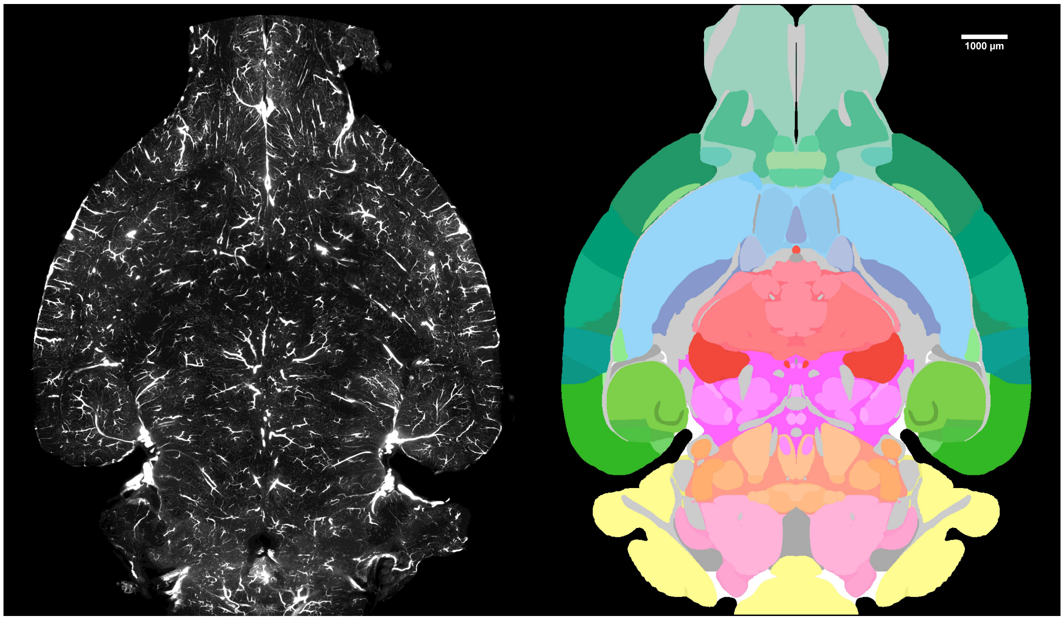

Figure 7: Rendering of the Allen brain atlas feature; on the left side a 2D image slice from the CD1-E-1 brain is depicted, on the right side a rendering of the Allen brain atlas regions corresponding to the coordinates of the image. A node n is assigned to a particular atlas region depending on the x_n, y_n, z_n coordinate of the node n .

C.1 Voreen parameters

In the following Sections, we discuss the details of the Voreen graph extraction pipeline which follows a four stage protocol introduced in Section 2. To recapitulate, the four stages are:

1. Skeletonization: The binary segmentation volume is reduced to a skeleton based representation by applying a standard topological thinning algorithm by Lee et al. [38].
2. Topology Extraction: memory efficient algorithms extract the vessel centerlines [39]. *Voreen* allows to store this intermediate representation in a combination with the graph.
3. Voxel-Branch Assignment: Computing of mapping between the so-called protograph (i.e. the initial graph) and the voxels of the binary segmentation.
4. Feature Extraction: On basis of the protograph and the mapping, several features can be computed from the foreground segmentation.

We chose the *Voreen* parameters in the following manner:

1. The *binarization threshold* is selected from the interval $[0, 1]$. This value is irrelevant for binary segmentation masks, e.g. VesSAP.
2. *Surface smoothing* is deactivated.
3. The relative *minimal bounding box diagonal* is set to 0.05.
4. The total *minimal bounding box diagonal* is set to 0 mm.
5. The *bulge size* is set to 3.0, see Figure 9.

Bulge Size As depicted in the figures below, the total number of nodes decreases when increasing the bulge size parameter. This is expected, as the bulge size describes the relation between parent vessel and branch, and the relation between vessel *bumpiness* and parent vessel [31]. The bulge size can be configured between $[0 < x < 10]$.

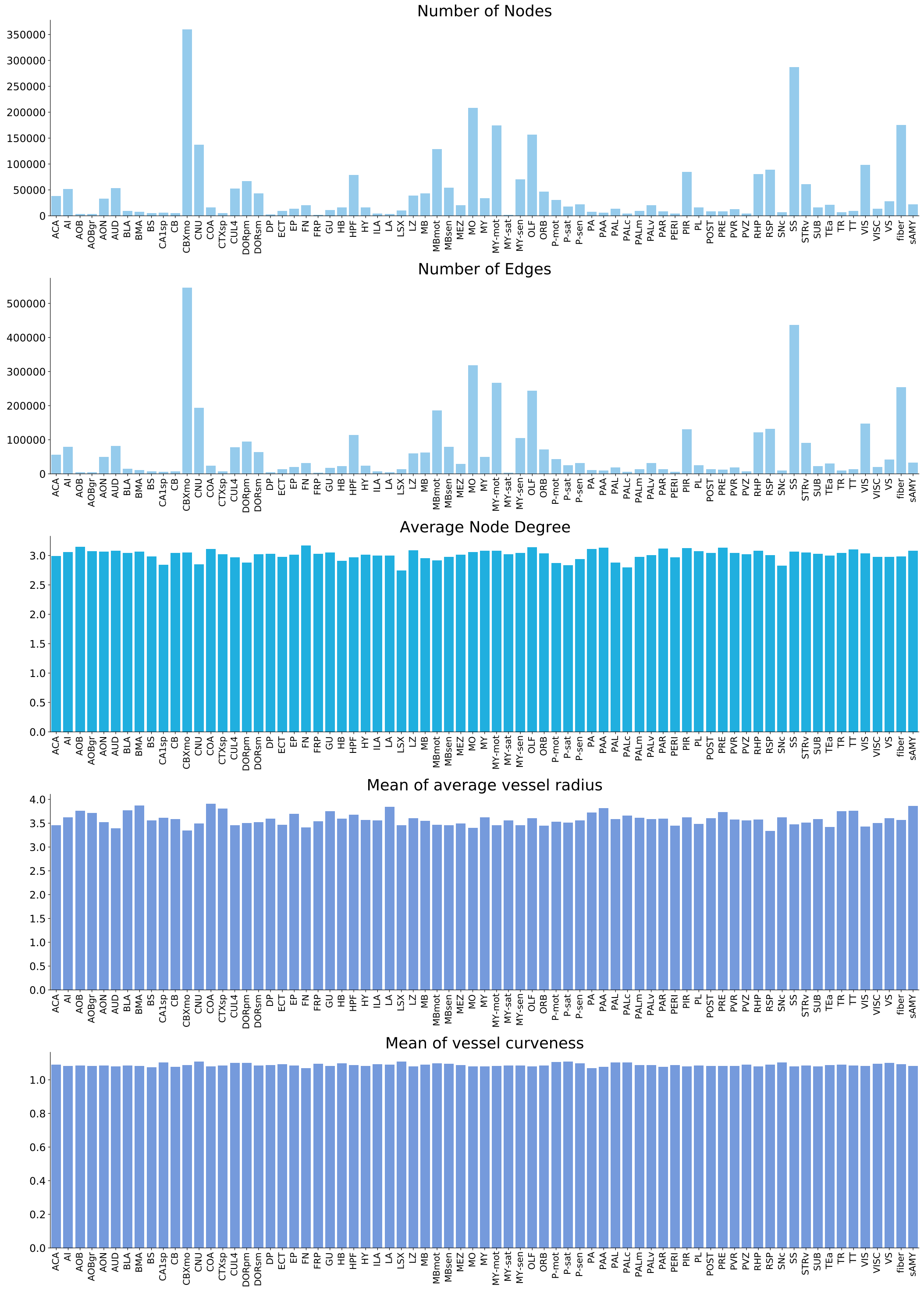

Figure 8: Different Node features of G plotted by the regions of the Allen brain atlas.

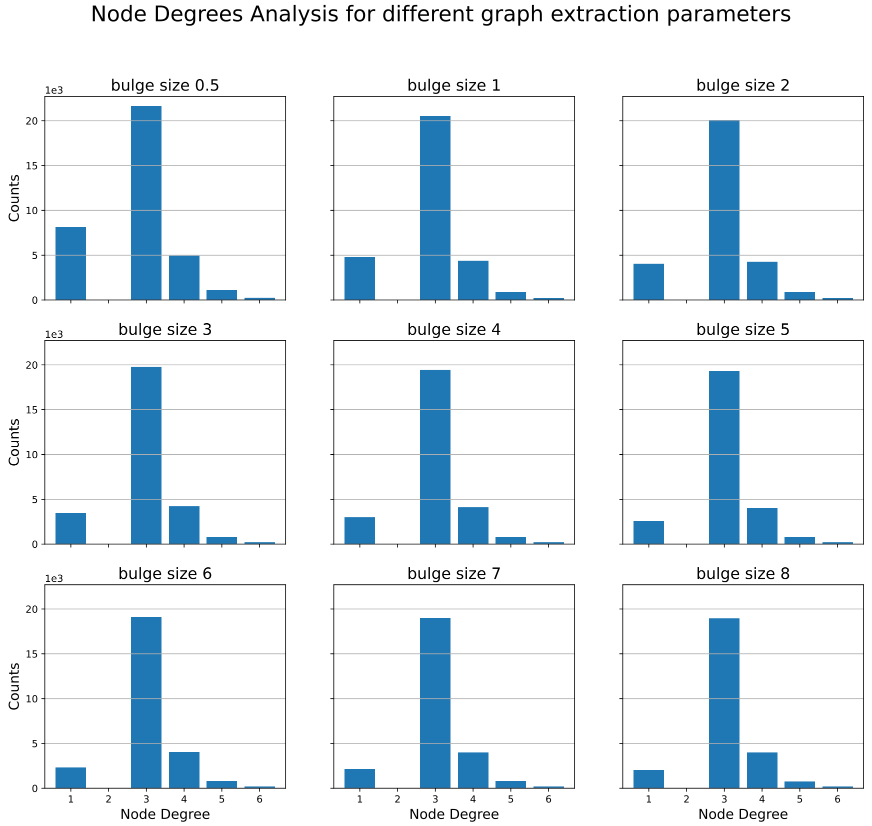

Figure 9: Bulge Size analysis in the *Voreen* pipeline for a parameter range of 0.5- 8.0.

For bulge _size = 3.0, we obtain a good relationship between capturing the essential vessels, while capturing the smoothness of the vascular trees. Following the recommendation of _size = 3.0 [31] for healthy vasculature, we keep _size = 3.0 as a maximum, to provide a reasonable _size = 3.0 value for future data with diseased animals.

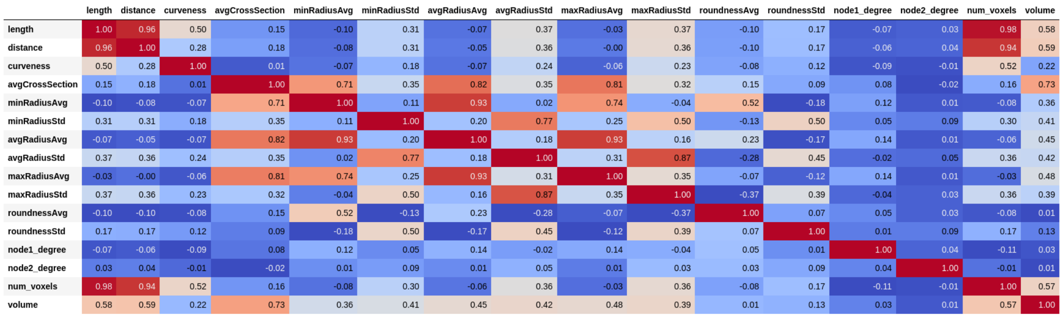

	length	distance	curveness	avgCrossSection	minRadiusAvg	minRadiusStd	avgRadiusAvg	avgRadiusStd	maxRadiusAvg	maxRadiusStd	roundnessAvg	roundnessStd	node1_degree	node2_degree	num_voxels	volume
length	1.00	0.96	0.50	0.15	-0.10	0.31	-0.07	0.37	-0.03	0.37	-0.10	0.17	-0.07	0.03	0.98	0.58
distance	0.96	1.00	0.28	0.18	-0.08	0.31	-0.05	0.36	-0.00	0.36	-0.10	0.17	-0.06	0.04	0.94	0.59
curveness	0.50	0.28	1.00	0.01	-0.07	0.18	-0.07	0.24	-0.06	0.23	-0.08	0.12	-0.09	-0.01	0.52	0.22
avgCrossSection	0.15	0.18	0.01	1.00	0.71	0.35	0.82	0.35	0.81	0.32	0.15	0.09	0.08	-0.02	0.16	0.73
minRadiusAvg	-0.10	-0.08	-0.07	0.71	1.00	0.11	0.93	0.02	0.74	-0.04	0.52	-0.18	0.12	0.01	-0.08	0.36
minRadiusStd	0.31	0.31	0.18	0.35	0.11	1.00	0.20	0.77	0.25	0.50	-0.13	0.50	0.05	0.09	0.30	0.41
avgRadiusAvg	-0.07	-0.05	-0.07	0.82	0.93	0.20	1.00	0.18	0.93	0.16	0.23	-0.17	0.14	0.01	-0.06	0.45
avgRadiusStd	0.37	0.36	0.24	0.35	0.02	0.77	0.18	1.00	0.31	0.87	-0.28	0.45	-0.02	0.05	0.36	0.42
maxRadiusAvg	-0.03	-0.00	-0.06	0.81	0.74	0.25	0.93	0.31	1.00	0.35	-0.07	-0.12	0.14	0.01	-0.03	0.48
maxRadiusStd	0.37	0.36	0.23	0.32	-0.04	0.50	0.16	0.87	0.35	1.00	-0.37	0.39	-0.04	0.03	0.36	0.39
roundnessAvg	-0.10	-0.10	-0.08	0.15	0.52	-0.13	0.23	-0.28	-0.07	-0.37	1.00	0.07	0.05	0.03	-0.08	0.01
roundnessStd	0.17	0.17	0.12	0.09	-0.18	0.50	-0.17	0.45	-0.12	0.39	0.07	1.00	0.01	0.09	0.17	0.13
node1_degree	-0.07	-0.06	-0.09	0.08	0.12	0.05	0.14	-0.02	0.14	-0.04	0.05	0.01	1.00	0.04	-0.11	0.03
node2_degree	0.03	0.04	-0.01	-0.02	0.01	0.09	0.01	0.05	0.01	0.03	0.03	0.09	0.04	1.00	-0.01	0.01
num_voxels	0.98	0.94	0.52	0.16	-0.08	0.30	-0.06	0.36	-0.03	0.36	-0.08	0.17	-0.11	-0.01	1.00	0.57
volume	0.58	0.59	0.22	0.73	0.36	0.41	0.45	0.42	0.48	0.39	0.01	0.13	0.03	0.01	0.57	1.00

Figure 10: Edge feature correlation plot.

Runtime of graph extraction: The *Voreen* pipeline used for graph extraction was run on a CPU cluster. We timed one exemplary graph extraction on this cluster using 8 logical CPUs. For one of our synthetic vessel datasets (500 × 500 × 401 pixels), the process described in Section 2 with 3 refinement iterations, resulting in 28538 nodes and 42727 edges required a total runtime of 3 minutes and 57 seconds. Importantly, the extraction times scale roughly linearly with the number of nodes which are extracted [31].

C.2 Post processing of graphs

In order to remove evident artifacts from the generated graphs we implemented rule based post processing or pruning steps.

Feature merging: In a small percentage of the extracted graphs ($< 1\%$), we obtain multiple edges e_{ij}^b for $b = 1 : B$ with the same vertices. This can be attributed to imaging artifacts and irregularities in the vessel staining process. For instance, holes in the segmentation mask, if not properly filled, can result in multiple edges spanning from the same source node n_i to the same target node n_j, respectively n_j to n_i, as the underlying graph is undirected. As our focus lies on biologically realistic graphs, in particular correct branching structures, we merge the edge features of two identically labeled edges by obtain approximations. As the greater percentage of irregularities have been already mitigated in various preprocessing steps, we are confident that approximations in a small number of edges should not affect the performance and generalization of the deep learning models. When we merge features we update them according to:

1. Length: $l_{ij} = \frac{1}{B}\sum_{b=1}^{B} l_{ij}^b$
2. Shortest Distance: $d_{ij} = \min_k\{d_{ij}^b\}$
3. Volume: $v_{ij} = \sum_{b=1}^{B} v_{ij}^b$
4. Number of Voxels: $nv_{ij} = \sum_{b=1}^{B} nv_{ij}^b$
5. Curvature: $\rho_{ij} = \frac{1}{B}\sum_{b=1}^{B} \rho_{ij}^b$
6. Mean Cross Section Area: $\alpha_{ij} = \sum_{b=1}^{B} \alpha_{ij}^b$

As radius features are highly shape-dependent, and highly variable in the vessel itself, we can only approximate the vessel attributes, as we cannot access the meta-information Voreen utilizes to calculate the minimum, average and maximum vessel radius and the corresponding standard deviations.

Consequently, we obtain the average radius by summing the average radius of all identically labeled edges. We calculate the standard deviation by obtaining the median of the mathematical relationship of standard deviation of average radius to average radius.

1. $\mu_{ij}^r = \mu_{ij}^{\bar{r}} = \mu_{ij}^R = \sum_{b=1}^{B} \mu_{ij}^{\bar{r}b}$
2. $\sigma_{ij}^r = \sigma_{ij}^{\bar{r}} = \sigma_{ij}^R = \sqrt{\sum_{b=1}^{B}(\sigma_{ij}^{\bar{r}b})^2}$

We fit a linear function $\mu^o = f(\mu^{\overline{r}}) = a \cdot \mu^{\overline{r}} + b$ to map the average radius $\mu^{\overline{r}}$ to the vessel roundness μ^o. Similarly to the radius approximations, we obtain the newly computed roundness standard deviation by obtaining the median of the mathematical relationship of standard deviation to roundness.

1. $\mu_{ij}^o = f(\mu_{ij}^{\overline{r}})$
2. $\sigma_{ij}^o = median\left[\left\{\frac{\sigma_{ij}^{ob}}{\mu_{ij}^{ob}}\right\}_{b=1:B}\right] \cdot \mu_{ij}^o$

The following properties are computationally updated.

- ν_{ij}^1 is updated.
- ν_{ij}^2 is updated.

D Baseline experimentation and discussion

D.1 Link prediction

We implemented a set of baselines from the literature. All of these implementations, including documentation are available in our GitHub repository . The model architecture, learning rate, number of GCN layers, dropout and batch size are the hyperparameters we optimized for our training and document below. We selected our models according to the highest ROC AUC score on the validation set.

In order to select the values, we employed Grid Search, please see the tables below. Owing to the huge size of our dataset, hyperparameter tuning is challenging. To overcome this challenge, we subsample a region of the mouse brain in order to create a small graph. To ensure we are not introducing any bias, we measured the KL-Divergence [53] to ensure that our small graph is representative of the whole brain in its distribution of

Table 5: Details of the hyper-parameters search for Link prediction with the selected parameters for the final training of each of our baseline models.

Model	Parameter Range	Selected Parameters	Model Select.
Matrix Factorization	lr $\in \{1 \cdot 10^{-3}, 1 \cdot 10^{-4}, 1 \cdot 10^{-5}\}$ num of layers $\in \{2, 3, 4\}$ hidden channels $\in \{32, 64, 128, 256\}$ dropout $\in \{0, 0.2, 0.5\}$	lr = $1 \cdot 10^{-5}$ num of layers = 3 hidden channels = 64 dropout = 0.2	epochs 3000
MLP	lr $\in \{1 \cdot 10^{-2}, 1 \cdot 10^{-3}, 1 \cdot 10^{-4}, 1 \cdot 10^{-5}\}$ num of layers $\in \{2, 3, 4\}$ hidden channels $\in \{128, 256, 512\}$ dropout $\in \{0, 0.2, 0.5\}$	lr = $1 \cdot 10^{-5}$ num of layers = 4 hidden channels = 256 dropout = 0.2	epochs 3000
GCN [14]	lr $\in \{1 \cdot 10^{-2}, 1 \cdot 10^{-3}, 1 \cdot 10^{-4}, 1 \cdot 10^{-5}\}$ num of layers $\in \{2, 3, 4\}$ hidden channels $\in \{128, 256, 512\}$ dropout $\in \{0, 0.2, 0.5\}$	lr = $1 \cdot 10^{5}$ num of layers = 2 hidden channels = 256 dropout = 0.2	epochs 3000
GNN + N2Vec Embeddings [43]	lr $\in \{1 \cdot 10^{-2}, 1 \cdot 10^{-3}, 1 \cdot 10^{-4}, 1 \cdot 10^{-5}\}$ num of layers $\in \{2, 3, 4\}$ hidden channels $\in \{128, 256, 512\}$ dropout $\in \{0, 0.2, 0.5\}$	lr = $1 \cdot 10^{-5}$ num of layers = 2 hidden channels = 256 dropout = 0.2	epochs 3000
GNN + SAGE [17]	lr $\in \{1 \cdot 10^{-2}, 1 \cdot 10^{-3}, 1 \cdot 10^{-4}, 1 \cdot 10^{-5}\}$ num of layers $\in \{2, 3, 4\}$ hidden channels $\in \{128, 256, 512\}$ dropout $\in \{0, 0.2, 0.5\}$	lr = $1 \cdot 10^{-4}$ num of layers = 3 hidden channels = 16 dropout = 0.5	epochs 3000
GNN + SAGE [17] + N2Vec Embeddings [43]	lr $\in \{1 \cdot 10^{-02}, 1 \cdot 10^{-3}, 1 \cdot 10^{-4}, 1 \cdot 10^{-5}\}$ num of layers $\in \{2, 3, 4\}$ hidden channels $\in \{128, 256, 512\}$ dropout $\in \{0, 0.2, 0.5\}$	lr = $1 \cdot 10^{-3}$ num of layers = 2 hidden channels = 16 dropout = 0.5	epochs 3000
SEAL [25]	lr $\in \{1 \cdot 10^{-4}, 1 \cdot 10^{-5}\}$ num of layers $\in \{2, 3, 4\}$ hidden channels $\in \{32, 64, 128\}$ dropout $\in \{0, 0.2, 0.5\}$ num of hops$\in \{1, 2, 3\}$ labeling $\in$ {drnl,de,de+,zo} model = DGCNN, GCN	lr = $1 \cdot 10^{-4}\}$ num of layers = 2 hidden channels = 32 dropout = 0.0 num of hops = 1 labeling = drnl model = DGCNN	epochs 100
N2Vec [43]	lr $\in \{1 \cdot 10^{-2}, 1 \cdot 10^{-3}, 1 \cdot 10^{-4}, 1 \cdot 10^{-5}, 1 \cdot 10^{-6}\}$ walk length $\in \{5, 10, 20\}$ walks per_node $\in \{5, 10, 20\}$ embedding_dim $\in \{16, 32, 64, 128, 256\}$	lr = $1 \cdot 10^{-6}$ walk length = 5 walks_per_node = 10 embedding_dim = 64	epochs 2

vasculature. We selected the best set of hyperparameters on the small graph and used it on the actual graph with small modifications if needed. We summarize our results in Table 5 and Table 6.

For Matrix Factorization, we tune the number of layers, hidden channels and dropout rate. To estimate the best hyperparameters, we employed grid search. We observe that the Matrix Factorization method is not sensitive to the choice of hyper-parameters as long as they are in a reasonable range (learning rate 1e-3 to 1e-5, dropout 0 to 0.5, hidden channels 32 to 256). We obtained the best results for a learning rate of 1e-4 with 3 layers, 64 hidden channels and a dropout rate of 0.2. When extending to the entire BALBc1 whole mouse brain dataset (5.35 million edges, 3.54 million nodes), we reduced the number of hidden channels to 64 owing to GPU memory constraints. We experimentally found out that the model with 64 channels was easily able to overfit to the training data, showing that the model is sufficiently complex.

The MLP model is trained with the Adam optimizer and a learning rate of 1e-4. This combination of hyperparameters provides us the best performance on the validation and test splits. We experimented with fully connected layers of 128 and 256 features, the latter resulting in better scores. Thus, our final model has 4 layers each with 256 channels.

For the Graph Neural Networks, we use two setups. A GCN setup without embeddings (which we refer to as GCN in the experiments) and a GCN with embeddings (which we refer to as GCN + Node2Vec Embeddings in the experiments, Tab. 5). Both models are trained with Adam and 1e-5 and 1e-7 learning rate, respectively.

We discover that GCN+node embeddings do not perform superior to the GCN which is trained only on the node features. Moreover, in our experiments, we find that the predictions made by the models result in scores close to chance (approx. 51 for both). The model is overfitting on the training data almost immediately and is not able to generalize to the unseen data. Reducing the model complexity by reducing the number of layers, hidden channels and increasing the dropout did not improve performance.

We observe poor generalization and immediate overfitting in all cases. We hypothesize that this behaviour is caused by the model not being able to distinguish symmetrically placed nodes while making the prediction (something that the SEAL algorithm achieves using the Labeling trick). Our experiments done using SEAL with a similar set of hyper-parameters substantiate this hypothesis. Please refer to the section on SEAL for more details below.

In our experiments, we find that the GraphSAGE models tend to outperform the GCN baseline. The *ROC AUC* increases to approximately 60 meaning a performance boost of almost 7% We initialized the nodes with the Node2Vec embeddings[43] (we refer to this model as GraphSAGE + Node2Vec Embeddings) and findthat the inclusion of pretrained Node2Vec embeddings as features leads to deterioration in model performance. We observed the best model performance with a shallow network (2 hidden layers), a learning rate of $1e-4$ and 0.5 dropout. The hyperparameters were chosen according to the GCN baseline.

When we ran our model on the entire mouse brain graph, we observed behaviour similar to GCN and GCN+embedding. Although the GraphSAGE performance is slightly superior to the GCN baseline, it is still dwindling in the region of being random (approx 59%). The GraphSAGE algorithm tends to improve the update of node features by concatenating the features of the node and its aggregated neighbourhood features. As such, this may enable the network to assign different weights to the self nodes and its neighbours. However, this does not allow it to break the symmetry while performing the link prediction task. Indicating that these models suffer from the same issue in regards to node labeling as was described in the GCN discussion above. Further, inclusion of Node2Vec features decreases the performance resulting in an 53% ROC AUC value.

Since Node2Vec is an unsupervised process we use the SGD optimizer with negative sampling, to maximize the log likelihood objective on the random walks in the graph. We perform a hyperparameter search on the learning rate, walk lengths, walks per node and embedding dimension.

We find the best combination to be a walk length of 5, 10 walks per node and an embedding dimension of 64. In our experiments with the small sub-graph, we observed that the loss quickly plateaus after 3 epochs. We use the same hyperparameter combination for the entire mouse brain graph. We observe that the inclusion of Node2Vec features does not improve performance and in most cases, leads to worse results. Empirically we observe that the inclusion of Node2Vec features is not useful for the link prediction task and as discussed above, the Labeling trick constitutes a much more important component.

SEAL: For the SEAL algorithm we implement a similar hyperparameter search. We discover a general pattern in the selection of different labeling tricks, and find the DE and DRNL to perform best on the training set.

Moreover, we find SEAL to perform very well at different rates. However, we do get a general trend of optimal performance for a learning rate of $1e-4$ and 2 hops. For the whole brain graph, we find Double-Radius Node Labeling (DRNL) to better capture the hierarchical structure [25]. Further, a DGCNN outperforms a GCN. When training on a small region of interest we observe a gradual improvement for up to 50 epochs, for the whole brain graph we discover that SEAL almost converges the first epochs while inducing significant inductive bias, making it the superior model for our spatial and hierarchical graph. The training quickly plateaus. In all our experiments, the SEAL method performs best amongst all the baselines. All performance measures are given in Table 3 in the main paper.

D.2 Node classification

Similar to the link prediction task, we employ a grid Search for hyperparameters. For each graph neural network, we explore the number of layers, hidden channels, learning rate and dropout ratio on the smaller sets validation and test set. For each model, if applicable, we select a set of hyper-parameters specific to the architecture and thus optimize. We selected our models according to the highest ROC AUC score on the validation set.

The Cluster GCN algorithm provides a memory efficient alternative to other graph learning algorithms and is specifically designed to handle large-scale graphs efficiently. The number of partitions constitutes the essential hyper-parameter. We find it to consistently outperform other models, irrespective of its number of partitions.

Further we implement the base GCN by Kipf et.al. and extend it to the GNN GCN and GNN SAGE (SAGE introduces convolutional operator). For all we vary the number of hidden channels, number of layers and dropout ratio. In direct comparison, the GNN SAGE outperforms the GNN GCN by high margins (>10%) for the ROC-AUC metric on the whole brain graph. Similar to the link prediction task, indicating that the base GCN is not suited for this task.

For the Node2Vec embeddings of the node classification task, we find similar trends for walk length, walks per node and embedding dimension as in the link prediction task. Please refer to Table 6 for the exact hyper-parameter selection.

For the MLP we select a comparative number of layers and obtain the best result for a high dropout ratio of 0.4. We observe that the the model is unable to generalize to unseen data, indicating the absence of an appropriate inductive bias.

For the MLP-CS, we selected similar values in comparison to the MLP implementation. Incorporating the Correct&Smooth methodology into the model increases the F1 score but does not improve the metrics which account for imbalanced datasets.

The SIGN applies subsampling techniques. Similar to the graph neural network baselines, we explore the hidden channels and number of layers. We obtain the best for a high model complexity with 4 layers and 512 hidden channels. The model converges very fast with a high learning rate but performs only on par with the base GCN.

Table 6: Details of the hyper-parameter search for node classification with the final parameters selected for the our baseline models.

Model	Parameter Range	Selected Parameters	Model Select.
Cluster-GCN	lr $\in \{2 \cdot 10^{-5}, 1 \cdot 10^{-4}, 1 \cdot 10^{-3}, 3 \cdot 10^{-3}\}$ number of layers $\in \{3, 4, 5\}$ hidden channels $\in \{128, 256, 512\}$ number of partitions $\in \{3, 6, 9\}$ dropout $\in \{0.0, 0.2, 0.5\}$	lr = $3 \cdot 10^{-3}$ number of layers = 4 hidden channels = 128 number of partitions = 9 dropout = 0.2	1500 epochs
GNN	lr $\in \{2 \cdot 10^{-5}, 1 \cdot 10^{-4}, 1 \cdot 10^{-3}, 3 \cdot 10^{-3}\}$ number of layers $\in \{3, 4, 5\}$ hidden channels $\in \{32, 128, 256, 512, 1024\}$ dropout $\in \{0.1, 0.4, 0.5\}$	lr = $3 \cdot 10^{-3}$ number of layers = 3 hidden channels = 256 dropout = 0.4	1500 epochs
GNN-SAGE	lr $\in \{2 \cdot 10^{-5}, 1 \cdot 10^{-4}, 1 \cdot 10^{-3}, 3 \cdot 10^{-3}\}$ number of layers $\in \{2, 3, 4\}$ hidden channels $\in \{32, 128, 256, 512, 1024\}$ dropout $\in \{0.0, 0.2, 0.4\}$	lr = $3 \cdot 10^{-3}$ number of layers = 4 hidden channels = 128 dropout = 0.4	1500 epochs
Graph-Saint	lr $\in \{1 \cdot 10^{-6}, 1 \cdot 10^{-5}, 1 \cdot 10^{-4}, 1 \cdot 10^{-3}, 5 \cdot 10^{-3}, 1 \cdot 10^{-2}\}$ number of layers $\in \{2, 3, 4\}$ hidden channels $\in \{64, 256, 512, 1024\}$ walk length $\in \{3, 5, 7\}$ dropout $\in \{0.0, 0.35, 0.5\}$	lr = $5 \cdot 10^{-4}$ number of layers = 4 hidden channels = 64 walk length = 7 dropout = 0.35	1000 epochs
SIGN	lr $\in \{1 \cdot 10^{-5}, 1 \cdot 10^{-4}, 1 \cdot 10^{-3}, 5 \cdot 10^{-3}\}$ number of layers $\in \{2, 3, 4\}$ hidden channels $\in \{32, 64, 128, 256, 512, 1024\}$ dropout $\in \{0.0, 0.1, 0.3, 0.5\}$	lr = $1 \cdot 10^{-3}$ number of layers = 3 hidden channels = 128 dropout = 0.1	1000 epochs
MLP	lr $\in \{2 \cdot 10^{-5}, 1 \cdot 10^{-4}, 5 \cdot 10^{-4}, 1 \cdot 10^{-3}, 3 \cdot 10^{-3}, 1 \cdot 10^{-2}\}$ number of layers $\in \{2, 3, 4\}$ hidden channels $\in \{32, 128, 256, 512\}$ dropout $\in \{0.0, 0.3, 0.4\}$	lr = $1 \cdot 10^{-3}$ number of layers = 3 hidden channels = 256 dropout = 0.0	1500 epochs
SpecMLP-W + C&S	lr $\in \{1 \cdot 10^{-5}, 5 \cdot 10^{-4}, 1 \cdot 10^{-3}, 3 \cdot 10^{-3}\}$ number of layers $\in \{3, 4, 5\}$ hidden channels $\in \{128, 512, 1024\}$ dropout $\in \{0.0, 0.5\}$	lr = $1 \cdot 10^{-3}$ number of layers = 5 hidden channels = 128 dropout = 0.5	1500 epochs
N2Vec	lr $\in \{1 \cdot 10^{-5}, 1 \cdot 10^{-3}, 1 \cdot 10^{-2}\}$ walk length $\in \{16, 40\}$ walks per node $\in \{4, 10\}$ embedding dim $\in \{16, 128\}$ batch size $\in \{16, 128\}$ epochs $\in \{1, 5, 32\}$	lr = $1 \cdot 10^{-2}\}$ walk length = 40 walks per node = 10 embedding dim = 128 batch size = 128 epochs = 5	5 epochs
SpecMLP-W + C&S + N2Vec	lr $\in \{1 \cdot 10^{-5}, 5 \cdot 10^{-4}, 1 \cdot 10^{-3}, 3 \cdot 10^{-3}\}$ number of layers $\in \{3, 4, 5\}$ hidden channels $\in \{128, 512, 1024\}$ dropout $\in \{0.0, 0.5\}$	lr = $1 \cdot 10^{-3}$ number of layers = 5 hidden channels = 128 dropout = 0.5	1500 epochs

D.3 Graph explainability

We use the concept of the GNNExplainer [54] as an initial graph explainability approach. GNNExplainer aims to identify a compact subgraph with a small subset of node features which play a crucial role in a given GNN for node classification.

We decided to run an initial GNNExpainer experiment on a small but representative subgraph of roughly 16000 nodes and 18000 edges. We predict node 2290 with our trained SAGEConv based model for the node classification task on the Line Graph, see Figure 11. The visualization represents the nodes which our model considers important for the node prediction of 2290. One can observe, that the model relies heavily on its immediate neighbourhood (denoted by thick edges). In our plot, we have visualized a 5 hop neighbourhood, for a SAGEConv GCN with 4 layers. Naturally, the model does not consider any node beyond its 4 hop neighbourhood in the computational graph.

D.4 Computational resources

All of our neural network trainings were performed on an Nvidia Quadro RTX 8000 GPU with 48GB memory.

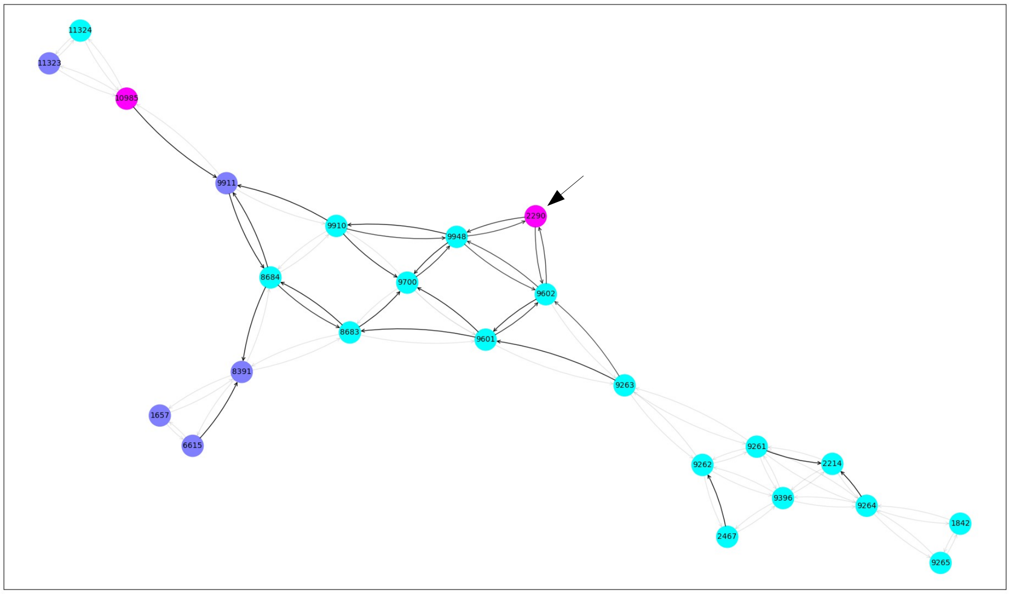

Figure 11: Graph explainability plot based on the GNNExplainer concept [54]. Our considered node of interest is node 2290. Pink nodes indicate nodes belonging artery/vein class, blue indicated arterioles/venules and green indicates capillaries. Thick edges represent a strong influence on the prediction. Please note that the considered graph is a spatial **Line Graph**.

E Datasheet for datasets

This description is an additional documentation intended to enhance reproducibility and follows the **Datasheets for Datasets**[3] working paper developed for the machine learning community.

- **For what purpose was the dataset created?** To foster research development in machine learning for graphs, in particular its application to neuroscience - specifically the brain vessel graph composition.
- **Who created the dataset (e.g., which team, research group) and on behalf of which entity (e.g., company, institution, organization)?** The dataset was created thorough a collaborative effort by neuro-scientists and computer-scientists at the Technical University of Munich and the Helmholtz Zentrum München (under the supervision of Ali Ertuerk, Bjoern Menze and Stephan Günnemann).
- **Who funded the creation of the dataset?** The creation of the dataset was funded only indirectly via the salaries of the scientists at the Technical University of Munich and the other corresponding affiliations of the authors.

E.1 Composition

- **What do the instances that comprise the dataset represent?** Our dataset represents graph representations of the whole brain vasculature. We are providing two alternative representations of the vascular graph. First, a representation where individual vessels are represented as edges in a Graph; and second, the corresponding Line graph were vessels are represented as nodes. One can interpret the graph of a single mouse brain as a single instance. Alternatively one can interpret each vessel (edge) and bifurcation (node) as a physical instance.
- **How many instances are there in total (of each type, if appropriate)?** By the instance definition of whole brain graphs as instances we are providing 17 graphs (with the option to generate the line graph) from 3 imaging sources as instances. In the future we plan to extend the dataset as soon as other whole brain vessel segmentations are made publicly available (open source).

  By the definition of vessels and bifurcation points we have millions of instances for each. Please see Table 1 for detailed numbers.
- **Does the dataset contain all possible instances or is it a sample of instances from a larger set?** We are providing all available instances.
- **What data does each instance consist of?** In either case, please provide a description. By definition 1); each instance represents a whole mouse brains' vascular graph saved in the widely used CSV format. By definition 2) each node represents a bifurcation point and each edge a vessel.
- **Is there a label or target associated with each instance?** Yes, in case of the edge and node instances, the information from the extracted graphs (features) can be used as the instance labels. E.g. in our node classification benchmark we use the vessel radius binned in three classes as an instance label.
- **Is any information missing from individual instances?** No, all of the information has been provided.
- **Are relationships between individual instances made explicit?** In our dataset the instances (brain graphs) are independent.
- **Are there recommended data splits (e.g., training, development/validation, testing)?** For the benchmark we split one whole brain into a train, validation and test set of 80/10/10.
- **Are there any errors, sources of noise, or redundancies in the dataset?** Our graph extraction is based on experimental imaging and segmentation techniques. Therefore, errors and uncertainty are inherent. We discuss these in detail in our Limitations section in the conclusion.
- **Is the dataset self-contained, or does it link to or otherwise rely on external resources (e.g., websites, tweets, other datasets)?** The provided dataset is self-contained.
- **Does the dataset contain data that might be considered confidential (e.g., data that is protected by legal privilege or by doctor-patient confidentiality, data that includes the content of individuals' non-public communications)?** No.
- **Does the dataset contain data that, if viewed directly, might be offensive, insulting, threatening, or might otherwise cause anxiety?** No.
- **Does the dataset relate to people?** No.

---

[3] `https://arxiv.org/abs/1803.09010`

E.2 Collection process

- **How was the data associated with each instance acquired?** The data was generated from a set of different publicly available datasets of whole murine brain images and segmentations. The specifics of the generation of each of these public segmentations are specified in the referenced literature and their licenses, see B.4.
- **What mechanisms or procedures were used to collect the data?** We use the *Voreen* framework [31, 30] to generate graphs from segmentations. *Voreen* is a software which runs on a CPU.
- **If the dataset is a sample from a larger set, what was the sampling strategy?** The dataset is complete.
- **Who was involved in the data collection process (e.g., students, crowdworkers, contractors) and how were they compensated (e.g., how much were crowdworkers paid)?** Only researchers (co-authors) of the Technical University of Munich and the Helmholtz Zentrum München were involved in the data collection process.
- **Over what timeframe was the data collected?** Does this timeframe match the creation timeframe of the data associated with the instances (e.g., recent crawl of old news articles)? The generation of the dataset, including dedicated research to gather the base segmentations and to optimize the graph extraction procedure took roughly one year.
- **Were any ethical review processes conducted (e.g., by an institutional review board)?** Our work is purely based on public and open sourced data. However, ethical review processes were carried out for each of these open sourced base segmentation sets:

  The three graphs from Ji et al. [1] are based on animal experiments, they followed the Guide for the Care and Use of Laboratory Animals and have been approved by the Institutional Animal Care and Use Committee, for details see `https://doi.org/10.1016/j.neuron.2021.02.006`.

  The animal experiments for the nine datasets from the VesSAP paper [6] were carried out under approval of the ethical review board of the government of Upper Bavaria (Regierung von Oberbayern, Munich, Germany), and in accordance with European directive 2010/63/EU for animal research, for details see `https://doi.org/10.1038/s41592-020-0792-1`.
- **Does the dataset relate to people?** No.

E.3 Preprocessing/cleaning/labeling

- **Was any preprocessing/cleaning/labeling of the data done ?** Yes, this actually constitutes a core contribution of our work, therefore please refer to Section 2 in the main paper and to Supplementary section C.
- **Was the 'raw' data saved in addition to the preprocessed/cleaned/labeled data (e.g., to support unanticipated future uses)?** The raw data are the base segmentations. They are publicly available, the links are provided in Supplementary section B.4.
- **Is the software used to preprocess/clean/label the instances available?** The *Voreen* software used for the graph extraction is publicly available, see our github repo.

E.4 Uses

- **Has the dataset been used for any tasks already?** In its current size and level of labeling detailization, the dataset was not used before (besides for the presented link prediction and node classification in this work).
- **Is there a repository that links to any or all papers or systems that use the dataset?** If so, please provide a link or other access point. Yes, `https://github.com/jocpae/VesselGraph`.
- **What (other) tasks could the dataset be used for?** In the main paper we discussed two standard tasks in machine learning on graphs; we think that our dataset can serve as a starting point for many interesting research directions in machine learning research and neurovascular research.
- **Is there anything about the composition of the dataset or the way it was collected and preprocessed/cleaned/labeled that might impact future uses?** No.
- **Are there tasks for which the dataset should not be used?** No.

E.5 Distribution

- **Will the dataset be distributed to third parties outside of the entity (e.g., company, institution, organization) on behalf of which the dataset was created?** Our Dataset is open sourced under a CC Attribution-NonCommercial 4.0 International (CC BY-NC 4.0) License. Therefore all third parties can openly access it.

- **How will the dataset will be distributed (e.g., tarball on website, API, GitHub)?** Yes, our DOI is `10.5281/zenodo.5301621`
- **When will the dataset be distributed?** The dataset is available from the moment of submission.
- **Will the dataset be distributed under a copyright or other intellectual property (IP) license, and/or under applicable terms of use (ToU)?** Our Dataset is open sourced under a CC Attribution-NonCommercial 4.0 International (CC BY-NC 4.0) License.
- **Have any third parties imposed IP-based or other restrictions on the data associated with the instances?** No.
- **Do any export controls or other regulatory restrictions apply to the dataset or to individual instances?** No.

E.6 Maintenance

- **Who is supporting/hosting/maintaining the dataset?** The dataset is initially supported and maintained by the lead authors of this paper. The data is initially hosted on a university server and links are provided in the github repository `https://github.com/jocpae/VesselGraph`. In the long term we aim to incorporate our dataset into the open graph benchmark (OGB) initiative[4].
- **How can the owner/curator/manager of the dataset be contacted (e.g., email address)?** Of course via e-mail: `johannes.paetzold@tum.de` and via the github repository, see question above.
- **Is there an erratum?** At this stage no, but we are happy to track them in a dedicated file in our github repository.
- **Will the dataset be updated (e.g., to correct labeling errors, add new instances, delete instances)?** Yes, we release the dataset on open platforms on which we plan to continuously update our dataset. Particularly to add novel whole brain vessel graphs to the dataset.
- **If the dataset relates to people, are there applicable limits on the retention of the data associated with the instances?** The dataset does not relate to people.
- **Will older versions of the dataset continue to be supported/hosted/maintained?** When novel versions of the dataset will be released we will continue to host and maintain the old versions of the dataset.
- **If others want to extend/augment/build on/contribute to the dataset, is there a mechanism for them to do so?** We encourage other researches to exactly that. Depending on their contribution they can contribute to our github repository (in case of implementations) or reach out to us via e-mail in case they want to contribute graphs to the dataset. Our dataset and code are open sourced, see above.

---

[4] `https://ogb.stanford.edu/`

Figure Copyrights

In the following the licenses for the figures which are not created by myself or are not part of one of my papers are provided.

Licensed Content Title	nnU-Net: a self-configuring method for deep learning-based biomedical image segmentation
License Number	5293531428666
License date	Apr 21, 2022
Licensed Content Publisher	Springer Nature
Licensed Content Publication	Nature Methods
Licensed Content Author	Fabian Isensee et al.
Licensed Content Date	Dec 7, 2020
Type of Use	Thesis/Dissertation
Requestor type	academic/university or research institute
Format	print and electronic
Portion	Fig. 1

Table E.1: Copyright for Figure 2.1 on Examples of CNN based segmentation of medical and biological images.

Licensed Content Title	Tau induces blood vessel abnormalities angiogenesis-related gene expression in P301L transgenic mice and human Alzheimer's disease
License	Open Access under the Attribution-NonCommercial-NoDerivatives 4.0 International (CC BY-NC-ND 4.0)
Author	Rachel E. Bennett et al.
Publication Date	Jan 22, 2018
Publisher	PNAS

Licensed Content Title	Traumatic brain injury results in acute rarefication of the vascular network
License	Open Access under the Attribution 4.0 International (CC BY 4.0) License
Author	Andre Obenaus et al.
Publication Date	Mar 22, 2017
Publisher	Springer Nature

Licensed Content Title	Chronic Cerebral Hypoperfusion Induced Synaptic Proteome Changes in the rat Cerebral Cortex
License Number	5306591133461
License date	May 12, 2022
Licensed Content Publisher	Springer Nature
Licensed Content Publication	Molecular Neurobiology
Licensed Content Author	Katalin Völgyi et al.
Licensed Content Date	Jun 15, 2017
Type of Use	Thesis/Dissertation
Requestor type	academic/university or research institute
Format	print and electronic
Portion	Fig. 1

Table E.2: Copyright for Figure 4.2 on common vessel pathologies.